UNIVERSITY OF LIVERPOOL

Theoretical and Experimental Study of Damage Identification of Beams and Plates

Thesis submitted in accordance with the requirements of the University of Liverpool for the degree of Doctor in Philosophy

By

Shancheng Cao

October 2017

Abstract

Structural characteristic deflection shapes (CDS's) such as mode shapes and operational deflection shapes which contain spatial information of structures are highly sensitive for damage detection and localisation in beam- or plate- type structures. Despite substantial advances in this kind of methods, several issues must be addressed to boost their efficiency and practical applications, including the following: (1) The estimation of CDS's involves substantial inaccuracies and is mainly affected by operational, environmental, measurement and computational uncertainties. (2) The curvature estimation of CDS's is much more sensitive to measurement noise. (3) The extraction of damage-caused singularities from CDS's or their curvatures is difficult when the baseline data of healthy structures is not available. (4) Damage index for multi-damage identification is challenging due to the different damage location sensitivities of each CDS. These problems have been investigated and the objective of this study is to enhance the accuracy and noise robustness of baseline-free damage detection and localisation.

The original contributions of this study have been made in several aspects. Firstly, common principal component analysis is proposed to enhance accuracy of mode shape estimation in operational modal analysis, which statistically evaluates the common subspace bases of a set of covariance or power spectral density matrices as the mode shapes. Secondly, without the baseline data of healthy structures, polynomial fitting approaches and low-rank models are investigated for damage localisation, which extract the damage-induced local shape singularities by using only mode shapes or mode shape curvatures of damaged structures. Thirdly, in order to fairly incorporate damage information of several modes, two robust damage indexes are proposed for beam-type structures and plate-type structures, respectively. The above studies focus

on linear damage such as open cracks in beam or plate structures without nonsmooth mass and stiffness distribution. Apart from these, the identification of fatigue cracks in stepped beam-type structures is investigated as well.

In the theoretical aspect, the relationship between damage and structural characteristic deflection shapes is explained. Then, the finite element models of beams and plates are coded in MATLAB, which are validated by comparing corresponding results with the commercial software ABAQUS. Moreover, the numerical models of beams and plates with multiple damage are used to verify the feasibility and efficiency of the proposed methods in damage identification. Here, the damage is introduced by reducing the depth of beams or thickness of plates. In the experimental aspect, beams and plates with multiple damage are tested to demonstrate the proposed damage detection and localisation methods. In order to acquire the data of a large number of measurement points, the advanced scanning laser Vibrometer is used.

It is found that the proposed mode shape estimation approaches are demonstrated to be more accurate and noise robust than the traditional frequency domain decomposition and time domain decomposition methods. Additionally, the noise effects on spatial domain features such as mode shape and mode shape curvatures can be significantly reduced by the polynomial fitting or multi-scale approaches. Furthermore, the developed robust multi-damage indexes for beams and plates are validated to be effective by using numerical simulations and experimental results. Finally, the proposed breathing crack identification approaches are effective in localising the breathing cracks but insensitive to the steps of the beams.

Acknowledgements

I would like to express my sincere gratitude and appreciation to my supervisor Professor Huajiang Ouyang for offering me the opportunity to pursue my PhD degree at the University of Liverpool. His supervision and support at all levels has helped me overcome many difficulties in research as well as daily life. Also, I want to thank Professor John Mottershead for his valuable suggestions and encouragements.

Moreover, I gratefully acknowledge the joint scholarship programme provided by the Chinese Scholarship Council and The University of Liverpool, which covers the tuition fees, research fees and living expenses. It guarantees the completion of my study for four years.

Many more thanks should be given to my colleagues and academic staff in the Dynamics and Control Group at the University of Liverpool for their suggestions and academic supports. I feel motivated and encouraged in this research environment.

Finally, I want to sincerely thank the supports of my family and friends for the past four years. It is their love and understanding that encourage me to finish the research and this thesis.

List of Publications

Journal papers:

1. **S. Cao**, H. Ouyang, *Robust structural damage detection and localization based on joint approximate diagonalization technique in frequency domain.* Smart Materials and Structures, 2017. DOI:10.1088/0964-1726/26/1/015005.

2. **S. Cao**, H. Ouyang, *Output-only damage identification using enhanced structural characteristic deflection shapes and adaptive gapped smoothing method,* ASME Journal of Vibration and Acoustics, 2017. DOI: 10.1115/1.4037469.

3. Z. Lu, D. Dong, **S. Cao**, H. Ouyang, C. Hua, *Multi-crack Localization in Rotors Based on Proper Orthogonal Decomposition Using Fractal Dimension and Gapped Smoothing Method*. Shock and Vibration, 2016. DOI: 10.1155/2016/2375859.

4. Z. Lu, D. Dong, H. Ouyang, **S. Cao**, C. Hua, *Localization of breathing cracks in stepped rotors using super-harmonic characteristic deflection shapes based on singular value decomposition in frequency domain,* Fatigue & Fracture of Engineering Materials & Structures, 2017. DOI: 10.1111/ffe.12601.

5. **S. Cao**, H. Ouyang, *Robust Multi-Damage Localisation Based on Changes of Common Eigenvectors of Covariance Matrices*, Mechanical Systems and Signal Processing, 2017. Submitted.

6. J. Yang, H. Ouyang, D. Stancioiu, **S. Cao**, *Dynamic responses of a four-span continuous plate structure subjected to two moving cars with time-varying speeds*, Archives of Civil and Mechanical Engineering, 2017. Submitted.

Conference papers:

1. **S. Cao**, H. Ouyang, *Multi-damage identification based on joint approximate diagonalisation and robust distance measure,* Journal of Physics: Conf. Series 842 (2017) 012022. 12th International Conference on Damage Assessment of Structures, Kitakyushu, Japan, 2017. DOI:10.1088/1742-6596/842/1/012022.

2. **S. Cao**, H. Ouyang, *Robust output-only multi-damage localisation using common eigenvector analysis and a measure of covariance changes.* International Conference on Structural engineering Dynamics, Ericeira, Portugal, 2017.

3. **S. Cao**, H. Ouyang, *Multi-crack Localization in Beam Structures Using Deviations between Empirical Cumulative Distributions of Vibration Responses*. The 7th International Congress on Vibration Engineering, Shanghai, China, 2015.

Table of Contents

List of Figures

List of Tables

Nomenclature

c	Coefficient of polynomial fitting
d, u	Subscript or superscript to indicate the damaged state and the undamaged state
d_x, d_y	The distance between two successive measurement points along *x* and *y* directions (m)
D	Plate flexural rigidity
E	Young's modulus (Pa)
$\mathbf{E}, \mathbf{e}$	Measurement noise matrix and vector
$\mathbf{f}(t)$	Force vector (N)
h	The thickness of a plate (m)
H	Conjugate transpose
H_{p}	Gaussian curvature
I	Area moment of inertia of cross section of a beam
K	Number of covariance matrices
K_{p}	Mean principal curvature
j	The imaginary unit
k_1, k_2	Stiffness of springs (N/m)
l	Indicator of the measurement point
$\mathbf{L}$	Low-rank matrix
n, n_1, n_2	Number of rows or columns of a matrix
n_{level}	Noise level
$\mathbf{n}$	Unit normal vector of mode shape surface at a point

$\mathbf{n}_{\mathrm{n}}$	Normally distributed random value vector with a zero mean and a unit variance
M_x, M_y, M_{xy}	The bending moments of *x* and *y* coordinates and the twisting moment
$\mathbf{M}, \mathbf{K}, \mathbf{C}$	Mass, stiffness and damping matrix
N	Number of measurement samples
N_{m}	Number of measurement locations
N_p	Number of polynomial terms
N_{r}	Number of mode shapes
p	Order of polynomial fitting
$\mathbf{q}, \mathbf{q}^{(1)}, \mathbf{q}^{(2)}$	Displacement (m), velocity (m/s) and acceleration (m/s^2) of modal coordinates
r	Indicator of r-th mode shape
$\mathbf{R}(\tau)$	Covariance matrix
$\mathbf{S}(\omega)$	Power spectral density matrix
t	Time (s)
T	Transpose operator
$\mathbf{U}, \mathbf{V}$	Orthogonal/ unitary matrices of singular value decomposition
$\overline{\mathbf{V}}$	Vandermonde matrix
$\mathbf{W}, w$	Weighting coefficient matrix or factor for damage index
$\mathbf{Y}(t), \mathbf{y}(t)$	Measured velocity response matrix and vector
α, β	Rayleigh damping coefficients of mass and stiffness matrices
ϵ	Threshold value
κ_1, κ_2	Principal curvatures
κ_{xx} , κ_{yy} , κ_{xy}	Curvatures of mode shape surface associated with different directions
λ	Eigenvalue of singular value decomposition
μ, σ	Mean value and standard deviation of Gaussian distribution
υ	Poisson's ratio
ρ	Mass density (kg/m^3)

τ	Time-delay
$\boldsymbol{\varphi}$	Mode shape vector
$\Phi(x, y)$	Mode shape value at coordinates (x, y)
Φ_{xx}, Φ_{yy}	Second-order partial derivatives of plate mode shape surface
$\boldsymbol{\Phi}$	Mode shape matrix
$\boldsymbol{\Phi}_{\mathrm{p}}$	Plate mode shape at a certain natural frequency arranged into a matrix by following the 2-D measurement grid
$\boldsymbol{\Phi}_{\mathrm{p}}''$	Curvature of plate mode shape $\boldsymbol{\Phi}_{\mathrm{p}}$
$\boldsymbol{\Phi}_{\mathrm{y}}$	Mode shape matrix of measured degrees
ω	Frequency (Hz)
ω_{F}	Excitation frequency of a sinusoidal force (Hz)
ℓ_1, ℓ_2, ℓ_p	Rectilinear distance, Euclidean distance, Minkowski distance
$\boldsymbol{\Theta}$	Damage-induced shape change matrix
$\boldsymbol{\mathcal{S}}$	Sparse matrix
$\boldsymbol{\mathcal{W}}$	Weingarten matrix
$\boldsymbol{\Sigma}$	Diagonal matrix of singular value decomposition
∇^2	Laplacian operator
$\otimes$	Convolution integral
$\mathcal{F}$	Fourier transform
$\lvert\mathrm{scalar}\rvert$	Absolute value
$\lvert\mathrm{vector}\rvert$	The absolute value of each term of a vector and the result is still a vector
$\lvert\mathrm{matrix}\rvert$	The determinant of a matrix
$\lVert\cdot\rVert$	ℓ_2 norm or Euclidean distance

Acronyms

1-D	One dimensional
2-D	Two dimensional
CCPA	Common principal component analysis
CDS	Characteristic deflection shape
CV	Coefficient of variation
DECD	Deviations between empirical cumulative distributions
DI	Damage index
DND	Deviations from normal distribution
DoG	Difference of Gaussian
EMA	Experimental modal analysis
EVD	Eigenvalue decomposition
FDD	Frequency domain decomposition
FE	Finite element
FRF	Frequency response function
GFT	Global polynomial fitting
GSM	Gapped smoothing method
IIR	Infinite impulse response
JAD	Joint approximate diagonalisation
LoG	Laplacian of Gaussian

LPF	Local polynomial fitting
MS	Mode shape
MSE	Modal strain energy
ODS	Operational deflection shape
OMA	Operational modal analysis
PCA	Principal component analysis
PCP	Principal component pursuit
POD	Proper orthogonal decomposition
POM	Proper orthogonal mode
PSD	Power spectral density
SOBI	Second order blind source identification
SVD	Singular value decomposition

Chapter 1

Introduction

1.1 Background

The fast development of modern societies depends more and more on engineering structures or mechanical systems such as aircraft, bridges, nuclear power plants, oil platforms, large ships and satellites. However, they all have finite life spans and will experience degradation or even damage such as corrosion, fatigue, erosion, wear and overloading during their service life due to natural causes or human activities [1]. Thus, it is critically important to monitor the health state of these structural and mechanical systems, as any existing damage could compromise the performance or even cause failures of service life.

Here, damage is defined as unwanted changes to structural material or geometric properties including boundary conditions and subsection connections. For example, damage can be a fracture crack, erosion of engineering components or loss of critical components. Traditionally, a structure can still operate satisfactorily with damage but not in its ideal or design condition [2]. While for a fault, the performance of the structure will exceed the acceptable operation range.

Damage identification techniques have been investigated in several closely related disciplines such as condition monitoring, non-destructive testing/evaluation and structural health monitoring [3]. Structural health monitoring aims to provide the approaches for the constant or periodic monitoring of critical structural assets in order to determine the need for remedial action, and to prevent catastrophic failures. Condition monitoring is similar to structural health monitoring but normally used on damage detection in rotating and reciprocating equipment such as internal combustion

engines and power generation devices [2]. Non-destructive testing/evaluation is usually conducted off-line around the vicinity of damage for severity check, which belongs to well-developed local inspection methods. Some typical non-destructive testing techniques include magnetic field, eddy-current, ultrasound and thermal field, which often demand bulky instrumentation and long measurement time [4].

It is apparent that with the approximate location information of damage, non-destructive testing is suitable for the quantification of damage and methodologies of fracture mechanics can be adopted for damage prognosis by predicting the remaining service life of structures [5, 6]. Hence, global detection methods are primarily required for the information of damage positions, which usually rely on the damage-induced changes in structural vibration characteristics such as modal parameters and transmissibility [7, 8, 9]. Therefore, vibration-based structural damage identification plays a significant role in structural health monitoring and has experienced a rapid development in the past several decades [10].

The fundamental techniques of vibration-based structural damage identification are data acquisition and signal processing. Sensors are required to acquire the responses of structures whilst signal processing is applied to derive features for damage detection and quantification. In recent years, with developments of sensing technologies such as Scanning Laser Vibrometer (SLV) and full-field measurement using image processing, data acquisition of a large number of measurement points is simple and convenient, which facilitates the process for damage identification [11, 12, 13]. Furthermore, the developments in advanced signal processing methods such as multi-scale approaches (including wavelet analysis and Gaussian smoothing), blind source separation and robust principal component analysis enable establishment of more reliable and robust damage identification methods [14, 15, 16].

Apart from the data acquisition and signal processing, another crucial procedure for damage identification is feature selection and extraction [3]. Without using the damage-sensitive features, even the most advanced data acquisition and signal processing techniques can not significantly improve damage identification accuracy. For linear damage such as open cracks, modal parameters such as natural frequencies and mode shapes are decent damage features, which contain global and local information of structure dynamic responses [17, 18]. Furthermore, evaluating the

modal parameters enables the interpretation of structural characteristics and dynamic behaviours. For non-linear damage like fatigue cracks, vibration-based nonlinear response characteristics such as distortions of frequency response function, deviations of probability function and harmonic distortions are commonly used for damage feature extraction [19, 20].

The task of damage feature extraction is to reduce the dimension of the original vibration data without compromising the damage information while supressing the effects of operational, environmental and measurement uncertainties. Once the changes of these damage features are dominated by damage only, the problem of damage identification will be easily addressed. Nevertheless, the changes of damage features are readily affected by various uncertainties, which degrade the identification of damage, especially when the damage is not severe. To alleviate the effects of operational, environmental and measurement uncertainties on damage features, statistical data reduction methods such as principal component analysis and kernel principal component analysis are widely utilised [21, 22]. In addition, before damage feature extraction, the process of vibration data cleansing is necessary to detect and correct the inaccurate or missing measurement data. Nowadays, this procedure is normally integrated into the advanced acquisition system such as speckle tracking and signal enhancement in the PSV-500 Scanning Laser Vibrometer.

With the damage features, damage identification in the forms of damage detection, damage localisation and severity quantification can be achieved by pattern recognition (requiring setting up of a damage feature bank of various damage scenarios), model updating (requiring the physics-based structural model), distance measure (requiring the damage features of intact structures) or deviation detection (requiring some properties of intact structures). There are two types of errors in damage identification: false-positive damage identification and false-negative damage identification. The former one happens when there is no damage but the damage index indicates the existence of damage, whilst the latter situation is a failure to detect damage when it occurs. Both types of errors are undesirable, as the first type error leads to the overestimate of the state of damage while the second type error causes the underestimate of the state of damage. In practical application, the consequences of the second type error is much more severe than the first type error.

The research of this dissertation focuses on the vibration-based structural damage identification using only vibration data of damaged structures, especially for multi-damage localisation. The non-contact PSV-500 Scanning Laser Vibrometer is applied to acquire the experimental data of beams and plates. Structural characteristic deflection shapes such as mode shapes and operational deflection shapes are taken as the basic damage features for damage detection, localisation and relative damage severity quantification.

1.2 Motivations

With wide-spread use of metallic and composite structures in modern society, a major challenge is to secure their normal operation by inspection and maintenance. Therefore, the monitoring of the structural health state is significantly important. Among the various non-destructive structural health monitoring techniques, vibration-based structural damage identification is one of the few methods that could provide both the global and local damage features, which is widely applied in buildings, bridges or aerospace structures [23].

Vibration-based structural damage identification is an inverse problem and the basic idea is through monitoring damage-induced changes of structural characteristics. However, during this process, a noticeable drawback of deriving damage features is that they are easily compromised by various uncertainties, which generally come from four sources: operational, environmental, measurement and computational [24]. Another challenge is that the baseline data of healthy structures is practically unavailable or hard to obtain. Moreover, the study of multi-damage identification is more and more desirable, which introduces new challenging problems.

In addition, the principles of nonlinear damage identification are different from the traditional linear damage identification and the linear damage features are not suitable for nonlinear damage identification. Therefore, it is necessary to interpret the characteristics of nonlinear damage and develop efficient nonlinear damage localisation methods.

1.3 Aim and objectives

The aim of this PhD project is to develop effective and reliable multi-damage identification approaches for beam- and plate- type structures by using advanced signal

processing techniques based on only vibration data of damaged structures, which should be sensitive to damage while robust to operational, environmental and measurement uncertainties. Moreover, the proposed damage identification methods should be able to provide the existence, locations and relative severity of damage. In addition, they should be more accurate and robust when compared with current damage identification algorithms.

1.4 Original contributions

In this research, the most significant original contribution is to statistically estimate the robust damage features in spatial domain and apply advanced signal processing techniques such as multi-scale analysis and robust principal component analysis to the spatial domain damage features for robust multi-damage identification. The main original contributions are summarised in the following five aspects:

(1) Robust structural mode shape estimation is proposed by using the common principle component analysis based on output-only vibration response (operational modal analysis), which enhances the estimation accuracy and noise robustness of mode shape-related features.

(2) For plate-type structures, apart from the traditional curvatures along x and y directions, the principal curvatures, mean principal curvature and Gaussian curvature are determined for damage identification. Moreover, robust curvature estimation approaches are investigated by using multi-scale approaches (such as wavelet transform and Gaussian smoothing) and polynomial fitting technique.

(3) Instead of using signal processing methods such as wavelet transform and fractal dimension methods to manifest the damage-induced changes of spatial domain damage features such as mode shapes and mode shape curvatures, surrogate models and low-rank models are utilised to extract the damage-induced shape changes. By doing this, the damage-induced shape changes of several modes are combined to define a robust damage identification index without using the baseline data of healthy structures.

(4) Robust multi-damage identification indexes for beam- and plate-type structures, which combine the normalised damage-induced changes of several modes, are established localising the damage and indicating the relative damage severity.

(5) Nonlinear multi-damage identification of stepped beam structures is studied in two approaches by taking advantage of the damage-induced nonlinear vibration responses. The first approach evaluates the deviations between empirical probability distributions of vibration responses of damaged structures to localise the damage. The second approach detects the sudden shapes changes of operational deflection shapes corresponding to the super-harmonic frequencies.

Finally, the original contributions about baseline-free linear multi-damage identification in beams have been published in two journal papers and two conference papers. In addition, another journal paper about this work has been submitted for review. Furthermore, the proposed nonlinear multi-damage identification for beams has contributed to a conference paper and two published journal papers on damage identification of cracked rotors with the student being a co-author. Lastly, the original contribution of baseline-free multi-damage identification in plates is being written into new journal papers.

1.5 Outline of the dissertation

This dissertation includes eight chapters and the overall structure of this dissertation is shown in Figure 1.1 and the outline of each chapter is given as follows:

Chapter 1 introduces the background of vibration based damage identification and structural healthy monitoring, the motivations and objectives of this dissertation, and the outline of this dissertation.

Chapter 2 provides a comprehensive literature review on the damage modelling approaches, challenges and methods for damage feature estimation, damage identification categories and common damage identification methods, especially for beam-type and plate-type structures.

Chapter 3 proposes two robust mode shape estimation approaches using only output vibration responses, which are termed enhanced time domain decomposition method and enhanced frequency domain decomposition method. In both methods, the common principal component analysis is applied to diagonalise a set of covariance or power spectral density matrices to determine the common subspace bases as the mode shapes, which statistically improves the noise robustness of estimated mode shapes.

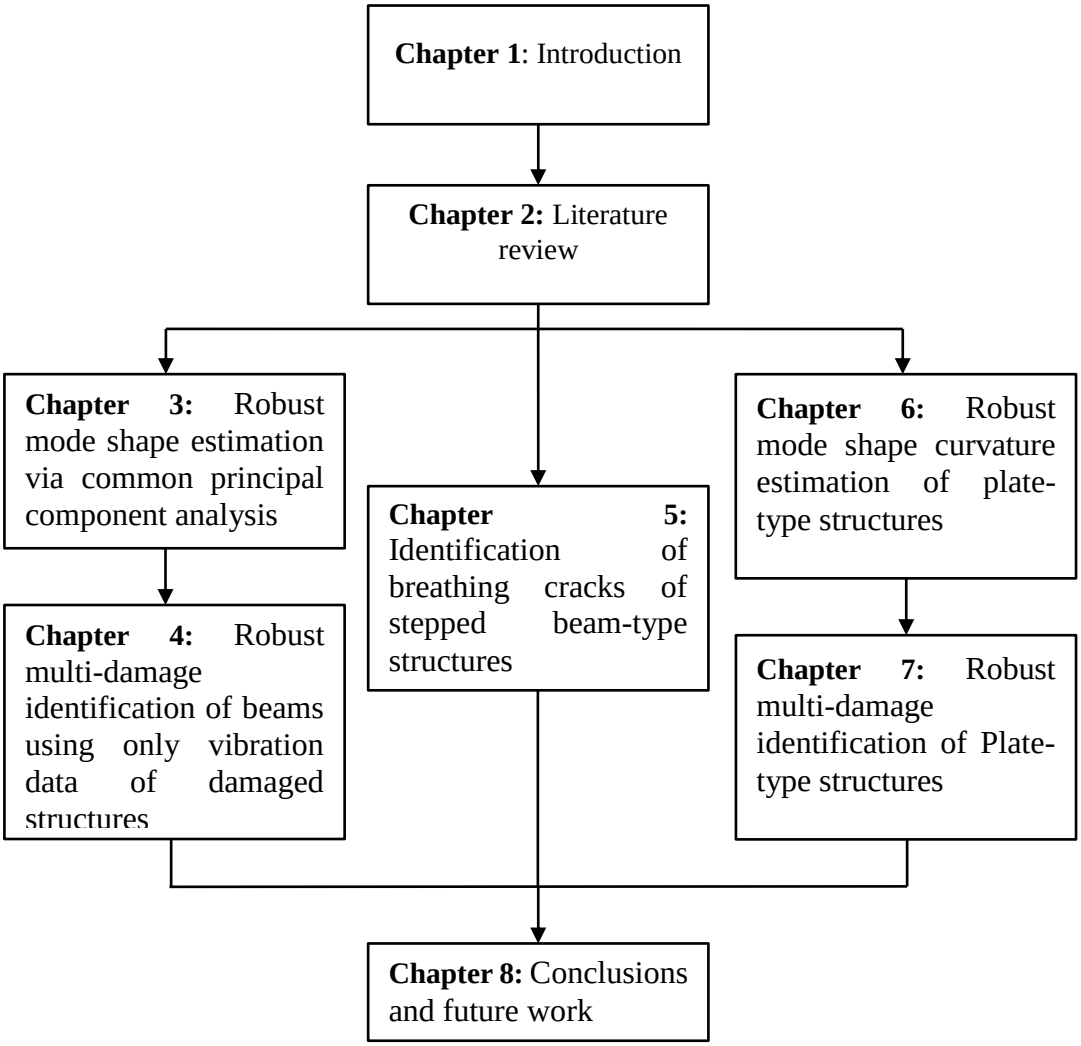

Figure 1.1The structural flowchart of the dissertation

Chapter 4 develops a baseline-free robust damage identification index for beam-type structures, which is evaluated using only output vibration responses of damaged structures. An adaptive gapped smoothing method (GSM) is proposed based on cross-validation approach to determine the optimal polynomial fitting order, which is more noise robust than the traditional gapped smoothing method. The damage-induced shape changes of mode shape curvatures are assessed by the adaptive GSM. Furthermore, the proposed damage index incorporates the damage information of several modes instead of depending on a certain single mode, which is robust for multi-damage localisation. In addition, the damage information of each mode shape is normalised to avoid one mode from dominating the damage index.

Chapter 5 studies the localisation of breathing cracks in stepped beam-type structures. Two approaches, deviations between empirical probability distributions and

irregularities of CDS's associated with super-harmonic components, are proposed to identify breathing cracks of stepped structures. In addition, a comparative study with a method using the deviations from normal distribution is conducted to show the better damage identification performance of the present method based on deviations between empirical probability distributions.

Chapter 6 investigates the noise robust curvature estimation techniques of structural characteristic deflection shapes for plates. Firstly, apart from the traditional curvatures along the x and y coordinates, the principal, mean and Gaussian curvatures are investigated for damage identification in plates. Secondly, to alleviate the noise effects, a 2-D Laplacian of Gaussian approach is employed to enhance the curvature estimation along the x and y coordinates. For the principal, mean and Gaussian curvatures, a local bivariate polynomial fitting technique is proposed to boost their noise robustness.

Chapter 7 proposes a robust multi-damage index for plate-type structures by using low-rank models and surrogate models based on only the vibration data of damaged structures. In the low-rank models, the mode shape curvature matrix of damaged structures is decomposed into a low-rank matrix (corresponding to the mode shape curvature of healthy state) and a sparse component matrix (associated with damage-induced changes). For the surrogate models such as polynomial fitting approach and Kriging regression, they try to construct the mode shape curvature of the healthy state by using mode shape curvature of damaged state based on the assumption that the mode shape curvature of the healthy structure must be smooth.

Chapter 8 provides the key conclusions of this PhD project and some suggestions for the future work.

Chapter 2

Literature review

In this chapter, the literature review focuses on four aspects: damage modelling, common damage feature estimation, categories of vibration-based damage identification and damage identification methods. For damage modelling, the traditional models for open cracks and fatigue cracks are reviewed. For damage feature estimation, the major sources of uncertainty and variability are discussed and some common estimation methods for mode shapes and mode shape curvatures are presented. For categories of vibration-based damage identification, a new classification criterion is proposed, which categorises the vibration-based damage identification methods based on the degrees of available baseline information. For vibration-based damage identification, the literature review is first categorised according to the types of damage-sensitive features. Then, for a specific damage feature, damage identification is discussed depending on the practically available baseline information.

2.1 Damage modelling

Modelling of damage in structures is an essential task, as damage identification methods are normally validated by using simulated damage in numerical analysis. Moreover, the modelling of damage is helpful to interpret the characteristics of damage in order for better damage identification. In addition, damage identification methods based on model updating require an accurate analytical/numerical structural model as well as the damage model.

Damage in the form of open cracks (linear damage) and fatigue cracks (nonlinear damage) is widely studied. A comprehensive review of crack modelling in beams was presented by Dimarogonas [25]. Broda et al. [26] reviewed various nonlinear crack modelling such as bilinear stiffness and clapping contacts. Moreover, the physical mechanisms associated with different crack models were also discussed.

Generally, open cracks are modelled as a local stiffness reduction, as they increase the local structural flexibility [27]. In an FE model of beams or plates, open cracks are simulated by decreasing the local Young's Modulus or thickness but this kind of methods cannot establish the relationship between the reduced stiffness and crack depth. Hence, Christides and Barr [28] proposed an exponential function to represent the element stiffness of damaged beams, which directly associated the crack depth and location with the reduced element stiffness. An alternative approach is to compute the local element stiffness reduction via a fracture mechanics approach, which uses the empirical expressions of stress intensity factors to explicitly associate the reduced stiffness matrix with crack depth [29].

Fatigue cracks widely exist in structures such as aircraft frames and beams of bridges that bear oscillatory and/or impact loads. For beam-type structures, a bilinear stiffness model is one of the most popular and simple approaches to simulate the nonlinear behaviour of fatigue cracks [30, 31]. To avoid the sudden stiffness changes of a bilinear stiffness model, a rotational spring is normally used to simulate the continuously varying stiffness of a crack but this still does not take into account the practical physical structure of fatigue cracks [32, 33, 34]. Moreover, the fatigue cracks could be modelled as a frictionless surface-to-surface contact in a 2-D FE model, which defines the stiffness as a function of the distance between two contact surfaces [35].

Another remarkable damage of nonlinear response is delamination in bonded, layered materials such as fibre reinforced composite plates and shells. There are many approaches of modelling delamination, which could be found in related references [18, 36, 37].

2.2 Damage-sensitive feature estimation

The purpose of this section is to review some challenging problems and methods of damage-sensitive feature estimation. In vibration-based damage identification, damage-sensitive features are normally evaluated in three domains: time domain, frequency domain and time-frequency domain [38, 39].

Extracting damage features in terms of simple statistics such as mean value and variance are simple and easy, but they are difficult to use to identify damage due to their high dependence on inputs and susceptibility to various uncertainties. Thus, the crucial task of structural damage identification is to evaluate the robust, accurate and damage-sensitive features. It is well known that modal parameters and their derivatives are common damage-sensitive features for damage identification. In addition, some other parameters such as frequency responses functions (FRFs) and transmissibility are commonly utilised as well.

2.2.1 Uncertainty and variability in damage feature estimation

Uncertainty describes quantities that cannot be determined with precision due to measurement noise or estimation errors and are quantified by a probability distribution, whereas variability refers to quantities that are inherently variable and cannot be described by a single value at different locations or times, such as the temperature and humidity of experimental environments. There are many sources of both uncertainty and variability in the process of damage feature estimation [24], which are mainly categorised into four aspects: operational, environmental, measurement and computational. Figure 2.1 illustrates the flowchart and the uncertainty or variability sources of damage feature estimation (including damage index calculation), where B. C. denotes boundary conditions.

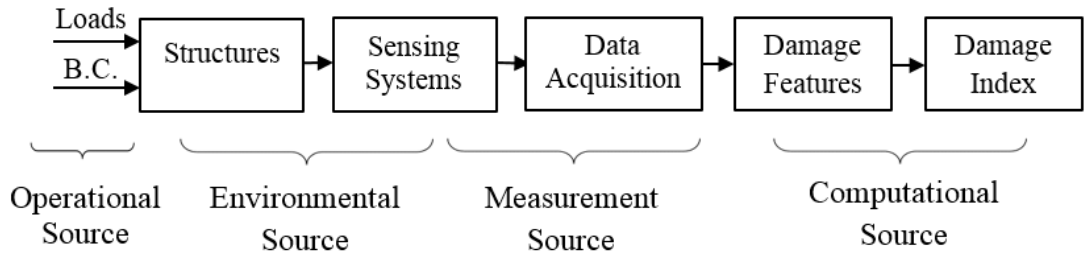

Figure 2.1 Flowchart and the sources of uncertainty or variability in damage feature estimation.

A thorough understanding of the effects of uncertainty and variability on damage features is necessary, as the changes of damage features due to uncertainty or variability should be discriminated from changes caused by damage. Uncertainty is mainly present during data acquisition (measurement noise) and data processing (estimation errors) whilst variability normally origins from the operational and environmental conditions.

For the measurement uncertainty, it is naturally inevitable even for the most advanced sensor techniques. A common solution is to include the measurement noise in the theoretical model during the estimation process of damage features. Moreover, the measurement noise sensitivity of modal parameter identification has been studied, which considered the measurement noise white noise [40, 41]. In addition, the noise uncertainty quantification of frequency response function and transmissibility have been presented by Zhu and Todd [42, 43]. In terms of computational uncertainty, it is naturally due to the assumptions of mathematical models. Therefore, advanced modelling and signal processing methods are necessary to deal with the measurement and computational uncertainties.

For the operational and environmental variability, the effects of excitation sources and temperature on damage feature estimation have been investigated by several authors. Cornwell et al. [44] studied the effects of temperature on natural frequencies of Alamosa Canyon Bridge, which showed that the modal frequencies could vary up to 6% over a 24-hour period. Peeters et al. [45, 46] investigated the effects of excitation forces and temperature on modal parameters. They concluded that the ambient excitation provided the comparable results with band-limited noise excitation and impact excitation, and the effects of temperature on modal frequencies were

undeniable. Yu and Zhu [47] studied the operational variability by changing the shaker input level and the measured data were normalised to eliminate effects caused by the operational variability. It was concluded that the extracted damage features were robust to the changes of excitation levels.

2.2.2 Methods of damage feature identification

In this section, the estimation methods of damage-sensitive features in the form of modal parameters are mainly discussed. An emphasis is given on the estimation of mode shapes and mode shape curvatures, which are useful spatial domain features for damage localisation. Some other common damage features or their extraction methods are reviewed in references [3, 48].

2.2.2.1 Modal analysis methods

The approaches of modal parameter identification can be categorised according to the availability of measurement data [49]. For input-output measurements, the deterministic input-output model could be established and it is commonly applied in the experimental modal analysis (EMA). When only the output measurements are available, the stochastic output-only model will be applied and this method is well known as operational modal analysis (OMA).

Experimental modal analysis has been a common technique to study the dynamic characteristics of mechanical and civil structures [50]. Normally, in EMA, the structural components, instead of the complete system, are tested with artificial excitation and the frequency response functions are used as primary data. However, for practical engineering structures, the excitation forces are difficult or impossible to be measured. Furthermore, it is desirable to identify the modal parameters under the operational conditions. Hence, the OMA becomes more and more attractive [51, 52].

A comprehensive review of various methods for OMA was presented in [53]. Among them, two common methods of OMA are stochastic subspace identification in time domain and frequency domain decomposition in frequency domain, which deal well with the closely spaced modes and measurement noise. A recent trend of OMA is applying second-order blind source identification (SOBI) to estimate modal parameters, which extends the concepts of sources and mixing matrix into modal analysis to evaluate modal coordinates and mode shape matrix [54, 55]. In addition,

the Bayesian operational modal analysis developed by Yuen and Au can not only provide the most probable values of modal parameters but also their associated uncertainties [56, 57]. A disadvantage of the above OMA methods is that they assume that the input excitation is statistically random (white noise). In order to overcome this limitation, a transmissibility-based OMA was proposed [49, 58], which does not require any assumption about the nature of excitation forces.

2.2.2.2 Mode shape estimation

Compared with natural frequencies, mode shapes are less sensitive to environmental variability such as temperature and humidity. But mode shapes are more prone to measurement uncertainties, as the data acquisition of discrete spatial points is easily affected by measurement noise.

For EMA, the mode shapes are traditionally estimated by connecting the FRF peak values of measurement points at resonant frequencies. While in OMA, mode shapes are generally estimated as the Eigen structure (eigenvectors or singular vectors) of matrices such as covariance matrix (or derived matrix based on covariance matrix), power spectral density matrix and transmissibility matrix.

In stochastic subspace method, the state matrix and observation matrix are first evaluated via covariance-driven or data-driven methods. Then, the mode shape matrix is calculated as the product of observation matrix and eigenvector matrix of state matrix [59]. In frequency domain decomposition method, the mode shapes are estimated individually as the dominant singular vector of the power spectral density matrix at each resonant frequency [60]. Similarly, for the transmissibility based OMA, mode shapes are computed as the dominant singular vector of the transmissibility matrix at each resonant frequency [58]. For Bayesian OMA in frequency domain, the mode shapes are determined individually as the dominant singular vector of a linear combination of power spectral density matrices corresponding to a narrow frequency band around each resonance frequency [61]. In the second-order blind source separation method, a whitening procedure is required primarily to transform the covariance matrix at a certain time-delay to unit matrix before joint diagonal decomposition is applied to determine the orthogonal matrix that diagonalises a set of whitened covariance matrices. Then the mode shapes are estimated as the product of the whitening matrix and the orthogonal matrix [62].

The afore-mentioned mode shape estimation indicates that mode shapes can be computed from a matrix, some linear combinations of matrices or using a set of matrices. In practice, due to limited measurement data and various uncertainties in the data, the matrices do not exactly share the same Eigen structure. But from a statistical point of view, it is necessary to define a kind of 'averaged Eigen structure' by using a set of matrices, which promises an accurate and robust mode shape estimation [63]. Therefore, robust mode shape estimation methods are required, which are based on a set of covariance matrices or PSD matrices.

2.2.3 Estimation of curvature mode shapes

Normally, the curvature of mode shapes is much more sensitive to damage than the mode shapes themselves [64]. Traditionally, the curvature of mode shapes is readily computed form mode shapes by using the second-order central difference approach. Nevertheless, this approach is susceptibly affected by the density of measurement points and the measurement noise. To overcome the noise vulnerability, de-noising techniques such as polynomial smoothing or fitting are commonly adopted to enhance the noise robustness of mode shape curvature estimation.

Multi-scale approaches such as wavelet transform and Gaussian smoothing are well developed to represent the import features at multiple scales in time or spatial domain [65, 66]. Hence, the curvature of mode shapes could be estimated at a certain scale or by using the differentiation property of convolution integral to boost the noise robustness. The differentiation property of convolution integral is expressed as

$$\nabla^2(\Phi(x,y)\otimes g(x,y;\sigma)) = \nabla^2\Phi(x,y)\otimes g(x,y;\sigma)$$

$$= \Phi(x,y)\otimes\nabla^2 g(x,y;\sigma) \tag{2.1}$$

where $\Phi(x,y)$ is the mode shape value at location (x,y), and $g(x,y;\sigma)$ indicate the Gaussian function at scale σ. ∇^2 represents Laplace operator and $\otimes$ denotes convolution operator, which is expressed as

$$\Phi(x,y)\otimes g(x,y;\sigma) = \int_{-\infty}^{+\infty}\int_{-\infty}^{+\infty}\Phi(x-u,y-v)g(u,v;\sigma)\mathrm{d}u\mathrm{d}v \tag{2.2}$$

The negative normalised second derivative of Gaussian function is the Mexican hat wavelet. Therefore, the Mexican hat wavelet transform of mode shapes will acquire an equivalent form of mode shape curvature.

Moreover, for plate-type structures, apart from the curvatures of mode shapes along x and y directions, other types of curvatures such as the principal curvatures, mean principal curvature and Gaussian curvature are also damage-sensitive features. For these kinds of curvatures, the curvature estimation methods are classified as discrete and continuous. The discrete methods compute the mode shape curvatures by formulating a closed form for differential geometry operators, which deal directly with the discrete mode shape data, whereas the continuous methods first fit the discrete mode shape data locally by using the neighbouring points and then interrogate the fitted mode shape for curvature estimation, which are more accurate and noise robust [67].

The above discussed curvature estimation techniques are not constrained to mode shapes, but can also be extended to other types of structural characteristic deflection shapes such as operational deflection shapes and proper orthogonal modes [68].

2.3 Classification of vibration-based damage identification

Vibration-based structural health monitoring and damage identification can be applied continuously under various operational and environmental conditions and have been studied for the last several decades [8, 69]. Numerous vibration-based damage identification methods have been proposed and validated. Generally, they are categorised according to different criteria such as levels of damage identification, linear or nonlinear vibration responses and whether using physics-based models or not [3, 70]. Here, a new classification criterion is proposed, which categorises the vibration-based damage identification methods based on the degrees of available baseline information. In addition, two typical classification methods (damage identification levels and linear / nonlinear damage identification) are also presented.

2.3.1 Damage identification levels

A basic classification of vibration-based damage identification is according to the damage identification levels, which was presented by Rytter [71] as follows:

- Level 1: Detection of the existence of damage in the structure
- Level 2: Determination of the location of the damage
- Level 3: Quantification of the size or severity of the damage
- Level 4: Evaluation of the remaining service life of the structure

Level 1 is often referred to as novelty detection or anomaly detection, which generally does not need the physics-based structural model or baseline data of healthy structures. Nevertheless, damage identification always aims to obtain further information about the damage: damage location (level 2) or size of damage (level 3). The identification methods to accomplish Level 2 and Level 3 can be categorised into non physics-model-based methods and physics-model-based methods.

Non physics-model based identification methods for Level 2 and Level 3 rely on the local damage information in spatial domain damage features such as mode shapes and operational deflection shapes. For this kinds of methods, it is possible to localise the damage and indicate the relative damage severity of damage but impossible to quantify the size of damage. To overcome this, physics-model-based identification methods are traditionally applied for vibration-based damage identification through model updating. But when the location information of damage is available, a more promising approach for damage severity quantification is the application of non-destructive testing techniques such as acoustic emission, magnetic resonance imaging and ultrasonic testing. For level 4, the assessment of remaining service life is closely associated with the fields of fracture mechanics, which will not be discussed in detail in this thesis [72].

2.3.2 Linear and nonlinear damage identification

According to the effects of damage on structures, structural damage identification methods can be classified as linear and nonlinear. The basic idea of linear-response-based methods is that damage-induced changes in structural physical properties (mass, damping or stiffness) alter the structural dynamic characteristics such as modal parameters, FRFs and transmissibility, which are used to indicate damage [73]. For nonlinear damage, linear damage features are not suitable or less sensitive. Hence, nonlinear response characteristics such as distortions of frequency response function, deviations of probability function and harmonic distortions are efficiently utilised for nonlinear damage identification [19, 20].

2.3.3 Damage identification depending on available baseline information

One purpose of this study is to accomplish multi-damage detection, localisation and relative severity quantification without baseline data, which means using only the

vibration data of damaged structures. The relative severity quantification is not the quantification of damage size but to indicate the relative severity of different damage on the same structure. Basically, the practical availability of baseline information could determine the types of damage identification methods. Therefore, a new classification criterion about the degrees of available baseline information is presented.

Generally, structural damage identification can be considered a pattern recognition problem as shown in Figure 2.2, which compares the extracted features of current state of structures with the benchmark features to determine the damage state [3, 74, 75]. The damage feature bank contains the damage features of various possible damage scenarios, which are normally obtained experimentally. However, establishing the damage feature bank for pattern recognition is challenging due to the vast number of possible damage scenarios.

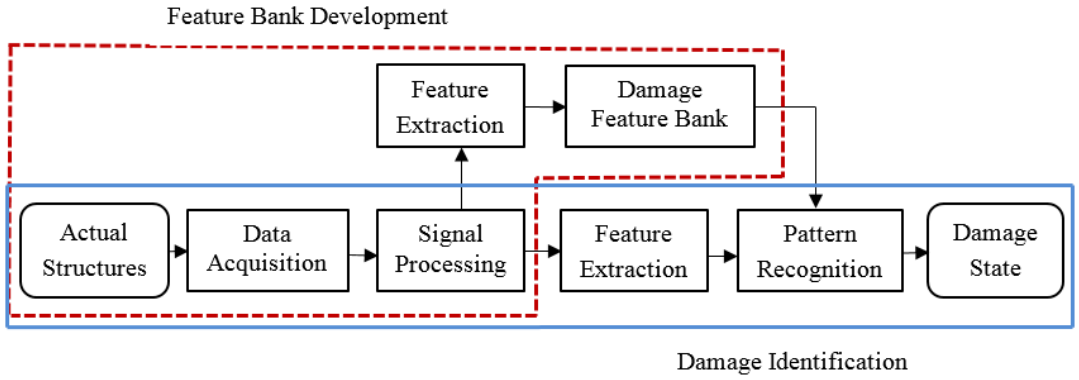

Figure 2.2 Statistical pattern recognition based structural damage identification.

An alternative solution is to build the physics-based models of structures such as FE models to simulate the various possible damage scenarios for a damage feature bank. But with the physics-based models of structures, a more efficient damage identification approach is via model updating techniques [76, 77, 78], as shown in Figure 2.3. Nevertheless, a well correlated structural model and the accurate initial state of the structure are primarily required before using physics-based damage identification. Moreover, for model-updating based damage identification, the large number of updating parameters and the non-uniqueness of updated models increase its difficulties and degrade the accuracy [79, 80].

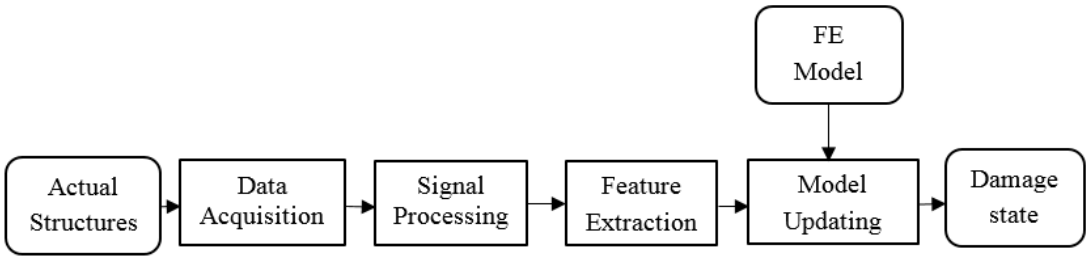

Figure 2.3 Model updating based structural damage identification.

When only the baseline data of healthy structures is available, damage identification can be accomplished by comparing the damage features of damaged structures with baseline damage features of heathy structures, which is illustrated in Figure 2.4 [81, 82, 83]. The baseline data of healthy structures could be provided by either experiments or physics-based structural models. In addition, the distance measure or similarity measure is used during the damage feature comparison to identify the damage.

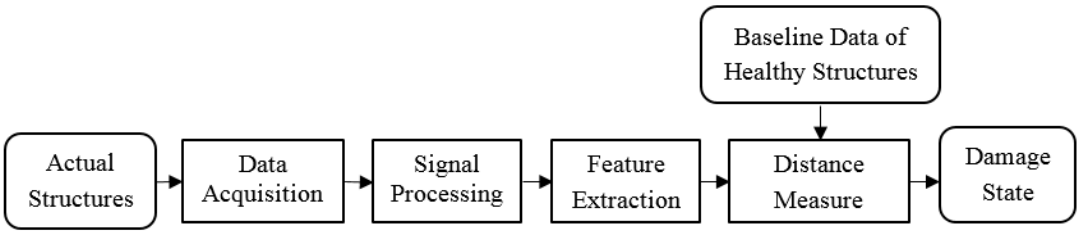

Figure 2.4 Structural damage identification with baseline data of healthy state.

Even when the baseline data of healthy structures is not available, structural damage identification in the form of detection, localisation and relative severity quantification can still be achieved by measuring the deviations from some properties of healthy structures such as normal distribution of probability density function under random excitation and smoothness of mode shapes for geometrically uniform and material isotropic structures [84, 85, 86]. The process of baseline-free damage identification is diagrammed in Figure 2.5.

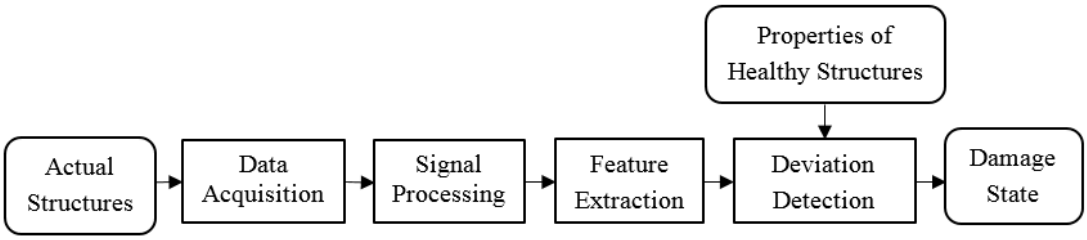

Figure 2.5 Structural damage identification without baseline data.

In conclusion, damage identification depending on the practical available baseline information can be categorised as pattern recognition (requiring setting up of a damage feature bank of various damage scenarios), model updating (requiring the physics-based structural model), distance measure (requiring the damage features of intact structures) or deviation detection (requiring some properties of intact structures).

Pattern recognition: For damage identification, patterns mainly represent the different damage scenarios corresponding to different locations or severities. The primarily step of pattern recognition approach is to establish a relationship model between damage features and their associated damage cases. Then, the extracted damage features of current state of structures is the input to the established relationship model for damage state prediction [3]. There are traditionally two categories of pattern recognition approaches, supervised learning and unsupervised learning. Without supervised learning, the pattern recognition approach can only indicate the presence of damage [87]. With supervised learning, the pattern recognition approach is able to provide the damage locations or severities, which is desirable and promising for practical applications. Moreover, computational techniques like artificial neural networks, support vector classification or fuzzy logic are popularly applied to establish the relationship between damage features and their associated damage cases [88, 89, 90] .

Model updating: Model updating aims to modify the structural model parameters or matrices (such as mass, stiffness and damping) of an FE model in order to obtain better dynamic response agreement between the FE model and the tested structure, which is essentially an optimisation problem [80]. During the process, an objective function is primarily formed to measure the dynamic response discrepancy between the FE model and the tested structure. Here, the dynamic response is normally represented by modal parameters, FRFs, transmissibility or a combination of these. For damage

identification, the damage locations or severities are determined by comparing the updated mass or stiffness matrices with the original correlated matrices [91, 92].

Traditionally, the model updating methods are categorised as: direct methods and iterative methods [93]. Moreover, according to different implementation techniques, model updating methods are commonly discussed as matrix update methods, optimal matrix methods, sensitivity-based methods, iterative optimization methods or computational intelligence methods (such as genetic algorithm, particle-swarm optimisation and simulated annealing) [94].

Distance measure: Distance or similarity measure evaluates the distance or similarity between two sequences or datasets, which plays an important role in the fields of pattern recognition, optimisation and estimation [95]. For damage identification, the distance of damage features between damaged structures and healthy structures are basically used to detect, localise or quantify the damage. The typical distance measure approaches are rectilinear distance (ℓ_1 norm), Euclidean distance (ℓ_2 norm), Mahalanobis distance, Minkowski distance (ℓ_p norm) and weighted squared Euclidean distance [96].

Deviation detection: Deviation detection or outlier detection is the method to detect the unexpected patterns or outlier values. For damage identification, it is normally limited to the detection of damage presence. But when applied to spatial domain features, it enables the localisation and relative severity quantification of damage. For example, detecting the damage-induced local shape singularities in mode shapes or mode shape curvatures is an effective approach for damage localisation in beam-type and plate-type structures.

2.4 Review of damage identification methods

Some comprehensive literature reviews about the important advances in vibration-based damage identification and health monitoring can be found in Doebling et al. [97], Sohn et al. [98], Montalvao et al. [18], Fan and Qiao [99] and Cao et al. [100]. This section is organised according to the types of damage-sensitive features. Moreover, for a specific damage feature, damage identification is discussed according to the practical available baseline information.

2.4.1 Natural frequencies

Natural Frequencies are a global dynamic feature, which are readily measured without dependence on the measurement positions. The change of natural frequencies has been extensively studied for damage identification for several decades.

Salawu [101] presented a comprehensive literature review of natural frequency based damage identification methods, which concluded that natural frequencies had the potential for damage identification but maybe not sufficient for an unique damage localisation. The detection of damage presence is simply achieved by comparing the natural frequencies of current state of structures with the natural frequencies of healthy structures, while the localisation of damage based on natural frequencies is achieved via FE model updating or pattern recognition by requiring a finite element model of structures and a set of natural frequency associated with different damage scenarios. Related papers using natural frequency based damage localisation include Cawley and Adams [102], Cerri and Vestroni [103], Sinha et al. [9] and Gao et al. [104].

However, the natural frequency shifts are demonstrated to be not sensitive to local damage and more easily contaminated by operational and environmental variability [105]. Due to these drawbacks, the application of natural frequency shifts are mainly in numerical analysis or small simple laboratory structures.

2.4.2 Frequency response functions

FRF data provides much more information on damage than the modal parameters, which represents the dynamic characteristics between structural response and excitation in a certain frequency range. Moreover, FRFs can be acquired directly in experiments to avoid the extraction errors during modal analysis. Therefore, the use of FRFs is a very promising damage feature for damage identification.

Firstly, FRF-based model updating for damage identification is discussed. Wang et al. [106] proposed a damage vector for detecting location and magnitude of damage by updating the undamaged and damaged system matrices based on the FRF data, which could be extended to the cases when measured coordinates were incomplete. Lee and Shin [83] developed a damage localisation and quantification approach for beam-type structures by using analytical model and FRF data. With the help of mode shapes and

natural frequencies of intact structures, the damage was identified by solving dynamic equations.

When only the FRFs of healthy structures are available, frequency response vector assurance criterion proposed by Heylen and Lammens [107] is effective for damage identification. Zang et al. [108] presented two criteria, global shape correlation and global amplitude correlation function, for correlating measured frequency responses, which were damage sensitive indicators for structural damage detection. Sampaio and Maia [109] utilised frequency domain assurance criterion and the response vector assurance criterion based on frequency response function for effective damage identification.

In the absence of FRFs of healthy structure, the application of frequency response function curvature method was presented by Saravanan and Sekhar [110], which detected the damage-caused sudden shape changes for damage detection, localisation and relative damage severity quantification in rotors. Moreover, without baseline data, principal component analysis was applied to FRF matrix to evaluate the robust spatial shape features and then gapped smoothing method was adopted to localise the damage by Salehi et al. [111].

One disadvantage of FRF-based damage identification method is the requirement of excitation information, as FRFs is defined as the spectrum ratio between the outputs and inputs.

2.4.3 Transmissibility

Generally, transmissibility function represents the ratio relationship of two response spectra, which does not require the information of input excitation. By this definition, transmissibility only contains the zeros of FRFs, which are associated with local structural quantities. Similar to FRFs, transmissibility could be also used in modal analysis [49], damage identification [112] and FE model-updating [113].

With the baseline transmissibility of healthy structures, the application of transmissibility for damage identification has been studied widely. Multiple response vector assurance criterion was proposed by Maia et al. [8], which was demonstrated to be capable of damage detection and relative severity quantification. Zhou et al. [114] applied transmissibility based coherence analysis and modal assurance criterion for

damage detection and relative severity quantification, which was possible to detect nonlinear damage-induced changes. Principal component analysis of transmissibility matrices was conducted to reduce the environment variability of transmissibility and damage indicator for damage detection was proposed by using Mahalanobis distance of transmissibility between the damage state and the healthy state [96]. In addition, Fan et al. [115] proposed a novel concept of wavelet-based transmissibility and outlier analysis was used for damage detection without requiring the baseline data of healthy structures.

In terms of transmissibility-based damage localisation, one approach is via FE model-updating. The other approach is based on the extracted spatial shape features from transmissibility such as mode shapes and operational deflection shapes, which contain the local information of structures.

2.4.4 Mode shapes

In comparison with natural frequencies, mode shapes are effective for damage localisation, since they contain the spatial information of structures, especially the damage-induced local shape singularities. Moreover, the estimation of mode shapes are robust to the operational and environmental variability but prone to pollution of measurement uncertainties due to a large number of discrete measurement points.

With the help of analytical or numerical models of structures, damage detection, localisation and severity quantification can be achieved via model updating approaches or pattern recognition. But accurate structural models are hard to be established due to the uncertainties in boundary conditions, material properties, and connection types. Shi et al. [116] proposed a damage localisation method for truss structures by using the incomplete mode shapes and analytical structural model, which was an extension of the multiple damage location assurance criterion. Chen and Bicanic [117] applied Gauss-Newton Least-Squares technique for damage localisation and quantification, which was based on incomplete mode shapes and characteristic equations of structural dynamic systems. Xiang and Liang [118] applied wavelet transform to mode shapes to localise the local singularities for damage location and then the natural frequencies were used for severity quantification with the help of finite element model updating. Lee et al. [119] utilised the differences and ratios of mode

shapes between before and after damage as the inputs of neural networks for damage detection, which required a baseline finite element model to train the neural networks.

To measure the mode shape changes due to damage, the Modal Assurance Criterion (MAC) and Coordinate Modal Assurance Criterion (COMAC) are commonly utilised based on the mode shapes before and after damage [120]. Salawu and Williams [121] identified the damage of a bridge using MAC and COMAC and indicated that mode shapes were effective in localising the damage whilst the reduction of natural frequencies was less than 3%.

Without the baseline mode shapes of healthy states, damage identification, especially for localisation, could be accomplished by detecting the damage-induced singularities of mode shapes. Khan et al. [122] investigated the discontinuities of mode shapes for damage localisation, which indicated that that method was not sensitive to incipient damage. They also pointed out that the mode shapes acquired by continuously scanning laser Vibrometer were easily contaminated by speckle noise. Pawar et al. [123] applied Fourier transform to mode shapes and showed that the changes of Fourier coefficients could be used to locate the damage.

Moreover, wavelet analysis of mode shapes has been applied extensively for damage localisation, which could describe the mode shape in multi-scales [124, 125, 126]. Douka et al. [65] adopted 1-D wavelet transform of mode shapes for beam-type structures and the sudden changes of wavelet coefficients were used to indicate the damage location. Gentile and Messina [85] studied the Gaussian wavelet transforms in localising open cracks of beams and concluded that high-order Gaussian derivative wavelets were more sensitive to damage detection. The effects of edge and noise were also discussed. Cao and Qiao [127] employed stationary wavelet transform to improve the noise robustness of mode shapes and then continuous wavelet transform to localise the damage.

Another common approach to examine the local singularities of mode shapes for damage localisation is fractal dimension analysis. Fractal dimension analysis was applied to the fundamental vibration mode of beams and plates and the sudden changes in the value of fractal dimension were used for damage localisation [128, 129]. Bai et al. [130] investigated the application of fractal dimension analysis to high-order mode shapes of plates, which validated that fractal surface singularities were efficient for

damage localisation. Moreover, fractal dimension analysis could be combined with wavelet analysis to improve the noise robustness of damage localisation [131].

The majority of baseline-free mode shape based damage identification methods depends on a certain mode shape and rarely combines several modes together. It is well known that a single mode shape is sensitive to damage at some locations but insensitive to damage at some other locations. Thus, it is desirable and promising, for accuracy and robustness, to localise damage by integrating damage information of several mode shapes. For this purpose, polynomial fitting techniques can be used to approximate mode shapes of the healthy state based on the mode shapes of damaged state. Consequently, the difference between them could be calculated and the damage information of several modes could be combined together. Xu and Zhu [132] used polynomial fitting approach to construct the mode shapes of undamaged plates and the square of absolute differences between mode shapes of damaged plates and the constructed mode shapes of undamaged structures were used to localise the damage in plates. Cao and Ouyang [86] proposed a robust damage localisation index by fairly incorporating the damage information of several modes, which used gapped smoothing method to extract the irregularities of mode shapes.

In addition, Pandey and Biswas [133] compared the modal flexibility before and after damage to detect the damage, which used the first several natural frequencies and mode shapes. Zhang and Aktan [134] demonstrated that uniform load surface, which was defined as the deflection vector of the structure under uniform load, was more robust to measurement noise than the modal flexibility. Wang and Qiao [135] applied fractal dimension analysis to uniform load surface of beam-type structures and the damage was localised by detecting the singularities of uniform load surface.

2.4.5 Mode shape curvatures

In comparison with mode shapes, mode shape curvatures are more sensitive to the damage-induced local shape singularities, especially for less severe damage. Moreover, the mode shape curvatures are directly associated with the bending moments of beams and plates. The mode shape curvature based damage identification methods are mainly categorised into two groups: with the baseline mode shape curvatures of healthy state and without bassline data of healthy state.

When the baseline mode shape curvature of healthy state are available, Pandey, et al. [64] demonstrated that absolute changes in mode shape curvature before and after damage was an efficient indicator of damage. Hu and Afzal [136] proposed a statistical algorithm for damage detection in timber beam structures using difference of the curvature mode shapes before and after damage. Wahab and Guido [137] combined the curvature differences before and after damage of several modes for damage identification and this method was validated by localising damage in a real bridge.

Although it is simple to identify the damage by comparing the mode shape curvatures before and after damage, it is promising to identify damage by using signal processing techniques to examine the damage-induced curvature singularities without using bassline data of healthy state in practical application. Moreover, these advanced signal techniques could be classified into two groups. One group uses multi-scale approaches (such as wavelet analysis and Gaussian smoothing) or fractal dimension analysis to reveal the sudden changes/peaks of mode shape curvatures for damage localisation. The second group of methods such as gapped smoothing method and low rank modelling predict the approximated mode shape curvatures of healthy state based on the mode shape curvatures of damaged state. After this, the differences between them of several modes are employed to form a damage index for robust damage localisation, which is more sensitive to incipient damage.

For the first group of baseline-free damage identification, Cao et al. [138] investigated the application of complex-wavelet analysis of mode shape curvatures of beam-type structures for detecting multiple cracks and this method was verified to be noise robust and accurate. Xu et al. [139] improved the curvature mode shape estimation of plates by estimating an equivalent mode shape curvature using Mexican hat wavelet and then the Teager energy operator was applied to clearly indicate the local singularities for damage localisation.

For the second group of baseline-free damage identification, Ratcliffe [140] proposed the gapped smoothing method to localise less severe damage by using the mode shape curvature of damaged structures, which was demonstrated to be sensitive to damage simulated by reducing thickness by 0.5%. Yoon et al. [141] extended the gapped smoothing method to two-dimensional plates and damage localisation was achieved by examining the singularities in mode shape curvatures. Rucevskis et al. [142] defined

a damage localisation index for plates using the difference between the mode shape curvature of damaged structures, and the mode shape curvature of healthy structures approximated by smoothed polynomial approach.

In addition, the modal strain energy (MSE) is directly associated with mode shape curvatures for beam-type or plate-type structures, which has shown to be promising for damage localisation. The modal strain energy for a Bernoulli-Euler beam of the r-th mode is expressed as

$$MSE_r = 1/2 \int_0^{length} EI \left(\frac{\partial^2 \varphi_r}{\partial x^2}\right)^2 \mathrm{d}x \tag{2.3}$$

where $\frac{\partial^2 \varphi_r}{\partial x^2}$ can be also written as φ_r''. Stubbs et al. [143] proposed a damage localisation index by using the modal strain energy changes before and after damage. Maia et al. [144] developed the discrete forms of the damage localisation index proposed by Stubbs et al. [143] and it was expressed as

$$DI_{l,r} = \frac{\left(\varphi_{l,r}^{\mathrm{d}\prime\prime 2} + \sum_{l=1}^{N_\mathrm{m}} \varphi_{l,r}^{\mathrm{d}\prime\prime 2}\right) \sum_{l=1}^{N_\mathrm{m}} \varphi_{l,r}^{\mathrm{u}\prime\prime 2}}{\left(\varphi_{l,r}^{\mathrm{u}\prime\prime 2} + \sum_{l=1}^{N_\mathrm{m}} \varphi_{l,r}^{\mathrm{u}\prime\prime 2}\right) \sum_{l=1}^{N_\mathrm{m}} \varphi_{l,r}^{\mathrm{d}\prime\prime 2}} \tag{2.4}$$

where the superscripts u and d indicates the undamaged state and damaged state, respectively. Also a comparison of damage localisation by methods of using mode shape changes, mode shape curvature changes was presented. Li et al. [145] developed a damage index based on fractal dimension and modal strain energy, which was effective in damage localisation and relative damage extent quantification of beams. Moreover, a comprehensive literature review of strain-based indicators for structural damage identification was presented by Li [146], which concluded that the selection of damage index relied on not only the requirements of damage identification quality but also the experimental conditions.

2.4.6 Nonlinear damage-sensitive features

Since nonlinear damage such as fatigue cracks introduces nonlinearities to the structures, the traditional linear damage features are naturally not suitable or less sensitive for nonlinear damage identification. Therefore, nonlinear damage features should be evaluated from the nonlinear vibration responses for effective damage identification.

A number of nonlinear damage features have been proposed such as distortions of frequency response function, deviations of probability function, Hilbert-Huang transform, Volterra series and harmonic distortions, which are mainly validated in cases involving fatigue cracks. Moreover, the majority of nonlinear damage identification methods uses only the test data of damaged structures.

Asnaashari and Sinha [147] used the deviation from normal distribution of vibration responses under sinusoidal excitation to localise breathing cracks in beam-type structures, which was also possible to indicate the relative damage severity. Douka and Hadjileontiadis [148] applied empirical mode decomposition and Hilbert transform to obtain instantaneous frequency of vibration responses, which could reveal the breathing process of a crack. In addition, the various instantaneous frequencies trends could be an indicator of crack size. Andreaus [35] modelled a breathing crack as a frictionless contact problem using two-dimensional finite elements. Sub- and super-harmonic components of vibration responses were used to illustrate the response characteristics due to the presence of breathing cracks. Chatterjee [31] applied a bilinear model to simulate a breathing crack and a nonlinear dynamic model was established by using Volterra series. The amplitudes of computed harmonic responses were found to indicate the crack severity. Lu et al. [149] proposed a super-harmonic characteristic deflection shapes to localise breathing cracks in stepped rotors, which was demonstrated to be robust to noise and steps in the structures.

Moreover, nonlinear systems can behave chaotically under certain forcing conditions. Thus, the indicators of chaotic phenomenon such as fractal attractor dimensions and Lyapunov exponents can be employed to detect the nonlinearity and further to identify the damage. Todd et al. [150] developed the local attractor variance ratio, which measured the state space geometry changes, to indicate the damage. Epureanu and Yin [151] proposed a multiple simultaneous damage detection method based on probability density functions of sampled attractors of the system dynamics.

2.5 Conclusions

A review of damage modelling, damage feature estimation, damage identification categories and common damage features for damage identification has been presented.

It provides a basic understanding of the problems and approaches for damage identification, which enable the development of new or improved damage identification methods in this project. In the next chapter, robust estimation of damage sensitive features will be investigated to assure the robust damage identification.

Chapter 3

Robust mode shape estimation via common principal component analysis

Mode shapes are highly sensitive to damage and thus effective for damage detection and localisation, but they are vulnerable to measurement noise and computational errors, which degrade their accuracy in damage identification. To enhance estimation accuracy of mode shapes and mode shape-based damage identification, common principal component analysis (CPCA) is investigated in this chapter for operational modal analysis, which evaluates the mode shape by finding a common subspace of a set of covariance or power spectral density matrices. Moreover, the common principal component analysis is conducted via joint approximation diagonalisation (JAD) or joint singular value decomposition according to the least-squares criterion.

First, one enhanced mode shape estimation approach is proposed based on the traditional time domain decomposition (TDD). Instead of using a digital band-pass filter to isolate the targeted mode, a set of digital band-pass filters are designed to extract the targeted mode. Then, CPCA is applied to a set of covariance matrices associated with the set of digital filters of the targeted mode for mode shape estimation. Secondly, another enhanced mode shape estimation approach is proposed based on the traditional frequency domain decomposition (FDD), which applies CPCA to a set of power spectral density matrices corresponding to a narrow frequency band around a certain resonant frequency. The estimated mode shapes will be statistically more noise robust. Finally, comparisons with the traditional methods will be presented to demonstrate the advantages of the proposed mode shape estimation methods in terms of noise robustness and accuracy.

3.1 Introduction

Structural damage is normally identified by model-based or non-model-based approaches [70, 98, 152]. Here, the model means the theoretical or numerical model of the structures. For model-based damage identification, a well-correlated structural model and the accurate initial state of the structure are required [27, 104, 153]. Furthermore, the large number of updating parameters and the non-uniqueness of updated models increase the difficulties of model updating-based damage identification methods [80]. For non-model based methods, damage detection and localization can be accomplished using input-output or only output responses. The majority of this kind of approaches is based on differences in structural modal parameters between damaged structures and healthy structures [22, 77]. However, in practical engineering applications, the baseline information of healthy structures is rarely available. Due to this, a kind of damage detection and localisation methods is very popular and attractive, which utilises the damage-induced local shape distortions of mode shapes or operational deflection shapes to identify damage without baseline data of healthy structures [84, 147, 154].

The identified structural characteristic deflection shapes (CDS's) possessing spatial information of structures are highly sensitive for damage localisation [155, 156, 157]. Here, CDS's refer to vector features that contain spatial structural information such as operational deflection shapes and mode shapes [68]. Basically, there are two approaches to increasing the accuracy and noise robustness of damage identification when using CDS's. One is to improve the noise robustness of CDS's during the estimation procedures and a robust mode shape evaluation method will be studied in this chapter. The other way is to apply signal processing techniques such as fractal dimension method, wavelet transform and gapped smoothing method to CDS's for noise reduction and damage feature extraction [131, 138, 158], which will be discussed in Chapter 4.

Mode shapes are generally estimated as the Eigen structure of matrices, which are functions of a number of vibration responses of available measurement locations. Generally, the Eigen structure could be evaluated from any member of the set of matrices or linear combinations of them. But, from a statistical point of view, mode shapes determined using a single matrix or two matrices are not satisfactory and tend

to be vulnerably contaminated by noise, which will lead to inaccurate damage identification. Therefore, it is necessary to acquire enhanced mode shapes by using a group of covariance or powers spectral density matrices. Common principal component analysis is one such method, which provides a common subspace of several matrices.

3.2 Subspace decomposition techniques

3.2.1 Subspace decomposition of a single matrix

Principal component analysis (PCA) is a statistical technique, which aims at representing the original data using low-dimensional subspace while preserving as much "energy" or variance as possible. Depending on the field of application, it is equivalent to proper orthogonal decomposition (POD) or discrete Karhunen–Loève transform [159, 160, 161]. Moreover, the principal components or principal modes of variation are normally computed by singular value decomposition (SVD) or Eigenvalue decomposition. They are an uncorrelated orthogonal basis set and are known as proper orthogonal modes (POM) in some literatures [162]. In addition, singular spectrum analysis (SSA) is an extension of PCA to a time series by embedding them in a vector space of a certain dimension, which is especially effective for extracting non-linear and non-harmonic components [163, 164, 165].

3.2.1.1 Singular value decomposition

For any $n_1 \times n_2$ matrix **A** (provided that $n_1 \geq n_2$), there exists a factorisation, termed as singular value decomposition, in the form of

$$\mathbf{A} = \mathbf{U}\boldsymbol{\Sigma}\mathbf{V}^{\mathrm{H}} = \sum_{i=1}^{n_2} \lambda_i \mathbf{u}_i \mathbf{v}_i^{\mathrm{H}} \tag{3.1}$$

where superscript H denotes the conjugate transpose, $\mathbf{U} = \left[\mathbf{u}_1, \mathbf{u}_2, \cdots, \mathbf{u}_{n_1}\right] \in \mathbb{R}^{n_1 \times n_1}$ and $\mathbf{V} = \left[\mathbf{v}_1, \mathbf{v}_2, \cdots, \mathbf{v}_{n_2}\right] \in \mathbb{R}^{n_2 \times n_2}$ are orthogonal matrices (if **A** is a real matrix) or unitary matrices (if **A** is a complex matrix), and $\boldsymbol{\Sigma} \in \mathbb{R}^{n_1 \times n_2}$ is a non-negative rectangular matrix with top n_2 rows forming a diagonal matrix containing singular values in a decreasing order: $\lambda_1 \geq \lambda_2 \geq \cdots \geq \lambda_{n_2} \geq 0$ and all zeros for the other $(n_1 - n_2)$ rows [166].

Moreover, the truncated SVD is a common approach for noise reduction and signal approximation, as the small singular values are mainly associated with noise. In

addition, it has extensive applications in modal analysis and damage identification [60, 159, 167, 168].

3.2.1.2 Eigenvalue decomposition

The eigenvalue decomposition (EVD) of a diagonalisable matrix $\mathbf{A} \in \mathbb{R}^{n\times n}$ is

$$\mathbf{A} = \mathbf{U}\boldsymbol{\Sigma}\mathbf{U}^{-1} \tag{3.2}$$

where $\mathbf{U} = [\mathbf{u}_1, \mathbf{u}_2, \cdots, \mathbf{u}_n] \in \mathbb{R}^{n\times n}$ contains the eigenvectors which are orthonormal with each other and $\boldsymbol{\Sigma} = \mathrm{diag}(\lambda_1, \lambda_2, \cdots, \lambda_n)$ is a diagonal matrix with eigenvalues of ascending order, which correspond to eigenvectors in $\mathbf{U}$.

Eigenvalue decomposition is commonly used to calculate the eigenvalues and eigenvectors of the structural system. For instance, it is employed in stochastic or deterministic subspace identification algorithms to evaluate the natural frequencies, damping ratios and mode shapes based on experimental data [59, 169].

3.2.2 Subspace decomposition of two matrices

For generalised eigenvalue problem of two $n \times n$ matrices $\mathbf{A}_1$ and $\mathbf{A}_2$, the factorisation is in the form of

$$\mathbf{A}_1\mathbf{U} = \mathbf{A}_2\mathbf{U}\boldsymbol{\Sigma} \tag{3.3}$$

If $\mathbf{A}_2$ is non-singular, Eq. (3.3) is equivalent to EVD problem by multiplying ${\mathbf{A}_2}^{-1}$ on the left. A generalised eigenvalue problem is solved to give the common eigenvectors of two matrices and has many applications such as complexity pursuit-based blind source separation [170] and smooth orthogonal decomposition [171].

3.2.3 Subspace decomposition of a group of matrices

Common principal component analysis is an extension of the traditional principal component analysis to simultaneously diagonalise a set of matrices, which finds a common low-dimensional subspace for accurately representing all the matrices while preserving as much "energy" or variance as possible. For example, in modal analysis, each covariance matrix may have some degenerate Eigen structure, but a set of covariance matrices will provide an accurate common Eigen structure. Moreover, the dominant or the first several subspace bases are a good estimation of the mode shapes. According to the least-squares criterion, the joint approximation diagonalisation or the

joint singular value decomposition is employed to determine the common principal components.

3.2.3.1 Joint approximation diagonalisation

Joint approximation diagonalisation (JAD) approach aims to estimate an orthogonal or unitary matrix that diagonalises a set of symmetric (Hermitian) square matrices according to the least-squares or weighted least-squares criteria, which performs better in determining the joint subspace, especially for data with low signal to noise ratio [86, 172]. For a set of symmetric (Hermitian) $n \times n$ matrices $\mathbf{A}_i$ $(i = 1, 2, \cdots, K)$, the JAD is expressed as

$$\mathbf{A}_i = \mathbf{U}\boldsymbol{\Sigma}_i\mathbf{U}^{\mathrm{H}} + \mathbf{E}_i \tag{3.4}$$

where $\mathbf{U} = [\mathbf{u}_1, \mathbf{u}_2, \cdots, \mathbf{u}_n] \in \mathbb{R}^{n\times n}$ is the joint orthogonal (unitary) matrix, $\boldsymbol{\Sigma}_i$ indicates the diagonal matrix and $\mathbf{E}_i$ denotes the noise matrix. For any $K > 2$, the problem in Eq. (3.4) is over determined and an exact solution $\mathbf{U}$ with $\mathbf{E}_i = 0, \forall i$ is not available. A common approach for solving this problem is the least-squares criterion and Eq. (3.4) is converted to find $\mathbf{U}$ and $\boldsymbol{\Sigma}_i$ that minimise cost function J

$$J(\boldsymbol{\Sigma}_i, \mathbf{U}) = \sum_{i=1}^{K} \|\mathbf{A}_i - \mathbf{U}\boldsymbol{\Sigma}_i\mathbf{U}^{\mathbf{H}}\| \tag{3.5}$$

where $\|\cdot\|$ denotes ℓ_2 norm. The details about the solution of Eq. (3.5) are given in Appendix A. In addition, JAD is an essential technique for independent component analysis and second-order blind identification, which have been investigated in operational modal analysis by many authors [54, 173, 174].

3.2.3.2 Joint singular value decomposition

Joint singular value decomposition (Joint SVD) is a problem of finding a pair of orthogonal matrices which simultaneously diagonalise a group of rectangular matrices. Generally, for a set of $n_1 \geq n_2$ matrices $\mathbf{A}_i(i = 1,2, \cdots, K)$, the Joint SVD is expressed as

$$\mathbf{A}_i = \mathbf{U}\boldsymbol{\Sigma}_i\mathbf{V}^{\mathrm{H}} + \mathbf{E}_i \tag{3.6}$$

Pesquet-Popescu et al. [175] proposed a Jacobi-like algorithm to solve Eq. (3.6) and apply it to image representation. Hori [176] investigated matrix gradient flows to address Joint SVD. Here, a direct approach is presented, which solves the Joint SVD via JAD in the form of

$$\begin{aligned}\mathbf{A}_i\mathbf{A}_i{}^{\mathrm{H}} &= \mathbf{U}\boldsymbol{\Sigma}_i{}^{\mathbf{2}}\mathbf{U}^{\mathrm{H}} + \mathbf{E}_i\mathbf{E}_i{}^{\mathrm{H}} \\ \mathbf{A}_i{}^{\mathrm{H}}\mathbf{A}_i &= \mathbf{V}\boldsymbol{\Sigma}_i{}^{\mathbf{2}}\mathbf{V}^{\mathrm{H}} + \mathbf{E}_i{}^{\mathrm{H}}\mathbf{E}_i\end{aligned} \tag{3.7}$$

Joint SVD is a natural extension of the singular value decomposition to a set of matrices. And it is a more general tool for non-symmetric, possibly rectangular matrices while JAD method is restrained to a Hermitian or a symmetric matrix set [177].

3.3 Robust mode shape estimation

In this section, common principal component analysis will be combined with some current operational modal analysis methods to enhance noise robustness and accuracy of mode shape estimation by using output-only data under random excitation. Consequently, the proposed methods are suitable for operational modal analysis as well.

Estimating mode shapes requires a set of spatial measurement locations along the structure. Moreover, the damage localisation accuracy largely depends on the density of measurement points. Fortunately, with the advanced measurement techniques such as embedded sensors or non-contact scanning laser scanning Vibrometer, experimental data of many measurement points are readily acquired.

Consider the equation of motion of an n degree-of-freedom system subjected to general excitation forces:

$$\mathbf{M}\ddot{\mathbf{x}}(t) + \mathbf{C}\dot{\mathbf{x}}(t) + \mathbf{K}\mathbf{x}(t) = \mathbf{f}(t) \tag{3.8}$$

where $\mathbf{x}(t) \in \mathbb{R}^{n\times 1}$is displacement vector, $\mathbf{f}(t) \in \mathbb{R}^{n\times 1}$indicates the excitation force vector, and $\mathbf{M} \in \mathbb{R}^{n\times n}$, $\mathbf{C} \in \mathbb{R}^{n\times n}$ and $\mathbf{K} \in \mathbb{R}^{n\times n}$ denote the mass matrix, damping matrix and stiffness matrix, respectively. According to the modal expansion theorem of structural response, vibration responses can be expressed in terms of mode shapes and modal coordinates as

$$\mathbf{x}^{(i)}(t) = \boldsymbol{\Phi}\mathbf{q}^{(i)}(t) \tag{3.9}$$

where $\boldsymbol{\Phi} \in \mathbb{R}^{n\times n}$ represents the modal matrix with the r-th column indicating the r-th mode shape), $\mathbf{q}(t) \in \mathbb{R}^{n\times 1}$ is the vector of modal coordinates and $i = 0,1,2$

indicates the interested responses are displacement, velocity or acceleration, respectively.

In order to use the experimental velocity measurements from a scanning laser Doppler Vibrometer, the following equations are derived in terms of velocity. The measured velocity response $\mathbf{y}(t) \in \mathbb{R}^{N_\mathrm{m}\times 1}$ of random vibration using Scanning Laser Vibrometer is acquired at N_m locations with N samples as

$$\mathbf{y}(t_j) = \boldsymbol{\Phi}_\mathbf{y}\mathbf{q}^{(1)}(t_j) + \mathbf{e}(t_j), j = 1, 2, \cdots, N \tag{3.10}$$

where $\mathbf{q}^{(1)}(t_j)$ indicates the velocity response of modal coordinate vector at time instant t_j, $\boldsymbol{\Phi}_\mathrm{y} = [\boldsymbol{\varphi}_1, \boldsymbol{\varphi}_2, \cdots, \boldsymbol{\varphi}_{N_\mathrm{m}}]$ represents the matrix of mode shape vectors corresponding to the measured degrees of freedom and $\mathbf{e}(t_j)$ denotes a vector of measurement noise.

Before computing the covariance matrix of vibration responses, a zero mean procedure is required. Provided that $\mathbf{e}(t)$ and $\boldsymbol{\Phi}_\mathrm{y}\mathbf{q}^{(1)}(t)$ are uncorrelated, covariance matrix of the responses should be computed from covariance matrices of the modal coordinates and noise as

$$\mathbf{R}_{\mathrm{yy}}(\tau) = \boldsymbol{\Phi}_\mathbf{y}\mathbf{R}_{\mathrm{q}^{(1)}\mathrm{q}^{(1)}}(\tau)\boldsymbol{\Phi}_\mathrm{y}^\mathrm{T} + \mathbf{R}_{\mathrm{ee}}(\tau) \tag{3.11}$$

where $\tau\ (= 0,1,2\cdots, N-1)$ represents time-delay (which is an integer multiple of the sampling period).

It is clear in Eq. (3.11) that $\mathbf{R}_{\mathrm{yy}}(\tau)$ possesses the same mode shape matrix $\boldsymbol{\Phi}_\mathrm{y}$ for all the time-lags (time-delays). Traditionally, $\mathbf{R}_{\mathrm{q}^{(1)}\mathrm{q}^{(1)}}(\tau)$ is a diagonal matrix at any time-lag τ, as the modal coordinate responses are assumed to be mutually uncorrelated. However, a necessary and sufficient condition for $\mathbf{R}_{\mathrm{q}^{(1)}\mathrm{q}^{(1)}}(\tau)$ to be exactly diagonal is that the structural system is conservative, which means that there is zero damping [54]. To overcome this restriction, the mode shapes can be determined using the covariance matrices of mode-isolated responses in time domain or using power spectral density matrices around a resonant frequency in frequency domain, which will be discussed in detail in the following sections.

3.3.1 Enhanced mode shape estimation based on TDD

3.3.1.1 Time domain decomposition

Time domain decomposition method is an operational modal analysis method to extract the mode shapes and natural frequencies for undamped or lightly damped structures [178]. There are three steps in the TDD method. First, a digital band-pass filter is designed to extract the filtered responses of the targeted mode. Secondly, based on the filtered responses, the covariance matrix is constructed. Finally, applying singular value decomposition to diagonalise the covariance matrix at zero time-delay, the first singular vector is a good estimation of the targeted mode shape.

It is assumed that there are N_{r} dominant and well separated poles present in the measured discrete velocity response. Equation (3.10) should be rewritten as

$$\mathbf{y}(t_j) = \sum_{r=1}^{N_{\mathrm{r}}} \boldsymbol{\varphi}_r \, q_r^{(1)}(t_j) + \mathbf{e}(t_j) \tag{3.12}$$

where $\boldsymbol{\varphi}_r = \left[\varphi_{r1}, \varphi_{r2}, \cdots, \varphi_{rN_{\mathrm{m}}}\right]^{\mathrm{T}}$ is the r-th mode shape of the measured degrees of freedom and $q_r^{(1)}(t_j)$ indicates the r-th modal velocity.

With the help of the digital band-pass filter, the r-th mode-isolated velocity response $\tilde{\mathbf{y}}_r(t_j)$ can be expressed as

$$\tilde{\mathbf{y}}_r(t_j) = \boldsymbol{\varphi}_r q_r^{(1)}(t_j) + \tilde{\mathbf{e}}_r(t_j) \tag{3.13}$$

where $\tilde{\mathbf{e}}_r(t_j)$ denotes the noise vector caused by the digital filter and measurement noise.

The covariance matrix of filtered mode isolated response is

$$\mathbf{R}^r_{\tilde{\mathrm{y}}\tilde{\mathrm{y}}}(\tau) = \boldsymbol{\varphi}_r \mathbf{R}_{q_r^{(1)} q_r^{(1)}}(\tau) \boldsymbol{\varphi}_r^{\mathrm{T}} + \mathbf{R}^r_{\tilde{\mathrm{e}}\tilde{\mathrm{e}}} \tag{3.14}$$

The singular value decomposition of $\mathbf{R}^r_{\tilde{\mathrm{y}}\tilde{\mathrm{y}}}(0)$ is

$$\mathbf{R}^r_{\tilde{\mathrm{y}}\tilde{\mathrm{y}}}(0) = \mathbf{U}_r \boldsymbol{\Sigma} \mathbf{U}_r^{\mathrm{T}} = \mathbf{u}_1 \lambda_1 \mathbf{u}_1{}^{\mathrm{T}} + \mathbf{U}_{\mathrm{noise}} \boldsymbol{\Sigma}_{\mathrm{noise}} \mathbf{U}_{\mathrm{noise}}{}^{\mathrm{T}} \tag{3.15}$$

Therefore, $\mathbf{u}_1$ is a good estimation of $\boldsymbol{\varphi}_r$. The advantage of this TDD method is that it is an operational modal analysis method and is efficient when a large number of excited modes are involved in the measured velocity responses.

However, for obtaining the mode isolated vibration data, designing an appropriate digital filter with the right order and band width is very important, which is very hard to do. Therefore, it is a little arbitrary to estimate the mode shape using a single digital band-pass filter. In the next section, an enhanced mode shape estimation is proposed, which designs a bank of digital band-pass filters to extract the targeted mode and common principal component analysis will be applied to determine the mode shape as the common singular vector of a set of covariance matrices.

3.3.1.2 **The enhanced method of TDD**

The first step of the proposed method is to acquire filtered data around a certain resonant frequency. Then, a set of covariance matrices can be constructed by a bank of suitably designed digital filters.

$$\mathbf{R}_{\tilde{\mathrm{y}}\tilde{\mathrm{y}}}^{r,i}(0) = \boldsymbol{\Phi}\mathbf{R}_{q_r^{(1)}q_r^{(1)}}^{r,i}(0)\boldsymbol{\Phi}^{\mathbf{T}} + \mathbf{R}_{\tilde{\mathrm{e}}\tilde{\mathrm{e}}}^{r,i} \tag{3.16}$$

where r represents the interested mode and $i(=1,2,\cdots,K)$ indicates the number of covariance matrix of different digital band-pass filter.

Define an orthogonal basis $\mathbf{U}_r = \left\{\mathbf{u}_j \in \mathbb{R}^{N_\mathrm{m}\times 1}, j=1,\cdots,N_\mathrm{m}\right\}$ with $\mathbf{u}_1 = \boldsymbol{\varphi}_r$ and $\left\{\mathbf{u}_2,\mathbf{u}_3,\cdots,\mathbf{u}_{N_\mathrm{m}}\right\}$ is orthogonal complementary vector basis. Assuming that the experimental data is not contaminated by noise, the spatial orthogonal basis of each covariance matrix $\mathbf{R}_{\tilde{\mathrm{y}}\tilde{\mathrm{y}}}^{r,i}(0), \forall i$ in Eq. (3.16) can be calculated by SVD as

$$\mathbf{R}_{\tilde{\mathrm{y}}\tilde{\mathrm{y}}}^{r,i}(0) = \mathbf{U}_{r,i}\boldsymbol{\Sigma}_{r,i}\,\mathbf{U}_{r,i}^{\mathrm{T}},\ \mathbf{U}_{r,i} = \left(\mathbf{u}_r^{\mathrm{c}}, \mathbf{U}_{r,i}^{\mathrm{s}}\right), \forall i \tag{3.17}$$

In Eq. (3.17), $\mathbf{u}_r^{\mathrm{c}}$=$\boldsymbol{\varphi}_r$ is the common singular vector while $\mathbf{U}_{r,i}^{\mathrm{s}} = \left\{\mathbf{u}_2,\mathbf{u}_3,\cdots,\mathbf{u}_{N_\mathrm{m}}\right\}$ is not guaranteed to be identical for all covariance matrices. According to the hierarchy of similarities among several covariance matrices, this is a partial common eigenvector problem. The hierarchy of similarities between K covariance matrices of dimensions $N_\mathrm{m} \times N_\mathrm{m}$ is presented in Table 3.1 [179].

Table 3.1 Hierarchy of similarities between K covariance matrices.

Level	Similarities	Number of parameters
1	Equality	$\frac{1}{2}N_{\mathrm{m}}(N_{\mathrm{m}}-1)+N_{\mathrm{m}}$
2	Proportionality	$\frac{1}{2}N_{\mathrm{m}}(N_{\mathrm{m}}-1)+N_{\mathrm{m}}+K-1$
3	Common eigenvectors	$\frac{1}{2}N_{\mathrm{m}}(N_{\mathrm{m}}-1)+KN_{\mathrm{m}}$
4	Partial common eigenvectors of number n_{c}	$\frac{1}{2}N_{\mathrm{m}}(N_{\mathrm{m}}-1)+KN_{\mathrm{m}}$ $+\frac{1}{2}(K-1)(N_{\mathrm{m}}-n_{\mathrm{c}})(N_{\mathrm{m}}-n_{\mathrm{c}}-1)$
5	Arbitrary covariance matrices	$K\left(\frac{1}{2}N_{\mathrm{m}}(N_{\mathrm{m}}-1)+N_{\mathrm{m}}\right)$

Although SVD deals well with the noise but it does not consider the additional noise matrix during singular vector estimation. In order to take into account the noise effects in covariance matrices as shown in Eq. (3.16), common principal component analysis is employed here. For this partial common eigenvector problem in Eq. (3.16), it is reasonable to assume that the covariance matrices $\mathbf{R}_{\tilde{\mathrm{y}}\tilde{\mathrm{y}}}^{r,i}(0), \forall i$ share all m common eigenvectors, because the mode shape $\boldsymbol{\varphi}_r$ plays a dominant role in each covariance matrix $\mathbf{R}_{\tilde{\mathrm{y}}\tilde{\mathrm{y}}}^{r,i}(0), \forall i$ while the contribution of $\mathbf{U}_{r,i}^{\mathrm{s}}$ is small. Now, the equation of applying the common principal component analysis to obtain the close solution of partial common eigenvector problem is formulated as

$$\mathbf{R}_{\tilde{\mathrm{y}}\tilde{\mathrm{y}}}^{r,i}(0)=\mathbf{U}_r\boldsymbol{\Sigma}_{r,i}\mathbf{U}_r^{\mathrm{T}}+\mathbf{E}_i, \forall i \tag{3.18}$$

If more than one mode is present in the selected frequency band $\omega_{r_1} \le \omega_r \le \omega_{r_2}$, the estimated mode shapes for closely spaced modes will be biased due to the orthogonality of CPCA and the bias mainly affects the weak mode whilst the dominant mode shape is still robust. And the bias depends on the gap between the first and second singular values: the bigger the gap, the smaller the error. In order to keep the robustness of the estimated mode shapes, only the largest dominant common singular vector in the selected frequency band is estimated and used for subsequent multi-damage localisation.

3.3.2 Enhanced mode shape estimation based on FDD

Taking discrete Fourier transform of Eq. (3.11), the power spectral density (PSD) matrix should be obtained as

$$\mathbf{S}_{\mathrm{yy}}(\omega) = \boldsymbol{\Phi}_{\mathbf{y}}\mathbf{S}_{\mathrm{q}^{(1)}\mathrm{q}^{(1)}}(\omega)\boldsymbol{\Phi}_{\mathbf{y}}^{\mathrm{H}} + \mathbf{S}_{\mathrm{ee}}(\omega) \tag{3.19}$$

where ω indicates the discrete frequency of excitation.

3.3.2.1 Frequency domain decomposition method

In Eq. (3.19), PSD matrix $\mathbf{S}_{\mathrm{yy}}(\omega) \in \mathbb{R}^{N_{\mathrm{m}} \times N_{\mathrm{m}}}$ is a Hermitian (positive definite) matrix having the common mode shape matrix $\boldsymbol{\Phi}_{\mathrm{y}}$ at the measurement degrees of freedom. The factorization of $\mathbf{S}_{\mathrm{yy}}(\omega_r)$ by SVD is

$$\mathbf{S}_{\mathrm{yy}}(\omega_r) = \mathbf{U}\boldsymbol{\Sigma}(\omega_r)\mathbf{U}^{\mathbf{H}} \tag{3.20}$$

where $\mathbf{U} = \left[\mathbf{u}_1, \mathbf{u}_2, \cdots, \mathbf{u}_{N_{\mathrm{m}}}\right]$ is an unitary matrix and $\boldsymbol{\Sigma}(\omega_r)$ is a diagonal matrix with non-negative singular values. If only one mode plays a dominant role at the response of this frequency, the first singular value $\mathbf{u}_1$is a good estimate of the mode shape $\boldsymbol{\varphi}_r$. If more than one mode is present in the response of this frequency, the estimated mode shapes will be biased due to the orthogonal property and the bias mainly affects the weak modes whilst the dominant mode shape is still robust [53].

Statistically, as far as accuracy and noise robustness are concerned, estimating the dominant mode shape using merely a single PSD matrix is often not satisfactory. Moreover, the dominant mode shape that contributes to the responses of several adjacent frequencies around the resonant frequency does not change much. Therefore, PSD matrices associated with a narrow frequency band around the resonant frequency can be used simultaneously for a better mode shape estimation. In addition, by doing this, the effect of leakage error can be minimised as well.

3.3.2.2 The enhanced method of FDD

Common principal component analysis is the right tool to extract the information of several PSD matrices corresponding to frequencies around a resonant frequency and obtain a common unitary diagonaliser. Equation (3.21) shows the simultaneous diagonalisation of a set of PSD matrices to find the common unitary matrix $\mathbf{U}_r$:

$$\mathbf{S}_{\mathrm{yy}}(\omega_{r+k}) = \mathbf{\Phi}_{\mathbf{y}}\mathbf{S}_{\mathrm{q}^{(1)}\mathrm{q}^{(1)}}(\omega_{r+k})\mathbf{\Phi}_{\mathbf{y}}^{\mathrm{H}} + \mathbf{S}_{\mathrm{ee}}(\boldsymbol{\omega}_{r+k}) = \mathbf{U}_r\mathbf{\Sigma}_{r+k}\mathbf{U}_r^{\mathrm{H}} + \mathbf{E}_{r+k} \quad (3.21)$$

where k ($k = [-K, -K+1, \cdots, K]$) denotes the adjacent frequency around ω_r and $\mathbf{S}_{\mathrm{yy}}(\omega_{r+k})$ represents a set of $2K+1$ PSD matrices. The joint unitary diagonalizer $\mathbf{U}_r \in \mathbb{R}^{N_{\mathrm{m}} \times N_{\mathrm{m}}}$ is identical but diagonal matrix $\mathbf{\Sigma}_{r+k} \in \mathbb{R}^{N_{\mathrm{m}} \times N_{\mathrm{m}}}$ and noise matrix $\mathbf{E}_{r+k} \in \mathbb{R}^{N_{\mathrm{m}} \times N_{\mathrm{m}}}$ are different at different k. For any K >0, the decomposition problem is over determined and generally an exact unitary matrix $\mathbf{U}_r$ with $\mathbf{E}_{r+k} = 0, \forall k$ is not available. A natural and common approach is to apply the least-squares criterion and the over-determined diagonalisation is formulated as a minimisation problem of variables $\mathbf{U}_r$ and $\mathbf{\Sigma}_{r+k}$:

$$J(\mathbf{U}_r, \mathbf{\Sigma}_{r+k}) = \sum_{k=-K}^{K} \left\| \mathbf{S}_{\mathrm{yy}}(\omega_{r+k}) - \mathbf{U}_r\mathbf{\Sigma}_{r+k}\mathbf{U}_r^{\mathbf{H}} \right\| \quad (3.22)$$

The details about the solution of Eq. (3.22) are presented in Appendix A. The non-diagonalisation of $\mathbf{S}_{\mathrm{q}^{(1)}\mathrm{q}^{(1)}}(\omega_{r+k})$ caused by damping and noise effects mainly deteriorates the singular vectors in $\mathbf{U}_r$ associated with the smaller singular values of $\mathbf{\Sigma}_r$ while the singular vector corresponding to the largest singular value is robust to these effects. As a consequence, only the estimated dominant mode shape at each resonant frequency will be used for structural damage identification.

3.4 The criteria to assess the noise robustness of mode shapes

In order to assess noise robustness of the evaluated mode shapes, Gaussian white noise is added to contaminate the simulated velocity responses $\mathbf{Y} \in \mathbb{R}^{N_{\mathrm{m}} \times N}$ in the form of

$$\widehat{\mathbf{Y}}_l = \mathbf{Y}_l + \mathbf{n}_{\mathrm{n}} n_{\mathrm{level}} \sigma(\mathbf{Y}_l), l = 1, 2, \cdots, N_{\mathrm{m}} \quad (3.23)$$

where $\mathbf{n}_{\mathrm{n}} \in \mathbb{R}^{1 \times N}$ contains normally distributed random values with a zero mean and a unit variance, n_{level} is the noise level range of [0 1] and $\sigma(\mathbf{Y}_l)$ denotes standard deviation of vibration responses at lth measurement point.

Moreover, two indicators: the averaged relative error and coefficient of variation, are introduced are adopted to assess the noise robustness of the proposed two mode shape estimation methods

3.4.1 Averaged relative error

The averaged relative error (ARE) is calculated according to Eq. (3.24)

$$ARE_{\varphi_{r,l}} = \frac{1}{N_a}\sum_{j=1}^{N_a}\frac{\left|\varphi_{r,l}-\overline{\varphi_{r,l}}_j\right|}{|\varphi_{r,l}|} \tag{3.24}$$

where $\varphi_{r,l}$ and $\overline{\varphi}_{r,l}$ denote the mode shape values at measurement point l without noise and with noise, respectively. N_a indicates the number of noise realisation.

3.4.2 Coefficient of variation

The coefficient of variation (CV) is defined as

$$CV\left(\overline{\varphi}_{r,l}\right) = \text{std}(\overline{\varphi}_{r,l})/\text{mean}(\overline{\varphi}_{r,l}) \tag{3.25}$$

where 'std' and 'mean' stand for standard deviation and mean operator, respectively.

3.5 Numerical studies

A cantilever beam is simulated to demonstrate the noise robustness of the proposed mode shape estimation methods. This cantilever beam is modelled using 40 elements in MATLAB according to Euler-Bernoulli beam theory with Rayleigh damping, $\mathbf{C} = \alpha\mathbf{M} + \beta\mathbf{K}$ ($\alpha = 4.0136$ and $\beta = 5.0850 \times 10^{-6}$), which leads to a modal damping level of 1% for the first and third modes and 0.5% for the second mode of this beam. Its geometrical and material properties are tabulated in Table 3.2. Random excitation is applied at point 20 and velocity time series are 'measured' at the prescribed 20 nodes along the beam at an equal distance of 0.035m, as shown in Figure 3.1.

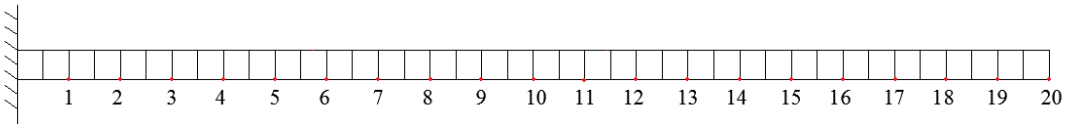

Figure 3.1 A steel cantilever beam.

Table 3.2 Material properties of steel beam.

Properties	Value
Length (m)	0.7
Cross-section (m × m)	0.02×0.02
Young's modulus (GPa)	210
Mass density (kg/m^3)	7850
Poisson ratio	0.33

Noise of the same level of 5% is added independently of **Y** 1000 times. With each noise realisation, the first three mode shapes are estimated by the proposed methods, respectively. The comparisons with other popular mode shape estimation methods are presented as well.

3.5.1 Numerical study of the enhanced TDD method

An example of the enhanced TDD method is given here to show its noise robustness, which combines the infinite impulse response (IIR) filters and JAD approach. There are three steps: (1) identify the resonant frequencies; (2) design a set of infinite impulse response (IIR) filters with different orders and bandwidths to extract the targeted mode and compute the covariance matrices of the filtered data; (3) apply JAD approach to the covariance matrices in step 2 to estimate the mode shape.

An estimate of the number of resonant frequencies in the output measurements can be made in a few ways, for instance, using the number of peaks in the trace plot of power spectral density matrix or in the singular value spectrum plot obtained by SVD of power spectral density matrix. Here, the latter is adopted and the singular value spectrum using the velocity responses is presented in Figure 3.2.

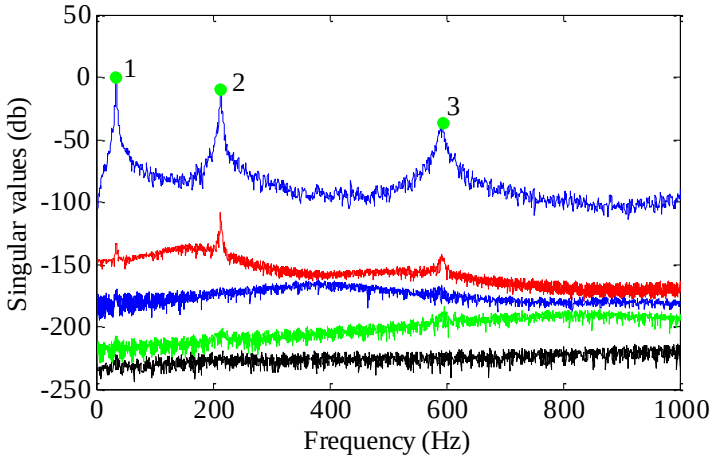

Figure 3.2 Singular value spectrum plot of numerical study.

At a resonant frequency ω_r such as peaks 1, 2 and 3 in Figure 3.2, two parameters, the filter orders and the band-pass widths $((1-k\%)\omega_r \leq \omega_r \leq (1+k\%)\omega_r)$, are

adjusted to obtain a series of IIR filters. An IIR filter includes both feedback and feed-forward terms, which is expressed as

$$\hat{y}(j) = \sum_{h_1=1}^{N_1} a_{h_1}\, \hat{y}(j-h_1) + \sum_{h_2=0}^{N_2} b_{h_2}\, y(j-h_2) \tag{3.26}$$

where N_1 denotes the feedback filter order, N_2 indicates the feed-forward filter order and $\hat{y}(j)$ is the output signal. Taking the Z-transform of Eq. (3.26), the IIR filter is converted to

$$H(z) = \frac{\sum_{h_2=0}^{N2} b_{h_2} z^{-h_2}}{1-\sum_{h_1=1}^{N1} a_{h_1} z^{-h_1}} \tag{3.27}$$

And its frequency response form is

$$H\left(\mathrm{e}^{\mathrm{j}\omega}\right) = \frac{\sum_{h_2=0}^{N2} b_{h_2} \mathrm{e}^{-\mathrm{j}h_2\omega}}{1-\sum_{h_1=1}^{N1} a_{h_1} \mathrm{e}^{-\mathrm{j}h_1\omega}} \tag{3.28}$$

In this study, the filter order $N_1 = N_2 = 8,10,12,14$ and the band-pass control parameter $k = 2,4,6,8$ are used. Thus a total number of 16 IIR filters is designed to isolate each targeted mode. Figure 3.3 shows an example of the eighth-order IIR filter with band-pass 28-35Hz.

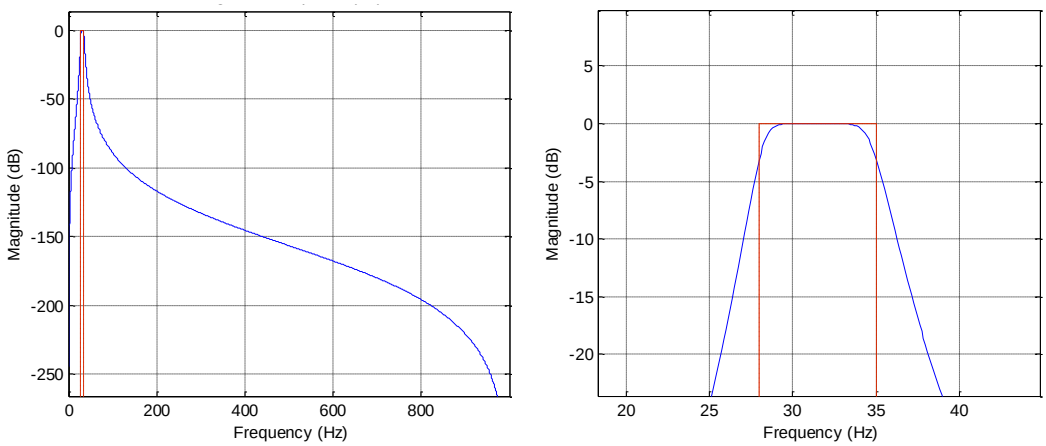

(a) (b)

Figure 3.3 Eighth-order IIR filter with band-pass 28-35Hz: (a) the whole frequency band (b) local magnification; the red line indicates the designed filter in theory while the blue line denotes the practical filter.

Now, the covariance matrices of filtered vibration data associated with the r-th mode shape is

$$\mathbf{R}_{\tilde{y}\tilde{y}}^{r,i}(0) = \boldsymbol{\Phi}\mathbf{R}_{\mathrm{q}^{(1)}\mathrm{q}^{(1)}}^{r,i}(0)\boldsymbol{\Phi}^{\mathrm{T}} + \mathbf{R}_{\tilde{\mathrm{e}}\tilde{\mathrm{e}}}^{r,i}(0) \tag{3.29}$$

where i indicates the covariance matrix calculated using the i-th IIR filter and r denotes the targeted mode. Figure 3.4 presents the mode shape estimation results over 1000 independent simulation.

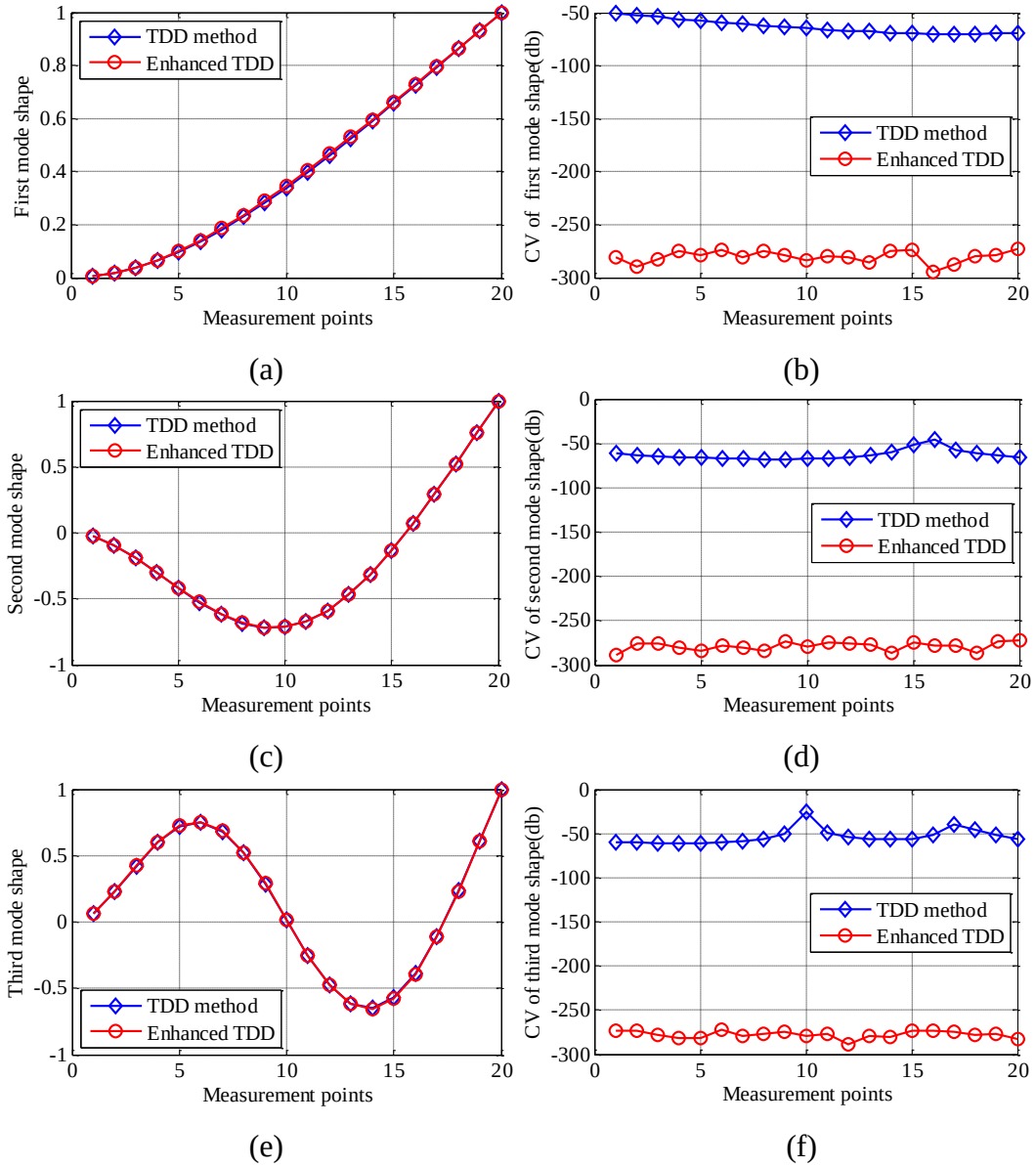

Figure 3.4 Mode shapes and their CVs over 1000 noise realisations.

It is clear in Figure 3.4 (b), (d) and (f) that the identified mode shapes of the proposed enhanced TDD method are much more accurate and noise robust than those by the traditional TDD method, as they have smaller CV values. Hence, CPCA performs better in mode shape estimation than the traditional PCA.

3.5.2 Numerical study of the enhanced FDD method

Figure 3.5 illustrates the mode shapes and their CVs of FDD method and enhanced FDD method.

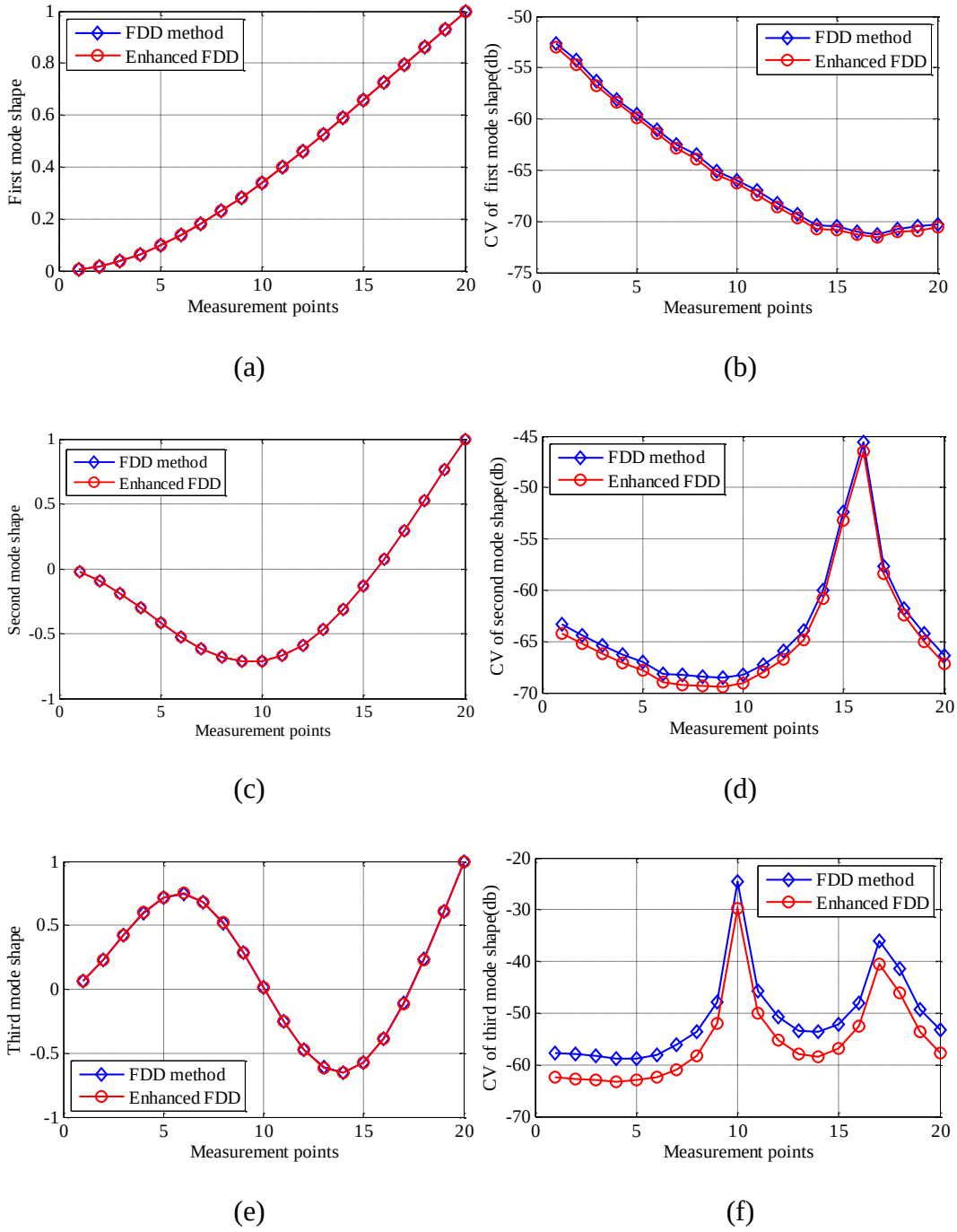

Figure 3.5 Mean real part of MS's and CV of absolute MS's.

It is indicated in Figure 3.5 (d)-(f) that the identified MS's of JAD method are more robust to noise than those of FDD method due to their smaller CV values.

3.6 Conclusions

In this chapter, two enhanced mode shape estimation methods are proposed based on common principal component analysis of multiple covariance matrices and power spectral density matrices, respectively. The advantage of doing this is that these methods provide a kind of 'average Eigen structure' shared by a group of matrices, which statistically deals better with the measurement noise than methods base on a single matrix such as principal component analysis or SVD method. Moreover, in frequency domain, using the PSD matrices associated with a narrow frequency band can minimise the leakage effects as well.

Numerical simulation of responses contaminated by Gaussian white noise demonstrates that the proposed common principal component analysis of multiple matrices perform better in estimation of mode shapes. The noise robustness of the estimated mode shapes promise a good accuracy of damage identification.

Moreover, the identified CDS's are an estimate of mode shapes and this indicates that common component analysis method has the potential to improve the accuracy of operational modal analysis, compared with traditional modal identification methods using one or two matrices.

Chapter 4

Robust multi-damage identification of beams using only output responses of damaged structures

The robust estimation of mode shapes from output-only responses has been studied in Chapter 3. The purpose of this chapter is to develop a baseline-free robust damage index for multi-damage identification by using damage-induced curvature changes of estimated mode shapes in Chapter 3. Although baseline-free damage identification methods have great advantages in practical applications, they face two main challenges: (1) the lack of baseline data of healthy structures for damage information extraction and (2) the demand of robust index for multi-damage localisation. For the first problem, an adaptive gapped smoothing method (GSM) is proposed to overcome the noise susceptibility and low accuracy of traditional GSM. For the second problem, a robust multi-damage index is developed based on damage-induced curvature changes of several modes, which is capable of damage localisation and relative severity quantification. Finally, numerical and experimental examples of beams with multi-cracks are studied to verify the effectiveness and advantages of the proposed baseline-free robust multi-damage index. Moreover, a comparison with some typical damage localisation methods is presented to demonstrate the better damage localisation performance of the new robust multi-damage index.

4.1 Introduction

The popular approaches of non-model-based damage identification are through a distance or similarity measure, which discerns the differences between damage features before and after damage for damage detection, localisation and severity quantification. For examples, Pandey et al. [64] demonstrated that absolute changes of mode shape curvatures before and after damage was an efficient indicator of damage. Galvanetto and Violaris [180] utilised the differences of proper orthogonal modes (POM) between healthy and damaged structures to localise damage in beams.

However, the drawback of this kind of methods is that they require the CDS's of undamaged structures, which are difficult or impossible to be acquired in practical application. Moreover, even when the CDS's of healthy structures are available, the operational and environmental variability or various uncertainties increases the CDS discrepancy between the healthy and damaged structures, which degrades the accuracy of extracting damage-induced CDS changes. Therefore, it is desirable and promising to develop a kind of baseline-free robust multi-damage identification methods that only require information of output responses of damaged structures [154, 181, 182].

In some studies [183, 184, 185], the localisation of structural damage is achieved directly by detecting the positions of sudden CDS curvature changes. However, this kind of approaches is vulnerably affected by the density of measurement points and measurement noise. Nowadays, the vibration responses of a large number of measurement points are readily acquired by non-contact scanning laser Vibrometer with high accuracy but the measurement noise is inevitable. Furthermore, the measurements of continuously scanning laser Vibrometer are easily contaminated by speckle noise [122]. To boost the efficiency and accuracy of damage identification using the damage-induced curvature singularities of CDS's, some advanced spatial feature processing approaches such as fractal dimension method, multi-scale approaches and Teager energy operator are widely utilised to examine the damage-induced local shape singularities while suppressing the effects of measurement noise.

Moreover, it is worth to notice that methods like fractal dimension, multi-scale approaches or Teager energy operator still use the sudden shape changes of a single CDS for damage identification. For instances, Hadjileontiadis et al. [129] developed a fractal dimension based crack indicator based on fundamental vibration mode, which

could localise and relatively quantify the crack. Rucka and Wilde [14] applied continuous wavelet transform to fundamental mode shapes of beams and plates, which detects the shape singularities of a single mode shape for damage localisation. Cao et al. [186] employed the Teagar energy operator to manifest the damage-caused local mode shape curvature changes. And wavelet transform was applied to reduce the noise effects on the mode shape curvature estimation.

It is well known that a certain CDS (such as a mode shape) is sensitive to damage at some locations whilst less sensitive to damage at some other locations. Hence, a multi-damage index relying on a single CDS is not reliable and accurate. A robust multi-damage index should be defined based on damage information of several CDS's. In this case, polynomial fitting/smoothing methods like GSM are able to extract damage-induced changes of CDS's for a baseline-free robust multi-damage index, as they can approximate the CDS's of healthy structures based on CDS's of damaged structures [140].

Nevertheless, when using the GSM, the polynomial order is usually determined without taking into consideration the data of CDS's. In order to enhance the accuracy and noise robustness of extracted damage-induced shape changes, an adaptive GSM is proposed, which adopts the cross validation method to obtain the optimal polynomial order. Moreover, before applying GSM method, de-noising methods such as wavelet transform and moving average filtering can be used to improve the noise robustness.

4.2 Baseline-free robust multi-damage index

With the estimated CDS's $\boldsymbol{\Phi}^{\mathrm{d}} = \left(\boldsymbol{\varphi}_1^{\mathrm{d}}, \boldsymbol{\varphi}_2^{\mathrm{d}}, \cdots, \boldsymbol{\varphi}_{N_{\mathrm{r}}}^{\mathrm{d}}\right)$ of damaged structures, damage identification is conventionally accomplished by comparing with the CDS's $\boldsymbol{\Phi} = \left(\boldsymbol{\varphi}_1, \boldsymbol{\varphi}_2, \cdots, \boldsymbol{\varphi}_{N_{\mathrm{r}}}\right)$ of healthy structures. The difference or distance between $\boldsymbol{\Phi}$ and $\boldsymbol{\Phi}^{\mathrm{d}}$ at measurement point l is measured by

$$DI_l\left(\boldsymbol{\Phi} \parallel \boldsymbol{\Phi}^{\mathrm{d}}\right) = \sum_{r=1}^{N_{\mathrm{r}}} w_{r,l}\left|\varphi_{r,l} - \varphi_{r,l}^{\mathrm{d}}\right|^2 \tag{4.1}$$

where w denotes the weighting coefficient, r indicates the r-th CDS $\boldsymbol{\varphi}_r$ and N_{r} represents the total number of CDS's concerned for damage identification. Normally, the absolute CDS difference $\Delta\boldsymbol{\varphi}_r = \left|\boldsymbol{\varphi}_r - \boldsymbol{\varphi}_r^{\mathrm{d}}\right|$ has a big variation in magnitude for different CDS's (|vector| denotes the absolute value of each term of a

vector not the traditional Euclidean distance in this thesis). If they are simply added together, the contribution of each $\Delta\boldsymbol{\varphi}_r$ to the multi-damage index is not even. Table 4.1 tabulates some common damage identification indexes.

Table 4.1 Some typical damage identification indexes.

Method	Damage index
Co-ordinate modal assurance criterion [121]	$\frac{\left\lvert\sum_{r=1}^{N_\mathrm{r}} \varphi_{r,l}^{\mathrm{u}} \varphi_{r,l}^{\mathrm{d}}\right\rvert^2}{\sum_{r=1}^{N_\mathrm{r}}\left(\varphi_{r,l}^{\mathrm{u}}\right)^2 \sum_{r=1}^{N_\mathrm{r}}\left(\varphi_{r,l}^{\mathrm{d}}\right)^2}$
Mode shape difference method	$\sum_{r=1}^{N_\mathrm{r}}\left\lvert\boldsymbol{\varphi}_r^{\mathrm{d}} - \boldsymbol{\varphi}_r^{\mathrm{u}}\right\rvert$
Weighted mode shape difference method	$\sum_{r=1}^{N_\mathrm{r}}\left\lvert\frac{\boldsymbol{\varphi}_r^{\mathrm{d}}}{\omega_r^{\mathrm{d}}} - \frac{\boldsymbol{\varphi}_r^{\mathrm{u}}}{\omega_r^{\mathrm{u}}}\right\rvert$
Mode shape curvature difference method	$\sum_{r=1}^{N_\mathrm{r}}\left\lvert\boldsymbol{\varphi}^{\mathrm{d}''}{}_r - \boldsymbol{\varphi}^{\mathrm{u}''}{}_r\right\rvert$
Damage index method [144]	$\sum_{r=1}^{N_\mathrm{r}} \frac{\left(\varphi_{r,l}^{\mathrm{d}''2} + \sum_{l=1}^{N_\mathrm{m}} \varphi_{r,l}^{\mathrm{d}''2}\right)\sum_{l=1}^{N_\mathrm{m}} \varphi_{rl}^{\mathrm{u}''2}}{\left(\varphi_{r,l}^{\mathrm{u}''2} + \sum_{l=1}^{N_\mathrm{m}} \varphi_{r,l}^{\mathrm{u}''2}\right)\sum_{l=1}^{N_\mathrm{m}} \varphi_{rl}^{\mathrm{d}''2}}$
Flexibility matrix changes method [133]	$\sum_{r=1}^{N_\mathrm{r}}\left(\frac{\boldsymbol{\varphi}_r^{\mathrm{d}}\boldsymbol{\varphi}_r^{\mathrm{d}\mathrm{T}}}{\left(\omega_r^{\mathrm{d}}\right)^2} - \frac{\boldsymbol{\varphi}_r^{\mathrm{u}}\boldsymbol{\varphi}_r^{\mathrm{u}\mathrm{T}}}{(\omega_r^{\mathrm{u}})^2}\right)$

It is shown in Table 4.1 that the damage indexes normally combine the damage information of several mode shapes or mode shape curvatures, which are simply added up or weighted by natural frequencies. In order to evenly using the damage information of each CDS, a robust multi-damage index (DI) is proposed in Eq. (4.2) by incorporating the damage-induced curvature changes of several CDS's. Furthermore, the proposed robust multi-damage index is baseline-free, which is defined as the distance between smoothed CDS curvature $\widehat{\boldsymbol{\Phi}}''$ and original CDS curvature $\boldsymbol{\Phi}^{\mathrm{d}''}$ of the damaged structure.

$$
\begin{aligned}
DI_l &= \rho_l \gamma_l \delta_l \,, \\
\rho_l &= \left(\prod_{r=1}^{N_\mathrm{r}} \max\left(\left|\widehat{\boldsymbol{\varphi}}_r'' - \boldsymbol{\varphi}_r^{\mathrm{d}''}\right|\right)\right)^{\frac{1}{N_\mathrm{r}}} \\
\gamma_l\left(\widehat{\boldsymbol{\Phi}}'' \parallel \boldsymbol{\Phi}^{\mathrm{d}''}\right) &= \sum_{r=1}^{N_\mathrm{r}} w_r \left|\widehat{\varphi}_{r,l}'' - \varphi_{r,l}^{\mathrm{d}}{}''\right| \\
\delta_l\left(\widehat{\boldsymbol{\Phi}}'' \parallel \boldsymbol{\Phi}^{\mathrm{d}''}\right) &= \sum_{r=1}^{N_\mathrm{r}} w_r^2 \left|\widehat{\varphi}_{r,l}'' - \varphi_{r,l}^{\mathrm{d}}{}''\right|^2
\end{aligned}
\tag{4.2}
$$

where the weighing coefficient w_r is $1/\max \Delta\boldsymbol{\varphi}_r''$ ($\Delta\boldsymbol{\varphi}_r'' = \left|\widehat{\boldsymbol{\varphi}}_r'' - \boldsymbol{\varphi}_r^{\mathrm{d}''}\right|$). Moreover, γ_l and δ_l denote the normalised first-order and second-order moments of shape

distortions $\Delta\varphi''_{r,l}$. In addition, ρ_l provides a global magnitude measure, which enables the proposed multi-damage index to quantify the relative damage severity.

In Eq. (4.2), the curvature of CDS's is used as it is more sensitive to damage than the CDS's themselves, which is computed through the second-order central difference approach as

$$\varphi^{\mathrm{d}}_{r,l}{}'' = \frac{\varphi^{\mathrm{d}}_{r,l+1} - 2\varphi^{\mathrm{d}}_{r,l} + \varphi^{\mathrm{d}}_{r,l-1}}{{d_{\mathrm{x}}}^2} \tag{4.3}$$

where d_{x} represents the distance between two successive measurement points and a prime indicates differentiation with respect to the spatial coordinate. Although it is fairly straightforward to compute the curvature of CDS's using Eq. (4.3), the accuracy is affected by the density of measurement points and noise level. Basically, to achieve good accuracy of CDS curvature estimation, a dense measurement grid and an accurate extraction of CDS's are required.

The purpose of this chapter is to develop baseline-free robust multi-damage identification index. In this case, $\boldsymbol{\Phi}$ of healthy structures is not available and $\boldsymbol{\Phi}$ is approximated by applying polynomial smoothing approach to the CDS's $\boldsymbol{\Phi}^{\mathrm{d}}$ of damaged structures.

4.3 Estimate $\widehat{\boldsymbol{\Phi}}''$ based on CDS's of damaged state

Now, the crucial work is to estimate the smoothed CDS $\widehat{\boldsymbol{\varphi}}''_r$ and shape distortion $\Delta\boldsymbol{\varphi}''_r$. In theory, there are two approaches to calculate $\widehat{\boldsymbol{\Phi}}''$: one is to fit the CDS first and then calculate its curvature and the other one is to fit the curvature of CDS's directly. The latter approach is selected due to its higher damage sensitivity and accuracy. Ratcliffe [140] proposed a gapped smooth method, which is

$$\hat{\varphi}''_r(x, \mathbf{c}) = c_0 + c_1 x + c_2 x^2 + c_3 x^3 \tag{4.4}$$

where x indicates location of the measured CDS curvature along a beam-type structure and $\mathbf{c} = [c_0, c_1, c_2, c_3]$ are coefficients of the cubic polynomial. The two CDS curvature values $\varphi''_{r,l-2}$ and $\varphi''_{r,l-1}$ before measurement point l and the two CDS curvature values $\varphi''_{r,l+1}$ and $\varphi''_{r,l+2}$ after measurement point l are used to compute $\mathbf{c}$ and predict $\hat{\varphi}''_{r,l}$ at measurement point l.

If damage-induced shape distortions are present at several adjacent measurement points, the damage index determined by GSM cannot detect and localise the damage accurately. As an improvement, an adaptive gapped smoothing method is proposed in Eq. (4.5) to enhance the noise robustness and accuracy of damage identification.

$$\widehat{\boldsymbol{\varphi}}_r''(z, \mathbf{c}, p) = c_0 + c_1 x + c_2 x^2 + \cdots + c_p x^p \tag{4.5}$$

where $\mathbf{c} = [c_0, c_1, c_2, \cdots, c_p]$ contains the polynomial coefficients and p indicates the adaptive polynomial order. Figure 4.1 illustrates the calculation of CDS curvature difference $\Delta\varphi_{r,l}''$ by adaptive GSM.

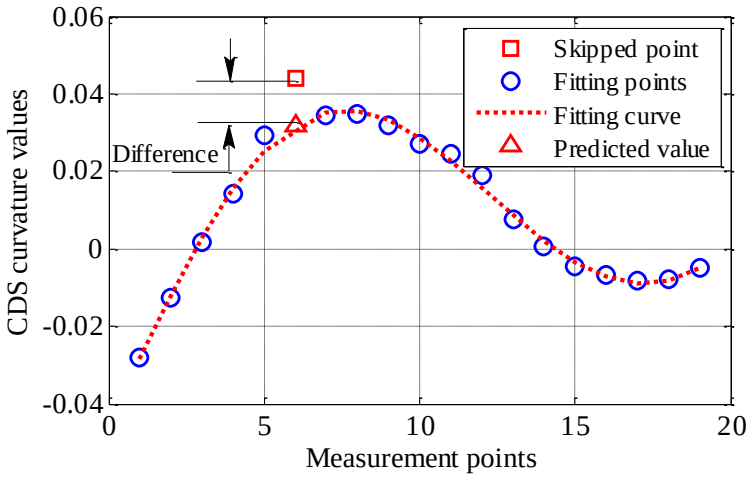

Figure 4.1 Illustration of adaptive gapped smoothing method.

In fact, the greater the order of polynomial in Eq. (4.5), the more accurate and flexible the fitting is. However, over fitting the training data with a great order causes poor generalisation and leads to inaccurate $\hat{\varphi}_{r,l}''$, which also degrades the accuracy of damage identification. In order to obtain the optimal polynomial order p for polynomial approximation and generalisation, cross-validation method is adopted to determine p in the range of $[0, p_{\max}]$ for different skipped points of each CDS curvature. In this chapter, the cross-validation subsets $k_c = 3$ is used and the maximum order $p_{\max}$ is calculated as

$$p_{\max} = \lfloor (k_c - 1)/k_c \, (N_m - 2) - 1 \rfloor \tag{4.6}$$

where $\lfloor \, \rfloor$ is the floor operator. If the number of measurement points N_m is large, it is better to separate them into several segments.

4.4 Numerical examples

4.4.1 A beam with two open cracks

A cantilever beam with two open cracks is first studied to demonstrate the damage identification performance of the proposed adaptive GSM and multi-damage index. The material properties of the cantilever beam are listed in Table 4.2 and the crack configurations are tabulated in Table 4.3.

Table 4.2 Material properties of steel beam.

Property	Value
Cross-section dimensions (m × m)	0.02×0.02
Young's modulus (GPa)	210
Mass density (kg/m^3)	7861
Poisson ratio	0.33

Table 4.3 Information of crack configurations.

Cracks	Location	Measurement points	Width	Depth percentage
Crack 1	0.2m	10~11	0.001m	2%, 5%, 20%
Crack 2	0.4m	20~21	0.001m	2%, 5%, 20%

A cantilever beam of length 0.7m with two open cracks is modelled in ABAQUS using 672 CPS8R elements as shown in Figure 4.2. CPS8R is an 8-node biquadratic plane stress quadrilateral element with reduced integration. It is selected as the quadratic approximation tends to be better than the linear one and reduced integration is used to decrease the computational costs. During the simulation, Rayleigh damping, $\mathbf{C} = \alpha\mathbf{M} + \beta\mathbf{K}$ with $\alpha = 4.0136$ and $\beta = 5.0850 \times 10^{-6}$ is considered, which leads to a modal damping level of 1% for the first and third modes and 0.5% for the second mode of this beam. Pseudo-random excitation in frequency range of 0-800Hz is applied at the free end of the beam and velocity time series are 'measured' at the prescribed 35 red points with an equal distance of 0.02m. The singular value spectrum plot is presented here to show the number of excited modes, which is computed by applying SVD to the PSD matrix at each frequency. In Figure 4.3, the first five singular values at each frequency are plotted to indicate the first three excited modes. In addition, the

numerical simulation is solved by using 215, 672 and 3746 CPS8R elements to assure that 672 CPS8R elements are enough to promise a convergence solution.

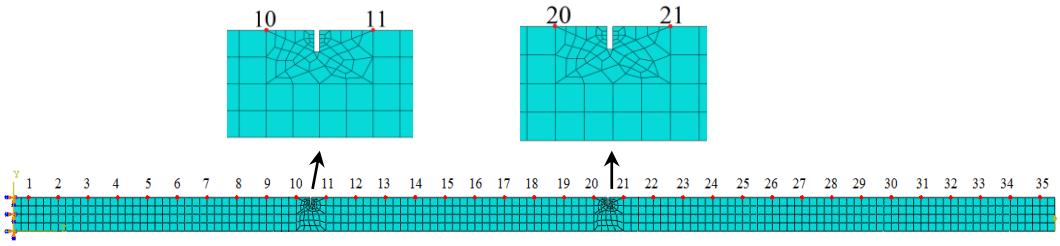

Figure 4.2 Meshed cantilever beam with two open cracks of 20% depth.

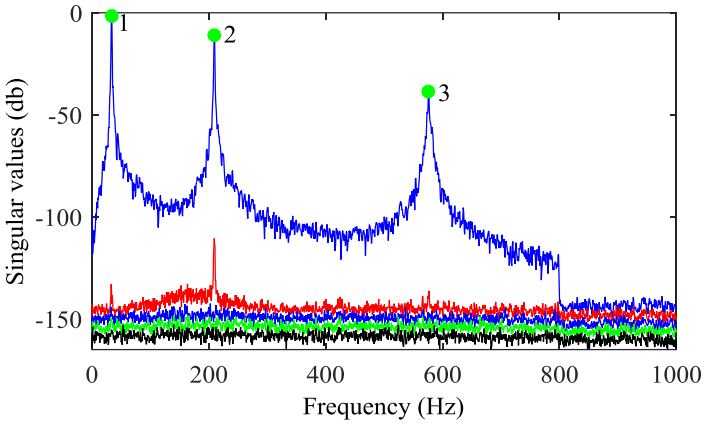

Figure 4.3 Singular value spectrum plot of PSD matrices.

The first three mode shapes and their associated curvatures are presented in Figure 4.4, which are estimated by the enhanced TDD method in Chapter 3. By comparison between Figure 4.4 (a) and Figure 4.4 (b), it is concluded that mode shape curvatures are much more sensitive to damage, since the damage locations are manifested clearly in the mode shape curvature plots. Moreover, a certain mode shape is demonstrated to be sensitive to damage at specific positions. For instance, the curvature of second mode shape (Figure 4.4 (d)) is sensitive to crack 2 whilst the curvature of first and third mode shape (Figure 4.4 (b) and Figure 4.4 (f)) are more sensitive to crack 1. In addition, the magnitude of mode shape curvatures in Figure 4.4 (b), (d) and (f) indicates that the second and third mode shapes are much more sensitive to damage than the first mode shape, which can be further validated by Figure 4.5 (a), (c) and (e).

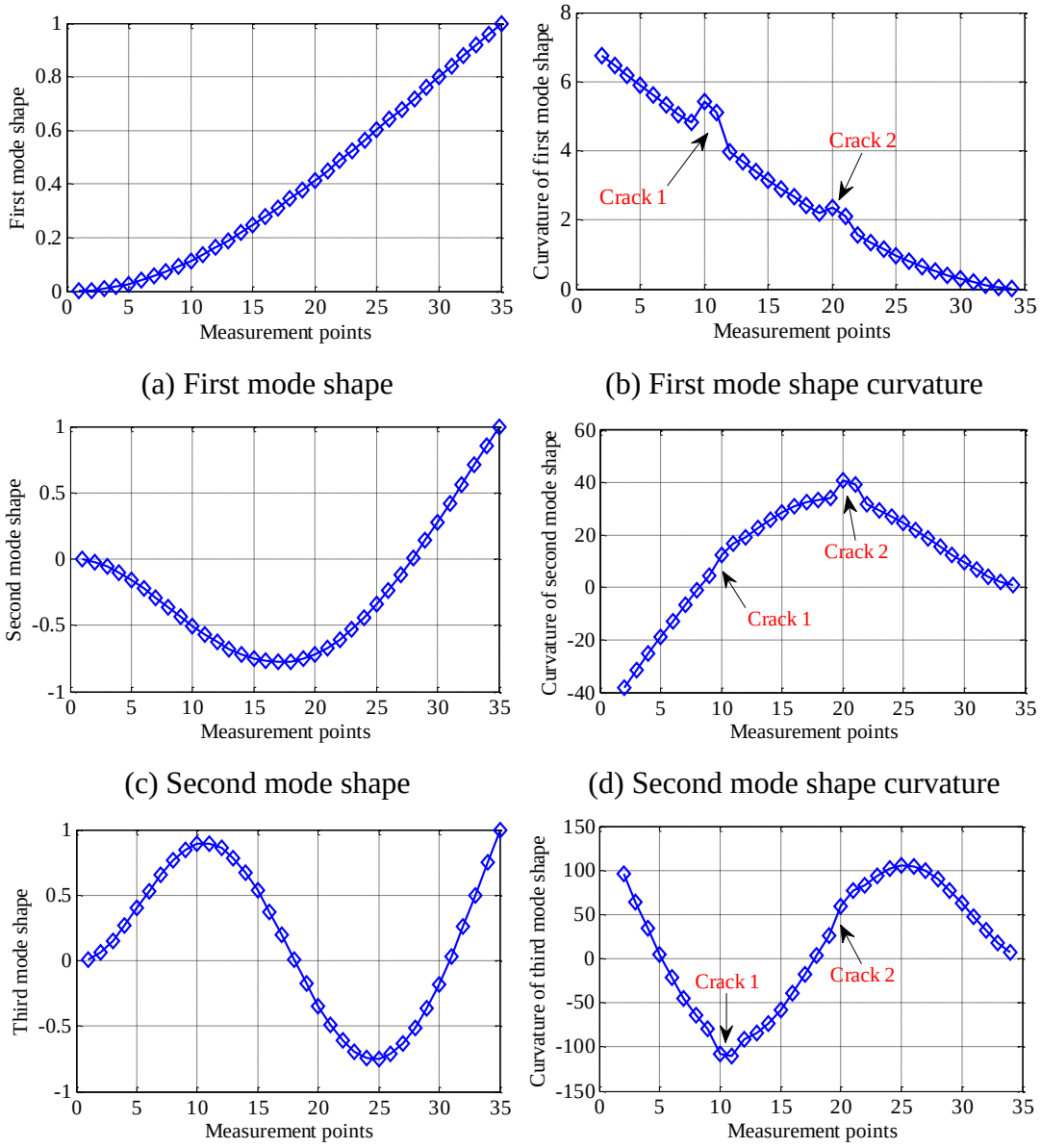

(a) First mode shape

(b) First mode shape curvature

(c) Second mode shape

(d) Second mode shape curvature

(e) Third mode shape

(f) Third mode shape curvature

Figure 4.4 Mode shapes and their curvatures of numerical study of 20% depth.

4.4.1.1 Comparison between adaptive GSM and traditional GSM

In this example, for the adaptive GSM, only one window is used, which means all the measurement points are used to find the optimal polynomial order. The extracted damage features of the first three mode shape curvatures are presented in Figure 4.5.

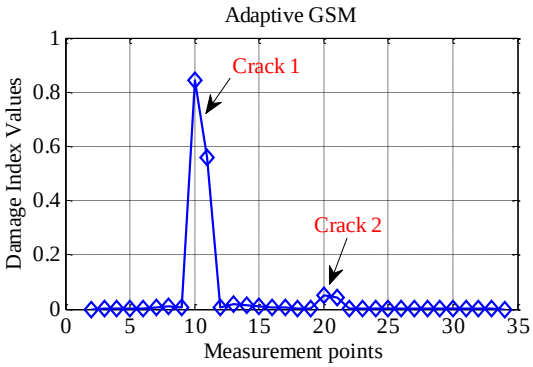

(a) First mode shape curvature

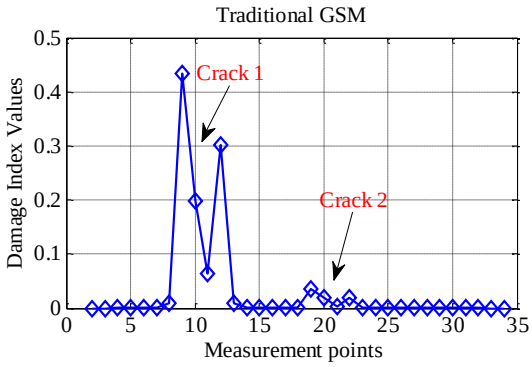

(b) First mode shape curvature

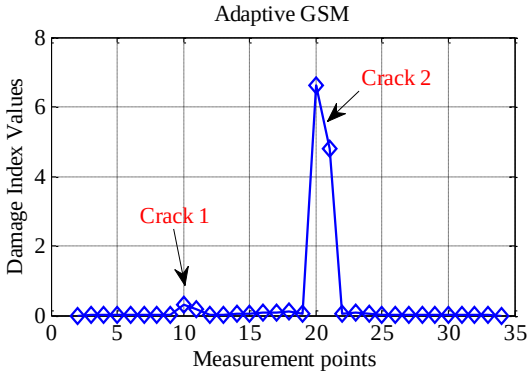

(c) Second mode shape curvature

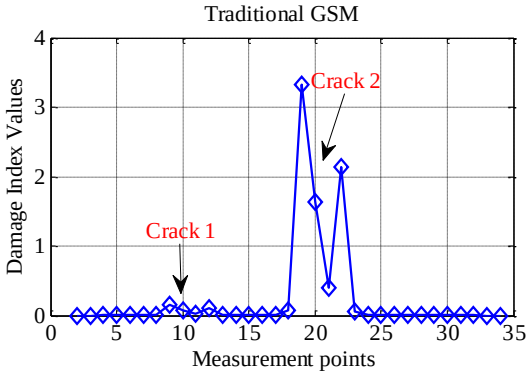

(d) Second mode shape curvature

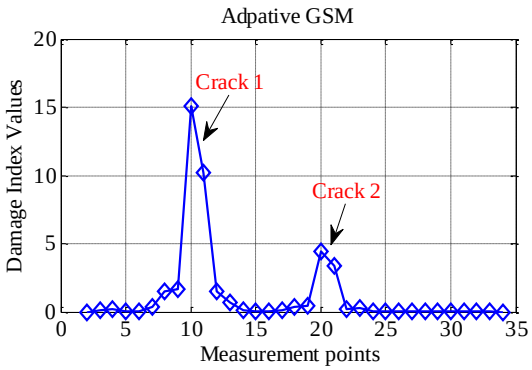

(e) Third mode shape curvature

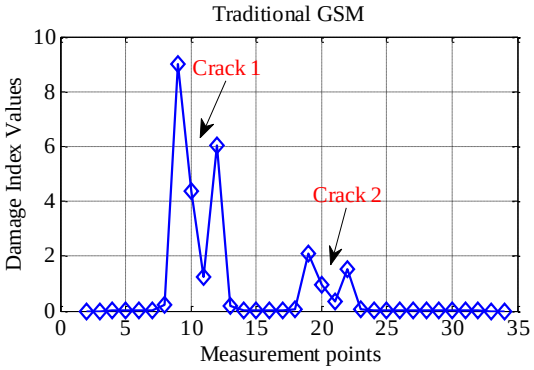

(f) Third mode shape curvature

Figure 4.5 Damage identification using adaptive GSM and traditional GSM.

It is clear from Figure 4.5 that damage index values around the damage locations have sharp peaks for the adaptive GSM whereas there are several distortion points for the traditional GSM, which is not accurate for the damage localisation in this example. Furthermore, Figure 4.5 also implies that different mode shapes are sensitive to damage at different positions. Therefore, it is not accurate and robust to detect damage just using damage information of a single mode shape. The proposed damage index for multi-damage localisation is shown in Figure 4.6, which combines the damage information of the first three mode shapes. In comparison with the damage

identification base on an individual mode shape curvature, the integrated damage index is sensitive to both cracks. Moreover, the damage index magnitudes of adaptive GSM is larger than these of traditional GSM, which demonstrates that the damage index based on adaptive GSM is more sensitive to damage.

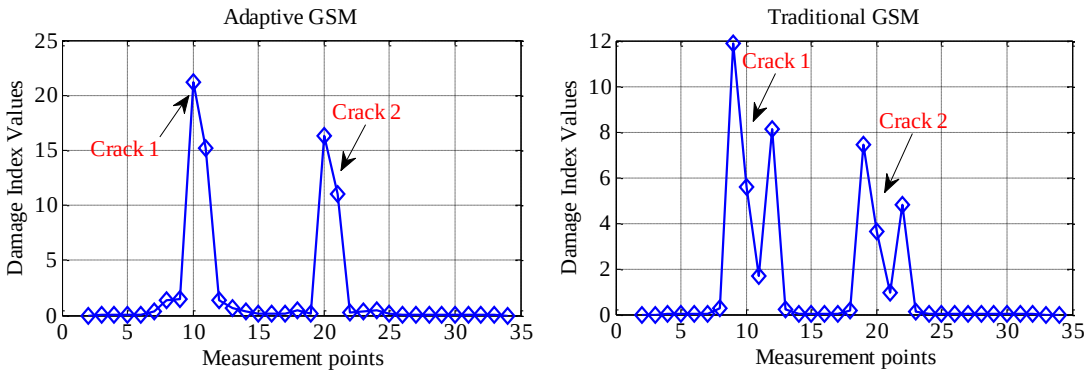

(a) (b)

Figure 4.6 Integrated damage index based on first three mode shapes.

4.4.1.2 Damage index of different crack depths and noise levels

Figure 4.7 presents the damage index values of a beam with two open cracks of 2%, 5% and 20% depths, respectively. Moreover, different levels of Gaussian white noise are added to study the noise robustness of the proposed multi-damage index.

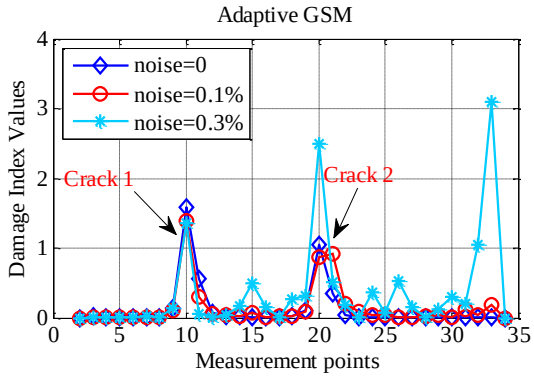

(a) 2% depth

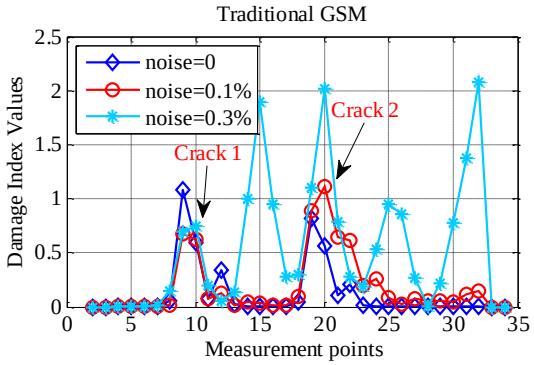

(b) 2% depth

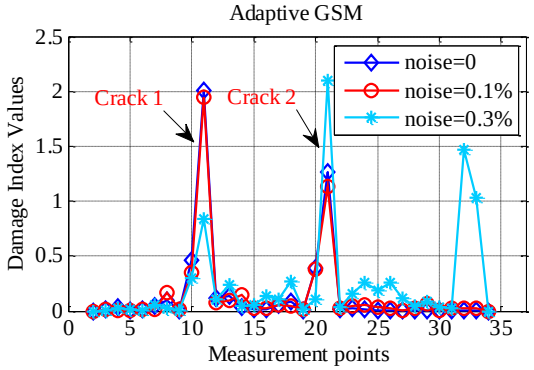

(c) 5% depth

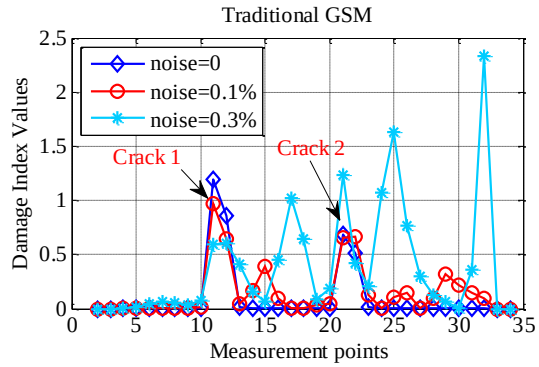

(d) 5% depth

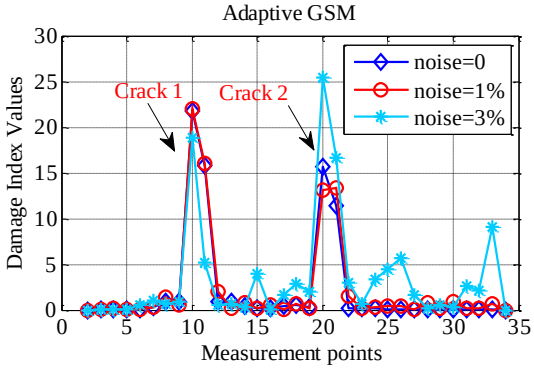

(e) 20% depth

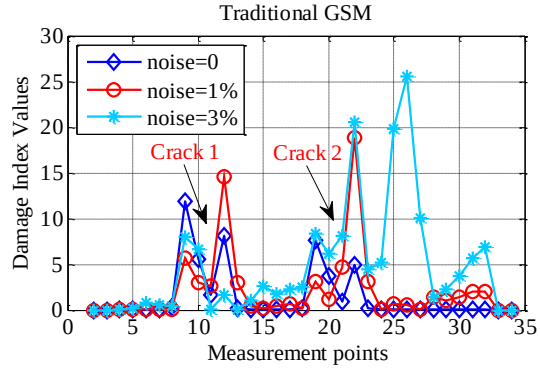

(f) 20% depth

Figure 4.7 Damage index values of three damage depth and noise levels.

Without noise effects, the two cracks of all the three depths can be accurately localised by using either adaptive GSM or traditional GSM. But the comparison between Figure 4.7 (e) and Figure 4.7 (f) shows that damage identification of adaptive GSM is much more accurate and noise robust than traditional GSM. Furthermore, Figure 4.7 (a), Figure 4.7 (c) and Figure 4.7 (e) indicate that the deeper the crack is, the bigger the magnitude of the damage index values and the more noise robust it is. Thus, the proposed multi-damage index is effective to localise the damage positions and indicate the relative damage severity.

4.4.2 A beam with two breathing cracks

In section 4.4.1, the proposed multi-damage index is validated to be effective for a beam with multiple open cracks. In this section, the proposed damage identification method will be applied to localise breathing cracks in a beam to test its feasibility and efficiency for breathing crack identification.

A cantilever beam with two breathing cracks is simulated and tested under the same condition as the example of a beam with two open cracks in section 4.4.1. The breathing cracks are modelled in ABAQUS using 2-D FE model as shown in Figure 4.8. More details about breathing crack modelling will be presented in Section 5.2.2 of Chapter 5.

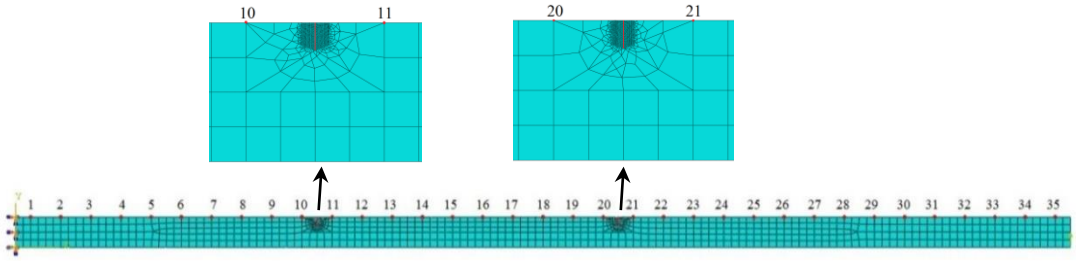

Figure 4.8 Meshed cantilever beam with two breathing cracks of 20% depth.

Figure 4.9 shows the damage index values of a beam with two breathing cracks of 2%, 5% and 20% depths, respectively, which are based on adaptive GSM not the traditional GSM.

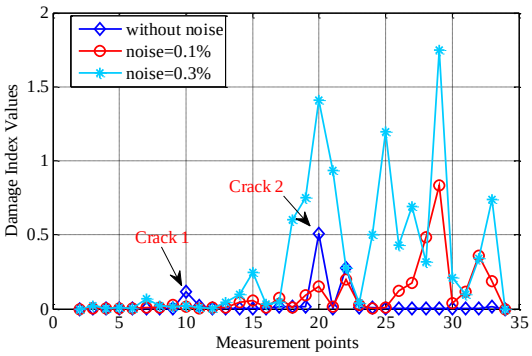

(a) 2% depth using adaptive GSM

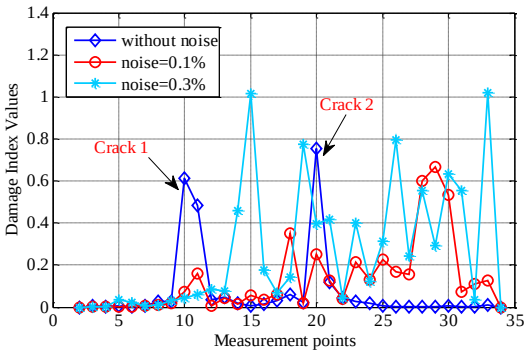

(b) 5% depth using adaptive GSM

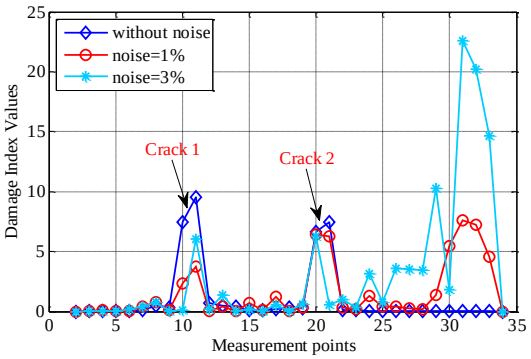

(c) 20% depth using adaptive GSM

Figure 4.9 Damage index values of a beam with two breathing cracks.

In comparison with Figures 4.7 (a), (c) and (e), the damage index values for the breathing cracks in Figure 4.9 are much smaller than those of the open cracks with the same depths. Moreover, it is harder to localise the smaller depth of breathing cracks than open cracks. For instance, the first breathing crack in Figure 4.9 (a) is hard to be detected whilst the open crack can be clearly localised in Figure 4.7(a), especially for noisy data. In conclusion, the proposed damage index is less sensitive for the identification of breathing cracks.

4.5 Experimental studies

The purposes of this section are threefold. First, the proposed adaptive GSM and robust multi-damage index will be validated. In addition, a comparison with some traditional damage indexes will be presented. Secondly, the damage identification performance of real part, imaginary part and the absolute values of modes shape curvatures will be investigated. The mode shapes are evaluated by proposed enhanced FDD method in Chapter 3 and the mode shape curvatures are calculated by second-order central difference approach. Finally, by comparison with the damage identification results

based on traditional FDD method, damage identification results using the enhanced FDD method are demonstrated to be much more accurate and noise robust.

Two steel beams having dimensions of $0.7 \times 0.02 \times 0.02\ m^3$ with two open cracks are tested. Experimental set-up and the test beam sample are presented in Figure 4.10 and Figure 4.11, respectively. A PSV-500 scanning laser Vibrometer is used to acquire velocity responses of the prescribed 21 points (see the blue dots) along the beams as shown in Figure 4.11. Although the accuracy of damage localisation is highly dependent on the density of measurement points, for the demonstration of the proposed CDS estimation method and the new damage localisation index, a few measurement points are enough. In this experiment, a low measurement point density strategy is adopted. The highest frequency concerned is the third natural frequency and its mode shape is graphed in Figure 4.4 (e), which can be regarded as 1.25 cycles of a sinusoidal signal. In order to capture the damage-induced local mode shape changes, 16 measurement points are used for each cycle. Thus, a number of measurement points around 20 is used.

Pseudo-random excitation of frequency range 0-800Hz is generated by the PSV-500 integration system and applied to the free end of cantilever beam by a shaker (LDS V406). Damage is cut as small slots at different locations and depths. The information of cracks in two experimental examples are listed in Table 4.4 and the cracks are located on the back surface and marked by red lines on the front surface in Figure 4.11.

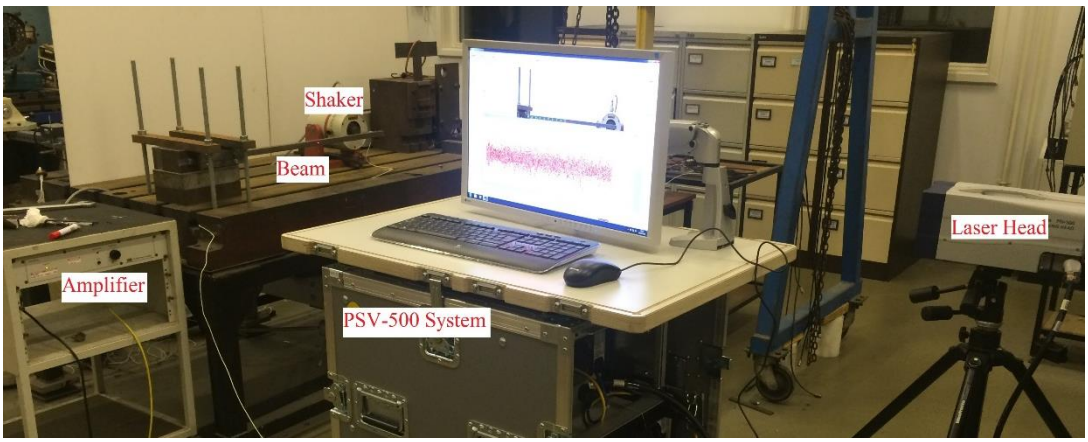

Figure 4.10 Experimental set-up.

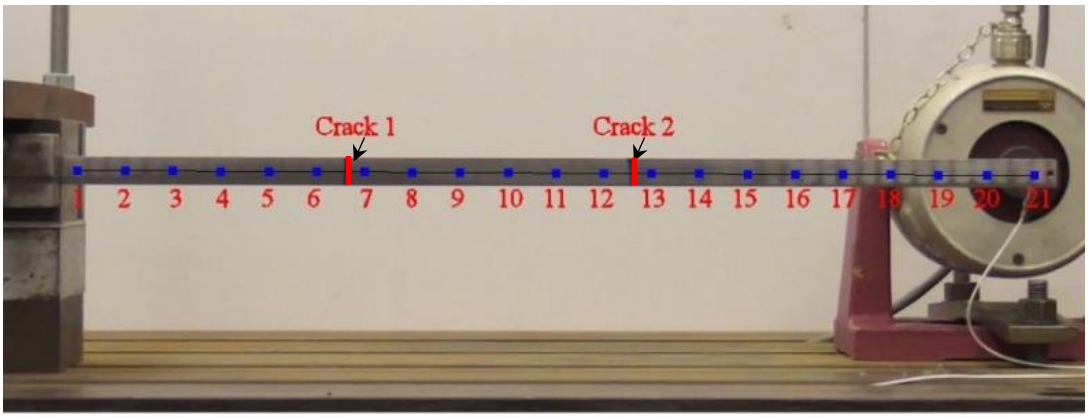

Figure 4.11 A cantilever beam with two open cracks.

Table 4.4 Information of crack configurations for experiments.

Examples	Cracks	Location	Measurement points	Depth percentage	Width
1	Crack 1	0.2m	6~7	20%	0.001m
1	Crack 2	0.4m	12~13	20%	0.001m
2	Crack 1	0.2m	6~7	30%	0.001m
2	Crack 2	0.4m	12~13	30%	0.001m

Before performing damage identification, the drop-out phenomenon under random excitation and its effects on the proposed damage identification method are discussed. Figure 4.12 presents power spectral density comparison between the output signal of PSV-500 system to the shaker and the practical input force from the shaker to the cantilever beam. It is clear that decreases occur in the vicinity of resonant frequencies in Figure 4.12 (b) due to the shaker-structure interactions [42].

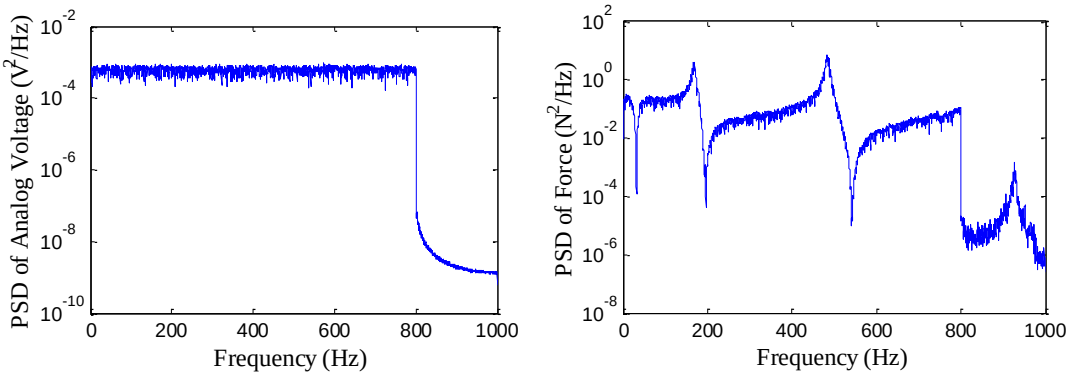

(a) (b)

Figure 4.12 Power spectral density: (a) Output signal of system (b) Input force.

Under the effects of exciter-structure interactions, the frequencies of singular peak values are not the exact resonant frequencies of the cantilever beam but they are the resonant frequencies of the integrated system of shaker and cantilever beam. Thus, the estimated mode shapes still contain the damage information of the cantilever beam and the proposed damage identification method is still feasible and effective in this case.

First, a beam with two open cracks (both 20% of the beam depth) is tested under pseudo-random exaction. Figure 4.13 presents the singular value spectrum calculated by SVD of PSD matrices. The three peak points, which correspond to the resonant frequencies of the combined beam-shaker system, are selected to estimate the associated mode shapes.

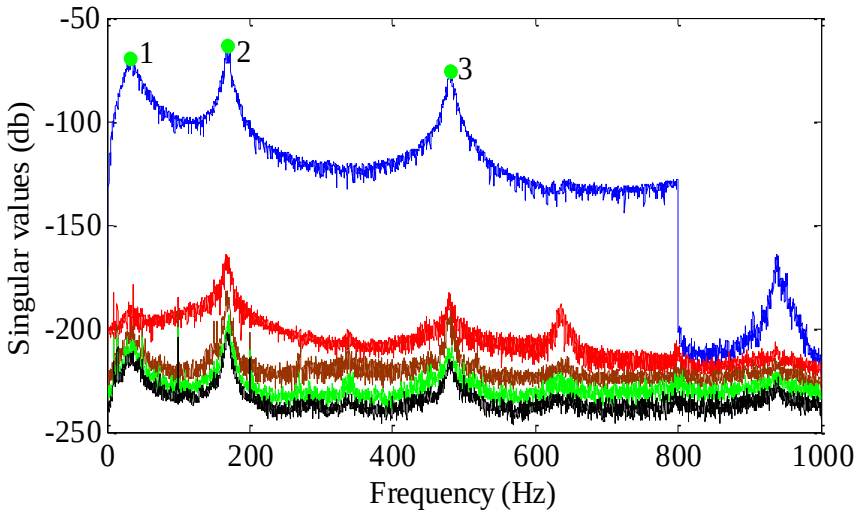

Figure 4.13 Singular value spectrum plot of experimental example 1.

4.5.1 Real part of mode shapes for damage identification

Figure 4.14 presents the first three mode shapes and their curvatures evaluated by FDD method and enhanced FDD method, respectively. From Figure 4.14 (b), (d) and (f), it is shown that mode shape curvatures estimated by enhanced FDD method are smoother than these by FDD method, which indicates the better noise robustness of enhanced FDD method during mode shape estimation. With the smoother mode shape curvatures, enhanced FDD method is able to enhance the accuracy of damage detection and localisation.

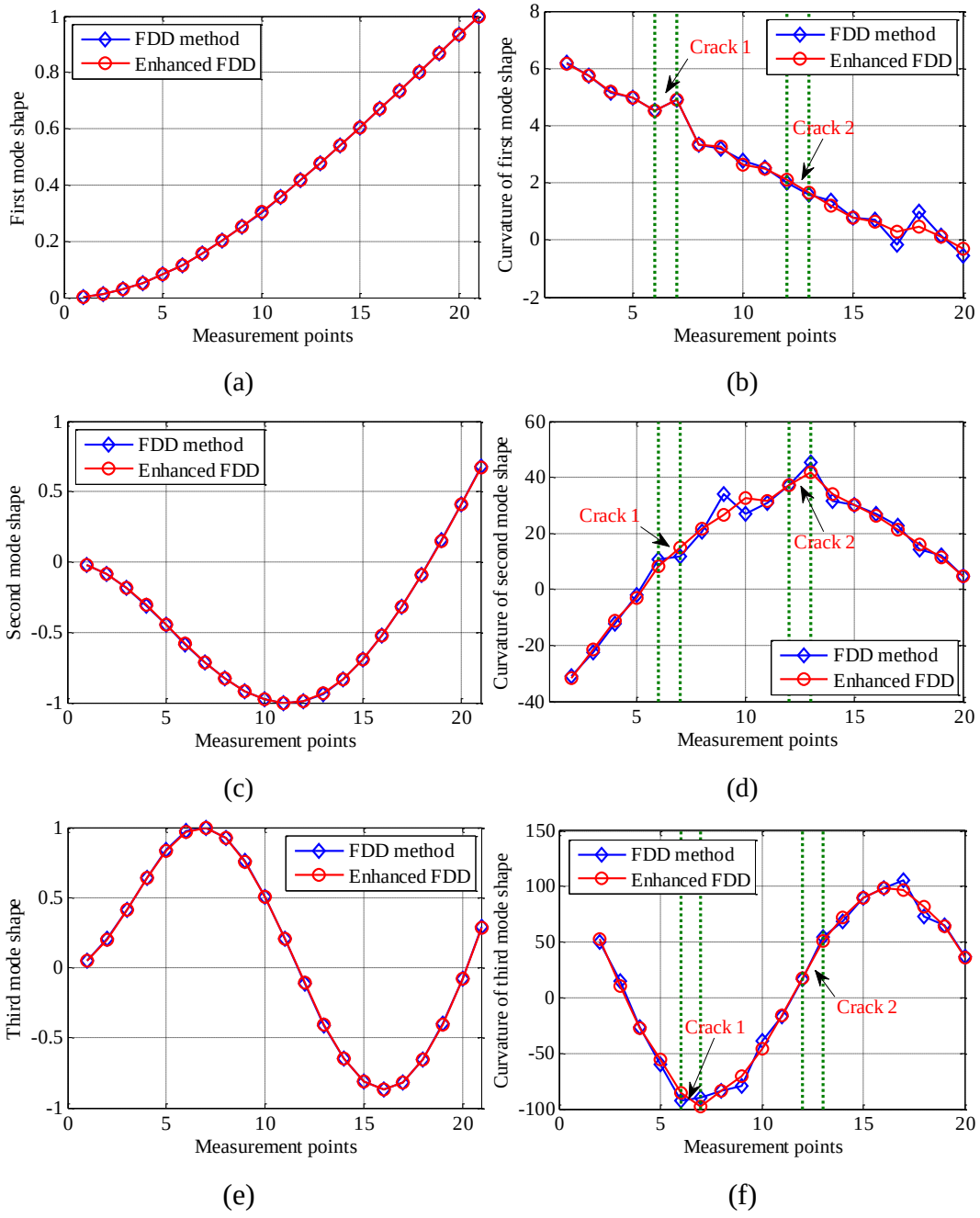

Figure 4.14 Mode shapes and their curvatures of the first three modes.

The damage index values calculated using adaptive GSM and GSM based on mode shape curvatures are presented in Figure 4.15. The comparison of Figure 4.15 (a) with Figure 4.15 (b) shows that the damage identification results by adaptive GSM are more accurate and noise robust than those of traditional GSM. Another conclusion is that damage identification of enhanced FDD method tends to be more sensitive to damage and robust to noise, which correctly identifies the two cracks.

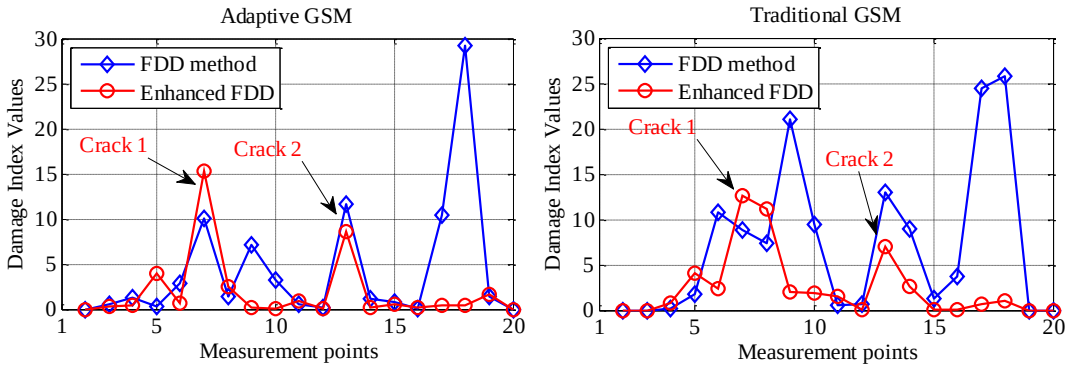

(a) Adaptive GSM (b) Traditional GSM

Figure 4.15 Damage index values of a beam with two cracks of 20% depth.

Experimental example 2 is tested to make some further discoveries. Figure 4.16 shows the damage identification results based on the first three mode shapes. From the comparison of damage index magnitude with Figure 4.15, it is depicted that the damage index is able to indicate the relative damage severity.

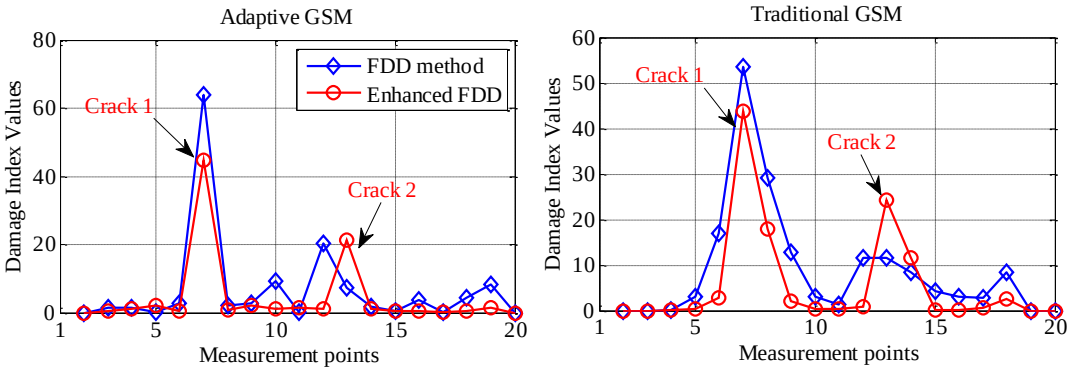

(a) Adaptive GSM (b) Traditional GSM

Figure 4.16 Damage index values of a beam with two cracks of 30% depth

Moreover, by increasing the depth of the two cracks, all the two mode shape estimation methods are shown to be effective in detecting and localising the damage in Figure 4.16 (a). For smaller cracks in Figure 4.15, the identification results are sensitive to noise. Therefore, it is essential, for the sake of accurate and robust identification of smaller cracks, to investigate noise-robust mode shape estimation and damage-induced shape distortion extraction methods.

4.5.2 Imaginary part and absolute value of mode shapes

In the above study, damage identification is studied using the real part amplitude changes of mode shapes without considering the imaginary part or the absolute value

of mode shapes. However, the imaginary part of mode shapes corresponds to the out-of-phase vibration and should be more sensitive to phase changes and the absolute value of mode shapes includes the total vibration information and thus can be also used to detect the damage-induced local stiffness reduction [187, 188]. Thus, a damage identification performance comparison of the real part, imaginary part and the absolute value of mode shapes should be conducted. Before investigating the imaginary part and the absolute value of mode shapes, the approach to improve damage identification accuracy using the real part of mode shapes is presented firstly.

4.5.2.1 Improvements of real part of mode shapes for damage identification.

In order to measure the relative vibration magnitude (RVM) between the real part and imaginary part of mode shapes, a criterion is defined as

$$RVM_{\boldsymbol{\varphi}_r} = \frac{\|\mathrm{real}(\boldsymbol{\varphi}_r)\|}{\|\mathrm{imag}(\boldsymbol{\varphi}_r)\|} \tag{4.7}$$

where 'real' implies the real part of mode shapes and 'imag' denotes the imaginary part of mode shapes. Then the relative vibration magnitude results in experimental examples 1 and 2 are listed in Table 4.5.

Table 4.5 Relative vibration magnitude measure $RVM_{\boldsymbol{\varphi}_r}$.

Methods	Experimental example 1			Experimental example 2		
	$RVM_{\boldsymbol{\varphi}_1}$	$RVM_{\boldsymbol{\varphi}_2}$	$RVM_{\boldsymbol{\varphi}_3}$	$RVM_{\boldsymbol{\varphi}_1}$	$RVM_{\boldsymbol{\varphi}_2}$	$RVM_{\boldsymbol{\varphi}_3}$
Enhanced FDD	572.2	111.4	28.72	966.4	62.43	32.41
FDD method	12.28	5.491	3.372	8.647	2.919	4.535
Rotated FDD	586.5	97.24	39.07	871.6	89.05	46.39

It is clear from Table 4.5 that the relative vibration magnitude measure $RVM_{\boldsymbol{\varphi}_r}$ of enhanced FDD method is much larger than traditional FDD method. In order to validate that maximizing $RVM_{\boldsymbol{\varphi}_r}$ is possible to improve the damage identification accuracy of the real part of mode shapes, a rotated FDD method is proposed to increase $RVM_{\boldsymbol{\varphi}_r}$ of mode shapes provided by FDD method through a plane rotation. In this method, the best straight line fit to all the elements of a mode shape plotted on a complex plane is determined and then the whole mode shape vector is rotated to make this best line to align with the horizontal (real) axis, which will boost $RVM_{\boldsymbol{\varphi}_r}$ of mode

shapes from FDD method. $RVM_{\boldsymbol{\varphi}_r}$ of the rotated FDD method is also tabulated in the last row of Table 4.5 and $RVM_{\boldsymbol{\varphi}_r}$ increase is remarkable when compared with the traditional FDD method.

In addition, Figure 4.17 presents the damage identification comparison between enhanced FDD method and the rotated FDD method using the curvature of the real part of mode shapes. It is clear in Figure 4.17 that the rotated FDD method pinpoints the damage locations whereas the traditional FDD method provides inaccurate damage identification results in Figure 4.15 (a) and Figure 4.16 (a), which confirms that maximizing $RVM_{\boldsymbol{\varphi}_r}$ is a feasible way to enhance damage identification accuracy when using the curvature of the real part of mode shapes. Nevertheless, the damage identification results of enhanced FDD method is still better than the rotated FDD method as the rotated FDD method provides false damage alarms around measurement point 5 in Figure 4.17 (a) and measurement point 19 in Figure 4.17 (b).

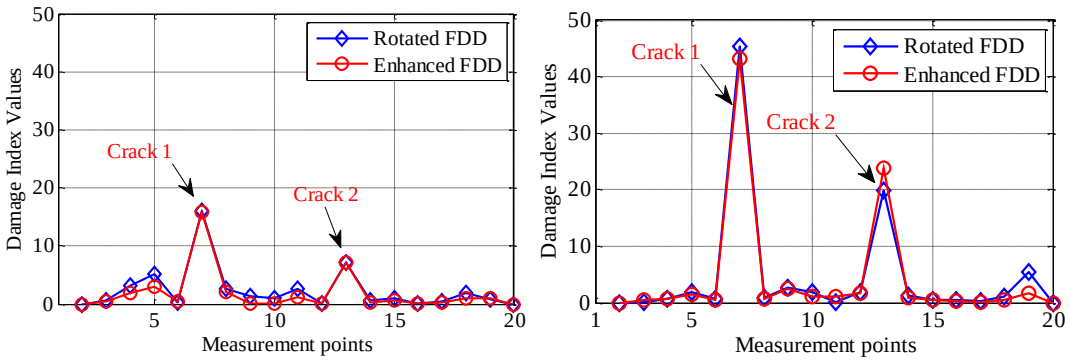

(a) Two cracks of 20% depth (b) Two cracks of 30% depth

Figure 4.17 Damage identification results using real part of mode shapes.

4.5.2.2 Imaginary part of mode shapes for damage identification.

The imaginary part of mode shapes contains the out-of-phase vibration due to the phase differences between vibrations of measurement points of the original structure, and the phase differences between vibrations of measurement points of the damaged structure induced by the local damage. For practical engineering structures, the phase differences should be considered a sensitive damage feature since the local damage tends to cause unsynchronized movements [188]. In this study, the imaginary part curvature of mode shapes in experimental example 1 (two open cracks of 20% depth) is shown in Figure 4.18.

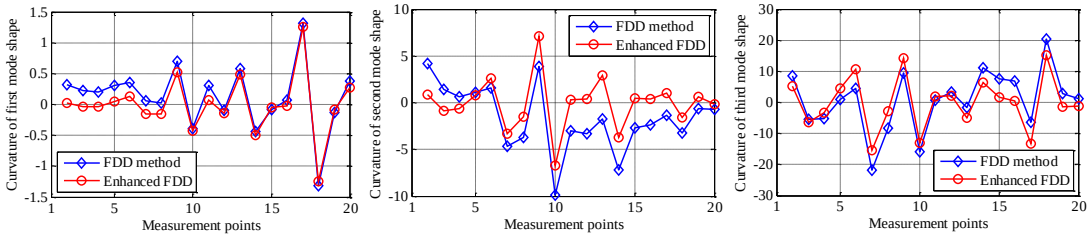

(a) (b) (c)

Figure 4.18 Curvature of the mode shape imaginary part of experimental example 1.

It can be seen that the imaginary part does not provide reliable damage detection due to the uncertainties caused by measurement noise. The other reason for this is that the damage in the beams under study is linear damage (open cracks), which mainly affect the vibration amplitudes by reducing the local stiffness and the resultant local unsynchronised vibrations are not obvious. However, when using the complex mode shapes for damage identification, the imaginary part should be always investigated due to its sensitivity to phase changes.

4.5.2.3 Absolute value of mode shapes for damage identification

It is worth noting that the rotated FDD method is merely a plane rotation of mode shapes from FDD method and has the same absolute value. Thus, the rotated FDD method will not be discussed here. The absolute mode shapes of experimental example 1 are presented in Figure 4.19.

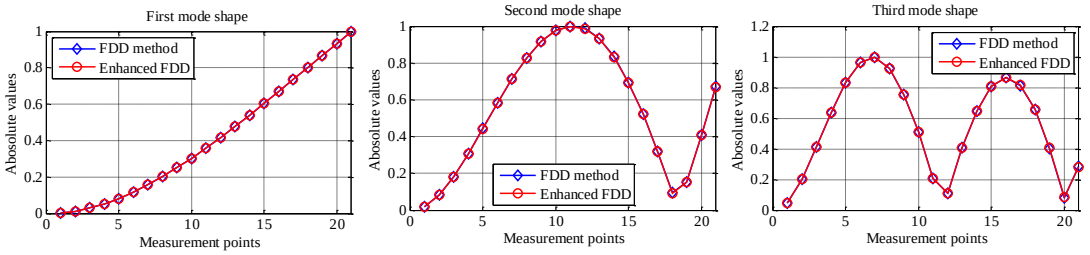

(a) (b) (c)

Figure 4.19 Absolute value of mode shapes in experimental example 1.

The absolute mode shape value plots show irregular shape features in mode shapes caused by taking absolute value (Figure 4.19 (b) and Figure 4.19 (c)), which lead to false damage alarms and as a result adaptive GSM is difficult to be applied. But in this case, damage could be identified by comparing the absolute mode shapes of undamaged structures with these of the damaged state. In order to apply adaptive GSM to the absolute value of mode shapes for damage identification without baseline data

of the healthy structures, the signed absolute value of mode shapes (having the same sign as the real part of mode shapes) is adopted. Then the damage identification index values are calculated and shown in Figure 4.20.

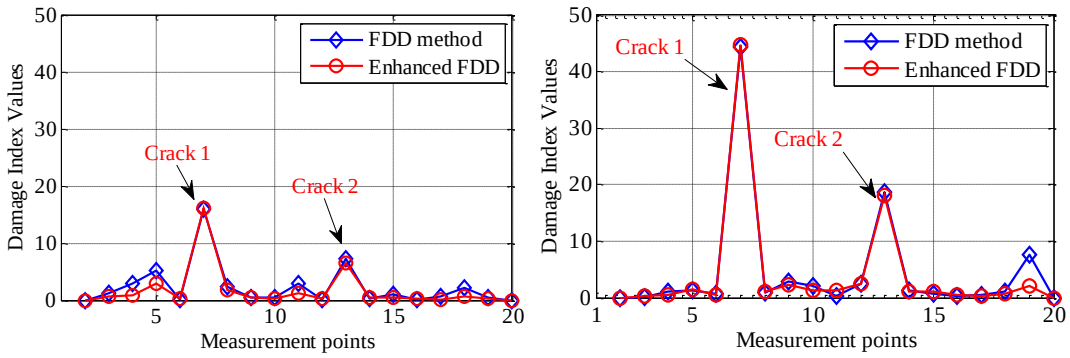

(a) Experimental example 1 (b) Experimental example 2

Figure 4.20 Damage identification results using the curvature of signed absolute value of mode shapes.

Figure 4.20 illustrates that the signed absolute value of mode shapes can improve the damage identification results of traditional FDD method but the improvement for enhanced FDD method is not obvious when compared with the results in Figure 4.15 (a) and Figure 4.16 (a). Moreover, it is demonstrated that enhanced FDD method performs better than FDD method when using the signed absolute value of mode shapes, as FDD method gives false damage detection around measurement points 4, 11 and 18 in Figure 4.20 (a) and measurement point 19 in Figure 4.20 (b). In addition, the magnitude of the damage index values in Figure 4.20 (a) and Figure 4.20 (b) indicates the relative damage severity. It is apparent that the damage of experiential example 2 is more severe than damage of experiential example 1.

4.5.3 The advantages of the proposed multi-damage index

In order to validate the proposed weighing criterion and evaluate the performance of the proposed multi-damage index, a comparison with co-ordinate modal assurance criterion method (COMAC), mode shape curvature difference method (MSCD) and damage index method (DIM) is presented in Figure 4.21. Moreover, the formulations of these traditional damage indexes are tabulated in Table 4.6.

Table 4.6 A list of some common damage identification methods

Method	Damage index
Co-ordinate modal assurance criterion [121]	$\frac{\left\lvert\sum_{r=1}^{N_r}\varphi_{r,l}^{\mathrm{u}}\varphi_{r,l}^{\mathrm{d}}\right\rvert^2}{\sum_{r=1}^{N_r}\left(\varphi_{r,l}^{\mathrm{u}}\right)^2\sum_{r=1}^{N_r}\left(\varphi_{r,l}^{\mathrm{d}}\right)^2}$
Mode shape difference method	$\sum_{r=1}^{N_r}\left\lvert\boldsymbol{\varphi}_r^{\mathrm{d}}-\boldsymbol{\varphi}_r^{\mathrm{u}}\right\rvert$
Mode shape curvature difference method	$\sum_{r=1}^{N_r}\left\lvert\boldsymbol{\varphi}^{\mathrm{d}''}_r-\boldsymbol{\varphi}^{\mathrm{u}''}_r\right\rvert$
Damage index method [144]	$\sum_{r=1}^{N_r}\frac{\left(\varphi_{r,l}^{\mathrm{d}''2}+\sum_{l=1}^{N_{\mathrm{m}}}\varphi_{rl}^{\mathrm{d}''2}\right)\sum_{l=1}^{N_{\mathrm{m}}}\varphi_{r,l}^{\mathrm{u}''2}}{\left(\varphi_{r,l}^{\mathrm{u}''2}+\sum_{l=1}^{N_{\mathrm{m}}}\varphi_{r,l}^{\mathrm{u}''2}\right)\sum_{l=1}^{N_{\mathrm{m}}}\varphi_{r,l}^{\mathrm{d}''2}}$

It can be observed that all the damage identification methods except COMAC method show some peaks around the damage positions, but the proposed damage index is the most robust to noise and provides fewer false alarms than other presented methods.

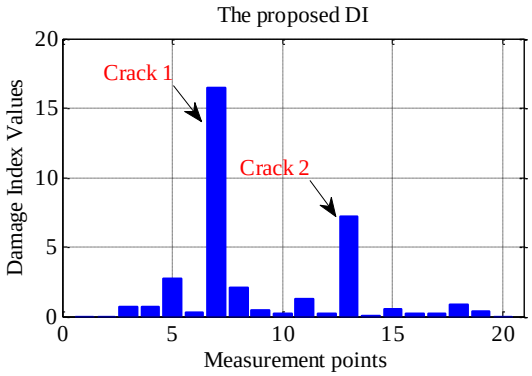

(a) Experimental example 1

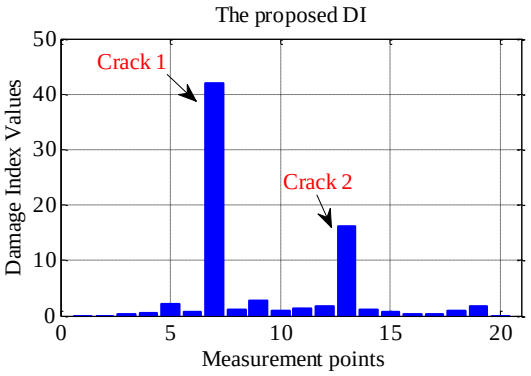

(b) Experimental example 2

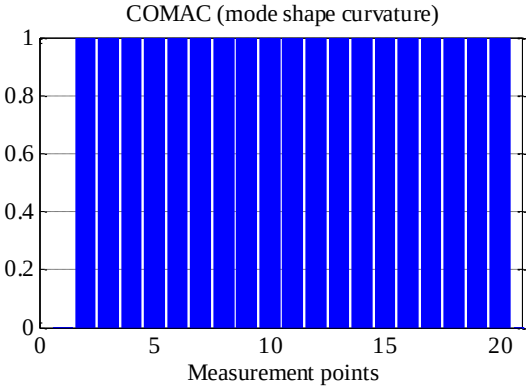

(c) Experimental example 1

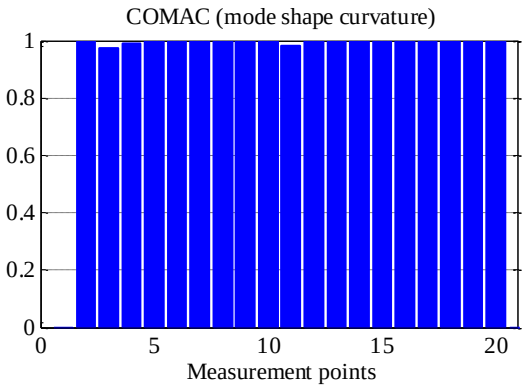

(d) Experimental example 2

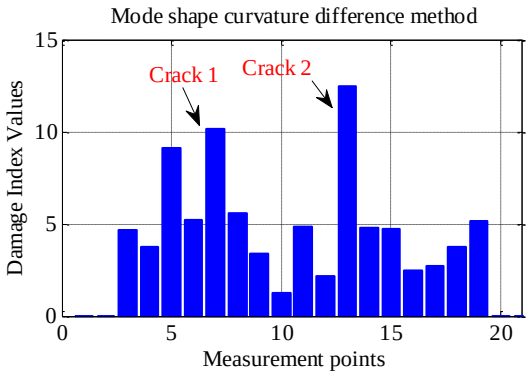

(e) Experimental example 1

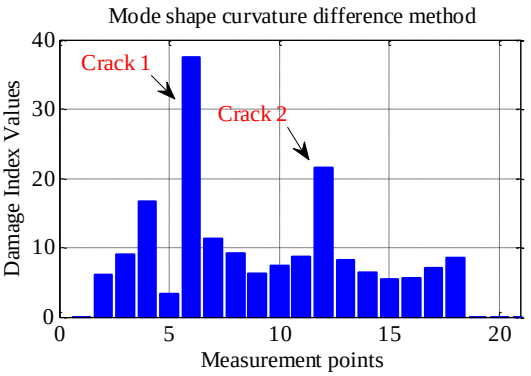

(f) Experimental example 2

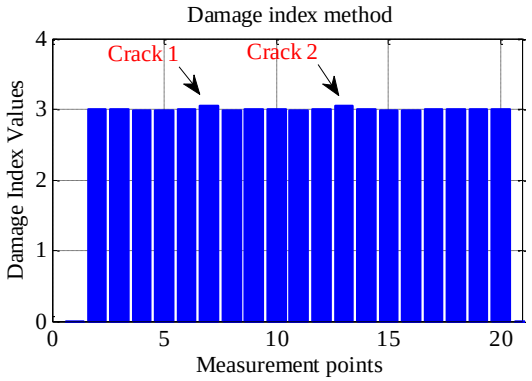

(g) Experimental example 1

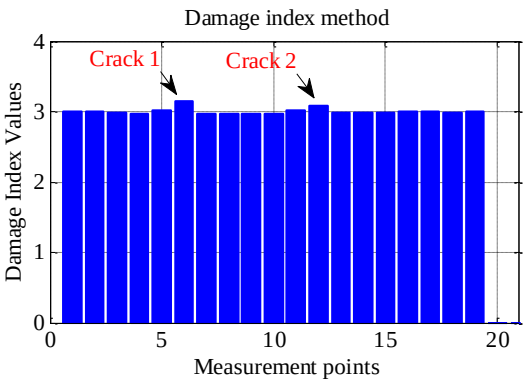

(h) Experimental example 2

Figure 4.21 Damage identification results of different damage indexes

4.6 Conclusions

This chapter studied two vital problems for mode shape based non-destructive damage identification: damage feature extraction without baseline information and robust multi-damage index. First, an adaptive GSM is proposed for better damage feature extraction. The better damage identification performance of adaptive GSM is validated numerically and experimentally using a beam with two open cracks by comparing with the traditional GSM. Secondly, the proposed multi-damage identification index combines the damage-induced curvature changes of several modes and a weighting criterion is applied to normalise the damage information contribution of each mode. In the numerical study, the proposed damage index is shown to be sensitive to smaller cracks of 2% of the beam depth and robust to the additive Gaussian white noise. The experimental studies validate that the proposed damage index is able to indicate the relative damage severity and it is more accurate and noise robust than some popular damage identification methods.

Moreover, the damage performance of the real part, imaginary part and absolute value of mode shapes are discussed based on the experimental studies and the damage identification results of enhanced FDD method is proved to be better than these of traditional FDD method. In addition, other advantages of the proposed damage identification method include that (1) this method is applicable under various environmental and operational conditions and does not require prior knowledge about excitation forces and (2) this method is capable of identifying multiple damage locations.

Chapter 5

Identification of breathing cracks in stepped beam-type structures

For open cracks, the damage-induced singularities of structural characteristic deflection shapes are investigated for robust multi-damage identification in Chapter 4. However, for breathing cracks, the damage-caused singularities will be much smaller and thus harder to be detected, as the breathing cracks mainly affect the vibration responses during the open state whereas the open cracks affect dynamic responses all the time (in relation to the undamaged beam). Fortunately, the identification of breathing cracks can take advantage of the inherent nonlinearity of breathing cracks to enhance its efficiency.

In this chapter, two approaches are investigated to identify breathing cracks of stepped beam structures, which are sensitive to breathing cracks while insensitive to the steps. For the first approach, the deviations between the empirical cumulative distributions of output responses at different locations are evaluated to indicate the damage locations, which is only based on the vibration data of damaged structures. For the second approach, the super-harmonic deflection shapes are used to identify the breathing cracks of stepped beam structures. In order to reduce the noise effects, singular value decomposition is adopted to extract the dominant singular vector associated with the largest singular value as the super-harmonic defection shape at each super-harmonic frequency. Finally, three numerical case studies of a stepped beam with one or two breathing cracks are made to validate the feasibility and advantages of the two proposed approaches.

5.1 Introduction

Cracks are a typical kind of damage and many studies have been carried out on the dynamic response of structures with cracks. Generally, open cracks are the most studied kind of structural damage and the resulting changes in modal parameters or their derivatives are applied to detect, localise or quantify the damage [17]. However, the assumption of cracks being constantly open is far from realistic situations. Fatigue cracks, normally modelled as breathing cracks, exist widely in structures that experience cyclic loads, which introduce nonlinearity to the structures due to the changing between open and closed states. Moreover, the physical principles of a fatigue crack and an open crack are obviously different. An open crack always has a measurable gap between the two crack surfaces, which never get into contact during vibration process. Chondros et al. [189] indicated that the crack severity of breathing cracks would be underestimated if the open-crack assumption was made to interpret vibration measurements. In addition, the application of linear multi-damage identification methods to identify breathing cracks has been demonstrated to be less sensitive in section 4.4.2 of Chapter 4. Overall, linear damage features are not suitable or less sensitive to identify fatigue cracks due to their nonlinearity [35].

Essentially, the nonlinear damage identification problem can be equivalent to the detection of nonlinearity in structures, provided that the nonlinear damage is the only source of nonlinearity. In this chapter, identification of breathing cracks in stepped beam-type structures is investigated, as stepped beam-like structures are widely used in various engineering fields. It is clear that the presence of steps in beams will increase the difficulties of damage localisation. For a stepped beam with open cracks, both the steps and open cracks will cause local shape singularities to spatial characteristic deflection shapes, which can be identified by the proposed damage identification method in Chapter 4. Thus, further examination is required to check if there is damage presence around the stepped positions. However, for a stepped beam with breathing cracks, the nonlinearity of breathing cracks makes it possible to avoid the interference of steps in damage identification, as the steps do not produce nonlinearity. In this case, the identification of nonlinear damage can be extended to more geometrically complex structures.

In literature, many nonlinear damage identification methods have been proposed by utilising nonlinear characteristics like distortions of frequency response function, deviations of probability density function or the presence of super-harmonic components. Rzeszucinski [190] suggested a condition indicator based on changes in the magnitude of normal probability density function, the increasing trend of which was much more robust and sensitive to fault propagation than kurtosis. Asnaashari [147] proposed a crack localisation method by using deviations from normal distribution of vibration responses. A normal distribution plot was adopted to calculate the deviations between the probability distribution of acceleration and the theoretical normal distribution. Nevertheless, the underlying theoretical probability distribution function of measured vibration data is not known. Hence, methods based on deviations between cumulative distribution and theoretical normal distribution of vibration may be unsuitable or less sensitive for non-random vibration. Todd [150] proposed a local attractor variance ratio approach to reveal damage-induced changes of geometric properties of the associated attractors. But it is not easy and takes much time to obtain the attractors, especially for complex structures.

Inspirited by Asnaashari [147] and Todd [150], the first nonlinear damage identification method is proposed by using deviations between empirical cumulative distributions of vibration responses at different measurement points, which is effective to detect and localise the breathing cracks in stepped beam-type structures. The idea behind this is that the nonlinearity due to breathing cracks results in much bigger changes in empirical cumulative distributions of nearby measurement points of breathing cracks than those of the points further away from the breathing cracks.

Traditionally, super-harmonic components of a sinusoidal excitation are used to indicate the presence of nonlinear damage in structures [19, 35]. Asnaashari and Sinha [184] applied the operational deflection shapes associated with the frequency of excitation and its higher harmonics to identify the location of the breathing cracks in beam structures. Inspired by this kind of methods, the super-harmonic deflection shapes estimated through frequency domain decomposition method is developed to localise breathing cracks in stepped beam structures.

The structure of this chapter is organised as follows. In section 5.2, the modelling of fatigue cracks is presented first. In section 5.3, the first nonlinear damage identification

method is proposed and validated, which is based on the deviations between the empirical cumulative distributions of vibration responses at different measurement points. Then, in section 5.4, the second nonlinear damage identification method is developed and validated, which is based on the super-harmonic deflection shapes. Finally, the conclusions of nonlinear damage identification in stepped structures are summarised in section 5.5.

5.2 Fatigue crack modelling

While a beam is vibrating, the state of its cracked section varies from detachment to compression. This results in a modification of the local stiffness, and the stiffness value changes constantly during vibration process [71]. For many practical applications, a fatigue crack can be introduced in the form of the so-called "breathing crack", and such a system can be considered bilinear.

5.2.1 Discrete spring system

The system shown in Figure 5.1 consists of a mass block m_{b} and two linear springs. The mass block is attached to a linear spring k_1 and contacts with the linear spring k_2 only when $x \leq 0$. The motion of the mass block starts at $x = 0$, when the linear spring k_2 and the mass block touch but without any reaction force at this point.

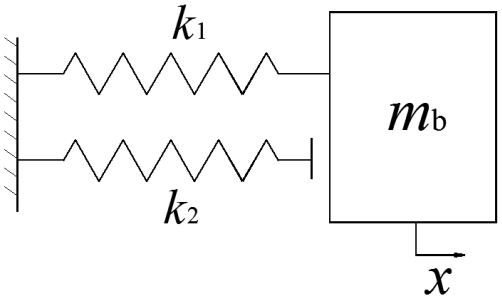

Figure 5.1 The one-degree-of freedom system.

The equations of motion for this system are

$$\begin{cases} m_{\mathrm{b}}\ddot{x} + k_1 x = 0 & \text{for } x > 0 \\ m_{\mathrm{b}}\ddot{x} + (k_1 + k_2)x = 0 & \text{for } x \leq 0 \end{cases} \tag{5.1}$$

And the two frequencies are

$$\omega_{\mathrm{o}} = \sqrt{\frac{k_1}{m_{\mathrm{b}}}} \text{ for } x > 0, \ \omega_{\mathrm{c}} = \sqrt{\frac{k_1 + k_2}{m_{\mathrm{b}}}} \text{ for } x \leq 0 \tag{5.2}$$

The natural frequency ω_{b} of this piecewise-linear single-degree-of-freedom system is calculated as

$$\omega_{\mathrm{b}} = \frac{2\omega_{\mathrm{o}}\omega_{\mathrm{c}}}{\omega_{\mathrm{o}}+\omega_{\mathrm{c}}} \tag{5.3}$$

For the beam, $\omega_{\mathrm{o}i}$ and $\omega_{\mathrm{c}i}$ represent the i–th frequency of the open and closed states, respectively. Analogous to Eq. (5.3), the effective natural frequencies (ω_i) of the breathing cracked beam is

$$\omega_i = \frac{2\omega_{\mathrm{o}i}\omega_{\mathrm{c}i}}{\omega_{\mathrm{o}i}+\omega_{\mathrm{c}i}} \tag{5.4}$$

It is clear that $\omega_{\mathrm{o}i} < \omega_i < \omega_{\mathrm{c}i}$, which indicates that the natural frequency of a structure with a breathing crack is smaller than the closed state (healthy state) but bigger than the open state.

5.2.2 2-D FE model of breathing cracks

Numerous FE models have been developed to study the nonlinear behaviour of fatigue cracks. Qian et al. [191] derived the element stiffness matrix of breathing-cracked beam by integrating the stress intensity factor of the crack, which was obtained by means of Castigliano's theorem in fracture mechanics. Simulation results of this FE model were in good agreement with experimental results. Andreaus et al. [35] addressed the breathing crack by a contact model using 2-D FE method, which discretised the contact surfaces to a series of linear contact segments. But each segment is only bounded by two nodes. In comparison with the node-to-node discretisation, ABAQUS Standard adopts surface-to-surface contact discretisation to define the contact constraints, which involves more master nodes per constraint to promise a better performance. Figure 5.2 presents the surface-to-surface discretisation of the contact surfaces, which allows the relative slide of the two contact surfaces.

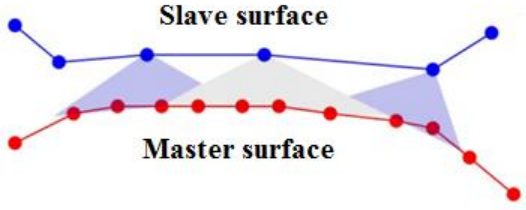

Figure 5.2 Surface-to-surface discretisation [192].

In this research, the breathing cracks are modelled as 2-D transverse edge cracks in ABAQUS using CPS8R plane stress element with reduced integration. In the model, the two surfaces of a breathing crack are allowed to contact in longitudinal direction without interpenetrating (corresponding to hard contact model in ABAQUS) and slide against each other without friction in the lateral direction. The lateral motion of the breathing crack is considered here but the relative lateral movement of the two interfaces is slight. It is the behaver of the breathing crack in the longitudinal direction that causes the nonlinear vibration response. Three steps are taken to model a breathing crack in a 2-D FE model. First, a line is drawn to represent the crack, which is normal to the up-edge. Then, a seam is assigned to the line in interaction module to form an open crack. Finally, hard frictionless contact is applied to the two surfaces of the crack and the definition of hard contact is as

$$\begin{aligned} p_c &= 0 \text{ for } d_c < 0 \\ d_c &= 0 \text{ for } p_c > 0 \end{aligned} \tag{5.5}$$

where p_c is the contact pressure and d_c is overclosure between two side surfaces of a breathing crack. Figure 5.3 illustrates the open and closed states of a breathing crack.

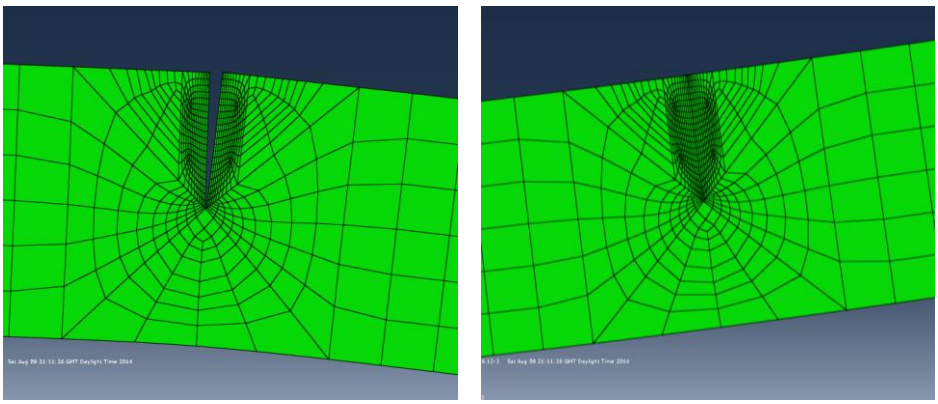

(a) (b)

Figure 5.3. An example of a breathing crack (a) open state and (b) closed state.

In order to demonstrate the feasibility and effectiveness of the proposed 2-D breathing crack model, a beam of dimensions $0.7 \times 0.02 \times 0.02$ m^3 with a breathing crack of 50% depth at its mid-span is modelled and excited by a sinusoidal force of ω_F =52.19 Hz at the free end of the beam. Super-harmonic components can be clearly observed in Figure 5.4, which are an indication of the presence of nonlinear stiffness (due to contact of the breathing cracks).

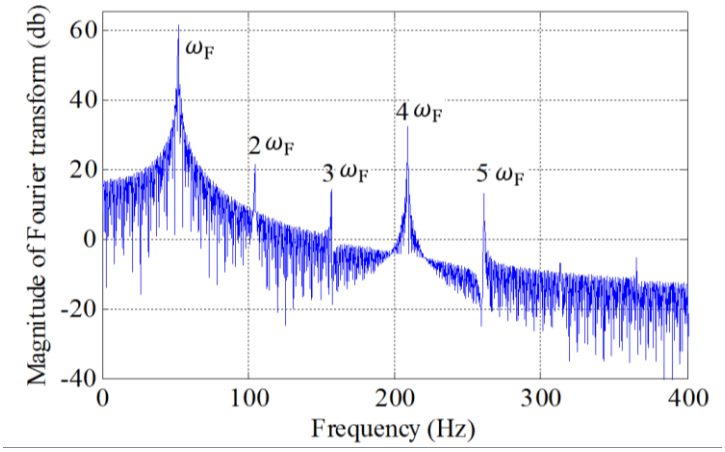

Figure 5.4 FFT spectrum of a beam with a breathing crack under a sinusoidal excitation at ω_F =52.19 Hz.

5.3 The first breathing crack identification method

In this section, deviations from normal distribution will be primarily presented to understand the fundamental theory. However, the theoretical distribution of practical measured responses is hard to obtain. Thus, a new breathing crack identification approach is proposed, which uses the deviations between empirical cumulative distributions of vibration responses at different measurement points, which is only based on the output responses of damaged structures.

5.3.1 Deviations from normal distribution (DND)

When a linear structure is subject to a random excitation, the vibration responses can be described by a normal distribution. But the presence of nonlinearity due to breathing cracks will disrupt the normal distribution. Therefore, the deviations from normal distribution can be used to detect the location of nonlinearity or localise the breathing crack.

The normal probability plot is a graphical technique to determine the DND, which represents the ordered vibration response of certain measurement point against the theoretical normal distribution. Consider $\mathbf{Y}_l = \{y_l(1), y_l(2), \cdots, y_l(N)\}$ denote an ascending ordered sample of vibration response at measurement point l and the order statistic medians are defined as:

$$Y(k) = G\big(U(k)\big) \tag{5.6}$$

where $G(\cdot)$ donates the percent point function of normal distribution, which is the inverse of normal cumulative distribution. $U(k)$ is the uniform order statistic medians [193], which is defined as

$$\begin{cases} U(k) = 1 - 0.5^{(1/N)} & \text{, for } k = 1 \\ U(k) = (k - 0.3175)/(N + 0.365) & \text{, for } k = 2, \cdots, N-1 \\ U(k) = 0.5^{(1/N)} & \text{, for } k = N \end{cases} \tag{5.7}$$

An example of normal probability distribution plot is presented in Figure 5.5. The vertical coordinate is the ordered response values while the horizontal coordinate is the normal order statistic medians. If the probability distribution of vibration response is a normal distribution, the points in normal probability plot will locate along a straight line. If not, the departures form this straight line indicate the deviations from normal distribution, which are calculated based on the dashed area in Figure 5.5.

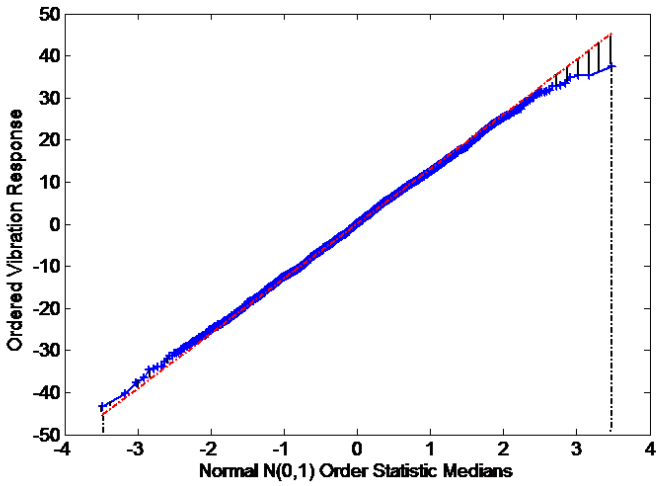

Figure 5.5 Normal Probability Plot.

$$DND_l = \sum_{k=2}^{N} \left(\frac{|y_l(k-1) - \tilde{y}_l(k-1)| + |y_l(k) - \tilde{y}_l(k)|}{2} \right) |Y(k) - Y(k-1)| \tag{5.8}$$

where $\tilde{y}_l(k)$ represents the theoretical value of $y_l(k)$ according to normal distribution, which is the corresponding value of $y_l(k)$ in the red reference line.

Although applying DND for damage identification is not limited in the case of random excitation, it is sensitive to the stepped geometry of structures and can be applied to only uniform structures [147]. To overcome this disadvantage, a new approach is proposed for breathing crack identification in stepped structures, which uses the deviations between empirical cumulative distributions.

5.3.2 Deviations between empirical cumulative distributions (DECD)

In statistics, the empirical cumulative distribution function is an empirical measure of the vibration response dataset. For an intact beam, the measured responses at different locations will have identical probability distribution [190]. When a beam is damaged by breathing cracks, the nonlinearity of breathing cracks will result in the changes of empirical cumulative distribution and the changes mainly affect the nearby measurement points of breathing cracks. Hence, the damage can be localised by comparing the empirical cumulative distributions between vibration responses of different measurement points.

In order to evaluate DECD, the Quantile-Quantile (Q-Q) plot is employed, which displays the quantiles of two datasets such as $y_i(t)$ and $y_j(t)$. First, they ordered ascendingly as $\{y_i(1) < y_i(2) < \cdots < y_i(N)\}$ and $\{y_j(1) < y_j(2) < \cdots < y_j(N)\}$, respectively. Then, the data of the first and third quartiles are estimated from $y_i(t)$ as $y_{iq1}$and y_{iq3}, and the same case for $y_j(t)$ to get $y_{jq1}$and y_{jq3}. Figure 5.6 shows an empirical Q-Q plot of $y_i(t)$ against $y_j(t)$. The equation of the red reference line in Figure 5.6 is expressed as

$$\tilde{y}_j(k) = \frac{y_{jq3} - y_{jq1}}{y_{iq3} - y_{iq1}}\left(y_i(k) - y_{iq1}\right) + y_{jq1}, k = 1, 2, \cdots, N \tag{5.9}$$

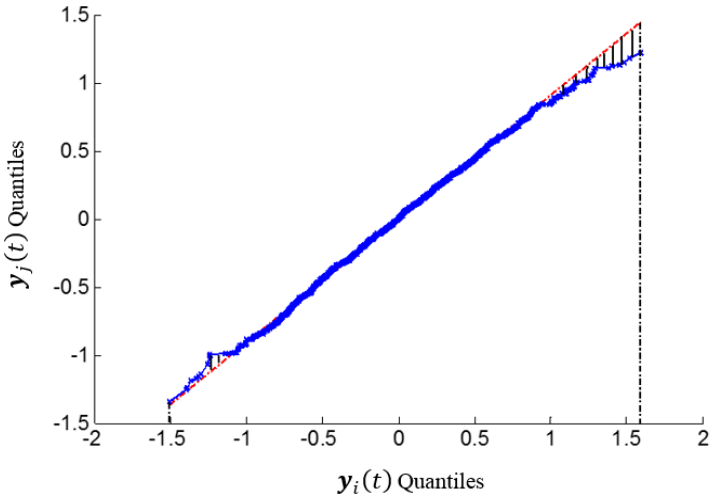

Figure 5.6 The Q-Q plot of $y_i(t)$ and $y_j(t)$

In Figure 5.6, if vibration responses $y_i(t)$ and $y_j(t)$ possess the same probability distribution, the data points should fall approximately on the red straight line. If not, the departures from the red reference line can be used to represent the empirical

distribution deviations between $y_i(t)$ and $y_j(t)$, which are determined by the dashed area

$$DECD = \sum_{k=2}^{N} \left[\left(\left|y_j(k) - \tilde{y}_j(k)\right| + \left|y_j(k-1) - \tilde{y}_j(k-1)\right|\right)\left|y_i(k) - y_i(k-1)\right|\right]/2 \quad (5.10)$$

where $\tilde{y}_j(k)$ represents the corresponding value of $y_j(k)$ in the red reference line.

5.3.3 Numerical studies

There are three purposes of this section. First, stepped beams with one or two breathing crack are used to validate the feasibility and efficiency of the proposed DECD method. Secondly, a comparison with DND method is presented to demonstrate the advantage of DECD method in breathing crack identification of stepped beams. Finally, DECD method is shown to have the ability to indicate the relative damage severity.

Three cases of a stepped beam with one or two breathing cracks at different locations are studied and the information of breathing cracks is given in Table 5.1. The total length of the stepped beam is 0.7 m and it is composed by two parts $0.35 \times 0.30 \times 0.20\text{m}^3$ and $0.35 \times 0.20 \times 0.20\text{m}^3$ as shown in Figure 5.7. Moreover, the Young's modulus is 210 GPa, mass density is 7861 kg/m^3 and Poisson ratio is 0.33.

Table 5.1 Cases of the stepped beam with cracks at different locations

Case	Crack 1	Crack 2	Position of the step
1	0.170 m (points 8 and 9)	--	0.350 m (points 17 and 18)
2	0.350 m (points 17 and 18)	--	0.350 m (points 17 and 18)
3	0.170 m (points 8 and 9)	0.530 m (points 25 and 26)	0.350 m (points 17 and 18)

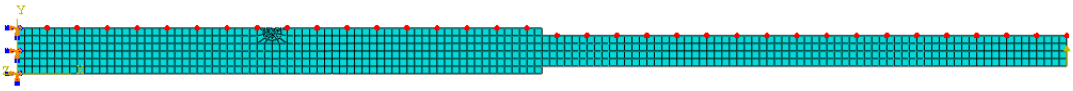

Figure 5.7 FE model of a stepped beam with a breathing crack (case 1).

In order to validate the proposed method, the beam is excited by a sinusoidal force at 50Hz. The depth of breathing crack is 10% of the local beam depth. The velocity responses of the prescribed 35 points are acquired. To simulate the experimental

condition, the measured velocity responses are contaminated by Gaussian white noise with signal to noise ratio (SNR) of 100dB. The damage identification results of DND and DECD methods are shown in Figure 5.8. The absolute magnitude of DND and DECD does not possess any physical meanings but the relative shape changes indicate the singularities of the structures.

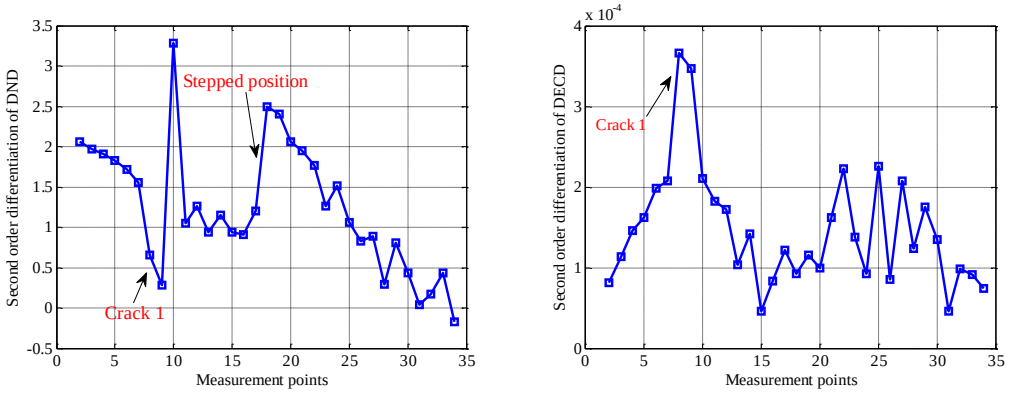

(a) (b)

Figure 5.8 Damage identification results of case 1: (a) DND and (b) DECD.

It can be concluded that both the DND and DECD methods are both efficient to localise the breathing crack. But the DND method is also sensitive to the steps of structures, which can provide false alarms of breathing cracks. The DECD presents a peak feature around the breathing crack position and does not have clear shape distortions around the steps.

In order to validate the proposed DECD method in multiple breathing crack identification, a stepped beam with two breathing cracks of 10% of their local beam depths is simulated. The FE model and the damage identification results are shown in Figure 5.9 and Figure 5.10, respectively.

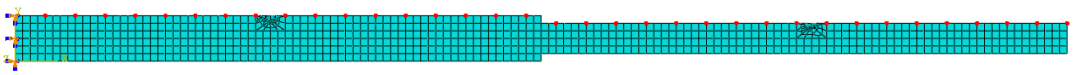

Figure 5.9 FE model of a stepped beam with two breathing cracks (case 3).

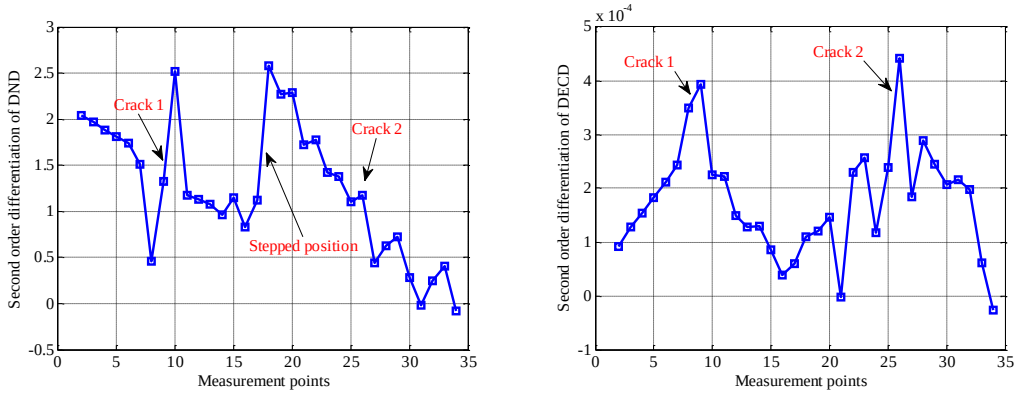

(a) (b)

Figure 5.10 Damage identification results of case 3: (a) DND and (b) DECD.

It is clear that the proposed DECD approach can accurately identify the positions of two breathing cracks and is immune to the stepped geometry of structures, whilst the DND method cannot detect the second breathing crack and extremely sensitive to the stepped geometry.

Another case is the breathing crack of 10% depth is located right at the stepped position, as shown in Figure 5.11. The presence of both stepped geometry and breathing crack makes the damage identification difficult. Figure 5.12 presents the damage identification results based on DND and DECD, respectively.

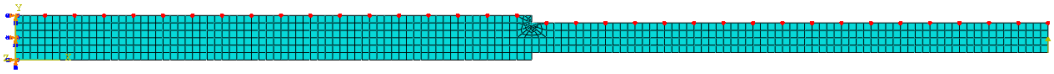

Figure 5.11 FE model of a stepped beam with a breathing crack (case 2).

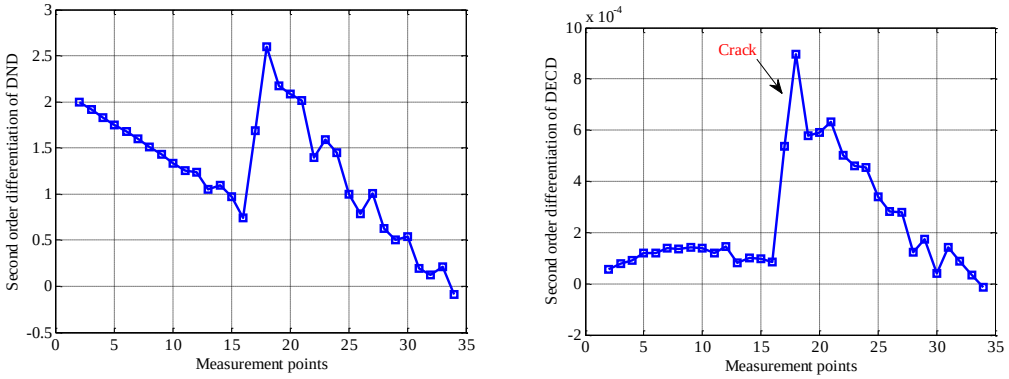

(a) (b)

Figure 5.12 Damage identification results of case 2: (a) DND and (b) DECD.

By comparing Figure 5.12 (a) with Figure 5.8 (a) or Figure 5.10 (a), the sudden increase feature of DND method is always present at the stepped position and it cannot be used to detect the breathing crack in this case. By comparing Figure 5.12 (b) with Figure 5.8 (b) or Figure 5.10 (b), the sudden increase feature of DECD method can be used to identify the breathing crack, as this damage feature is unique to this case. Through studying the three cases of breathing cracks, it is concluded that DECD method is much more effective than the DND method in breathing crack identification, especially for stepped beam-type structures.

Now, in order to study the effects of breathing crack depth on the DECD method, the breathing crack depth in case 1 is increased to 20% of the beam depth and the damage identification result is presented in Figure 5.13.

In comparison with Figure 5.8 (b), it is clear from Figure 5.13 that the more severe the breathing cracks, the bigger the magnitude of DECD, which means the proposed DECD is sensitive to crack depth. Thus, the relative severity of a breathing crack can be assessed. In addition, the effects of measurement noise decreases while the crack depth increases. The reason behind this is that the degree of nonlinearity increases as the increase of the breathing crack depth. Therefore, the DECD is suitable for nonlinear damage identification in stepped structures, which can be easily extended to fatigue crack identification in stepped rotors [149].

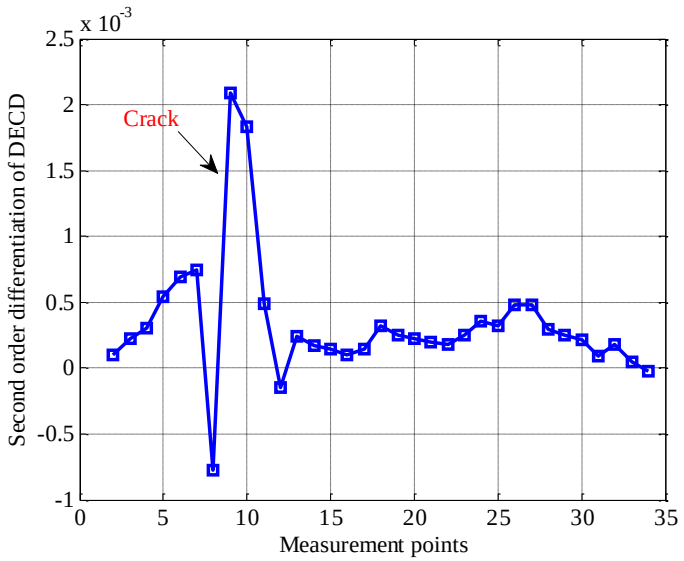

Figure 5.13 Damage identification results of case 1 of 20% depth.

5.4 The second breathing crack identification method

In order to reduce the interference of stepped geometry, CDS's associated with super-harmonic frequencies are investigated for breathing crack identification. Characteristic deflection shapes containing spatial information of structures are efficient for multi-damage localisation in beam or rotor type structures. However, the extracted spatial shape features from experimental data are prone to be compromised by measurement noise. To overcome this shortcoming, SVD, which is a statistical tool for spatial pattern extraction, is applied to PSD matrix for robust CDS extraction. Moreover, the PSD matrix contains the auto-and cross-spectral correlation of output vibration responses and provides average energy distribution in frequency domain, which is robust to the measurement noise.

5.4.1 Super-harmonic characteristic deflection shapes

Steps of beams will affect CDS's and make the crack localisation ambiguous. Nevertheless, super-harmonic CDS's are sensitive to fatigue cracks, as steps cannot cause super-harmonic components.

The vibration response $\mathbf{y}(t) \in \mathbb{R}^{N_\mathrm{m}\times 1}$ is acquired at N_m locations. Thus, the PSD matrix is computed as

$$\mathbf{S}_{\mathrm{yy}}(\omega) = \mathcal{F}\left(\mathbf{R}_{\mathrm{yy}}(\tau)\right) \tag{5.11}$$

Here, $\mathcal{F}(\cdot)$ indicates the Fourier operator and $\mathbf{R}_{\mathrm{yy}}(\tau) \in \mathbb{R}^{N_\mathrm{m}\times N_\mathrm{m}}$ is the covariance matrix of vibration responses, which can be written as

$$\mathbf{R}_{\mathrm{yy}}(\tau) = \mathrm{Exp}\Big((\mathbf{y}(t)-\bar{\mathbf{y}})(\mathbf{y}(t+\tau)-\bar{\mathbf{y}})^{\mathrm{T}}\Big) \tag{5.12}$$

where $\mathrm{Exp}(\cdot)$ is the expected value operator and $\bar{\mathbf{y}} \in \mathbb{R}^{N_\mathrm{m}\times 1}$ is the mean value vector. Then, the PSD matrix at excitation frequency ω_F is decomposed using SVD as

$$\mathbf{S}_{\mathrm{yy}}(\omega_\mathrm{F}) = \mathbf{U}(\omega_\mathrm{F})\mathbf{\Sigma}(\omega_\mathrm{F})\mathbf{V}^{\mathrm{H}}(\omega_\mathrm{F}) \tag{5.13}$$

Here, $\mathbf{U}(\omega_\mathrm{F})$ is a unitary matrix and $\mathbf{U}(\omega_\mathrm{F}) = \mathbf{V}(\omega_\mathrm{F})$**,** as the PSD matrix $\mathbf{S}_{\mathrm{yy}}(\omega_\mathrm{F})$ is square. According to SVD, the first singular vector $\mathbf{u}_1(\omega_\mathrm{F}) \in \mathbb{R}^{N_\mathrm{m}\times 1}$ of $\mathbf{U}(\omega_\mathrm{F})$ corresponding to the maximum singular value in $\mathbf{\Sigma}(\omega_\mathrm{F})$ makes the largest contribution to the vibration response at this frequency. Thus, $\mathbf{u}_1(\omega_\mathrm{F})$ is the dominant CDS

of $\mathbf{S}_{yy}(\omega_F)$, which is robust to measurement noise. The extracted CDS at frequency ω_F is termed as fundamental CDS. Similarly, the super-harmonic CDS's are estimated as $\mathbf{u}_1(2\omega_F), \mathbf{u}_1(3\omega_F), \cdots, \mathbf{u}_1(j\omega_F)$ at corresponding super-harmonic frequencies, where $j(= 2,3,4, \cdots)$ indicates the integer times of excitation frequency ω_F. Moreover, $\mathbf{u}_1(\omega_F), \mathbf{u}_1(2\omega_F), \cdots, \mathbf{u}_1(j\omega_F)$ are complex vectors and only the real part of them are discussed for damage identification, as the magnitude of imaginary part is much smaller and does not contain useful information for damage identification.

In addition, Gram-Schmidt orthogonalisation approach can be applied to remove the effects of fundamental CDS on super-harmonic CDS. Firstly, the projection of $\mathbf{u}_1(j\omega_F)$ on $\mathbf{u}_1(\omega_F)$

$$\text{Proj}_{\mathbf{u}_1(\omega_F)}\left(\mathbf{u}_1(j\omega_F)\right) = \frac{\mathbf{u}_1(\omega_F)^T \mathbf{u}_1(j\omega_F)}{\mathbf{u}_1(\omega_F)^T \mathbf{u}_1(\omega_F)} \mathbf{u}_1(\omega_F) \tag{5.14}$$

Then, the normalised super-harmonic CDS is

$$\tilde{\mathbf{u}}_1(j\omega_F) = \frac{\mathbf{u}_1(j\omega_F) - \text{Proj}_{\mathbf{u}_1(\omega_F)}\left(\mathbf{u}_1(j\omega_F)\right)}{\left\| \mathbf{u}_1(j\omega_F) - \text{Proj}_{\mathbf{u}_1(\omega_F)}\left(\mathbf{u}_1(j\omega_F)\right) \right\|} \tag{5.15}$$

5.4.2 Numerical studies

The same three cases as tabulated in Table 5.1 are studied to demonstrate the efficiency and advantages of the proposed super-harmonic CDS's for breathing crack identification in stepped structures. In order to simulate the experimental condition, all the simulated vibration velocity responses are contaminated by white noise with SNR being 80dB. Firstly, case 1 is studied to show the process of applying super-harmonic CDS's for damage identification. Figure 5.14 shows the singular value spectrum plot, which indicates the excitation frequency ω_F and the super-harmonic components. The damage identification results using the fundamental CDS and the super-harmonic CDS of $2\omega_F$ are demonstrated in Figure 5.15.

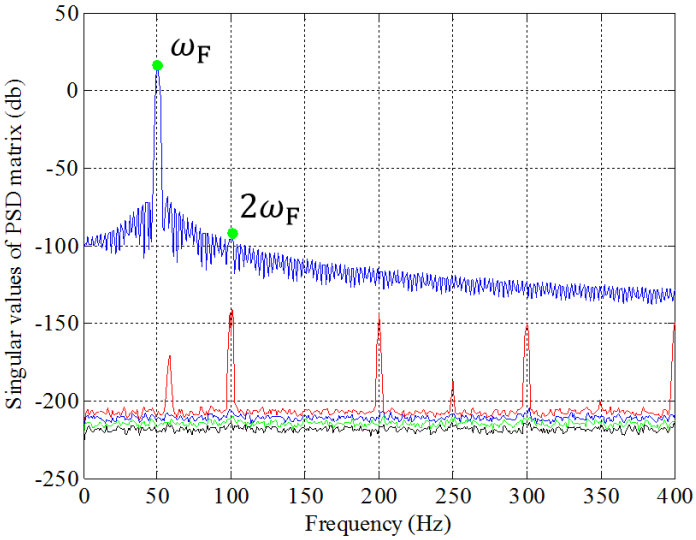

Figure 5.14 Singular value spectrum plot of PSD matrices.

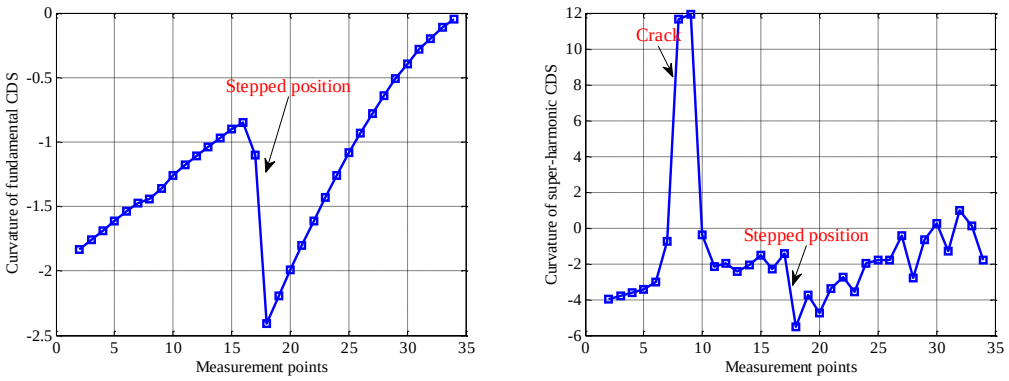

(a) (b)

Figure 5.15 Damage identification results of case 1: (a) Curvature of fundamental CDS and (b) Curvature of super-harmonic CDS at $2\omega_F$.

It is apparent in Figure 5.15 that the curvature of fundamental CDS is sensitive to the stepped geometry and is impossible to detect the breathing crack, whereas the curvature of super-harmonic CDS at $2\omega_F$ identifies this breathing crack robustly and presents no obvious distortion around the stepped position. The reason for this is that the super-harmonic CDS is caused by the presence of nonlinearity due to breathing cracks whilst the stepped geometry behaving like an open crack mainly affect the fundamental CDS.

In order to test the efficiency in multiple breathing crack identification of super-harmonic CDS's, case 3 is studied and the damage identification results are given in Figure 5.16.

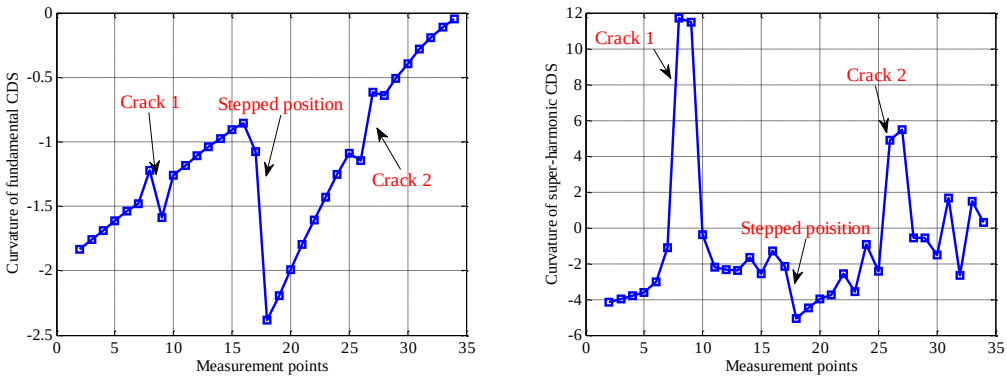

(a) (b)

Figure 5.16 Damage identification results of case 3: (a) fundamental CDS and (b) super-harmonic CDS at $2\omega_F$.

Figure 5.16 shows that the curvature of super-harmonic CDS at $2\omega_F$ is capable of multiple breathing crack identification and is less sensitive to the stepped geometry of structures. In comparison, the curvature of fundamental CDS is much more sensitive to the stepped geometry than the breathing cracks. Moreover, the breathing crack caused shape distortions in Figure 5.16 (b) are peak features while the step induced shape distortion is a small sudden decrease, which makes the identification of breathing cracks unique.

The next case study is that the breathing crack is coincidently located in the stepped position of the beam. Figure 5.17 presents the damage identification results based on fundamental CDS and super-harmonic CDS's of case 2.

In comparison with Figure 5.15 (a) or Figure 5.16 (a), it is impossible to detect the breathing crack in the stepped position from Figure 5.17 (a), as there are no special shape changes with or without the breathing crack. However, Figure 5.17 (b) and Figure 5.17 (c) show sharp peaks around the stepped position. In comparison with shape distortion features of stepped position in Figure 5.15 (b) or Figure 5.16 (b), Figure 5.17 (b) and Figure 5.17 (c) are able to indicate that there is a breathing crack in the stepped position.

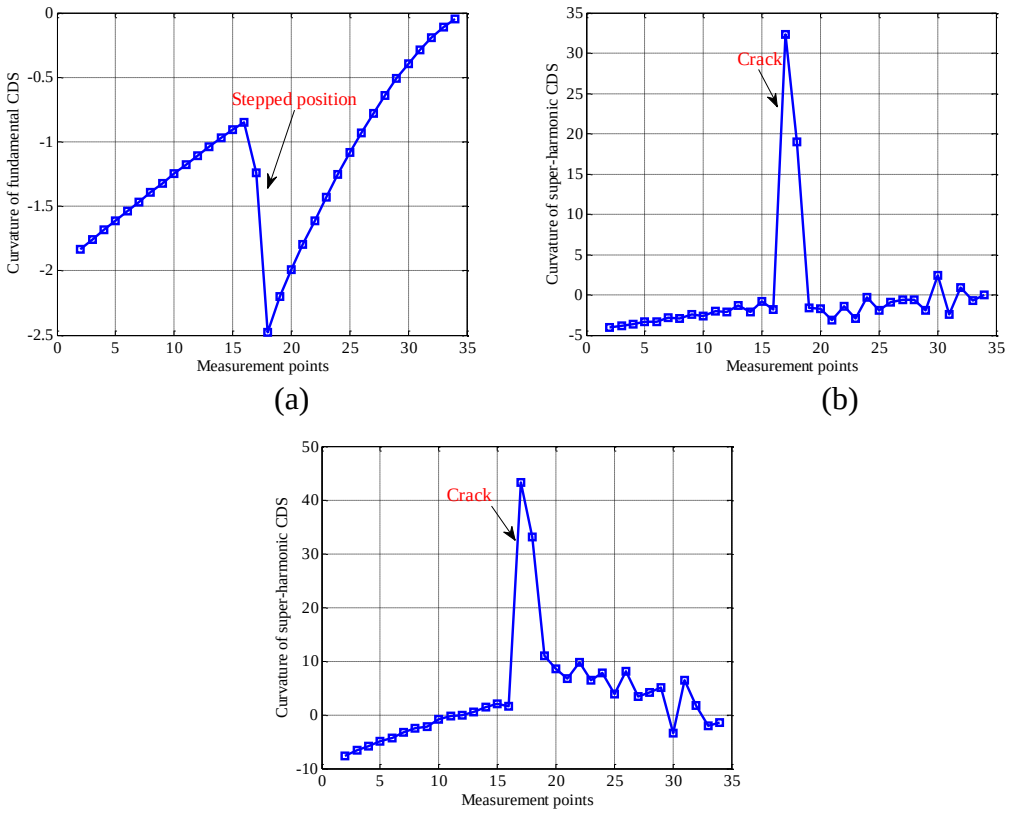

Figure 5.17 Damage identification results of case 2: (a) fundamental CDS, (b) super-harmonic CDS at $2\omega_F$ and (c) super-harmonic CDS at $4\omega_F$.

5.5 Conclusions

This chapter aims to study the finite element modelling of breathing cracks and identify them through their nonlinear characteristics in vibration responses. The major contribution is to identify the breathing cracks in stepped beams.

Two approaches are proposed to identify multiple breathing cracks in stepped beams. The first approach is a time domain method, which uses the deviation between empirical cumulative distributions of vibration responses at different locations. The other approach is a frequency domain method, which detects the breathing crack via the damage-induced shape distortions in super-harmonic characteristic deflection shapes.

Finally, the performance of the two proposed methods are investigated numerically for different damage cases of a stepped beam. Results show that these methods are effective and efficient for single or multiple breathing crack localisation in stepped beam-type structures.

Chapter 6

Robust mode shape curvature estimation of plate-type structures

Damage-induced local singularities in structural characteristic deflection shapes are widely used for non-model-based damage localisation of plate-type structures. Despite substantial advantages in this kind of methods, several issues must be addressed to boost their efficiency and practical applications. One of the crucial problems is that the curvature estimation of CDS's is significantly affected by measurement noise. To address this problem, this chapter aims to investigate the noise robust curvature estimation techniques for plates. Firstly, apart from the traditional curvatures along the *x* and *y* coordinates, the principal curvature, mean principal curvature and Gaussian curvature will be introduced for damage identification. Secondly, for the curvature estimation along the *x* and *y* coordinates, a 2-D Laplacian of Gaussian (LoG) method is employed to reduce the noise effects. For the principal, mean principal and Gaussian curvatures, a local bivariate polynomial fitting (LPF) technique is utilised to enhance their noise robustness.

Finally, effectiveness and robustness of LoG and LPF approaches in mode curvature estimation are demonstrated by numerical and experimental examples. Moreover, their performance on damage identification is discussed.

6.1 Introduction

Vibration-based damage identification in plates has been studied over the past few decades. The identified modal parameters, such as natural frequencies, mode shapes, and damping ratios are processed by various signal processing approaches for damage detection, localisation or quantification. The model updating based damage identification methods depend on the accuracy of the established theoretical or numerical structural model, which in turn affects the accuracy of damage identification. A current trend is to identify damage in plates based on non-contact measurement techniques by using only vibration data of damaged structures [66, 132, 142].

Different from natural frequency damage features, characteristic deflection shapes provide local information of structures, which makes them more sensitive to multiple damage detection and localisation. Moreover, in comparison with the natural frequencies, characteristic deflection shapes are more robust to the environmental variability like temperature or humidity. Nevertheless, one disadvantage is that the acquisition of CDS's requires a relatively large number of measurements points. Traditionally, experiments based on accelerometers are time-consuming and hard to obtain sufficient spatial resolution for CDS's. Nowadays, with the advanced measurement technique of Scanning Laser Vibrometer (SLV), the mode shapes or operational deflection shapes are readily acquired at a very high spatial resolution within a short time [194]. The laser heterodyne interferometry is used in SLV to measure the velocity (displacement/acceleration) at a surface point and a large number of measurement points can be measured sequentially [195]. When using SLV with one laser head, only the out-of-plane velocity signal of a plate can be acquired as long as the laser beam is not parallel with the plate surface. For the in-plane vibration, three laser heads should be employed. The data acquisition of this Chapter and Chapter 7 is conducted under 'FastScan' mode and much more details will be given in Section 6.6.

Since the quick acquisition of CDS's of large structure based on SLV, applying CDS's or their derivatives to damage identification in plates has been investigated by many authors [65, 128, 196, 197]. The fundamental idea is to detect the damage-induced local singularities in CDS's or their curvatures. The advantage of this kind of methods is that the identification of singularity from spatial shape features does not require the baseline data of healthy structures. Some of the singularity detection techniques for

plates are naturally extended from those of beam-type structures. Yoon, et al. [141] generalised the 1-D gapped smoothing method to 2-D approach to extract the local singularity features for damage localisation in plates. Surace et al. [198] employed a 2-D polynomial-annihilation edge technique to detect damage-caused discontinuities in mode shapes and their derivatives, which was originally proposed for damage detection in beam-type structures. Another popular technique of detecting the shape singularity for both beam-type and plate-type structures is wavelet transforms [14, 131, 139, 199]. For wavelet transforms, the continuous spatial wavelet is commonly utilised to represent the CDS's or their derivatives at different scales to examine the local details and suppress the effects of measurement noise. Then, the wavelet coefficients at a certain scale can be used to detect the presence and locations of damage depending on the local peaks or sudden changes [118].

Although there are various approaches to detecting damage in plates based on shape singularity, there are still two crucial problems that are not yet addressed. One is the robust curvature estimation of CDS's, as the traditional second-order central difference approach is extremely sensitive to noise and corrupts the damage-induced features, especially for incipient damage. The other difficulty is that how to define a robust damage index for multi-damage localisation without the baseline data of healthy structures. It is well known that a single CDS is impossible to identify all the damage locations, as it is just sensitive to damage in some regions while insensitive to damage in other regions. Therefore, a robust damage index should properly combine the damage information of several CDS's. In this chapter, the first problem of the robust curvature estimation of CDS's will be studied in the form of mode shape curvature estimation. Certainly, the proposed methods are not constrained to mode shapes but also applicable to other CDS's such as operational deflection shapes. Then, based on the estimated noise robust mode shape curvatures, a baseline-free robust multi-damage identification of plates will be presented in Chapter 7.

6.2 Background of curvature based damage identification

For damage identification of plates, the curvatures of plate deflections are commonly utilised due to their high sensitivity. For a homogeneous thin plate with a constant thickness, the relationship between bending moments and curvatures can be expressed as according to Kirchhoff theory [200]:

$$\begin{bmatrix} M_x \\ M_y \\ M_{xy} \end{bmatrix} = -\frac{Eh^3}{12(1-\upsilon^2)} \begin{bmatrix} 1 & \upsilon & 0 \\ \upsilon & 1 & 0 \\ 0 & 0 & 1-\upsilon \end{bmatrix} \begin{bmatrix} \kappa_{xx} \\ \kappa_{yy} \\ \kappa_{xy} \end{bmatrix} \tag{6.1}$$

where M_x and M_y are the bending moments of x and y coordinates and M_{xy} is the twisting moment. $D = \frac{Eh^3}{12(1-\upsilon^2)}$ is the plate flexural rigidity (also known as plate stiffness) with Young's modulus E, the thickness of the plate h and the Poisson's ratio υ. Moreover, κ_{xx}, κ_{yy} and κ_{xy} are the curvatures of plate transverse deflection, which can be approximated by the second-order partial derivatives due to the small slope assumption ($\partial W_{\mathrm{p}}/\partial x, \partial W_{\mathrm{p}}/\partial y \ll 1$).

$$\kappa_{xx} = \frac{\partial^2 W_{\mathrm{p}}(x,y;t)}{\partial x^2}, \kappa_{yy} = \frac{\partial^2 W_{\mathrm{p}}(x,y;t)}{\partial y^2}, \kappa_{xy} = \frac{\partial^2 W_{\mathrm{p}}(x,y;t)}{\partial x \partial y} \tag{6.2}$$

where $W_{\mathrm{p}}(x, y; t)$ represents the deflection of a plate and subscript p indicates plate.

For a plate, the damage are normally simulated by a reduction of Young's modulus E or the plate thickness h. Here, the reduction of plate thickness in FE elements is used to simulate the damage. The plate flexural rigidity of damaged region is expressed as

$$D_{\mathrm{d}} = \frac{E(h-h_{\mathrm{d}})^3}{12(1-\upsilon^2)} = D\left(1 - \frac{h_{\mathrm{d}}}{h}\right)^3 \tag{6.3}$$

where the subscript d indicates the damaged state.

According to Eq. (6.1), the physical property changes of plate flexural rigidity D due to damage can be reflected by the deflection curvature κ_{xx}, κ_{yy} or κ_{xy}. According to the modal expansion theorem of structural response, the plate transverse displacement function $W_{\mathrm{p}}(x, y; t)$ can be represented by the product of mode shapes and modal coordinates, which indicates that the curvatures of mode shapes are also sensitive for damage identification. For simplicity, the curvatures of mode shapes are also denoted by κ_{xx}, κ_{yy} or κ_{xy} below. Thereby, a formulation of damage index can be written as

$$DI(x,y) = \alpha_{xx}\left|\kappa_{xx}^{\mathrm{d}} - \kappa_{xx}\right| + \alpha_{yy}\left|\kappa_{yy}^{\mathrm{d}} - \kappa_{yy}\right| + \alpha_{xy}\left|\kappa_{xy}^{\mathrm{d}} - \kappa_{xy}\right| \tag{6.4}$$

where $\alpha_{xx}, \alpha_{yy}, \alpha_{xy}$ are the weighting coefficients indicating the contribution of the curvature in corresponding directions.

Without damage interference, the $DI(x,y)$ plot of a plate will be slightly around zero but not exactly zero due to the effects of measurement noise. When damage occurs, peaks or sudden changes will be obviously present around the damage area in the DI plot. However, the multi-damage identification by using a single mode shape curvature is not reliable and robust. Therefore, a robust multi-damage index should incorporate the damage information of several mode shape curvatures, which can be expressed as

$$DI(x,y) = \sum_{i=1}^{N_r} w_i \; DI_i(x,y) \tag{6.5}$$

where $\mathrm{DI}_i(x,y)$ indicates the individual damage index of the i-th mode shape curvature calculated using Eq. (6.4), N_r denotes the number of mode shapes concerned for damage identification and w_i is the weighing coefficient of each $DI_i(x,y)$.

However, for the robust multi-damage index in Eq. (6.5), there are three crucial issues, which are not yet solved properly. Firstly, the curvature calculated by second-order differentiation in Eq. (6.2) is considerably sensitive to measurement noise, which degrades or even misleads the damage identification. Secondly, the required baseline mode shape curvatures of the intact state for distance measure in Eq. (6.4) are typically unavailable. Finally, the determination of proper weighting coefficients to effectively combine the damage information of each mode shape curvature is challenging. For the first problem, several new types of curvatures are introduced and two approaches are presented to reduce the noise effects, while the second and third issues will be investigated in Chapter 7.

6.3 Robust curvature estimation via multi-scale approaches

Typically, the mode shape curvature is directly estimated via second-order central difference as shown in Eq. (6.6).

$$\begin{aligned} \Phi_{xx}(x_i,y_j) &= \frac{\Phi(x_{i+1},y_j)-2\Phi(x_i,y_j)+\Phi(x_{i-1},y_j)}{d_x^2} \\ \Phi_{yy}(x_i,y_j) &= \frac{\Phi(x_i,y_{j+1})-2\Phi(x_i,y_j)+\Phi(x_i,y_{j-1})}{d_y^2} \end{aligned} \tag{6.6}$$

Where Φ_{xx} and Φ_{yy} denote the partial mode shape curvature along x and y directions, respectively. Moreover, d_x and d_y represent the grid distances along x and y directions. It is worth noting that the second-order central difference method significantly amplifies the effects of measurement noise, which degrades the effectiveness of

damage identification [201]. Thus, the reduction of measurement noise in the acquired mode shape data should be addressed before damage identification. Three multi-scale approaches, LoG filter, Mexican hat wavelet transform and difference of Gaussian (DoG), are presented to carry out the robust mode shape curvature (Φ_{xx} andΦ_{yy}) estimation.

Inspired by the blob detection in computer vision, the LoG has been employed to enhance the mode shape curvature estimation and damage identification accuracy of plate-type structures [202, 203]. A blob represents a region of an image and inside the blob region some properties are constant or approximately constant, which is similar to the damage (reduction of local area stiffness) of plates. To smoothen the noisy mode shape $\Phi(x,y)$, Gaussian smoothing is applied, which convolves the mode shape $\Phi(x,y)$ with a Gaussian function at a certain scale σ.

$$L_{\mathrm{g}}(x,y;\sigma) = \Phi(x,y) \otimes g(x,y;\sigma)$$

$$= \int_{-\infty}^{+\infty}\int_{-\infty}^{+\infty} \Phi(x-u,y-v)g(u,v;\sigma)\,dudv \tag{6.7}$$

where σ denotes the standard deviation, $\otimes$ represents convolution operator and $g(x,y;\sigma)$ is a Gaussian function. For two-dimensional application, an isotropic Gaussian function is rotationally symmetric and has the form

$$g(x,y;\sigma) = \frac{1}{2\pi\sigma^2}\mathrm{e}^{-\left(\frac{x^2+y^2}{2\sigma^2}\right)} \tag{6.8}$$

By adjusting the scale parameter σ, the original mode shape can be handled at different scales. At a certain scale σ, the measurement noise and local shape details of the original mode shape will be suppressed and the mode shape so processed becomes smooth. In practice, without prior knowledge of the mode shape, no particular scale level can be determined and it is necessary to deal with the mode shape at all scales [204]. Figure 6.1 illustrates the multi-scale representation. A coarse scale level is better to supress noise whilst it is possible to remove the damage-induced singularity information.

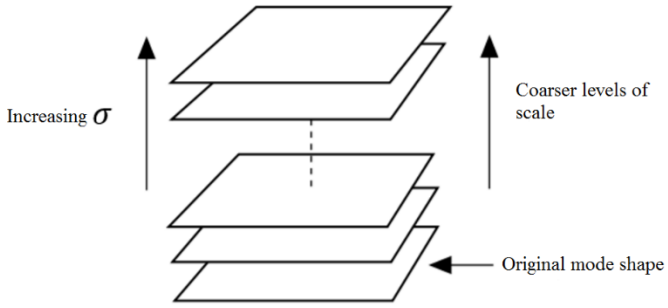

Figure 6.1 Multi-scale representation of the original mode shape.

For damage detection of plates, which is similar to the edge detection in an image, the derivative of scale space representation is calculated. Here, the Laplacian operator of $L_{\mathrm{g}}(x, y; \sigma)$ is used to implement the curvature estimation of mode shapes.

$$\nabla^2 L_{\mathrm{g}}(x, y; \sigma) = \nabla^2 (\Phi(x, y) \otimes g(x, y; \sigma)) \tag{6.9}$$

where $\nabla^2 = \frac{\partial^2}{\partial x^2} + \frac{\partial^2}{\partial y^2}$ represents the Laplacian operator. Due to differentiation property of the convolution integral, the Laplacian of $L_{\mathrm{g}}(x, y; \sigma)$ is equivalent to convolving the original mode shape function $\Phi(x, y)$ with a LoG filter $\nabla^2 g(x, y; \sigma)$, which is expressed as

$$\nabla^2 L_{\mathrm{g}}(x, y; \sigma) = \nabla^2 \Phi(x, y) \otimes g(x, y; \sigma) = \Phi(x, y) \otimes \nabla^2 g(x, y; \sigma) \tag{6.10}$$

in which, the LoG filter is

$$\nabla^2 g(x, y; \sigma) = -\frac{1}{\pi \sigma^4} \left(1 - \frac{x^2 + y^2}{2\sigma^2}\right) \mathrm{e}^{-\left(\frac{x^2 + y^2}{2\sigma^2}\right)} \tag{6.11}$$

Equation (6.10) shows that the direct application of second-order central difference approach to $\Phi(x, y)$ can be avoided by using a LoG filter. Furthermore, the effects of measurement noise on mode shape curvature can be tuned by changing the scale parameter σ of LoG filter. In addition, it is worth noting that the integral of Gaussian filter $g(x, y; \sigma)$ over all space is one as shown in Eq. (6.12), whilst the integral of LoG filter $\nabla^2 g(x, y; \sigma)$ over all space is zero, which indicates that changing the constant coefficient of LoG filter will not affect the integral. In this case, estimated mode shape curvatures by using LoG filter with various value of the constant coefficient are proportional with each other without altering the shape patterns.

$$\begin{cases} \int_{-\infty}^{+\infty}\int_{-\infty}^{+\infty} g(x,y;\sigma)\,dx\,dy = 1 \\ \int_{-\infty}^{+\infty}\int_{-\infty}^{+\infty} \nabla^2 g(x,y;\sigma)\,dx\,dy = 0 \end{cases} \tag{6.12}$$

The LoG filter can be fulfilled by combining the 'fspecial' function with 'imfilter' function in MATLAB. Moreover, the 2-D LoG approach can be applied via the Mexican hat wavelet transform, since the Mexican hat wavelet function is proportional to the second derivative of a Gaussian function, which is written as

$$\psi_{\mathrm{m}}(x,y;\sigma) = c_{\mathrm{w}}\left(1-\frac{x^2+y^2}{2\sigma^2}\right)\mathrm{e}^{-\left(\frac{x^2+y^2}{2\sigma^2}\right)} \tag{6.13}$$

where $\psi_{\mathrm{m}}(\cdot)$ represents the Mexican hat wavelet (also known as Marr wavelet) and c_{w} indicates the proportional coefficient.

The Mexican hat wavelet transform is implemented in MATLAB by using 'cwtft2' function with the 'mexh' wavelet, which is coded based on the 2-D Fourier transform. The coefficient c_{w} does not affect the shape patterns of estimated curvatures but results in the magnitude changes of curvatures. Another approach to implement LoG approach is by the difference of two Gaussians (DoG) at different scales [205], which is expressed as

$$\begin{gathered} \partial L_{\mathrm{g}}/\partial\,\sigma^2 = \nabla^2 L_{\mathrm{g}}/2\,,\partial L_{\mathrm{g}}/\partial\,\sigma = \sigma\times\nabla^2 L_{\mathrm{g}} \\ \nabla^2 L_{\mathrm{g}}(x,y;\sigma) \approx \frac{1}{\sigma\times\Delta\sigma}\left(L_{\mathrm{g}}(x,y;\sigma+\Delta\sigma) - L_{\mathrm{g}}(x,y;\sigma)\right) \end{gathered} \tag{6.14}$$

where $\partial L_{\mathrm{g}}/\partial\,\sigma^2 = \nabla^2 L_{\mathrm{g}}/2$ is derived based on the Gaussian function in Eq. (6.8). And this algorithm is achieved by using 'ispecial' or 'imgaussfilt' function in MATLAB.

For all the three LoG implementation approaches, by increasing the scale parameter σ, more measurement grid points are used in the curvature estimation and the noise resistance will be better. However, if the scale parameter is too big, it will decrease the possibility of detecting the damage-induced local shape singularity. Thus, an appropriate scale parameter should be chosen to guarantee both the noise robustness and damage sensitivity.

6.4 Principal, mean and Gaussian curvatures

Although the curvatures of mode shapes along the x and y coordinates are readily computed and commonly applied for damage identification in plates, they do not adequately describe the property of a mode shape. In this section, the characteristic curvatures such as Gaussian curvature, mean principal curvature and principal curvatures will be investigated for damage identification of plates. Moreover, a local polynomial fitting approach is applied to enhance their noise robustness.

At a given point of a mode shape, the two principal curvatures $\kappa_1$and κ_2 denote the maximum and minimum curvatures, respectively. Their relationship with κ_{xx}, κ_{yy} and κ_{xy} can be written as

$$\begin{cases} \kappa_1 = \kappa_{xx}\cos^2(\theta) + \kappa_{yy}\sin^2(\theta) + \kappa_{xy}\sin(2\theta) \\ \kappa_2 = \kappa_{xx}\sin^2(\theta) + \kappa_{yy}\cos^2(\theta) - \kappa_{xy}\sin(2\theta) \end{cases} \tag{6.15}$$

where θ represents the angle between κ_1 and κ_{xx}. Moreover, Eq. (6.15) indicates that κ_1+κ_2= κ_{xx}+κ_{yy}, which implies that the sum of curvatures along two orthogonal directions is invariant [206]. For a plate mode shape, $\kappa_{xx} = \Phi_{xx}$,$\kappa_{yy} = \Phi_{yy}$ and $\kappa_{xy} = \Phi_{xy}$. In this chapter, although κ_1+κ_2 and Φ_{xx}+Φ_{yy} are equal with each other in theory, they are estimated by using different de-noising approaches. To distinguish them, $(\Phi_{xx} + \Phi_{yy})/2$ and $(\kappa_1 + \kappa_2)/2$ are termed as mean *x*-*y* curvature and mean principal curvature, respectively.

It is clear from Eq. (6.15) that the damage-induced changes can be indicated by the principal curvatures as well. Moreover, if the two principal curvatures of a mode shape are obtained in advance, the product of them is the Gaussian curvature K_p and the average of them is the mean curvature H_p [207], which are computed as

$$\begin{cases} K_\mathrm{p} = \kappa_1 \cdot \kappa_2 \\ H_\mathrm{p} = \frac{1}{2}(\kappa_1 + \kappa_2) \end{cases} \tag{6.16}$$

For the principal, mean principal and Gaussian curvature estimation, several different approaches have been proposed and are normally categorised into discrete and continuous methods [67, 208, 209]. The discrete methods apply the direct calculation formula to the discrete representation points of the underlying mode shape surface. For

the continuous approaches, they firstly employ a local bivariate polynomial fitting technique to fit the current point and its several neighbourhood points, and then evaluate the curvatures using the fitted mode shape surface [210]. Due to the measurement noise of mode shape data, it is better to evaluate principal, mean principal and Gaussian curvatures by continuous approach rather than the direct calculation.

For the discrete curvature estimation method, the Gaussian curvature K_{p} and mean curvature H_{p} are determined from the formulas below

$$\begin{cases} K_{\mathrm{p}} = \frac{L_{\mathrm{p}}N_{\mathrm{p}} - {M_{\mathrm{p}}}^2}{E_{\mathrm{p}}G_{\mathrm{p}} - {F_{\mathrm{p}}}^2} \\ H_{\mathrm{p}} = \frac{1}{2}\frac{L_{\mathrm{p}}G_{\mathrm{p}} - 2M_{\mathrm{p}}F_{\mathrm{p}} + N_{\mathrm{p}}E_{\mathrm{p}}}{E_{\mathrm{p}}G_{\mathrm{p}} - {F_{\mathrm{p}}}^2} \end{cases} \tag{6.17}$$

where $E_{\mathrm{p}} = \|(1, 0, \Phi_x)\|^2$, $F_{\mathrm{p}} = (1, 0, \Phi_x) \cdot (0, 1, \Phi_y)$, $G_{\mathrm{p}} = \|(0, 1, \Phi_y)\|^2$, $L_{\mathrm{p}} = (0, 0, \Phi_{xx}) \cdot \mathbf{n}$, $M_{\mathrm{p}} = (0, 0, \Phi_{xy}) \cdot \mathbf{n}$ and $N_{\mathrm{p}} = (0, 0, \Phi_{yy}) \cdot \mathbf{n}$ come from the first and second fundamental forms of a mode shape surface $\Phi(x, y)$: $E_{\mathrm{p}}\mathrm{d}x^2 + 2F_{\mathrm{p}}\mathrm{d}x\mathrm{d}y + G_{\mathrm{p}}\mathrm{d}y^2$ and $L_{\mathrm{p}}\mathrm{d}x^2 + 2F_{\mathrm{p}}\mathrm{d}x\mathrm{d}y + G_{\mathrm{p}}\mathrm{d}y^2$. Here, $\mathbf{n}$ indicates the unit normal vector of the mode shape surface at a point, which is expressed as

$$\mathbf{n} = (-\Phi_x, -\Phi_y, 1) / \sqrt{{\Phi_x}^2 + {\Phi_y}^2 + 1} \tag{6.18}$$

For the transverse vibration of a thin plate, the deflection is assumed to be small compared with the overall dimensions of the plate. In this case, the important assumption of small slope is valid, which means Φ_x and $\Phi_y \ll 1$. Thus, $\mathbf{n} = (0,0,1)$ and Eq. (6.17) is simplified as

$$\begin{cases} K_{\mathrm{p}} = \Phi_{xx}\Phi_{yy} - \Phi_{xy}^2 \\ H_{\mathrm{p}} = (\Phi_{xx} + \Phi_{yy})/2 \end{cases} \tag{6.19}$$

With the determined Gaussian curvature K_{p} and mean curvature H_{p}, the two principal curvatures of a mode shape are computed as

$$\begin{cases} \kappa_1 = H_{\mathrm{p}} + \sqrt{H_{\mathrm{p}}^2 - K_{\mathrm{p}}} \\ \kappa_2 = H - \sqrt{H_{\mathrm{p}}^2 - K_{\mathrm{p}}} \end{cases} \tag{6.20}$$

Eq. (6.17) and Eq. (6.20) indicate that the Gaussian, mean principal and principal curvatures are the extracted geometric information from first and second fundamental forms of a mode shape surface, which are independent of measurement coordinates.

For the continuous curvature estimation method, the measured mode shape surface data are primarily rotated to obtain the normal vector at current point as $(0,0,-1)$. Thus, the mode shape data can be represented by (x, y) instead of (x, y, z) [211]. In the second stage, the current point and its local neighbourhood points are used to fit a quadratic polynomial as

$$f_{\mathrm{p}}(x, y) = c_1 x^2 + c_2 y^2 + c_3 xy + c_4 x + c_5 y + c_6 \tag{6.21}$$

The local neighbourhood points can be indicated by the rings around the current point such as the first-ring, second-ring and third-ring shown in Figure 6.2. Generally, the more rings are used, the more noise robust and smooth the curvature but less sensitive to local features. Another important parameter that controls the quality of estimated curvature is the average distance between the rings, which is determined by the mesh points used to represent the mode shape surface.

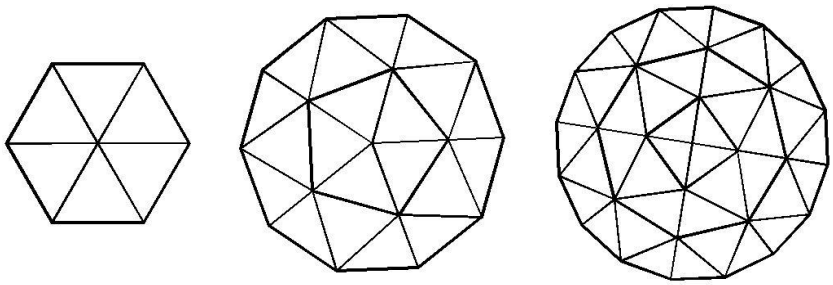

(a) (b) (c)

Figure 6.2 Neighbourhood points (a) 1 ring (b) 2 rings and (c) 3 rings

Finally, the Weingarten matrix of the mode shape surface at point l, which equals to the hessian matrix of $f_{\mathrm{p}}(x, y)$ that defined in Eq. (6.19), is applied to calculate the principal, mean and Gaussian curvatures. The Weingarten matrix is expressed as

$$\boldsymbol{W}_l = \begin{bmatrix} \frac{\partial^2 f_{\mathrm{p}}}{\partial x^2} & \frac{\partial^2 f_{\mathrm{p}}}{\partial x \partial y} \\ \frac{\partial^2 f_{\mathrm{p}}}{\partial x \partial y} & \frac{\partial^2 f_{\mathrm{p}}}{\partial y^2} \end{bmatrix} = \begin{bmatrix} 2c_1 & c_3 \\ c_3 & 2c_2 \end{bmatrix} \tag{6.22}$$

The principal curvatures κ_1 and κ_2 are the eigenvalues of Weingarten matrix. Then, the Gaussian and mean principal curvatures are calculated according to Eq. (6.16). And

Eq. (6.16) indicates that Gaussian and mean principal curvatures are the determinant and half of the trace of Weingarten matrix as shown in Eq. (6.22).

$$K_{\mathrm{p}} = \det(\boldsymbol{\mathcal{W}}_l)\,, H_{\mathrm{p}} = \mathrm{trace}(\boldsymbol{\mathcal{W}}_l)/2 \tag{6.23}$$

6.5 Numerical studies

There are three purposes of the numerical studies. First, the multi-damage simulation in plates will be presented. The numerical model is simulated according to the experiments, which provides a related numerical study for experiments. Secondly, the robust estimation of mode shape curvatures will be investigated under the Gaussian white noise to verify its effectiveness. Finally, a comparison is presented to demonstrate which kind of curvature or curvature estimation approach is more reliable and sensitive to the given two damage positions.

A cantilever aluminium plate of dimension $0.35 \times 0.23 \times 0.003\mathrm{m}^3$ with Young's modulus E=69 GPa, Poisson's ratio $\nu = 0.35$ and the mass density ρ=2700 kg/m^3 is studied as shown in Figure 6.3. The plate is modelled using the four-node quadrilateral shell element in MATLAB according to Mindlin plate theory [212]. During the numerical integration, 2×2 Gauss points are used for the bending contribution and 1 point is used for the shear contribution, which are proved to be one of the simplest approach to avoiding shear locking [213]. The cantilever plate is discretised into 70×46 elements with each element of $0.005 \times 0.005 \times 0.003\mathrm{m}^3$ and the clamped edge is located on the left, which is shown in Figure 6.3. Under damage cases, the damage-induced local stiffness reduction is modelled according to Eq. (6.3) by decreasing the thickness of associated FE elements. In this example, the two damage positions are centred at (0.10 m, 0.115 m) and (0.21 m, 0.115 m) with an equal area of $0.02 \times 0.02\ \mathrm{m}^2$.

Moreover, in order to assess the accuracy of the established FE model of plate in MATLAB, a comparative study of the first five natural frequencies under healthy state is carried out with the FE model built in ABAQUS. Table 6.1 displays the first five natural frequencies calculated from the ABAQUS software and the MATLAB code, respectively.

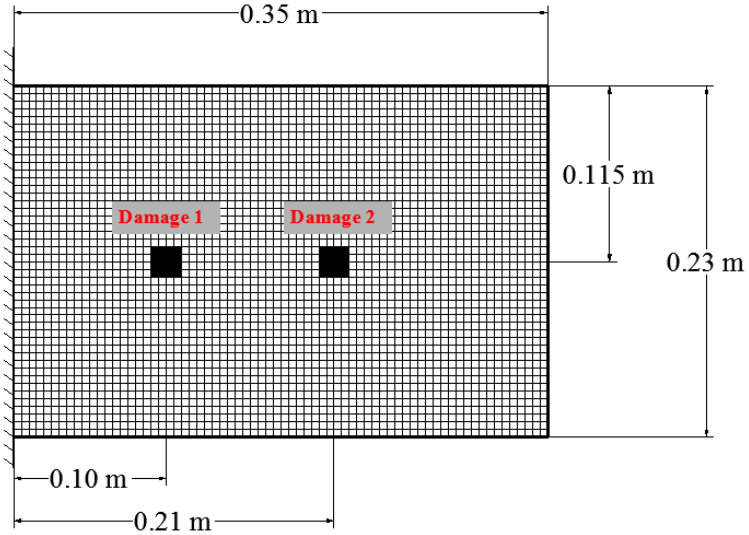

Figure 6.3 FE model of a plate with two damage positions.

Table 6.1 The first five natural frequencies of intact plate.

Natural frequencies (Hz)	Modes				
	1	2	3	4	5
Results of MATLAB	20.80	69.21	128.92	234.27	327.14
Results of ABAQUS	20.80	69.25	128.92	234.40	327.20
Relative errors (%)	0.00	0.06	0.00	0.06	0.02

It is clear from Table 6.1 that the differences of evaluated natural frequencies between the two approaches are very small, which indicates the high accuracy of the modelled cantilever plate using MATLAB. The reason for coding the plate model in MATLAB is that it is easy to adjust the parameters of damage such as thickness and positions when conducting simulations for many times. Furthermore, it is convenient to extract the mode shape data and apply signal processing approaches of MATLAB.

6.5.1 Damage sensitivity of different mode shape curvatures

Before applying the proposed approaches for robust mode shape curvature estimation, the damage sensitivity of different mode shape curvatures is studied based on noise-free mode shapes. Two problems are discussed. First, the mode shape curvatures associated with different natural frequencies will be demonstrated to be sensitive to damage at different locations. Secondly, the damage sensitivity of different types of curvatures (two principal curvatures, mean *x*-*y* curvature, mean principal curvature and Gaussian curvature) is investigated.

The two small damage areas with 10% thickness reduction as shown in Figure 6.3 are simulated. Then, the normalised 9th mode shape and 10th mode shape with their values range of [-1, 1] are obtained and presented in Figure 6.4. Here, they are chosen as the 10th mode shape is sensitive to both damage areas while the 9th mode shape is used to show that not any mode shape is sensitive to the two given damage areas.

First, the mean *x-y* curvature of the 9th and 10th mode shapes are obtained by second-order central difference approach and displayed in Figure 6.5 to show which mode shape is more sensitive to the two given damage positions in Figure 6.3.

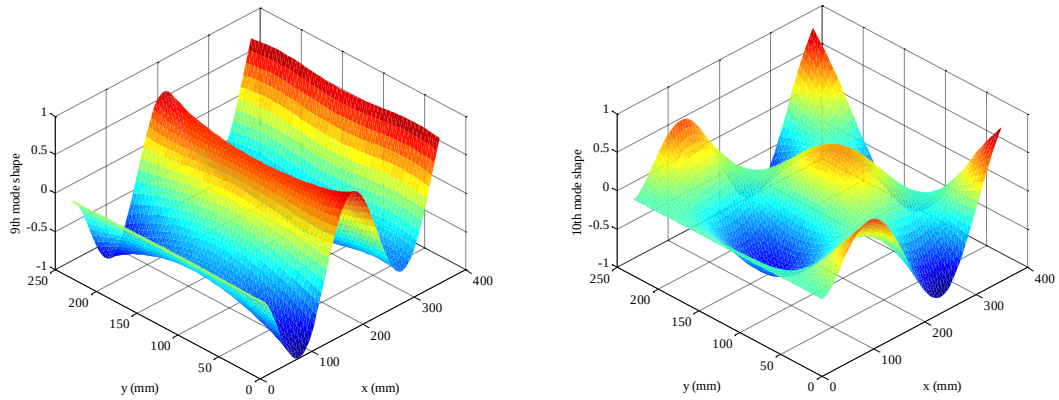

(a) (b)

Figure 6.4 (a) The 9th mode shape and (b) The 10th mode shape.

Apparently, the mean *x-y* curvature of 10th mode shape is much more sensitive to these two damage areas defined in Figure 6.3, as Figure 6.5 (b) presents much shaper peaks around damage areas than these of Figure 6.5 (a). Furthermore, it proves that damage identification based on a single mode shape is not reliable, especially for multi-damage localisation.

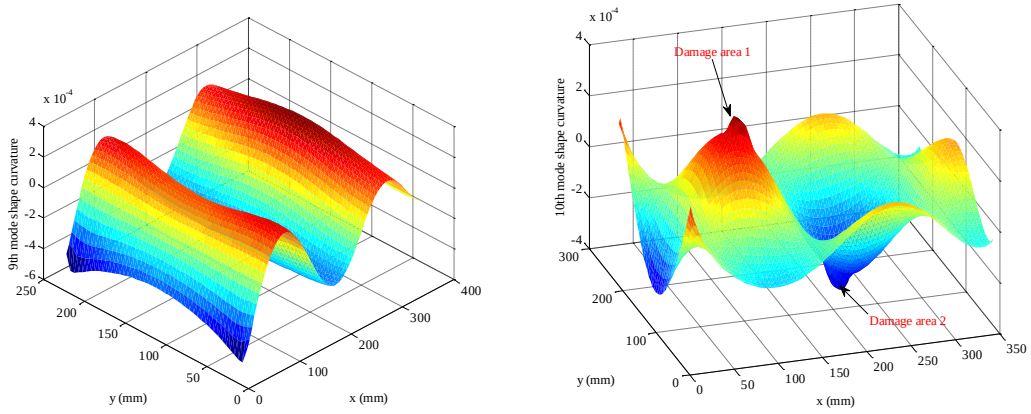

(a) (b)

Figure 6.5 Mean *x-y* curvature of (a) the 9th mode shape and (b) the 10th mode shape.

In addition, apart from the mean *x-y* curvature, the principal curvatures, mean principal curvature and Gaussian curvature of 10th mode shape are also computed according to Eq. (6.17) and Eq. (6.20) to show their sensitivities to damage, which are illustrated in Figure 6.6. In Figure 6.6, the absolute magnitudes of principal, mean and Gaussian curvature are not important but the shape patterns are useful for damage identification.

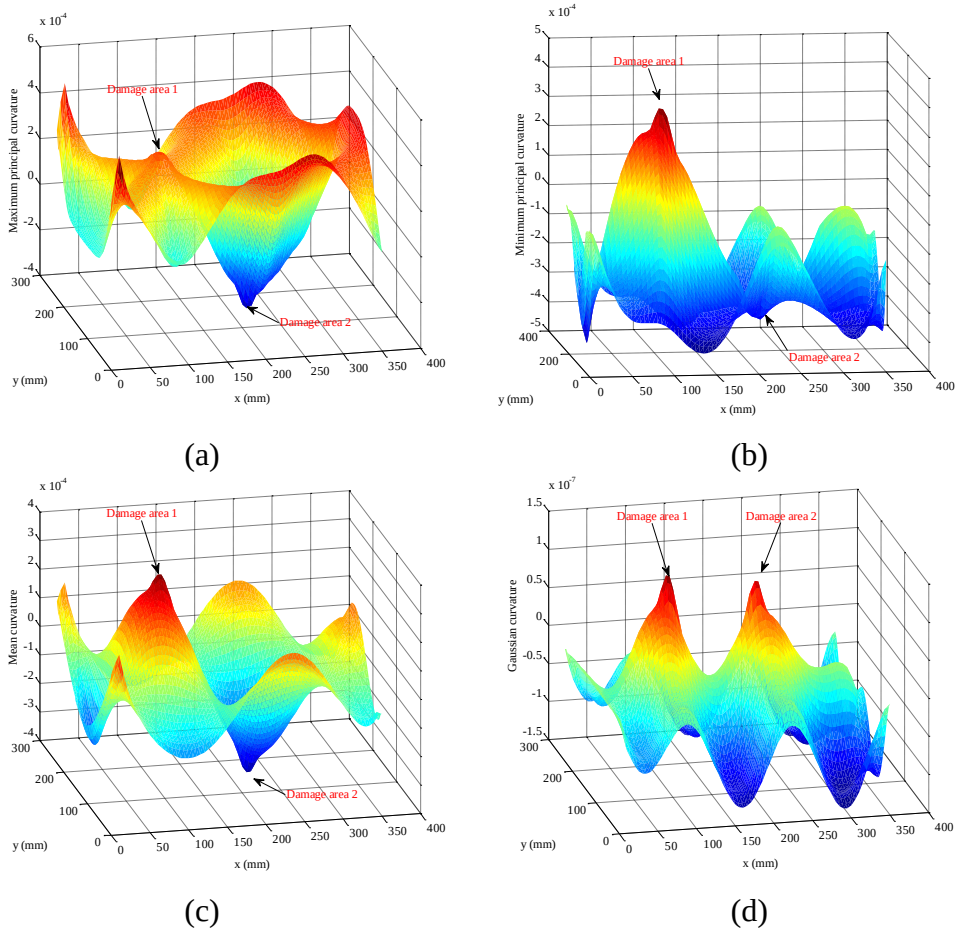

Figure 6.6 Curvatures of the 10th mode shape (a) Maximum principal curvature (b) Minimum principal curvature (c) Mean principal curvature and (d) Gaussian curvature.

It can be concluded from Figure 6.6 that principal, mean principal and Gaussian curvatures of the 10th mode shape are all sensitive to the two damage positions and can be used for damage identification. But the mean principal and Gaussian curvatures, which are the combinations of principal curvatures, perform better than the individual principal curvatures.

6.5.2 Robust mode shape curvature estimation

In section 6.5.1, the mode shape curvatures are shown to be sensitive for damage localisation. However, mode shape curvatures are susceptible to measurement noise,

which significantly decreases the accuracy of damage identification or even leads to wrong damage identification results. In this section, the improvements of estimated curvatures by using the LoG and LPF approaches will be demonstrated in terms of accuracy and noise robustness.

To make the numerical study more like practical experiments, Gaussian white noise is generated to contaminate the mode shapes in the form of

$$\widetilde{\Phi}_r(x,y) = \Phi_r(x,y) + \mathrm{n_n} n_{\mathrm{level}} \sigma\big(\Phi_r(x,y)\big) \tag{6.24}$$

where $\Phi_r(x,y)$ denotes the r-th mode shape with x and y indicating the locations along the x and y coordinates, $\widetilde{\Phi}_r(x,y)$ represents the noisy mode shape value and $\mathrm{n_n}$ is the normally distributed random white noise with a zero mean value and a variance being 1. In addition, n_{level} is the noise level ranging of [0, 1] and $\sigma\big(\Phi_r(x,y)\big)$ represents the standard variance of r-th mode shape.

6.5.2.1 Robust mean *x-y* curvature estimation

Three LoG implementation approaches (LoG filter, Mexican hat wavelet transform and DoG) are investigated to enhance the mode shape curvature along x and y directions. First, the Gaussian white noise of $n_{\mathrm{level}} = 0.1\%$ (SNR=60.10 dB) is added to pollute the 10th mode shape. Then, mean *x-y* curvature of the 10th mode shape are estimated by second-order central difference approach without noise processing and LoG filter with $\sigma = 1$, which are displayed in Figure 6.7.

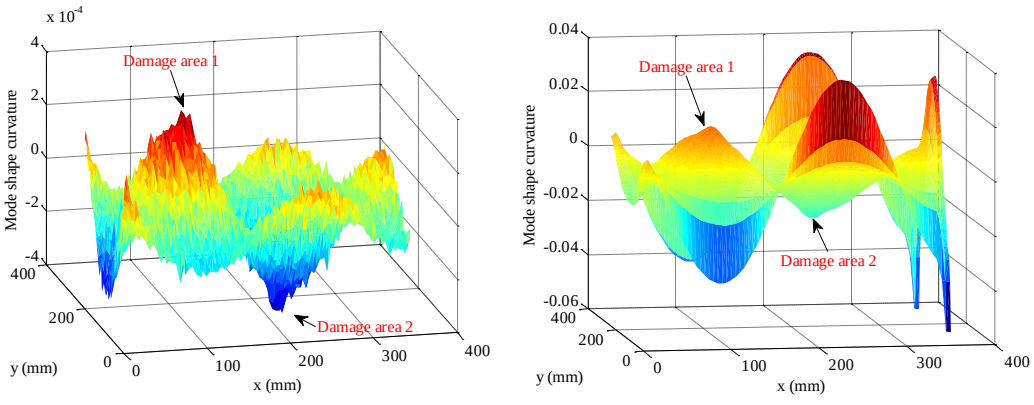

(a) (b)

Figure 6.7 Mean *x-y* curvature using: (a) second-order central difference (b) LoG filter with $\sigma = 1$.

In this Chapter, the damage locations as depicted in Figure 6.7 are known in advance and the purpose is to manifest the damage-caused changes around the damage locations and reduce the effects of measurement noise by investigating advanced signal processing approaches. In Chapter 7, a robust multi-damage localisation index based on normalisation and threshold techniques will be present. Figure 6.7 demonstrates that the second order central difference approach is sensitive to the measurement noise whereas LoG filter is good at processing the noisy mode shape. Nevertheless, the disadvantage of LoG filter is that it does not deal well with the boundary points. In addition, this problem is also present in Mexican hat wavelet transform and DoG approaches. In order to improve the performance of LoG method, the estimated curvature values around the boundary measurement points are ignored and the processed Figure 6.7 (b) is presented in Figure 6.8 (a). Figure 6.8 (b) shows the estimated mean *x-y* curvature using LoG filter with $\sigma = 3$. Figure 6.8 (c) and Figure 6.8 (d) illustrate the estimated mean *x-y* curvature based on Mexican hat wavelet transform and DoG with $\sigma = 1$, respectively.

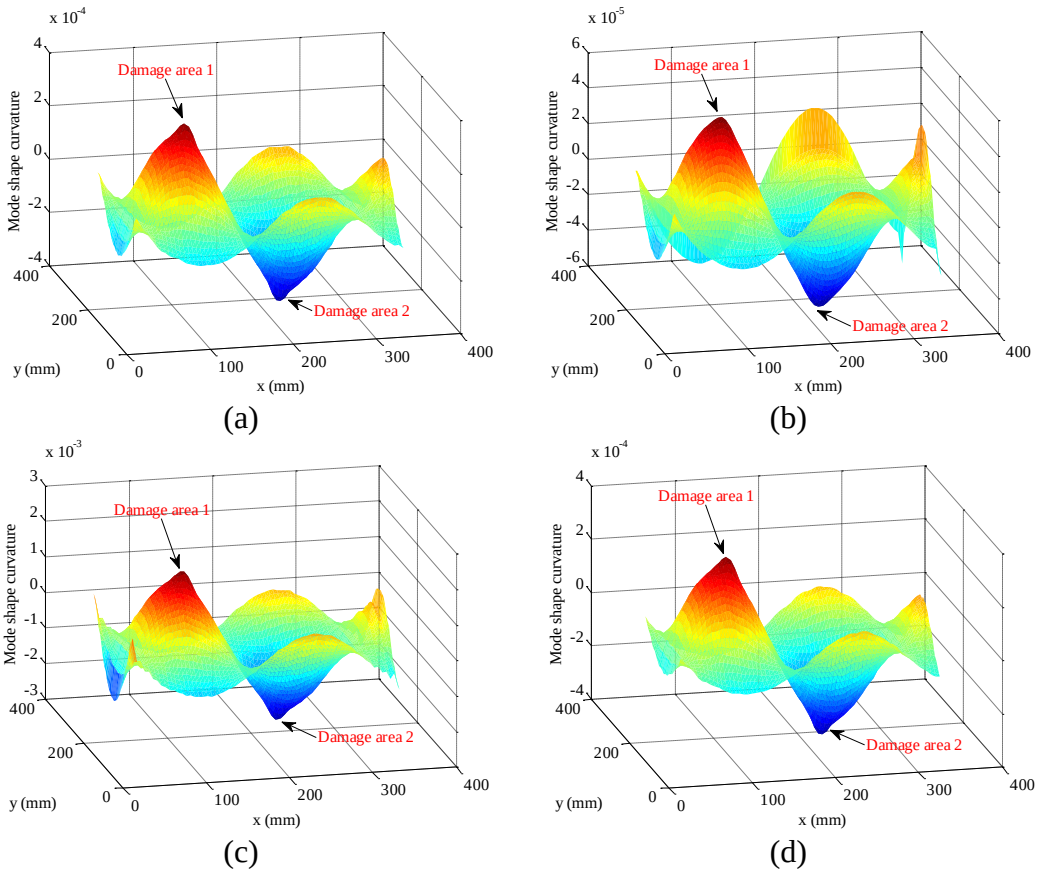

Figure 6.8 Mean *x-y* curvature using: (a) LoG filter with $\sigma = 1$ (b) LoG filter with $\sigma = 3$ (c) Mexican hat wavelet with $\sigma = 1$ and (d) DoG with $\sigma = 1$.

Firstly, in comparison with Figure 6.7 (b), Figure 6.8 (a) clearly indicates the two damage areas. Therefore, when using LoG filter for noise processing, the boundary measurement points should be given additional consideration. Secondly, by comparing Figure 6.8 (a) with Figure 6.8 (b), it is apparent that the damage-induced shape singularities decrease when increasing the scale parameter σ. Thus, the scale parameter should be selected appropriately to supress the measurement noise while keeping the damage-induced shape singularities. Finally, from Figure 6.8 (a), (c) and (d), it can be concluded that the curvature estimated by LoG filter, Mexican hat wavelet transform and DoG are all noise robust and accurate enough for damage identification.

6.5.2.2 Principal, mean principal and Gaussian curvatures

For the principal, mean principal and Gaussian curvatures, the LoG approach is not suitable as it works for the curvatures along *x* and *y* coordinates. Thus, in this section, local bivariate polynomial fitting methods will be used for robust principal, mean principal and Gaussian curvature estimation. Firstly, the discrete approach according to Eq. (6.17) and Eq. (6.20) is employed to obtain the principal, mean principal and Gaussian curvatures of the noisy 10^{th} mode shape (Gaussian white noise of $n_{\text{level}} = 0.1\%$ (SNR=60.10 dB)), which are shown in Figure 6.9.

By comparing Figure 6.9 with Figure 6.7 (a), it can be seen that the principal, mean principal and Gaussian curvatures tend to be more noise robust than mean *x*-*y* curvature when de-noising approaches are not adopted.

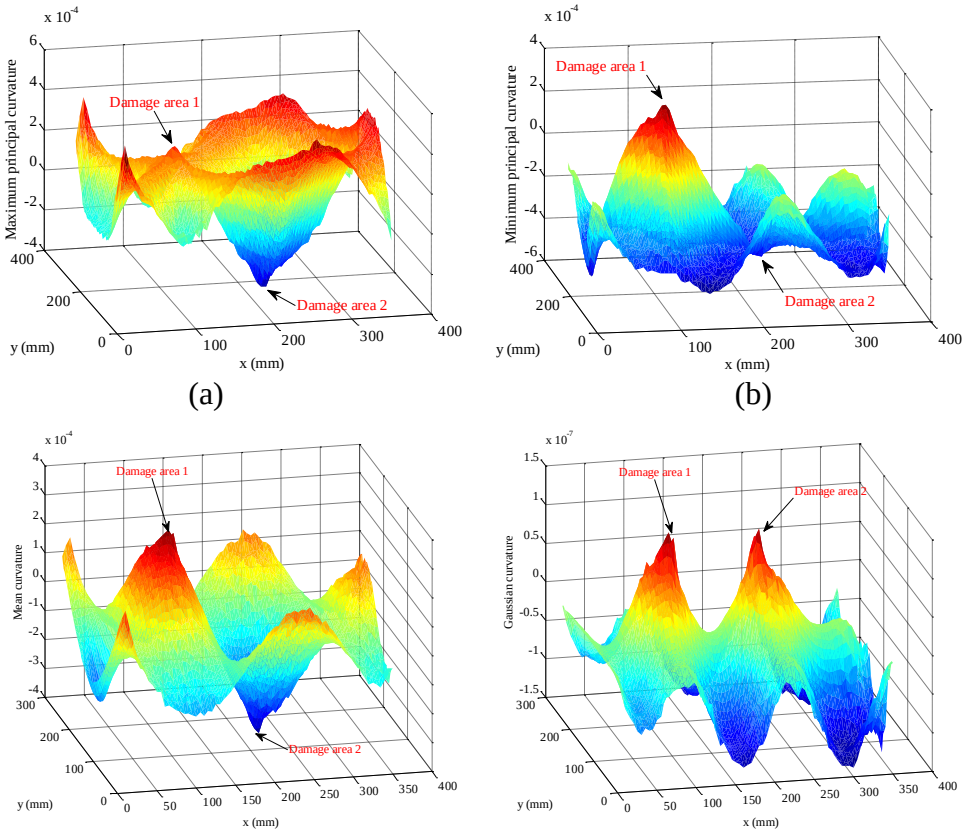

Figure 6.9 Curvatures of the10th mode shape using Eq. (6.17) and Eq. (6.20): (a) Maximum principal curvature (b) Minimum principal curvature (c) Mean principal curvature and (d) Gaussian curvature.

Then, the LPF is utilised to estimate the robust principal, mean principal and Gaussian curvature. Here, only the mean principal and Gaussian curvatures of the 10th mode shape are taken as examples to show the difference between the 2-ring LPF and 3-ring LPF, which are illustrated in Figure 6.10 and Figure 6.11.

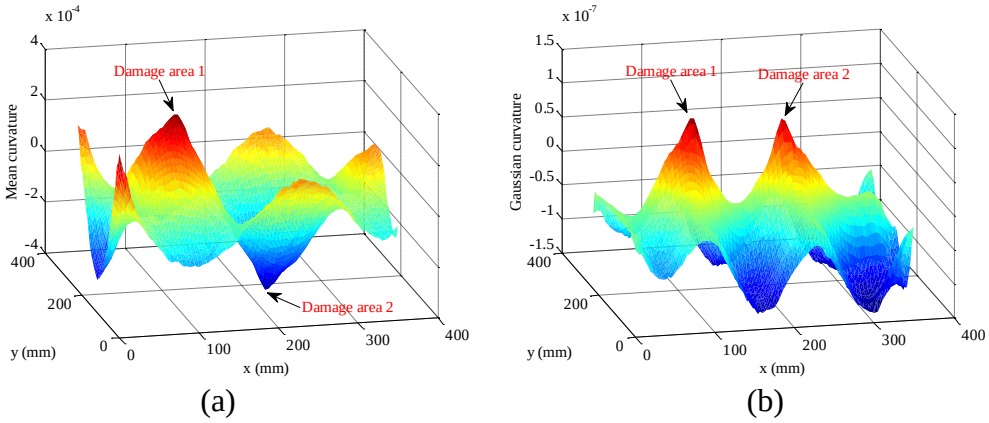

Figure 6.10 Curvatures of the 10th mode shape using 2-ring LPF (a) Mean principal curvature and (b) Gaussian curvature.

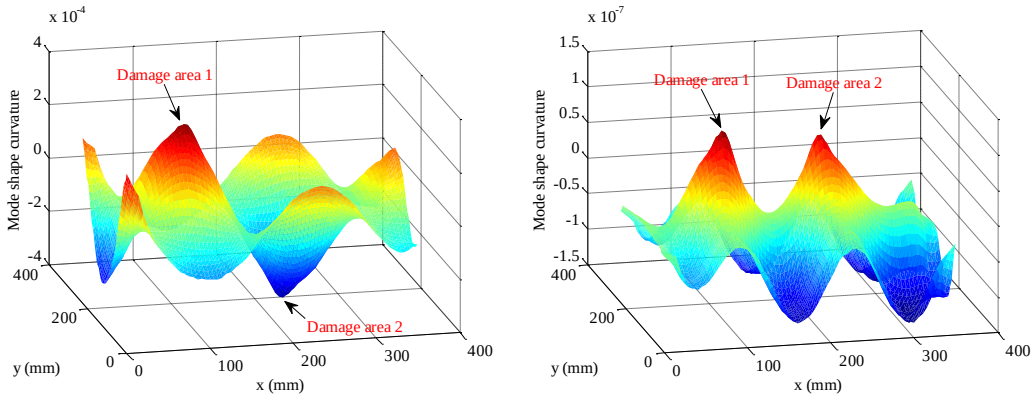

(a) (b)

Figure 6.11 Curvatures of the 10th mode shape using 3-ring LPF (a) Mean principal curvature and (b) Gaussian curvature.

A comparison between Figure 6.10 and Figure 6.11 suggests that the more rings for LPF, the more smooth the estimated mean and Gaussian curvatures, but the less sensitive to the damage singularities. Thus, like choosing the scale parameter σ of multi-scale approaches, the number of rings should be appropriately selected to filter the measurement noise whilst keeping the damage information.

In conclusion, both LPF and LoG methods are effective to reduce the effects of measurement noise during mode shape curvature estimation. But the principal, mean principal and Gaussian curvature estimated by suing LPF deals well with the boundary areas when compared with mean *x*-*y* curvature based on LoG approach,

6.5.3 Damage identification using robust mode shape curvatures

In this section, the damage identification effectiveness of the robust estimated mode shape curvatures is demonstrated with the help of baseline data of healthy plates. Firstly, Gaussian white noise of $n_{\text{level}} = 0.5\%$ (SNR=46.21 dB) is added to pollute the 10th mode shape before curvature estimation. Then, the damage identification results without and with de-noise processing are presented in Figure 6.12 and Figure 6.13, in which the damage index values are evaluated by calculating the absolute curvature difference before and after damage.

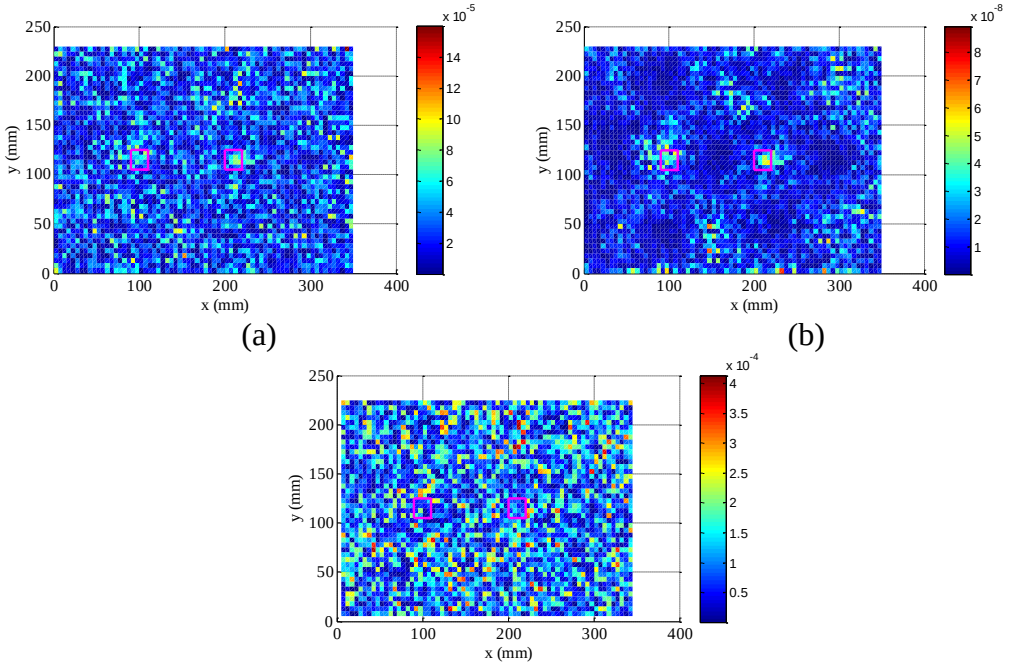

Figure 6.12 Damage identification results without de-noising: (a) Mean principal curvature and (b) Gaussian curvature and (c) Mean *x*-*y* curvature.

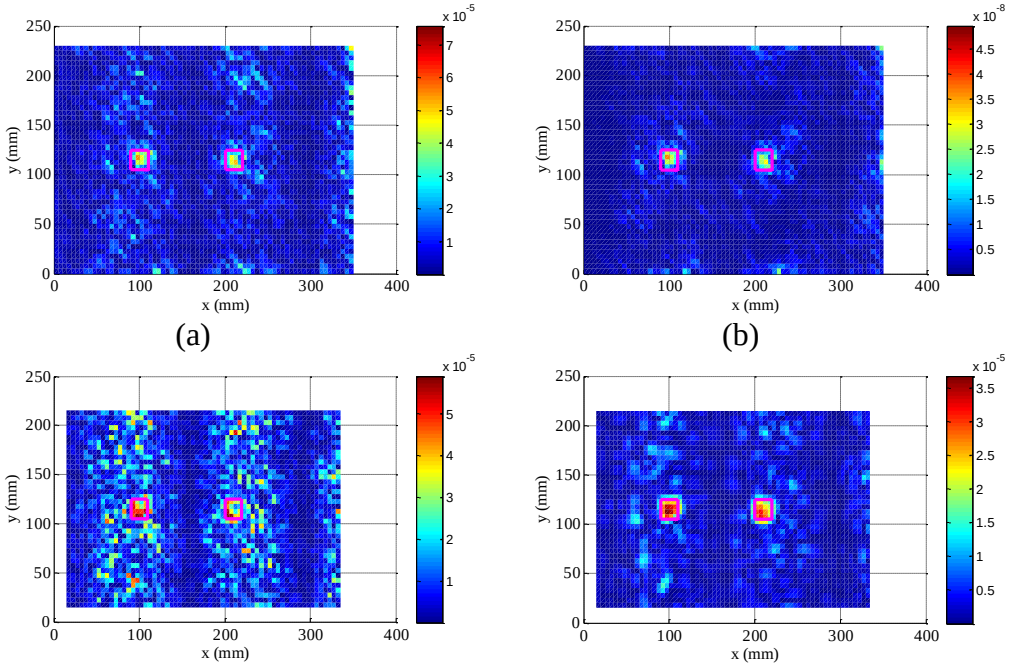

Figure 6.13 Damage identification results: (a) Mean principal curvature of 2-ring LPF (b) Gaussian curvature of 2-ring LPF (c) Mean *x*-*y* curvature of LoG filter with $\sigma = 1$ and (d) Mean *x*-*y* curvature of LoG filter with $\sigma = 1.5$.

Apparently, the estimated mean principal, Gaussian and mean *x-y* curvatures without de-noising are not able to identify the damage as shown in Figure 6.12, while Figure 6.13 provides acceptable damage identification results when proper de-noising techniques are used. Therefore, the robust mode shape curvature estimation is prerequisite for accurate damage identification and LoG and LPF are effective approaches for robust mode shape curvature estimation. In addition, by increasing the scale parameter σ of LoG filter, the damage identification of mean *x-y* curvature is improved, but still a little sensitive to the measurement noise.

6.6 Experimental study

In order to test the two robust mode shape curvature estimation approaches in practical applications, a cantilever aluminium plate with the same physical and geometrical properties as the numerical study in section 6.3.1 is tested. The experimental set-up is illustrated in Figure 6.14.

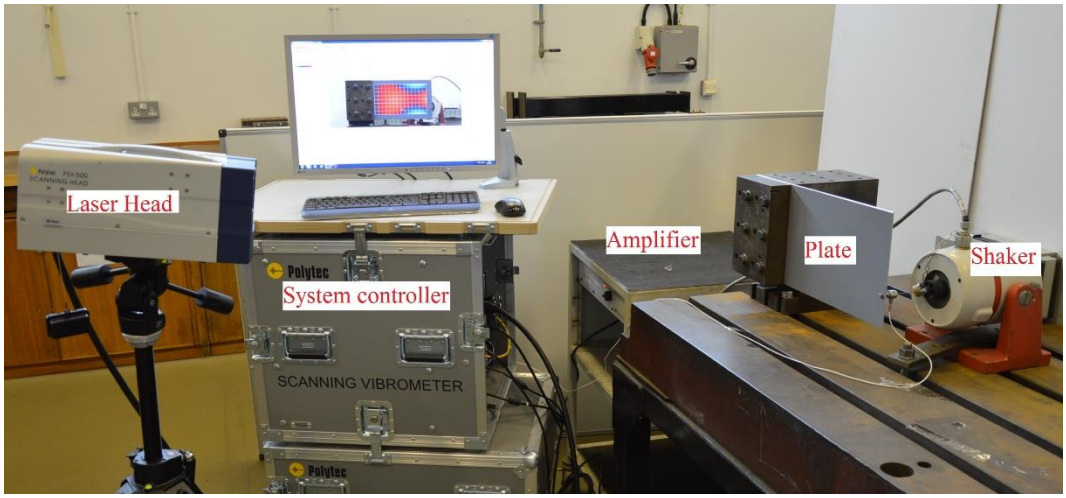

Figure 6.14 Experimental set-up of a cantilever plate

Moreover, the two damage areas marked as two small squares in Figure 6.15 are cut off 10% of their thickness in the opposite side and their position coordinates are given in Figure 6.3. In addition, the plate is clamped on the left and excited by a shaker (LDS V406) as shown in Figure 6.15.

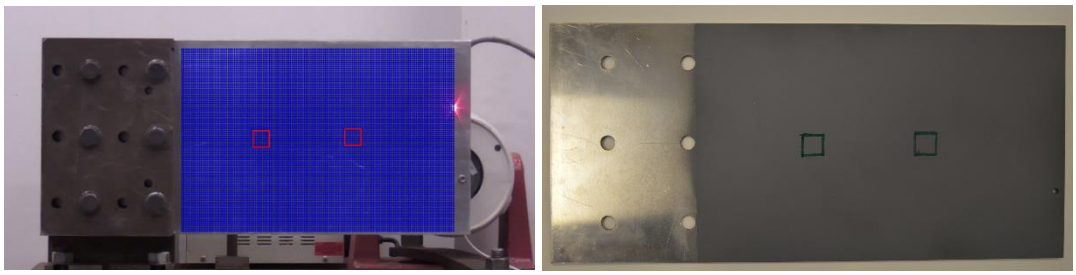

(a) Front surface view (b) Front surface view

Figure 6.15 A cantilever plate with two damage areas.

The vibration responses are measured by a PSV-500 Scanning Laser Vibrometer and the measured zone is slightly smaller than the original plate dimensions to avoid the effects of boundaries, which is $0.326\text{m} \times 0.219\text{m}$ spanning from 0.0084m to 0.3334m in the x direction and 0.0028m to 0.2218m in the y direction. Moreover, there are 141×95 measurement points with grid cell size of $0.00233\text{m} \times 0.00233\text{m}$.

To determine the resonant frequencies of the plate, a pseudo random signal of 0-2000 Hz is used to excite the plate, which is generated by the PSV-500 system. After the resonant frequencies are obtained from the frequency response function, the plate will be excited at a certain resonant frequency to acquire its associated mode shape data. Certainly, the operational deflection shapes at non-resonant frequencies can also be employed for damage identification.

Here, the 10^{th} resonant frequency at 798Hz is used to excite the plate and the velocities of measurement grid are acquired. Furthermore, since there is a single-sine excitation, the 'FastScan' mode of PSV-500 is selected to measure the mode shape due to its fast acquisition efficiency. In the 'FastScan' mode, the specific excitation frequency is 798Hz and the bandwidth of acquisition signal is set as 300Hz. A wider bandwidth can speed-up the measurement, whereas a narrow bandwidth will provide a better signal to noise ratio. For this experiment, 30 averages were used for each measurement point and the total measurement time is around 30 minutes. In addition, 40 and 80 averages were investigated as well but they did not further enhance the measurement accuracy. Figure 6.16 presented the measured 10^{th} mode shape, which is normalised with its values range of [-1, 1].

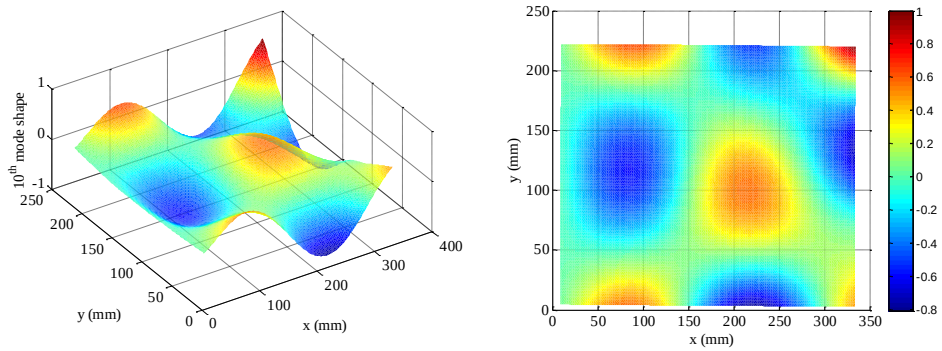

Figure 6.16 The normalised 10th mode shape of experimental plate.

The mean *x-y* curvature, mean principal curvature and Gaussian curvature of the10th mode shape are presented in Figure 6.17.

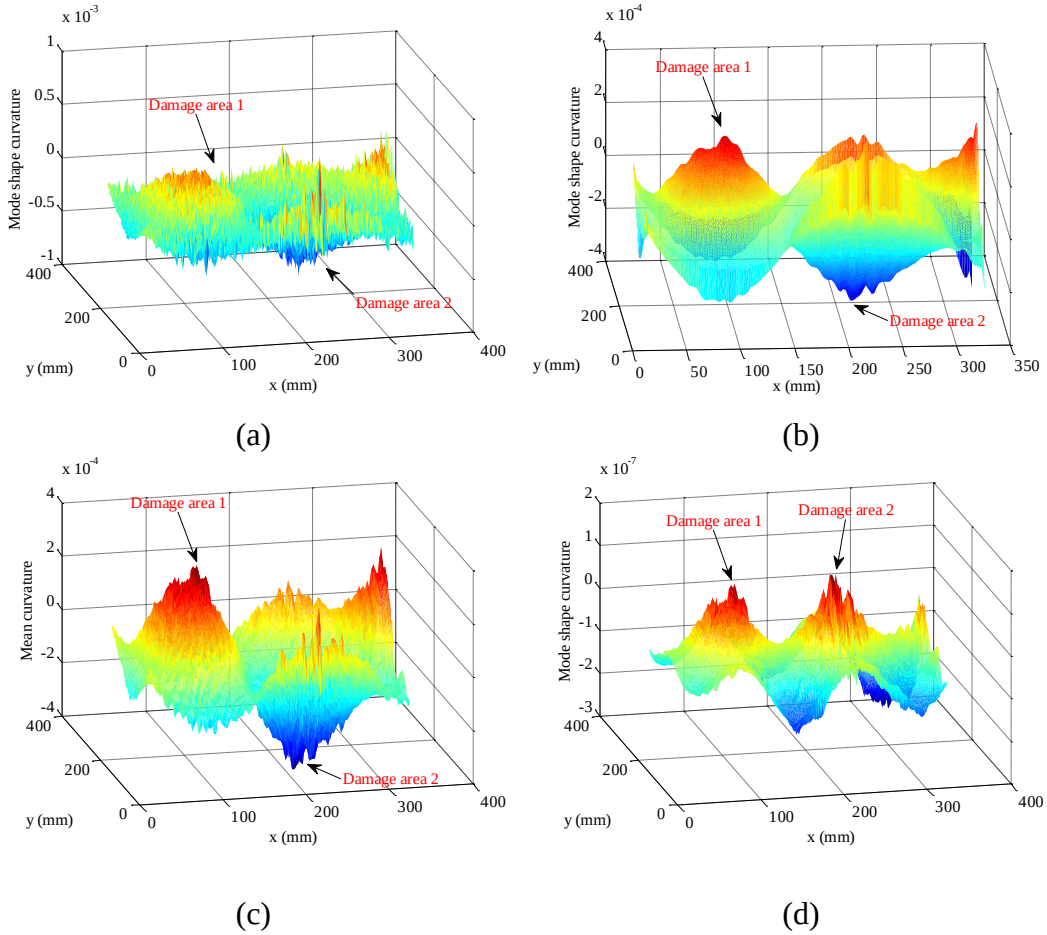

Figure 6.17 (a) Mean *x-y* curvature without de-noising (b) Mean *x-y* curvature of LoG filter with $\sigma = 1.5$ (c) Mean principal curvature of 2-ring LPF (d) Gaussian curvature of 2-ring LPF.

Clearly, without de-noise processing, it is hard to obtain useful information for damage identification as shown Figure 6.17 (a). By applying LoG and LPF approaches, the

estimated curvatures are much smoother. Nevertheless, they are still vulnerably affected by the measurement noise. Fortunately, apart from the scale parameter of LoG and the number of rings of LPF, there is another important parameter that can be adjusted to filter the measurement noise, which is the average distance between successive measurement points.

Thus, in order to further enhance the noise robustness of experimental data, a linear interpolation approach is adopted to increase the average distance of measurement points. Originally, there are 141×95 measurement points covering $326mm \times 219mm$. Now, based on these data, a 80×54 grid is assigned and the mode shape value of each point is evaluated by linear interpolation. For more information, please refer to the 'griddata' function in MATLAB. After linear interpolation of the original data, the three types of curvatures are recalculated and shown in Figure 6.18.

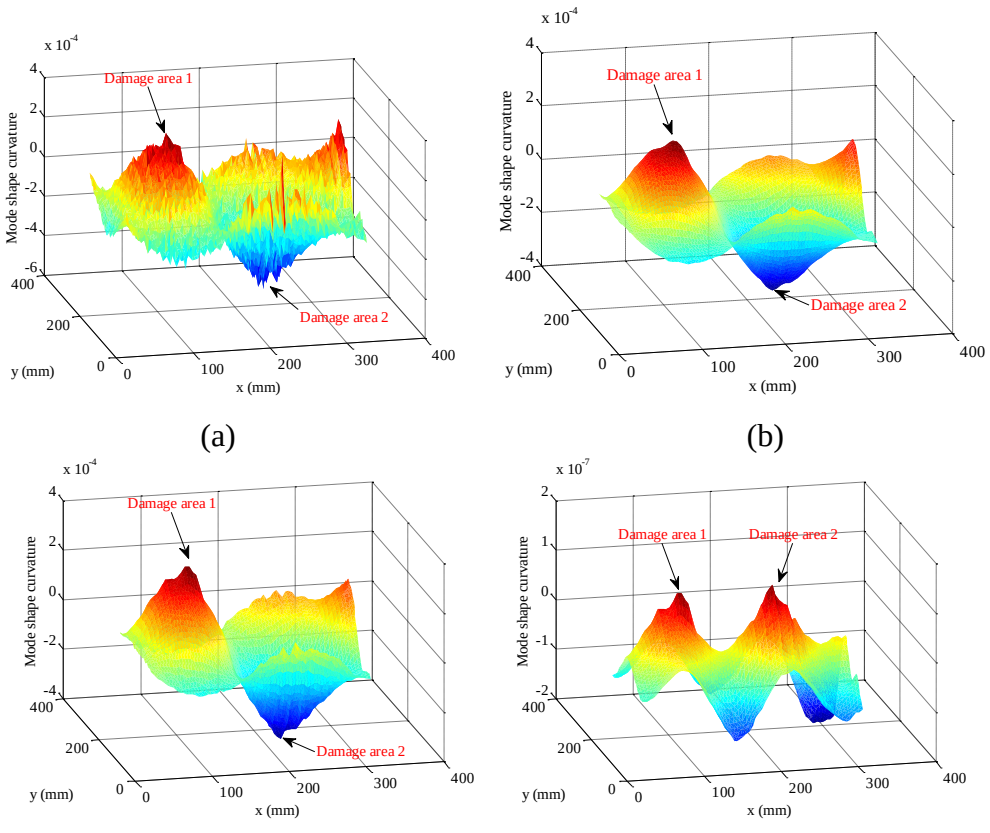

Figure 6.18 (a) Mean *x*-*y* curvature without de-noising. (b) Mean *x*-*y* curvature using LoG filter with $\sigma = 1.5$. (c) Mean principal curvature of 2-ring LPF. (d) Gaussian curvature of 2-ring LPF.

It is apparent that by increasing the average distance, the estimated curvatures are more sensitive to damage and less susceptible to the measurement noise. Moreover, the estimated mean *x*-*y* curvature using LoG filter with $\sigma = 1.5$ is smoother than the mean principal curvature using 2-ring LPF. Thus, the 3-ring LPF is used to estimate the mean curvature and Gaussian curvature of experiment data, which are presented in Figure 6.19.

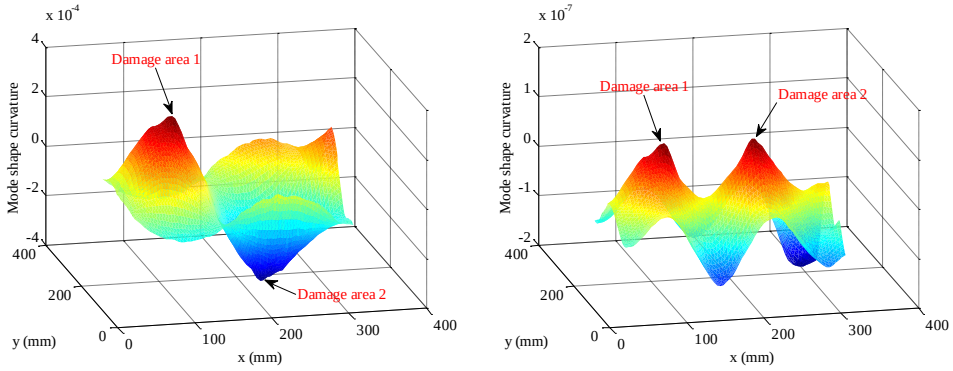

(a) (b)

Figure 6.19 (a) Mean principal curvature using 3-ring LPF and (b) Gaussian curvature using 3-ring LPF.

Now, the estimated mean principal curvature and Gaussian curvature are both more robust to measurement noise. It is obvious that the accuracy of estimated mean principal and Gaussian curvatures are affected by the distance between rings and the number of rings. With different values of these two parameters, the estimated mean principal and Gaussian curvatures have different sensitivities to damage and measurement noise. Moreover, the LoG method guarantees a robust and accurate mode shape curvature along the *x* and *y* directions. Thus, both the LoG and LPF can provide robust mode shape curvature for experiments, which will promise an accurate damage identification.

With the estimated noise robust curvature, the damage localisation can be coarsely determined by the local peaks or sudden change of the curvatures. But for more accurate and efficient damage localisation, a comparison with the curvature of undamaged state is required. However, the mode shape curvature information of healthy structure is usually unavailable. Moreover, a single mode shape is only sensitive to damage at some locations. Therefore, it is necessary to develop a baseline-free damage identification method for multi-damage localisation, which will be studied in the next chapter.

6.7 Conclusions

In this section, the relationship between the mode shape curvature and damage in a plate structure is discussed firstly. Then, the Laplacian of Gaussian is employed to improve the noise robustness for curvatures estimation along *x* and *y* directions. The Laplacian of Gaussian can be implemented by three multi-scale approaches: LoG filter, Mexican hat wavelet transform and difference of Gaussian filter. Thirdly, the principal curvatures, mean principal curvature and Gaussian curvature are studied, which are the intrinsic measures of a surface. Moreover, a local polynomial fitting approach based on the neighbourhood ring points is used to boost the noise robustness and accuracy of principal, mean principal and Gaussian curvatures.

A numerical cantilever aluminium plate with two damage areas is simulated, which also provides the theoretical background of the experimental study. Based on this numerical study, the Laplacian of Gaussian and local polynomial fitting approaches are validated to be effective in dealing with noisy measurement data for robust mode shape curvature estimation. Then, an experiment of a cantilever aluminium plate with two damage areas is tested to validate LoG and LPF in practical curvature estimation. It is concluded that the two methods both perform well in robust mode shape curvature estimation.

Chapter 7

Robust multi-damage identification of plate-type structures

The main purpose of this chapter is to develop a baseline-free multi-damage identification method for plates by examining the damage-induced singularities of mode shape curvatures. For robust multi-damage identification, the damage information of several modes should be combined, as a single mode is only sensitive to damage at some positions. To extract the damage-induced changes, baseline information is usually required.

Without baseline data of the healthy state, two approaches are investigated to construct the mode shape curvatures of healthy structures based on vibration data of damaged structures. The basic idea is that the mode shape curvatures of a mode of a plate in the healthy state are smooth; or, when arranged into a matrix by following the measurement grid, possess a low-rank structure (which means that this is a low-rank matrix). Based on the smoothness principle, surrogate models such as polynomial fitting and Kriging regression are first studied to approximate the mode shape curvature of the healthy state. Then, the low-rank models formed by methods such as principal component analysis and robust principal component analysis (robust PCA) are applied to construct the 2-D mode shape curvature of the healthy state and extract the damage-induced changes.

Moreover, a robust multi-damage index is developed to detect, localise, and quantify the relative severity of damage, which is based on the extracted damage information of several mode shape curvatures. Finally, effectiveness and robustness of the proposed baseline-free multi-damage identification method are validated by numerical and experimental studies.

7.1 Introduction

For non-model-based multi-damage identification methods, damage localisation can be achieved by the examination of damage-induced local shape singularities of mode shape curvatures. If the mode shape curvatures of healthy structures are available, the differences between the mode shape curvatures before and after damage are naturally utilised for damage identification. In the absence of baseline data of healthy structures, the sudden changes of mode shape shapes or curvatures are generally adopted to localise the positions of damage. For this purpose, signal processing methods such as wavelet transform and fractal dimension methods are widely employed to manifest the damage-induced singularities whilst decreasing the misleading results due to measurement noise [128, 139]. But this kind of methods is only based on curvatures of a single mode shape, which is not robust for multi-damage localisation, as a single mode shape is normally sensitive to damage at some locations whereas less sensitive at other locations.

In order to propose a robust multi-damage index without baseline data of healthy structures, the primary task is to extract the damage-induced changes of mode shape curvatures. However, extracting the damage-induced changes require the mode shape curvatures of healthy structures, which are usually not available. To address this, two properties of mode shape curvatures of healthy plate structures are used to construct the mode shape curvatures of the healthy state based on the mode shape curvatures of damaged structures, which are the smoothness and the low-rank of 2-D mode shape curvatures.

Based on the smoothness property, the polynomial fitting or smoothing methods are traditionally applied. Yoon et al. [141] generalised the 1-D gapped smoothing method to 2-D and localised the damage by using the damage-induced inhomogeneity of vibration curvature shapes. This method worked effectively under the condition that the damaged areas were much smaller than the surface area. Xu and Zhu [132] applied global polynomial fitting method to construct the mode shapes of the healthy state based on the mode shapes of the damaged state and then the square of the differences between them was used to indicate the position of damage.

For the 2-D mode shape or mode shape curvature of plates at a certain natural frequency, they are arranged into a matrix by following the measurement grid. Hence,

some matrix processing methods can be extended to damage identification of plates. Without damage, the ranks of 2-D mode shapes or mode shape curvatures are normally low, which means that they can be accurately approximated by using the first several principal components of PCA. The occurrence of damage in the plates will introduce the local singularities, which are revealed by the increasing rank of 2-D mode shapes or mode shape curvatures. Moreover, the damage-induced local singularities can be localised by robust PCA method, also known as principal component pursuit (PCP), which decomposes the 2-D mode shape or mode shape curvature into two components: a low-rank matrix and a sparse matrix. Yang et al. [214] investigated the low-rank modelling for damage identification in plates based on the simulated strain field measurements. The damage detection results showed that it was feasible to localise the damage by using low-resolution strain measurements. In this chapter, robust PCA is investigated for robust multi-damage localisation, especially for incipient damage. Moreover, the extracted sparse matrices form several mode shape curvatures are combined to form a robust multi-damage index.

7.2 Baseline-free multi-damage identification of plates

For plate-type structures, the mode shape and mode shape curvature values associated with a certain natural frequency are form a two dimensional grid and thus are represented as matrices $\boldsymbol{\Phi}_{\mathrm{p}}$ and $\boldsymbol{\Phi}_{\mathrm{p}}''$, respectively. The mode shape curvature $\boldsymbol{\Phi}_{\mathrm{p}}''^{\mathrm{d}}$ of damaged structures can be expressed as a superposition of mode shape curvature $\boldsymbol{\Phi}_{\mathrm{p}}''$ of the healthy state, damage-induced shape change matrix $\boldsymbol{\Theta}$ and noise matrix $\mathbf{E}$.

$$\boldsymbol{\Phi}_{\mathrm{p}}''^{\mathrm{d}} = \boldsymbol{\Phi}_{\mathrm{p}}'' + \boldsymbol{\Theta} + \mathbf{E} \tag{7.1}$$

where $\boldsymbol{\Theta}$ should be a sparse matrix with arbitrary magnitudes of entries, which is essential for damage identification. The 2-D mode shape curvature $\boldsymbol{\Phi}_{\mathrm{p}}''$ in Eq. (7.1) can be the mean *x*-*y* curvature, mean principal curvature or Gaussian curvature presented in Chapter 6.

Moreover, in Eq. (7.1), $\boldsymbol{\Phi}_{\mathrm{p}}''^{\mathrm{d}}$ is obtained directly from experimental data whilst $\boldsymbol{\Phi}_{\mathrm{p}}''$ is normally not available in practical applications. Two approaches are investigated to solve this problem. One is to reconstruct $\boldsymbol{\Phi}_{\mathrm{p}}''$ through $\boldsymbol{\Phi}_{\mathrm{p}}''^{\mathrm{d}}$ based on the assumption that $\boldsymbol{\Phi}_{\mathrm{p}}''$ is as smooth as possible in the healthy state. The other approach is the low-

rank models, which are based on low intrinsic dimensionality of mode shape curvature $\mathbf{\Phi}_{\mathrm{p}}''$ of the healthy state. In fact, these two approaches are also suitable for plate damage identification based on other characteristic deflection shape curvatures.

7.2.1 Construction of $\mathbf{\Phi}_{\mathrm{p}}''$ based on smoothness assumption

In this section, the difference matrix $\Delta\mathbf{\Phi}_{\mathrm{p}}''$ between mode shape curvatures before and after damage is computed as

$$\Delta\mathbf{\Phi}_{\mathrm{p}}'' = \mathbf{\Phi}_{\mathrm{p}}''^{\mathrm{d}} - \widehat{\mathbf{\Phi}}_{\mathrm{p}}'' \tag{7.2}$$

where $\widehat{\mathbf{\Phi}}_{\mathrm{p}}''$ is the estimated mode shape curvatures of the healthy state based on $\mathbf{\Phi}_{\mathrm{p}}''^{\mathrm{d}}$ by surrogate models under the smoothness assumption and $\Delta\mathbf{\Phi}_{\mathrm{p}}''$ being equal to $(\mathbf{\Theta} + \mathbf{E})$.

The general form of approximating any smooth and continuous function can be expressed as a linear combination of basis functions

$$\widehat{\Phi}''(x, y) = \sum_{i=1}^{N_p} c_i \psi^{(i)} \tag{7.3}$$

where N_p indicates the number of terms and ψ denotes the basis function. For example, for polynomial models of order 3 with two variables (x, y), the group of basis functions is $\psi^{(i)} \in \{1, x, y, xy, x^2, y^2, x^2y, xy^2, x^3, y^3\}$. In this case, not only the polynomial order but the coefficients **c** have to be determined for an accurate approximation. Moreover, instead of the above example of multivariable polynomials, the more versatile basis functions such as radial basis functions are investigated based on the Kriging regression model, which usually possess well-known properties.

7.2.1.1 Gapped smoothing method

The 2-D GSM is a local polynomial fitting approach, which is an extension of 1-D GSM method [141]. It is assumed that the mode shape curvature of healthy structures can be approximated by a polynomial function as

$$\widehat{\Phi}''(x, y) = \sum_{j=0}^{p} \sum_{i=0}^{j} c_{i,j-i} x^i y^{j-i} \tag{7.4}$$

For a 2-D grid, three types of measurement points (inner, boundary and corner points) are illustrated in Figure 7.1.

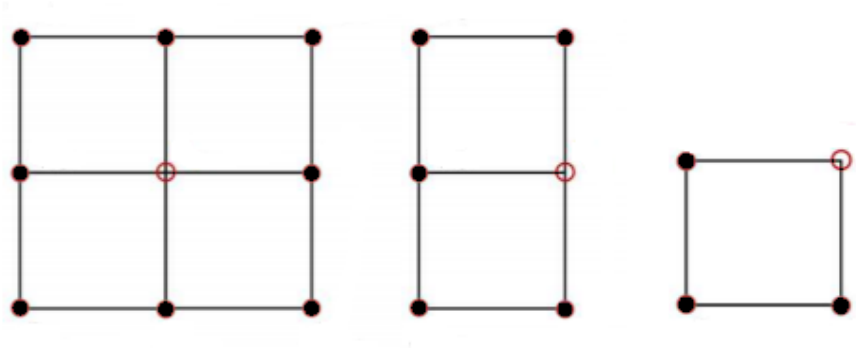

(a) (b) (c)

Figure 7.1 2-D GSM (points in red circles): (a) inner point (b) boundary point (c) corner point.

Due to different locations of the predicted point, there are three cases: (a) for the inner points, there are eight neighbouring points and Eq. (7.4) is written as $\widehat{\Phi}''(x,y) = c_0 + c_1x + c_2y + c_3xy + c_4x^2 + c_5y^2 + c_6xy^2 + c_7x^2y$; (b) for the boundary points in Figure 7.1(b), five adjacent points are available and Eq. (7.4) is expressed as $\widehat{\Phi}''(x,y) = c_0 + c_1x + c_2y + c_3x^2 + c_3y^2$; (c) for the corner points, there are only three neighbouring points and Eq. (7.4) is expressed as $\widehat{\Phi}''(x,y) = c_0 + c_1x + c_2y$. Then, the difference between the fitted value and the original value is calculated according to Eq. (7.2).

The outlier entries of $\Delta\mathbf{\Phi}_{\mathrm{p}}''$ indicates the damage locations. It is obvious that the GSM is implemented at each measurement point using neighbouring points in surface fitting and could be inefficient when the measured points are many and dense. Furthermore, 2-D gapped smoothing method is suitable for point-wise damage types but inefficient for small area damage.

7.2.1.2 Global polynomial fitting method

In this section, the global polynomial fitting technique will be investigated to evaluate the mode shape curvature $\widehat{\mathbf{\Phi}}_{\mathrm{p}}''$ of the healthy state based on the mode shape $\mathbf{\Phi}_{\mathrm{p}}''^{\mathrm{d}}$ of the damaged state. A general form of the polynomial fitting is

$$\widehat{\Phi}''(x,y) = \sum_{j=0}^{p}\sum_{i=0}^{j} c_{i,j-i}x^i y^{j-i} \tag{7.5}$$

Here, p indicates the polynomial order. The problem is to estimate $\mathbf{c} = \left[c_{0,0}, c_{1,0}, \cdots\ c_{i,j-i}, \cdots, c_{p,0}\right]^{\mathrm{T}}$ through the least-squares solution of $\bar{\mathbf{V}}\mathbf{c} = \mathbf{\Phi}_{\mathrm{p}}''^{\mathrm{d}}$, where $\bar{\mathbf{V}}$ is the bivariate Vandermonde matrix:

$$\bar{\mathbf{V}} = \begin{bmatrix} 1 & y_1 & x_1 & \cdots & {x_1}^i {y_1}^{j-i} & \cdots & x_1^p \\ 1 & y_2 & x_2 & \cdots & {x_2}^i {y_2}^{j-i} & \cdots & x_2^p \\ \cdots & \cdots & \cdots & \ddots & \cdots & \cdots & \cdots \\ 1 & y_{N_\mathrm{m}} & x_{N_\mathrm{m}} & \cdots & {x_{N_\mathrm{m}}}^i {y_{N_\mathrm{m}}}^{j-i} & \cdots & x_{N_\mathrm{m}}^p \end{bmatrix} \tag{7.6}$$

The maximum likelihood estimate of $\mathbf{c}$ is

$$\hat{\mathbf{c}} = \bar{\mathbf{V}}^{+} {\boldsymbol{\Phi}_\mathrm{p}''}^{\mathrm{d}} \tag{7.7}$$

where $\bar{\mathbf{V}}^{+} = (\bar{\mathbf{V}}^{\mathrm{T}}\bar{\mathbf{V}})^{-1}\bar{\mathbf{V}}^{\mathrm{T}}$ is the Moore-Penrose pseudo-inverse of $\bar{\mathbf{V}}$**.** Equation (7.7) presents a possible approach to estimate $\mathbf{c}$ but the crucial problem here is to determine the polynomial order p in order to provide a good estimation of mode shape curvature $\widehat{\boldsymbol{\Phi}}_\mathrm{p}''$ of the undamaged state. A possible rule is to determine the minimum polynomial order p satisfying

$$\frac{\mathrm{std}\left({\boldsymbol{\Phi}_\mathrm{p}''}^{\mathrm{d}} - \widehat{\boldsymbol{\Phi}}_\mathrm{p}''\right)}{\mathrm{std}\left({\boldsymbol{\Phi}_\mathrm{p}''}^{\mathrm{d}}\right)} \leq 0.05 \tag{7.8}$$

When the polynomial order p is large, the bivariate Vandermonde matrix $\bar{\mathbf{V}}$ can be ill-conditioned, which can lead to an inaccurate polynomial fit. To alleviate the ill-condition of $\bar{\mathbf{V}}$, it is proposed to normalise $\bar{\mathbf{V}} = \left[\bar{\mathbf{v}}_1, \bar{\mathbf{v}}_2 \cdots, \bar{\mathbf{v}}_{N_p}\right]$ by Gram-Schmidt orthogonalisation approach, where $N_p = (p+2)(p+1)/2$ is the total number of polynomial terms. First, the projection of $\mathbf{v}_i$ on $\mathbf{v}_j$ is defined as

$$\mathrm{Proj}_{\bar{\mathbf{v}}_j}(\bar{\mathbf{v}}_i) = \frac{{\bar{\mathbf{v}}_j}^{\mathrm{T}}\bar{\mathbf{v}}_i}{{\bar{\mathbf{v}}_j}^{\mathrm{T}}\bar{\mathbf{v}}_j}\bar{\mathbf{v}}_j \tag{7.9}$$

Then, the formula of Gram-Schmidt orthogonalisation is

$$\tilde{\mathbf{v}}_i = \frac{\mathbf{v}_i - \sum_{j=1}^{i-1} \mathrm{Proj}_{\bar{\mathbf{v}}_j}(\bar{\mathbf{v}}_i)}{\left\|\mathbf{v}_i - \sum_{j=1}^{i-1} \mathrm{Proj}_{\bar{\mathbf{v}}_j}(\bar{\mathbf{v}}_i)\right\|} \tag{7.10}$$

The normalised bivariate Vandermonde matrix is $\tilde{\mathbf{V}} = \left[\tilde{\mathbf{v}}_1, \tilde{\mathbf{v}}_2 \cdots, \tilde{\mathbf{v}}_{N_p}\right]$. Then, $\tilde{\mathbf{V}}$ is substituted into Eq. (7.7) to calculate the accurate polynomial coefficients $\hat{\mathbf{c}}$ and the smoothed mode shape curvature is determined as $\widehat{\boldsymbol{\Phi}}_\mathrm{p}'' = \tilde{\mathbf{V}}\hat{\mathbf{c}}$. After this, Eq. (7.8) is used to check if the approximation of mode shape curvature $\widehat{\boldsymbol{\Phi}}_\mathrm{p}''$ reaches the defined threshold of ${\boldsymbol{\Phi}_\mathrm{p}''}^{\mathrm{d}}$. If not, the polynomial order p is increased by 1 to recalculate $\widehat{\boldsymbol{\Phi}}_\mathrm{p}''$ until Eq. (7.8) is satisfied.

7.2.1.3 Kriging regression method

Kriging model plays a significant role in surrogate model and surrogate based optimisation, which evaluates the values of un-sampled points based on a stochastic model. The mathematical derivation of Kriging prediction was presented in [215]. Here, the main purpose is to illustrate the application of Kriging regression to estimate $\widehat{\boldsymbol{\Phi}}_{\mathrm{p}}''$.

Given a set of sampled surface locations $\mathbf{X} = \left\{\mathbf{x}^{(1)}, \mathbf{x}^{(2)}, \cdots, \mathbf{x}^{(N_{\mathrm{m}})}\right\}^{\mathrm{T}}$ (where $\mathbf{x}^{(i)} = (i\ , y_i)$ indicates the position of *i*-th sample) and their associated mode shape curvature values $\boldsymbol{\varphi}'' = \left\{\varphi''^{(1)}, \varphi''^{(2)}, \cdots, \varphi''^{(N_{\mathrm{m}})}\right\}^{\mathrm{T}}$ at a certain natural frequency, the purpose is to obtain the expression for a predicted modal curvature value at a new point. The observed mode shape curvature values are considered from a stochastic process in the theoretical model but this is not necessary in practical applications [216]. The likelihood of acquiring these mode shape curvature values is

$$L(\boldsymbol{\varphi}''|\mu, \sigma) = \frac{1}{(2\pi\sigma^2)^{N_{\mathrm{m}}/2}|\boldsymbol{\Psi}|^{1/2}} \exp\left(-\frac{(\boldsymbol{\varphi}''-\mathbf{1}\mu)^{\mathrm{T}}\boldsymbol{\Psi}^{-1}(\boldsymbol{\varphi}''-\mathbf{1}\mu)}{2\sigma^2}\right) \tag{7.11}$$

where μ and σ denote the mean value and the standard deviation of the Gaussian process and $\mathbf{1}$ is an $N_{\mathrm{m}} \times 1$ column vector of ones. $|\boldsymbol{\Psi}|$ denotes the determinant of $\boldsymbol{\Psi}$ and $\boldsymbol{\Psi}$ indicates the correlation matrix of the sampling points, which is written as

$$\boldsymbol{\Psi} = \begin{bmatrix} \mathrm{cor}\left[\varphi''\left(\mathbf{x}^{(1)}\right), \varphi''\left(\mathbf{x}^{(1)}\right)\right] & \cdots & \mathrm{cor}\left[\varphi''\left(\mathbf{x}^{(1)}\right), \varphi''\left(\mathbf{x}^{(N_{\mathrm{m}})}\right)\right] \\ \vdots & \ddots & \vdots \\ \mathrm{cor}\left[\varphi''\left(\mathbf{x}^{(N_{\mathrm{m}})}\right), \varphi''\left(\mathbf{x}^{(1)}\right)\right] & \cdots & \mathrm{cor}\left[\varphi''\left(\mathbf{x}^{(N_{\mathrm{m}})}\right), \varphi''\left(\mathbf{x}^{(N_{\mathrm{m}})}\right)\right] \end{bmatrix} \tag{7.12}$$

where $\mathrm{cor}\left[\varphi''\left(\mathbf{x}^{(i)}\right), \varphi''\left(\mathbf{x}^{(j)}\right)\right] = \exp\left(-\sum_{k=1}^{d} \theta_k \left|x_k^{(i)} - x_k^{(j)}\right|^{p_k}\right)$ is the basis function $\psi\left(\mathbf{x}^{(i)}, \mathbf{x}^{(j)}\right)$ correlating the random variables with each other. In the basis functions, d indicates the number of dimensions such as $d = 2$ for $\mathbf{x}^{(i)} = (x_i\ , y_i)$. Here, the relation between correlation matrix and covariance matrix is $\mathrm{cov}(\boldsymbol{\varphi}'', \boldsymbol{\varphi}'') = \sigma^2\boldsymbol{\Psi}$. Furthermore, it is clear that the basis function is determined by the absolute distance between sample points $\left|x_k^{(i)} - x_k^{(j)}\right|$, parameter θ_k and parameter p_k.

However, the measured mode shape curvature data $\boldsymbol{\varphi}'' = \left\{\varphi''^{(1)}, \varphi''^{(2)}, \cdots, \varphi''^{(N_{\mathrm{m}})}\right\}^{\mathrm{T}}$, are always corrupted by measurement noise, which may yield an overfitting model

with poor predictions. To resolve this problem, a common approach of modelling the noise is via adding a regularisation parameter η to the diagonal entries of correlation matrix as $\boldsymbol{\Psi}+\eta\mathbf{I}$ ($\mathbf{I}$ is an $N_\mathrm{m}\times N_\mathrm{m}$ identity matrix). Moreover, the regularisation parameter η is possible to take into account the damage-induced changes in mode shape data. Therefore, it enhances the recovery of the mode shapes of undamaged structures based on the mode shapes of the damaged structures.

By adding the regularisation parameter η, the likelihood of acquiring these mode shape curvature values is rewritten as

$$L(\boldsymbol{\varphi}''|\mu,\sigma)=\frac{1}{(2\pi\sigma^2)^{N_\mathrm{m}/2}|\boldsymbol{\Psi}+\eta\mathbf{I}|^{1/2}}\exp\left(-\frac{(\boldsymbol{\varphi}''-\mathbf{1}\mu)^\mathrm{T}(\boldsymbol{\Psi}+\eta\mathbf{I})^{-1}(\boldsymbol{\varphi}''-\mathbf{1}\mu)}{2\sigma^2}\right) \tag{7.13}$$

By taking the derivatives of μ and σ in Eq. (7.14) and setting them to zero, the maximum likelihood of μ and σ are estimated as

$$\begin{aligned}\hat{\mu}&=\frac{\mathbf{1}^\mathrm{T}(\boldsymbol{\Psi}+\eta\mathbf{I})^{-1}\boldsymbol{\varphi}''}{\mathbf{1}^\mathrm{T}(\boldsymbol{\Psi}+\eta\mathbf{I})^{-1}\mathbf{1}}\\ \hat{\sigma}^2&=\frac{(\boldsymbol{\varphi}''-\mathbf{1}\mu)^\mathrm{T}(\boldsymbol{\Psi}+\eta\mathbf{I})^{-1}(\boldsymbol{\varphi}''-\mathbf{1}\mu)}{N_\mathrm{m}}\end{aligned} \tag{7.14}$$

Substituting Eq. (7.14) into Eq. (7.13) and removing the constant terms, the *ln-likelihood* function is simplified as

$$\ln(L)\approx-\frac{N_\mathrm{m}}{2}\ln(\hat{\sigma}^2)-\frac{1}{2}\ln|(\boldsymbol{\Psi}+\eta\mathbf{I})| \tag{7.15}$$

The value of Eq. (7.15) depends on the unknown parameters $\boldsymbol{\theta}$, $\mathbf{p}$ and η. A global optimisation method termed as Genetic Algorithm is used to evaluate their optimum values [216]. Then, the identified values of $\hat{\mu}$, $\hat{\sigma}^2$,$\boldsymbol{\theta}$, $\mathbf{p}$ and η are used to determine $\hat{\boldsymbol{\Phi}}_\mathrm{p}''$ of the undamaged structures.

The prediction of regressing Kriging prediction is

$$\hat{\varphi}''(\mathbf{x}^*)=\hat{\mu}+\boldsymbol{\psi}^\mathrm{T}(\boldsymbol{\Psi}+\eta\mathbf{I})^{-1}(\boldsymbol{\varphi}''-\mathbf{1}\mu) \tag{7.16}$$

where $\boldsymbol{\psi}$ is the correlation between the untried point $\mathbf{x}^*$ and the sample points $\mathbf{x}^{(i)}$:

$$\boldsymbol{\psi}=\left[\psi\left(\mathbf{x}^*,\mathbf{x}^{(1)}\right),\psi\left(\mathbf{x}^*,\mathbf{x}^{(2)}\right),\cdots,\psi\left(\mathbf{x}^*,\mathbf{x}^{(N_\mathrm{m})}\right)\right] \tag{7.17}$$

7.2.2 Low-rank models for damage identification

Low-rank modelling refers to a group of methods that solve problems by using low-rank properties of the original data. For instance, principal component analysis is a well-known low-rank approach, which approximates the original dataset by a low-rank matrix. Moreover, matrix completion and robust PCA are powerful approaches for low-rank matrix recovery. Matrix completion is normally used to recover a matrix based on a small number of observed entries, which could be applied to recover the missing data in experiments. Robust PCA can recover a low-dimensional subspace from grossly corrupted data whilst the traditional PCA is vulnerably affected by the gross errors in the original dataset.

7.2.2.1 Principal component analysis

Principal component analysis is a multivariate statistical approach and widely used for subspace analysis and low-rank approximation. The problem of decomposing $\boldsymbol{\Phi}_{\mathrm{p}}^{\prime\prime\mathrm{d}}$ into a low-rank matrix $\mathbf{L}$ and a small perturbation matrix $\boldsymbol{\mathcal{S}}$ is expressed as

$$\begin{gathered}\boldsymbol{\Phi}_{\mathrm{p}}^{\prime\prime\mathrm{d}} = \mathbf{L} + \boldsymbol{\mathcal{S}} \\ \text{minimise } \left\|\boldsymbol{\Phi}_{\mathrm{p}}^{\prime\prime\mathrm{d}} - \mathbf{L}\right\| \quad \text{subject to } \mathrm{rank}(\mathbf{L}) \leq k\end{gathered} \tag{7.18}$$

where $\mathbf{L}$ can be an estimation of mode shape curvature $\boldsymbol{\Phi}_{\mathrm{p}}^{\prime\prime}$ of the heathy state and $\boldsymbol{\mathcal{S}}$ consists of damage information $\boldsymbol{\Theta}$ and measurement noise $\mathbf{E}$. Equation (7.18) can be efficiently solved via singular value decomposition. The singular value decomposition of $\boldsymbol{\Phi}_{\mathrm{p}}^{\prime\prime\mathrm{d}} \in \mathbb{R}^{n_1 \times n_2} (n_1 \geq n_2)$ is written as

$$\boldsymbol{\Phi}_{\mathrm{p}}^{\prime\prime\mathrm{d}} = \mathbf{U}\boldsymbol{\Sigma}\mathbf{V}^{\mathrm{T}} \tag{7.19}$$

In which, $\mathbf{U} = \left[\mathbf{u}_1, \mathbf{u}_2, \cdots, \mathbf{u}_{n_1}\right] \in \mathbb{R}^{n_1 \times n_1}$ and $\mathbf{V} = \left[\mathbf{v}_1, \mathbf{v}_2, \cdots, \mathbf{v}_{n_2}\right] \in \mathbb{R}^{n_2 \times n_2}$ are orthogonal matrices, respectively and $\boldsymbol{\Sigma} \in \mathbb{R}^{n_1 \times n_2}$ is a non-negative rectangular diagonal matrix with top n_2 rows containing singular values in a descending order: $\lambda_1 \geq \lambda_2 \geq \cdots \geq \lambda_{n_2} \geq 0$ and all zero for the other $(n_1 - n_2)$ rows.

Firstly, the singular values of $\boldsymbol{\Phi}_{\mathrm{p}}^{\prime\prime\mathrm{d}}$ can be used to indicate the existence of damage. The basic idea of applying PCA for damage identification is that the mode shape curvature of healthy structures could be approximated by the first several principal components while the damage increases the active principal components or rank of

mode shape curvature matrix. Figure 7.2 shows the singular value plot of a plate in the cases of no damage and two damage areas of different damage severities. It indicates that there will be more large singular values by increasing the damage severity.

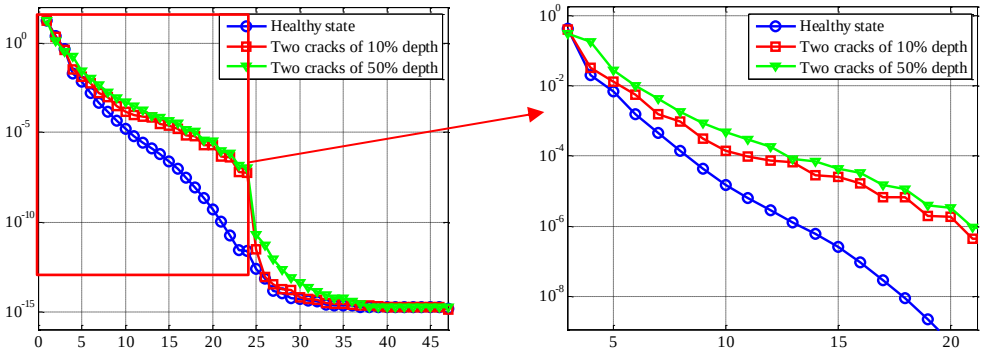

(a) (b)

Figure 7.2 Singular values of the 10th mode shape of a plate without damage and with two damage areas of different depths.

Secondly, it is possible to localise damage using matrix $\boldsymbol{S}$. The approximation of $\boldsymbol{\Phi}_{\mathrm{p}}''$ can be obtained by using the first several singular values $k(k < n_2)$ and singular vectors.

$$\widehat{\boldsymbol{\Phi}}_{\mathrm{p}}'' = \mathbf{L} = \mathbf{U}\widetilde{\boldsymbol{\Sigma}}\mathbf{V}^{\mathrm{T}};\ \widetilde{\boldsymbol{\Sigma}} = \mathrm{diag}[\lambda_1, \lambda_2, \cdots, \lambda_k, 0, 0, \cdots, 0] \tag{7.20}$$

where the diagonal entries of $\widetilde{\boldsymbol{\Sigma}}$ are comprised of the first k singular values and zeros for the others. Thus, matrix $\boldsymbol{S}$ is determined as

$$\boldsymbol{S} = \boldsymbol{\Phi}_{\mathrm{p}}''^{\,\mathrm{d}} - \widehat{\boldsymbol{\Phi}}_{\mathrm{p}}'' \tag{7.21}$$

In the process of calculating $\widehat{\boldsymbol{\Phi}}''$, any grossly corrupted (outlier) entries in $\boldsymbol{\Phi}_{\mathrm{p}}''^{\,\mathrm{d}}$ could cause the estimation of $\widehat{\boldsymbol{\Phi}}_{\mathrm{p}}''$ arbitrarily far from the true $\boldsymbol{\Phi}_{\mathrm{p}}''$ [217]. However, it is common to have grossly corrupted entries in $\boldsymbol{\Phi}_{\mathrm{p}}''^{\mathrm{d}}$, which are caused by damage or measurement noise. In order to improve the damage localisation accuracy, robust principal component analysis is studied for damage localisation.

7.2.2.2 Robust principal component analysis

Robust principal component analysis aims to estimate the low-rank $\mathbf{L}$ based on the grossly corrupted $\boldsymbol{\Phi}_{\mathrm{p}}''^{\mathrm{d}}$. The decomposition of $\boldsymbol{\Phi}_{\mathrm{p}}''^{\mathrm{d}}$ into a low-rank matrix plus a sparse component $\boldsymbol{S}$ can be achieved by several approaches such as principal

component pursuit (PCP), outlier pursuit and iteratively reweighted least-squares [16]. According to PCP, the problem is expressed as

$$\begin{gathered} \boldsymbol{\Phi}_{\mathrm{p}}^{\prime\prime \mathrm{d}}=\mathbf{L}+\boldsymbol{\mathcal{S}} \\ \text{minimise } \|\mathbf{L}\|_{*}+\xi\|\boldsymbol{\mathcal{S}}\|_{1} \quad \text{subject to } \mathbf{L}+\boldsymbol{\mathcal{S}}=\boldsymbol{\Phi}_{\mathrm{p}}^{\prime\prime \mathrm{d}} \end{gathered} \tag{7.22}$$

where $\xi > 0$ is an arbitrary balance parameter, $\|\mathbf{L}\|_{*}=\sum_{i} \lambda_{i}(\mathbf{L})$ represents the nuclear norm of matrix $\mathbf{L}$ (which is the ℓ_1 norm of singular values) and $\|\boldsymbol{\mathcal{S}}\|_{1}=\sum_{ij}\left|\mathcal{S}_{ij}\right|$ denotes the ℓ_1 norm of matrix $\boldsymbol{\mathcal{S}}$. For damage identification, it is clear that $\mathbf{L}$ corresponds to the mode shape $\boldsymbol{\Phi}_{\mathrm{p}}^{\prime\prime}$ of the healthy state whereas $\boldsymbol{\mathcal{S}}$ corresponds to damage-induced component $\boldsymbol{\Theta}$ as illustrated in Eq. (7.1). Moreover, the plot of $\|\boldsymbol{\mathcal{S}}\|_{1}$ under various damage scenarios is possible to indicate the relative damage severities. In Eq. (7.22), the minimisation of $\|\mathbf{L}\|_{*}$ and $\|\boldsymbol{\mathcal{S}}\|_{1}$ implies that $\mathbf{L}$ is approximated by a low-rank subspace whilst the damage-caused mode shape curvature changes constitute the correlated sparse outliers which are contained in $\boldsymbol{\mathcal{S}}$. If rank($\mathbf{L}$) is too high, $\mathbf{L}$ will incorporate the damage features in its representation. If rank($\mathbf{L}$) is too low, some mode shape curvature features will appear in $\boldsymbol{\mathcal{S}}$, which corrupts or misleads the damage identification results. In this case, the balance parameter ξ should be chosen appropriately to well separate the low-rank and sparse matrices.

For practical applications, $\boldsymbol{\Phi}_{\mathrm{p}}^{\prime\prime \mathrm{d}}$ is often contaminated by measurement noise, which can be stochastic or deterministic. Therefore, the entry-wise noise of $\boldsymbol{\Phi}_{\mathrm{p}}^{\prime\prime \mathrm{d}}$ must be taken into account to guarantee a robust and accurate solution of $\boldsymbol{\mathcal{S}}$. The new PCP considering the noise effects is modelled as

$$\begin{gathered} \boldsymbol{\Phi}_{\mathrm{p}}^{\prime\prime \mathrm{d}}=\mathbf{L}+\boldsymbol{\mathcal{S}}+\mathbf{E} \\ \text{minimise } \|\mathbf{L}\|_{*}+\xi\|\boldsymbol{\mathcal{S}}\|_{1} \quad \text{subject to } \left\|\boldsymbol{\Phi}_{\mathrm{p}}^{\prime\prime \mathrm{d}}-\mathbf{L}-\boldsymbol{\mathcal{S}}\right\| \leq \epsilon \end{gathered} \tag{7.23}$$

where the constraint in Eq. (7.22) is relaxed as $\left\|\boldsymbol{\Phi}_{\mathrm{p}}^{\prime\prime \mathrm{d}}-\mathbf{L}-\boldsymbol{\mathcal{S}}\right\| \leq \epsilon$ ($\epsilon > 0$) and ξ is chosen as $1/\sqrt{\max(n_1, n_2)}$ [218]. This PCP problem can be addressed efficiently by convex optimisation algorithms and encouraging performance has been demonstrated on face images and background modelling [219].

The challenging problem of applying robust PCA for damage identification is that robust PCA is normally used in the pixel domain based on images or videos. But the

mode shape curvature $\mathbf{\Phi}_{\mathrm{p}}^{\prime\prime\mathrm{d}}$ of plates in this study is acquired from discrete measurement points by Scanning Laser Vibrometer. Moreover, the spatial resolution of measurements points is much lower than an image, which increases the difficulties of applying robust PCA. Thus, the effectiveness and feasibility of applying robust PCA for damage identification based on discrete mode shapes are unknown. According to the published papers, this problem has not been studied before.

7.3 Robust multi-damage index

With the estimated mode shape curvature $\widehat{\mathbf{\Phi}}_{\mathrm{p}}^{\prime\prime}$ of the healthy state, the difference with the original value $\mathbf{\Phi}_{\mathrm{p}}^{\prime\prime\mathrm{d}}$ is

$$\Delta\mathbf{\Phi}_{\mathrm{p}}^{\prime\prime} = \mathbf{\Phi}_{\mathrm{p}}^{\prime\prime\mathbf{d}} - \widehat{\mathbf{\Phi}}_{\mathrm{p}}^{\prime\prime} \text{ or } \Delta\mathbf{\Phi}_{\mathrm{p}}^{\prime\prime} = \mathbf{\Phi}_{\mathrm{p}}^{\prime\prime\mathrm{d}} - \widehat{\mathbf{\Phi}}_{\mathrm{p}}^{\prime\prime} - \mathbf{E} \tag{7.24}$$

Here, $\Delta\mathbf{\Phi}_{\mathrm{p}}^{\prime\prime}$ contains the information of damage locations. But $\Delta\mathbf{\Phi}_{\mathrm{p}}^{\prime\prime}$ can present values where there is no damage. Thus, a robust multi-damage index is proposed based on a statistical criteria. First, the value $\Delta\Phi_{\mathrm{p}}^{\prime\prime}(x_l, y_l)$ (l indicates the measurement point) associated with each measurement point is regarded as a random value realisation.

Then, the normalised mode shape curvature difference is defined as

$$Z(x_l, y_l) = \left(\Delta\Phi_{\mathrm{p}}^{\prime\prime}(x_l, y_l) - u_{\Delta\mathbf{\Phi}_{\mathrm{p}}^{\prime\prime}}\right) / \sigma_{\Delta\mathbf{\Phi}_{\mathrm{p}}^{\prime\prime}} \tag{7.25}$$

where $u_{\Delta\mathbf{\Phi}_{\mathrm{p}}^{\prime\prime}}$ and $\sigma_{\Delta\mathbf{\Phi}_{\mathrm{p}}^{\prime\prime}}$ denote the mean and standard deviation of the mode shape curvature differences of $\Delta\mathbf{\Phi}_{\mathrm{p}}^{\prime\prime}$. Here, the outlier values of $\mathbf{Z}$ (large positive or negative values) indicate the damage locations, which are located in the two tail areas of normal distribution as shown in Figure 7.3.

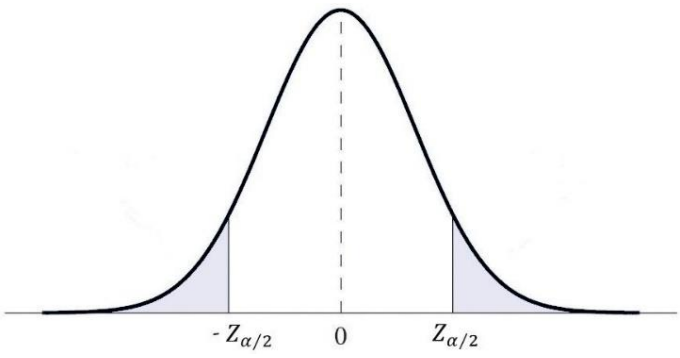

Figure 7.3 Tail probability of normal distribution.

From Figure 7.3, the damage localisation can be expressed as a decision regarding the likelihood. The null hypothesis (H_0) is that the damage does not occur at the l-th measurement point and its alternative hypothesis H_1 states that the damage occurs at the l-th measurement point. Thus, the damage localisation is to determine the confidence probability to accept H_1 or reject H_0 [220].

Simply, a threshold value $Z_{\alpha/2}$ (α represents the percentile) can be selected and the damage locations are determined as

$$|Z(x_l, y_l)| \geq Z_{\alpha/2} \tag{7.26}$$

In which, $\alpha = 0.05$ is used in this thesis and then the threshold $Z_{\alpha/2} = 2.8070$. For $|Z(x_l, y_l)| < Z_{\alpha/2}$, there is no damage and the associated Z_l is set as zero. Thus, for a certain mode shape, the updated mode shape curvature difference is

$$\tilde{Z}(x_l, y_l) = \begin{cases} |Z(x_l, y_l)|, |Z(x_l, y_l)| \geq Z_{\alpha/2} \\ 0, |Z(x_l, y_l)| < Z_{\alpha/2} \end{cases} \tag{7.27}$$

For the curvatures of N_r modes, the multi-damage index is defined as

$$DI_l = \frac{1}{N_\mathrm{r}} \sum_{r=1}^{N_\mathrm{r}} \tilde{Z}_r(x_l, y_l) \tag{7.28}$$

7.4 Numerical studies

The purposes of this section are trifold. First, the performance of the presented damage information extraction methods are illustrated based on a single mode shape. Then, a combination of several mode shapes for robust multi-damage identification is demonstrated. Finally, the damage identification abilities of different mode shape curvatures such as mean *x*-*y* curvature and mean principal curvature are tested base on the robust multi-damage index.

A cantilever aluminium plate of dimension $0.35 \times 0.23 \times 0.003\mathrm{m}^3$ with Young's modulus E=69 GPa, Poisson's ratio $\nu = 0.35$ and the mass density ρ=2700 kg/m^3 is analysed. The details of the numerical study have been presented in Section 6.5. Here, two damage cases of a plate with two damage areas are studied, which are shown in Figure 7.4. For numerical case 1, the two damage positions are centred at (0.10 m, 0.115 m) and (0.21 m, 0.115 m) with an equal area of 0.02×0.02 m^2. For numerical

case 2, the two damage positions are centred at (0.155 m, 0.075 m) and (0.155 m, 0.155 m) with an equal area of 0.02×0.02 m^2.

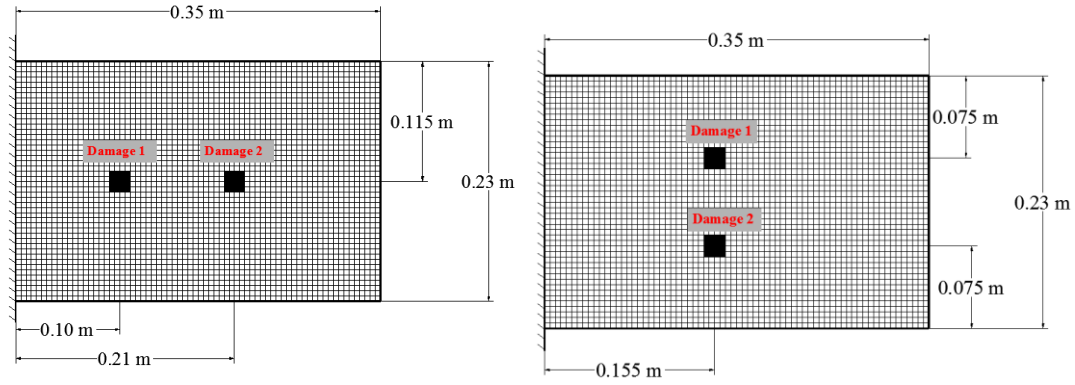

(a) (b)

Figure 7.4 FE model of a plate with two damaged areas (a) Case 1 (b) Case 2.

7.4.1 Baseline-free multi-damage identification using a single mode shape

First, with Gaussian white noise $n_{\text{level}} = 0.1\%$ (60.10 dB), the Gaussian curvature of 10$^{\text{th}}$ mode shape of numerical case 1 is taken as an example to show damage identification performance of different methods. Figure 7.5 presents the 10$^{\text{th}}$ mode shape of numerical case 1 and its Gaussian curvature.

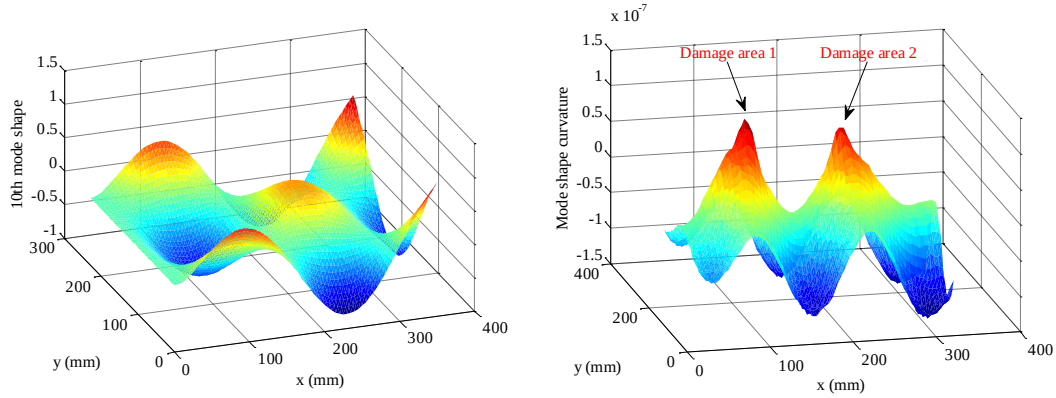

(a) (b)

Figure 7.5 (a) The 10$^{\text{th}}$ mode shape of numerical case 1 and (b) Gaussian curvature of the 10$^{\text{th}}$ mode shape using 2-ring LPF.

7.4.1.1 Multi-damage identification using polynomial fitting approaches

In this section, the polynomial fitting approaches are applied to demonstrate their damage identification performance. Figure 7.6 presents the damage localisation results of numerical case 1 (both damage areas of 10% thickness reduction) by using 2-D

gapped smoothing method. The damage identification results in Figure 7.6 (b) indicate that the 2-D GSM is not effective in extracting the damage-induced changes and provides poor damage identification results.

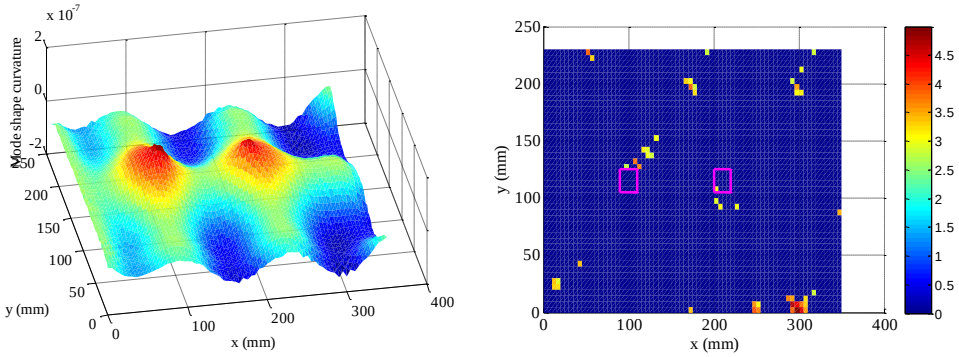

(a) (b)

Figure 7.6 (a) Constructed Gaussian curvature of numerical case 1 (both damage of 10% thickness reduction) and (b) Damage identification results based on 2-D GSM.

Furthermore, its ability for severe damage localisation is tested as well. Figure 7.7 illustrates the damage identification results of numerical case 1 with both damage of 30% and 60% thickness reduction. The damage localisation results from Figure 7.7 indicate that 2-D GSM works for very severe damage cases such as those presented in Figure 7.7. However, the identified damage positions of 2-D GSM are not accurate, which provides bigger alarming areas than the true damage areas as shown in Figure 7.7 (b) (the red rectangles indicate the actual damage areas).

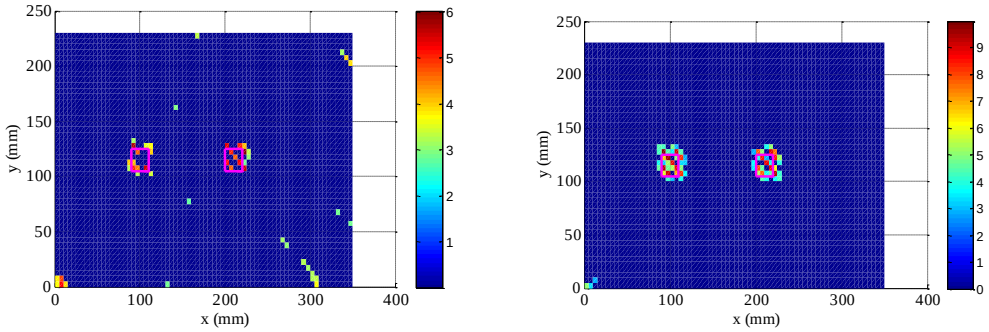

(a) (b)

Figure 7.7 Damage localisation results of numerical case 1 with both damage areas of (a) 30% thickness reduction and (b) 60% thickness reduction.

Next, global polynomial fitting method is adopted and the damage detection results of numerical case 1 (both damage of 10% thickness reduction) are given in Figure 7.8.

Form Figure 7.8, it is clear that GPF method is capable of identifying the two damage areas accurately, but the drawback of this method is overfitting. In this case, the polynomial order need to be chosen properly. Here, Eq. (7.9) is used to determine the best polynomial order.

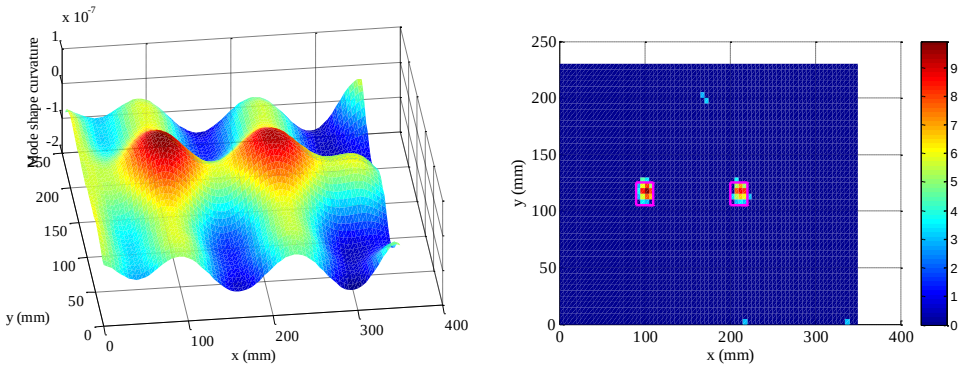

(a) (b)

Figure 7.8 (a) Constructed Gaussian curvature of numerical case 1 (both damage of 10% thickness reduction) and (b) Damage identification results of GPF method.

Finally, Kriging regression approach is used to approximate the mode shape curvature of the healthy state. The constructed mode shape curvature and the damage identification results are presented in Figure 7.9.

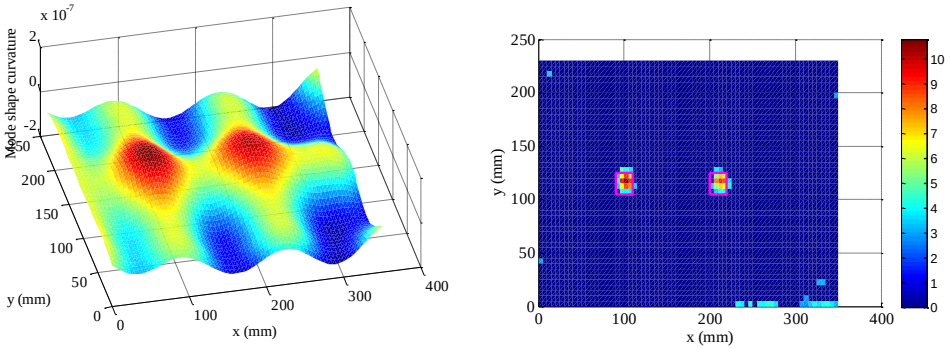

(a) (b)

Figure 7.9 (a) Constructed Gaussian curvature of numerical case 1 (both damage of 10% thickness reduction) and (b) Damage identification results of Kriging regression.

In this study, a sample of 400 measurement points are used to establish the Kriging regression model and it takes 427.51s. Normally, the large amount of sample points will increase the prediction accuracy but the computational complexity of establishing the Kriging regression model is high. Therefore, Kriging regression model is suitable for problems of limited sample points, which aims to obtain the optimal regression

model. Although the damage localisation results of Kriging regression model are accurate for this numerical study, it is not recommend for applying it to a large number of sample points due to its computational complexity.

7.4.1.2 Multi-damage identification using low-rank approaches

Traditional principal component analysis is first investigated for damage localisation. In which, the low-rank matrix **L** is determined by the singular values accounting 80% of all the singular values. The estimated Gaussian curvature using **L** and the normalised multi-damage index are presented in Figure 7.10.

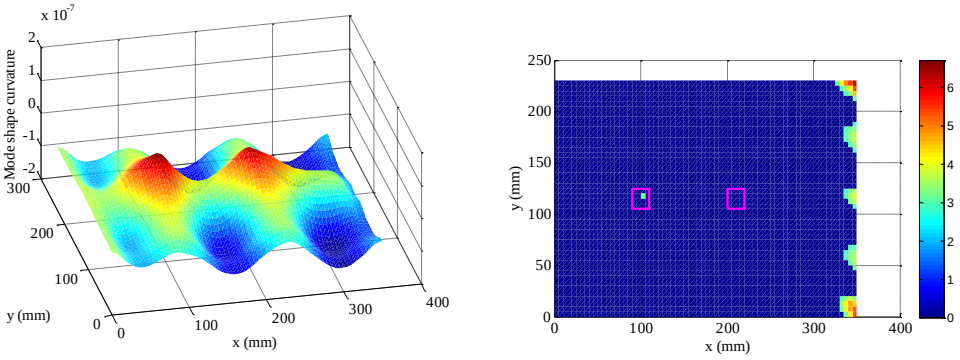

(a) (b)

Figure 7.10 (a) Constructed Gaussian curvature of numerical case 1 (both damage of 10% thickness reduction) and (b) Damage localisation results of PCA.

From Figure 7.10 (b), it is obvious that the traditional PCA is impossible to localise the two damage areas of numerical case 1. In order to test its feasibility for severe damage cases, Figure 7.11 shows the damage identification results of numerical case 1 with two damage areas of 30% and 60% thickness reduction, respectively.

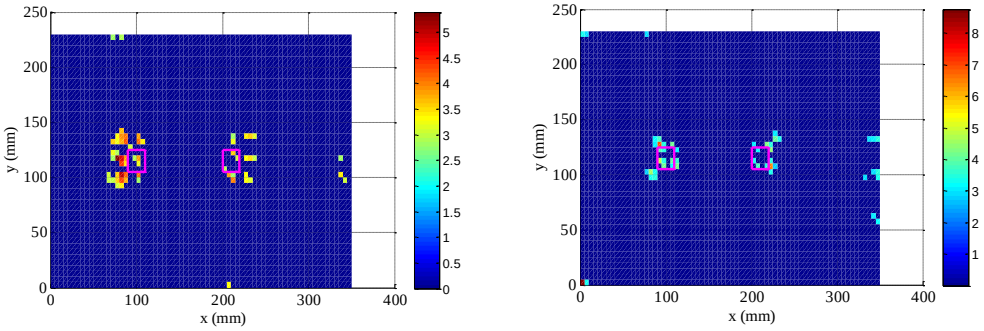

(a) (b)

Figure 7.11 Damage localisation results of numerical case 1 with two damage areas of: (a) 30% thickness reduction and (b) 60% thickness reduction.

The damage localisation results of traditional PCA are of poor quality as shown in Figure 7.11, which indicates that it is not effective for damage identification, even for severe damage cases. Then, the robust PCA is applied for damage identification. The estimated mode shape curvature of the undamaged state and the damage localisation results of numerical case 1 are given in Figure 7.12.

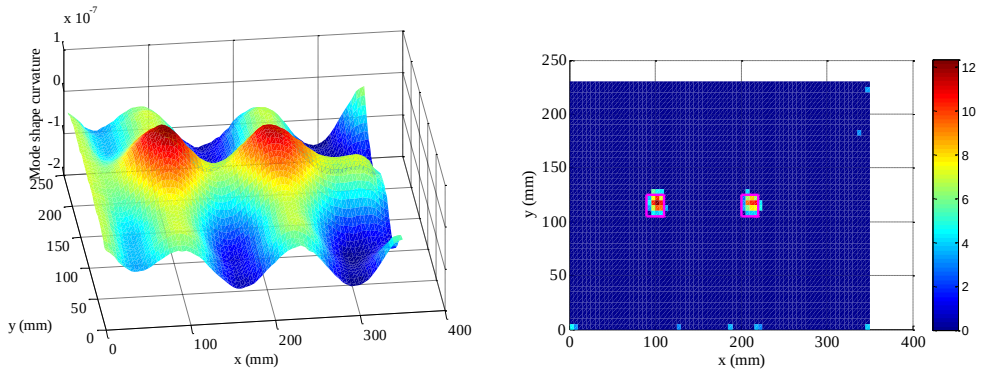

(a) (b)

Figure 7.12 (a) Constructed Gaussian curvature of numerical case 1 (both damage of 10% thickness reduction) and (b) Damage identification results of robust PCA.

From Figure 7.12, it is apparent that the damage index of robust PCA is accurate for multi-damage localisation. Furthermore, it is validated that the robust PCA originally proposed in pixel-domain is possible to be extended to damage identification based on mode shape of low-density discrete measurement points.

Above all, both robust PCA and GPF approach are effective in constructing the mode shape curvatures of the healthy state and providing robust and accurate damage identification results. But the computation efficiency of robust PCA is higher than GPF approach, as robust PCA takes about 0.5250s for each run while GPF consumes 1.6223s.

7.4.2 Baseline-free robust multi-damage index

The above study is based on the 10^{th} mode shape. However, it is unknown which mode shape is more sensitive for damage identification, as the information of damage is not available in practice. In order to demonstrate that a certain mode shape is inefficient in localising damage at some positions, numerical case 2 with two damage areas of 10% thickness reduction is studied.

First, the Gaussian curvature of 10th mode shape is used to identify the two damage areas of numerical case 2 via robust PCA approach. The damage localisation results are presented in Figure 7.13.

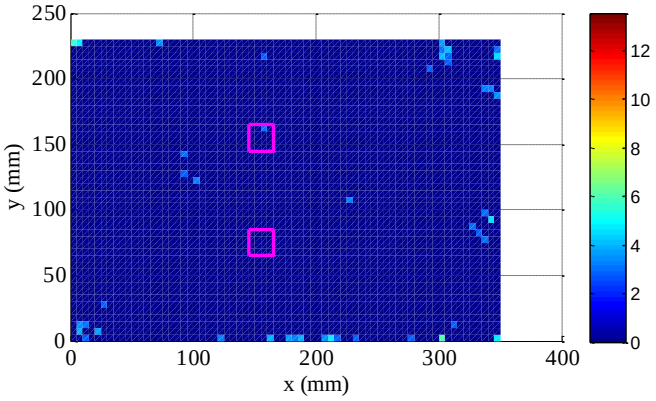

Figure 7.13 Damage localisation results of numerical case 2 (both damage areas of 10% thickness reduction) based on robust PCA.

It is clear that the two damage areas cannot be localised by using the 10th mode shape mode. Thus, a robust multi-damage localisation method should incorporate damage information of several mode shapes. The robust multi-damage index has been defined in Eq. (7.29). Here, Gaussian curvatures of 10th to 15th mode shapes are used to evaluate the proposed robust damage index for the two numerical cases and the damage localisation results are presented in Figure 7.14. In addition, the mode shapes from 10th to 15th are contaminated by 0.1% Gaussian noise.

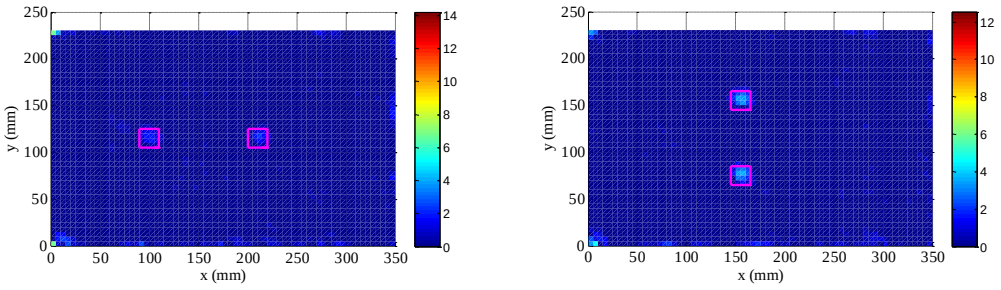

Figure 7.14 Robust multi-damage index using robust PCA (both damage areas of 10% thickness reduction): (a) Numerical case 1 and (b) Numerical case 2.

The two damage areas of two numerical cases can be both localised correctly in Figure 7.14 but the damage indexes are corrupted by some boundary points. Therefore, by

removing some boundary measurement points, Figure 7.15 presents the clear damage localisation results.

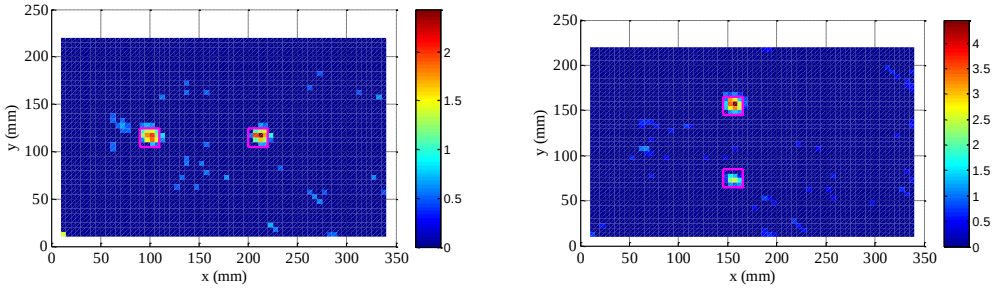

(a) (b)

Figure 7.15 Robust multi-damage index of robust PCA without boundary points (both damage of 10% thickness reduction): (a) Numerical case 1 and (b) Numerical case 2.

The above damage identification results are sensitive to the boundary measurement points, as only the information of one side of boundary measurement points is available, which degrades the efficiency of robust PCA. This problem mainly affects the damage localisation results of smaller damage. By increasing the damage depth to 30% reduction, the effects of boundary points will decrease, which are demonstrated in Figure 7.16.

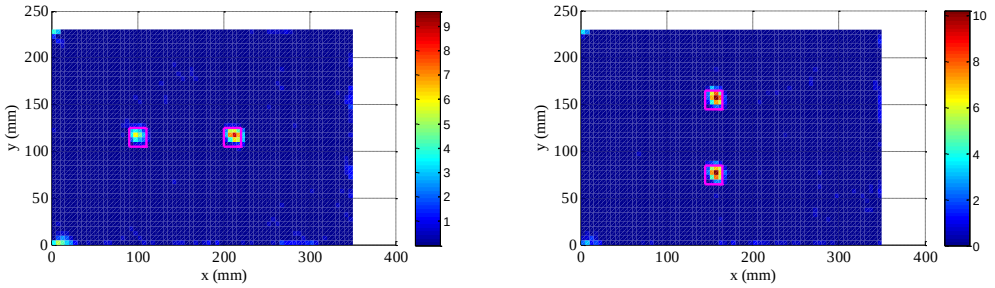

(a) (b)

Figure 7.16 Robust multi-damage index using robust PCA (both damage areas of 30% thickness reduction): (a) Numerical case 1 and (b) Numerical case 2.

Another conclusion by comparing Figure 7.16 with Figure 7.15 is that the amplitude of damage index is able to indicate the relative damage severity, as the damage index amplitude will increase with the damage depth. In conclusion, the proposed baseline-free robust multi-damage index is validated to be effective and accurate for multi-damage detection, localisation and relative severity quantification.

7.4.3 Robust multi-damage index of different curvature types

In this section, based on the robust multi-damage index, the damage localisation performance of two other types of curvatures are investigated, which are mean *x-y* curvature and mean principal curvature. First, Gaussian white noise of $n_{\text{level}} = 0.3\%$ is added to pollute the 10^{th} to 15^{th} mode shapes. Then, the damage identification results of numerical case 1 with two damage areas of 10% thickness reduction are presented in Figure 7.17, which is based on the mean *x-y* curvature and mean principal curvature, respectively.

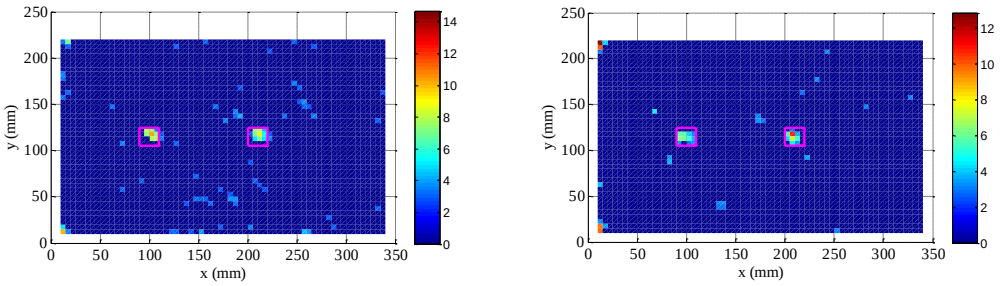

(a) (b)

Figure 7.17 Damage localisation results of numerical case 1 (both damage of 10% thickness reduction): (a) Mean principal curvature using 3-ring LPF (b) Mean *x-y* curvature using LoG filter with $\sigma = 1$.

From Figure 7.17, it indicates that both the mean principal and the mean x-y curvatures provide very accurate damage localisation results. But both curvatures are easily corrupted by boundary points. Hence, the boundary points are not presented in Figure 7.17.

In order to test their damage identification ability for fairly noisy data, Gaussian white noise of $n_{\text{level}} = 0.6\%$ is added and the damage identification results of numerical case 1 and case 2 are presented in Figure 7.18 and Figure 7.19, respectively.

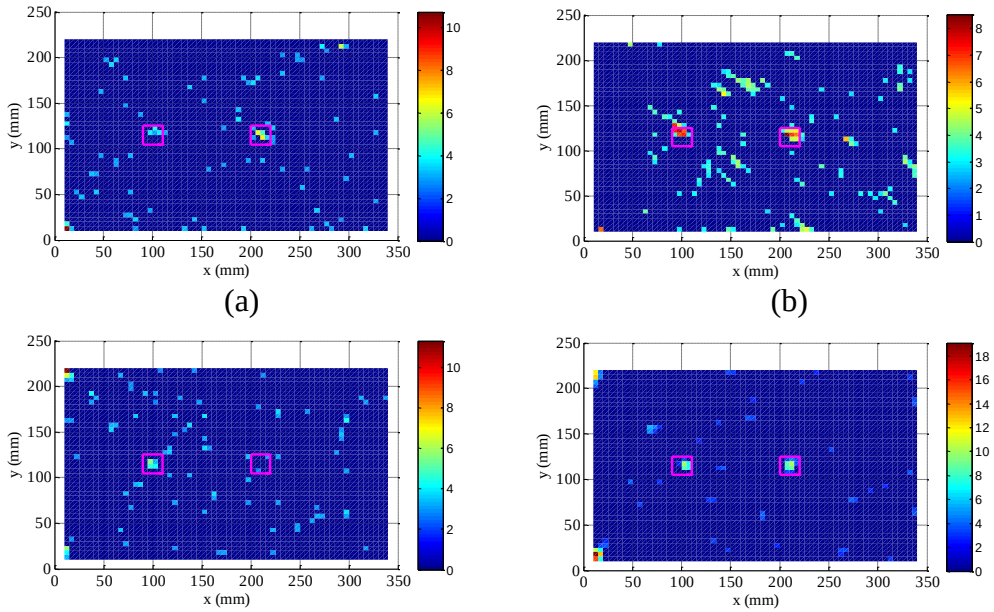

Figure 7.18 Damage localisation results of numerical case 1 (both damage of 10% thickness reduction): (a) Mean principal curvature using 3-ring LPF (b) Gaussian curvature using 3-ring LPF (c) Mean *x*-*y* curvature using LoG filter with $\sigma = 1$ and (d) Mean *x*-*y* curvature using LoG filter with $\sigma = 1.5$.

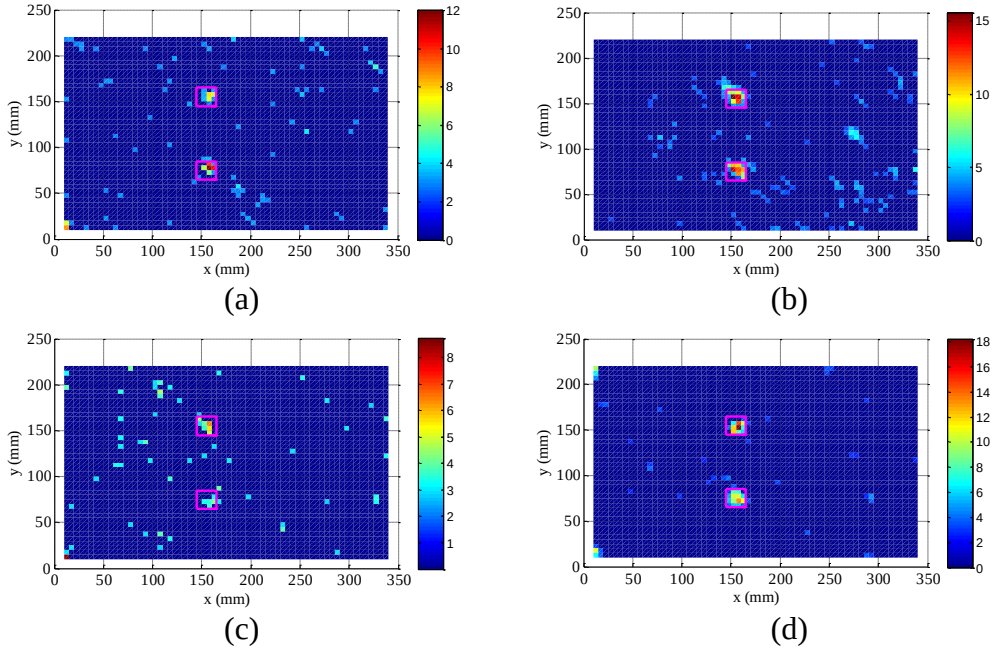

Figure 7.19 Damage localisation results of numerical case 2 (both damage of 10% thickness reduction): (a) Mean principal curvature using 3-ring LPF (b) Gaussian curvature using 3-ring LPF (c) Mean *x*-*y* curvature using LoG filter with $\sigma = 1$ and (d) Mean *x*-*y* curvature using LoG filter with $\sigma = 1$.

By comparing Figure 7.18 with Figure 7.19, it can be found that damage at different locations has different noise robustness. Then, it is hard to discern which kind of curvature provides the best damage identification results, as they are all sensitive to damage and robust to noise. For very noisy data, the larger scale parameter for LoG and more rings for LPF should be used.

7.5 Experimental studies

In this section, cantilever aluminium plates with one or two damage areas are tested to validate the feasibility and effectiveness of the proposed damage identification method based on robust PCA and GFT approaches. Firstly, the damage identification using robust PCA and GPF is validated based on the curvature of a single mode shape. Then, the damage index is computed by using curvatures of several mode shapes to show its robustness to measurement noise and damage localisation. Finally, different mode shape curvatures are investigated to evaluate their damage sensitivities.

Figure 20 presents the experimental set-up and the details of the experimental set-up have been given in Section 6.6 of Chapter 6.

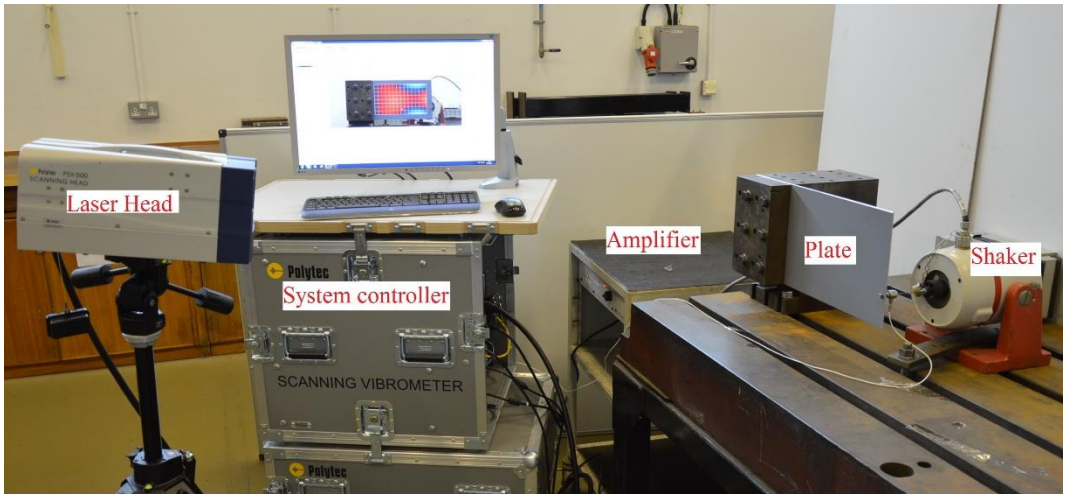

Figure 7.20 Experimental set-up of a plate.

7.5.1 Baseline-free multi-damage identification using a single mode shape

First, a plate with a single damage area is studied. The damage is centred at (10cm, 11.5cm) with an area of $0.02 \times 0.02\ \mathrm{m}^2$, which is displayed in Figure 7.21. The damage is introduced by reducing the plate thickness on the non-measuring surface. The 10^{th} mode shape is acquired by PSV-500 and its Gaussian curvature is estimated

using 3-ring LPF method. Finally, the damage identification results of different damage severity cases are presented in Figure 7.22 and Figure 7.23, respectively.

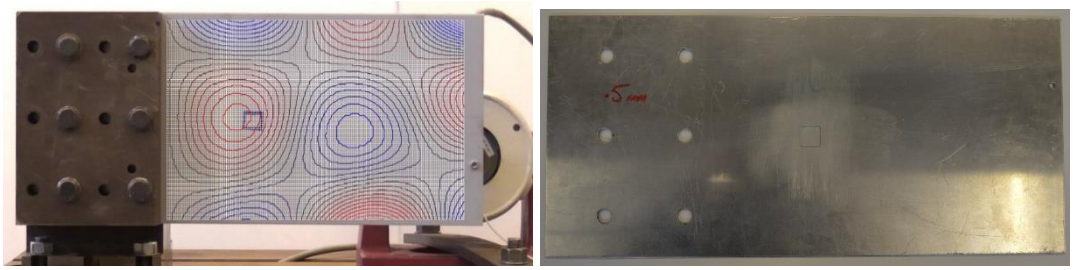

(a) Front surface view (b) Back surface view

Figure 7.21 A plate with a single damage area (experimental case 1).

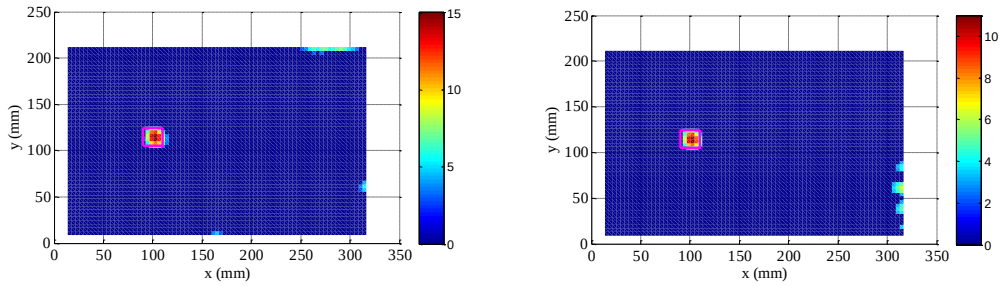

(a) (b)

Figure 7.22 Damage localisation results of experimental case 1 (10% thickness reduction) based on Gaussian curvature of the 10th mode shape: (a) Robust PCA and (b) GPF technique.

Figure 7.22 demonstrates that both methods are effective to extract the damage-induced local shape changes. But the robust PCA and GPF also provide some misleading damage identification results around the boundary points. Fortunately, the combination of robust PCA and GPF can present accurate damage identification results, as they are sensitive to different boundary points. In order to get some further conclusions, the depth of the damage is increased to 0.0005m (16.67% of the plate thickness) and the damage identification results using robust PCA and GPF are presented in Figure 7.23.

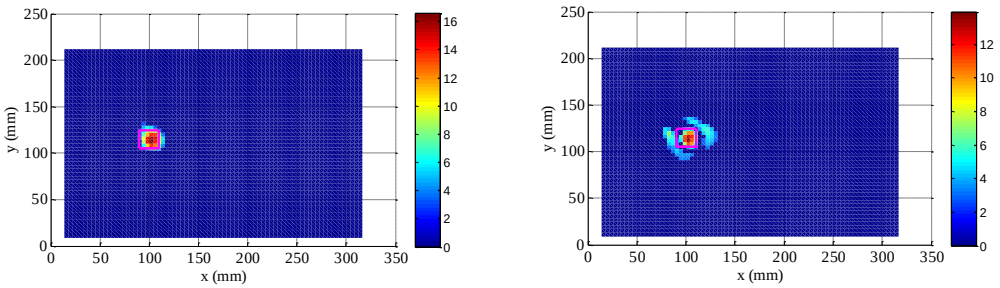

(a) (b)

Figure 7.23 Damage localisation results of experimental case 1 (16.67% thickness reduction) based on Gaussian curvature of the 10th mode shape: (a) Robust PCA and (b) GPF method.

In comparison with Figure 7.22, it can be seen that with the larger depth of damage, the damage identification results are more robust to measurement noise. Moreover, the magnitude of the proposed damage index is able to indicate the relative damage severity, as the magnitudes of damage index in Figure 7.23 are larger than those in Figure 7.22. However, in Figure 7.23, the robust PCA is able to pinpoint the damage position, whereas the GPF approach presents some misleading features around the damage area, which implies that GPF does not fare well around the damage area sometimes.

Next, experimental case 2 of a cantilever plate with two damage areas is tested. The experimental set-up and the experimental plate are shown in Figure 7.24. The central points of the two damage area are (10cm, 11.5cm) and (21cm, 11.5cm) with an equal area of 0.02×0.02 m^2. As discussed in Chapter 6, the robust mode shape curvature estimation approach has been proposed and validated. The purpose here is to localise the damage by using the proposed pseudo-mode shape construction methods: robust PCA and GPF. Figure 7.25 illustrates the damage localisation results of experimental case 2.

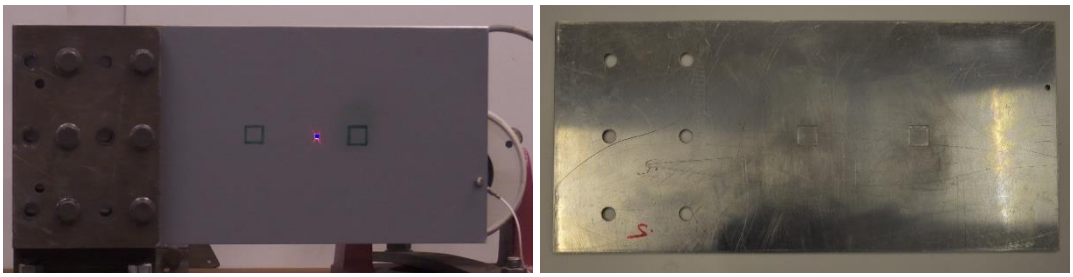

(a) Front surface view (b) Back surface view

Figure 7.24 A cantilever plate with two damage areas (experimental case 2).

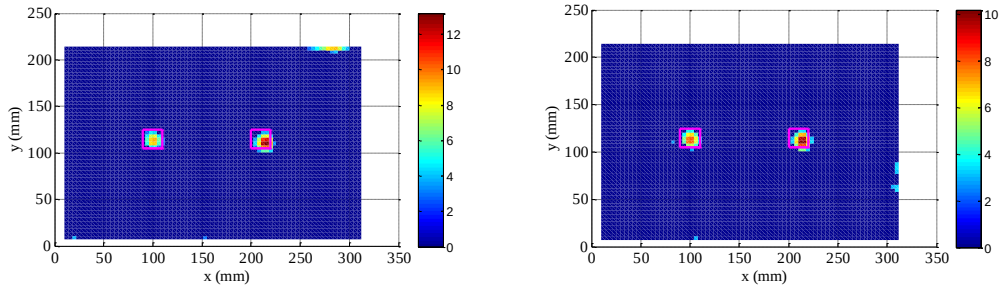

(a) (b)

Figure 7.25 Damage localisation results of experimental case 2 (both damage of 10% thickness reduction) using Gaussian curvature of the 10th mode shape: (a) Robust PCA and (b) GPF method.

Figure 7.25 (a) indicates that robust PCA is able to localise the two damage areas but provides false damage alarms around the boundary areas. In Figure 7.25 (b), the GPF method presents accurate damage identification results but also shows some false alarms around the boundary areas. However, the robust PCA and GPF are sensitive to different boundary areas, which promises an accurate damage identification by combining the damage identification results of these two methods.

7.5.2 Baseline-free robust multi-damage index

In section 7.5.1, the proposed robust PCA and GPF are validated for single or multiple damage identification based on a single mode shape. In practice, the damage information is not known in advance and it is impossible to choose the right mode shape that is capable of damage identification. Here, experimental case 3, a plate with two damage areas that are different from experimental case 2, is studied, which is shown in Figure 7.26.

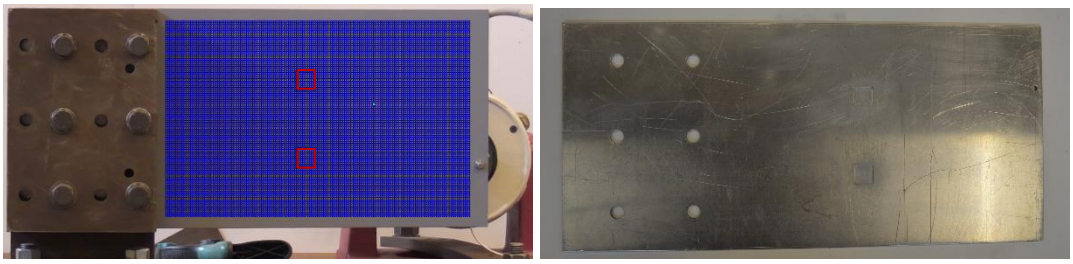

(a) Front surface view (b) Back surface view

Figure 7.26 A cantilever plate with two damage areas (experimental case 3).

First, the 10th mode shape is applied to identify the two damage areas of experimental case 3 and the identification results are displayed in Figure 7.27 (a). It indicates that the 10th mode shape is impossible to identify the two damage positions of experimental case 3. Then, the 13th mode shape is utilised to identify the two damage positions of experimental case 3, which is shown in Figure 7.27 (b). The two damage positions are correctly localised by using the 13th mode shape. Thus, for different mode shapes, they are sensitive to damage at different positions.

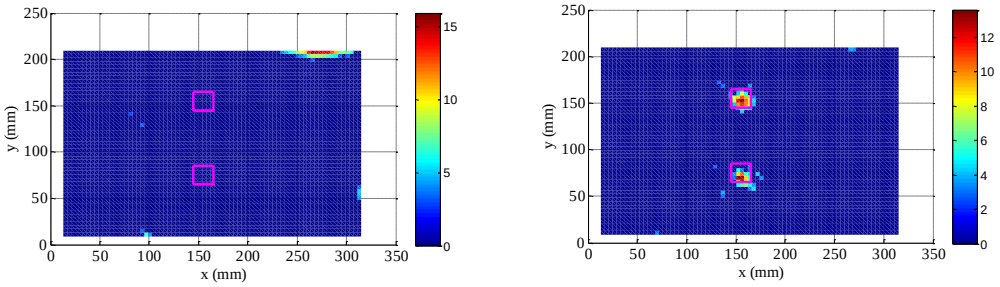

(a) (b)

Figure 7.27 Damage identification results of experimental case 3 (both damage of 10% thickness reduction) using robust PCA based on Gaussian curvature of (a) 10th mode shape (b) 13th mode shape.

A robust multi-damage index must contain the damage information of several modes to cover the damage of various possible positions. In this section, the damage information of the 10th and 13th mode shapes are combined to form a robust multi-damage index and the damage identiciation results for exerpimental case 3 based on robust PCA and GPF approach are presented in Figure 7.28. Moreover, the damage identificationr results of experimental case 2 based on the robust multi-damage index is presented in Figure 7.29.

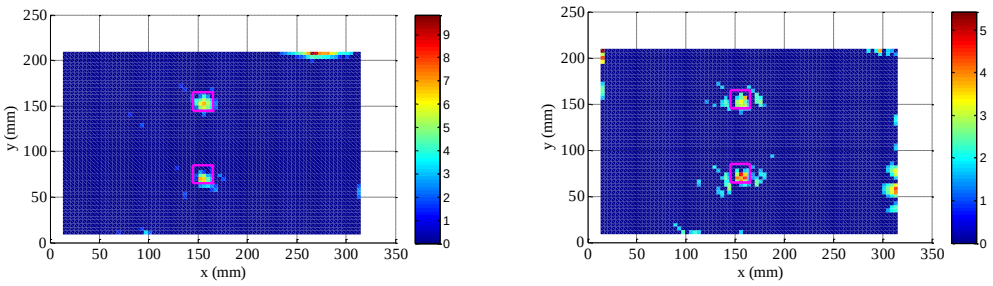

(a) (b)

Figure 7.28 Damage identification results of experimental case 3 (both damage of 10% thickness reduction) by combining the Gaussian curvature of 10th and 13th mode shapes (a) Robust PCA (b) GPF method.

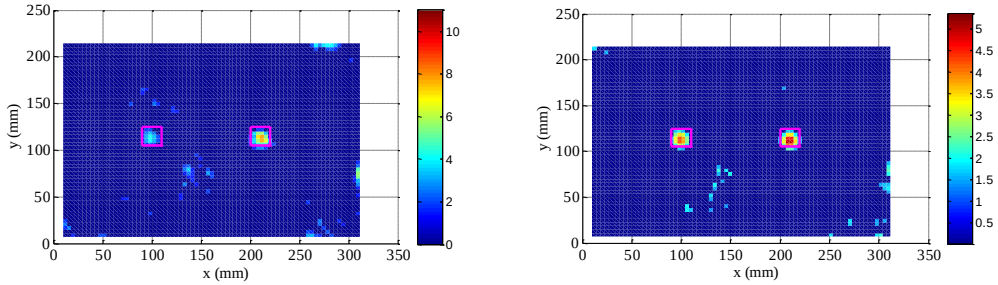

(a) (b)

Figure 7.29 Damage identification results of experimental case 2 (both damage of 10% thickness reduction) by combining the Gaussian curvature of 10th and 13th mode shapes (a) Robust PCA (b) GPF technique.

From the damage identification results of Figure 7.28 and Figure 7.29, it is shown that the multi-damage index based on the 10th and 13th mode shapes is robust and has the ability to localise damage of both experimental cases. Thus, robust multi-damage identification should be achieved by combing the damage information of more than one mode shape. Moreover, the combination of the damage identification results of robust PCA and GPF provides very accurate damage identification, as they individually present false damage alarms at different positions. In addition, the damage identification results in Figure 7.28 (b) also indicates that GPF does not fare well around the damage areas. Overall, the robust PCA is robust and accurate for damage identification.

7.5.3 Robust multi-damage index of different curvature types

In this section, based on the 10th and 13th mode shapes, the damage identification ability of the mean *x-y* curvature and the mean principal curvature is investigated based

on robust PCA. The damage identification results of experimental cases 2 and 3 are presented in Figure 7.30 and Figure 7.31, respectively.

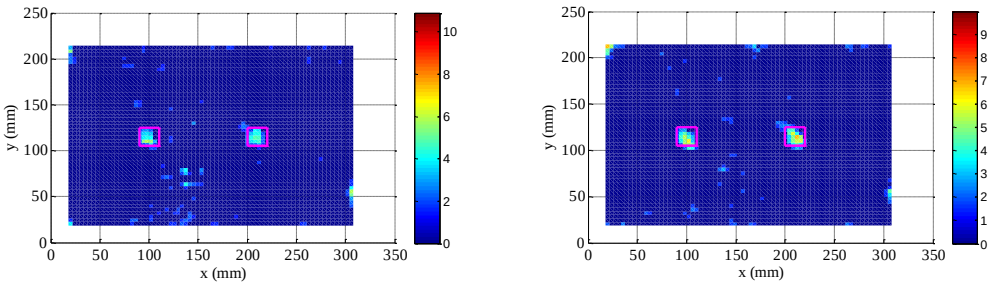

(a) (b)

Figure 7.30 Damage identification results of experimental case 2 (both damage of 10% thickness reduction) by combining the 10^{th} and 13^{th} mode shapes (a) mean *x-y* curvature using LoG filter with $\sigma = 1$ (b) Mean principal curvature using 3-ring LPF.

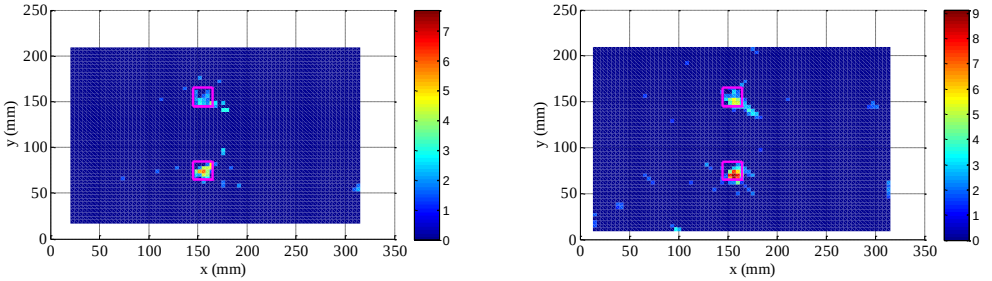

(a) (b)

Figure 7.31 Damage identification results of experimental case 3 (bothe damage of 10% thickness reduction) by combining the 10^{th} and 13^{th} mode shapes (a) Mean *x-y* curvature using LoG filter with $\sigma = 1$ (b) Mean principal curvature using 3-ring LPF.

From Figure 7.30 and Figure 7.31, it is indicated that both the mean *x-y* curvature and mean principal curvature are capable of identifying the two experimental cases. Moreover, by comparing with the damage identification results using Gaussian curvature in Figure 7.28 (a) and Figure 7.29 (b), it is found that the damage identification results using Gaussian curvature are slightly more robust to measurement noise but sensitive to the boundary areas. Overall, all the three curvatures — mean *x-y* curvature, mean principal curvature and Gaussian curvature, are effective for multi-damage localisation.

7.6 Conclusions

The main contribution in this chapter is to extract the damage-induced local shape changes without the baseline-line data of the healthy state. Surrogate models and low-rank models are investigated to determine the best approaches for damage information extraction. With the extracted damage information of several mode shapes, a robust multi-damage index is proposed for multi-damage localisation.

Two numerical cases of a plate with two damage areas are studied first. In these, Gaussian white noise is added to contaminate the mode shape data. Moreover, three experimental cases of plate with one or two damage areas are tested. The mode shape data is acquired by PSV-500 laser Vibrometer.

Based on these studies, the global polynomial fitting and robust principal component analysis are demonstrated to be much more effective and noise robust than the other methods. Then, the proposed multi-damage index is proved to be sensitive to damage at various possible locations. Moreover, the damage identification performances of mean *x*-*y* curvature, mean principal curvature and Gaussian curvature are compared to show that they are all effective in robust multi-damage identification.

Chapter 8

Conclusions and future work

8.1 Conclusions

In this thesis, robust multi-damage identification using only vibration data of damaged structures is studied for beam-type and plate-type structures. The proposed methods are data-driven by harnessing the properties of vibration data without requiring the theoretical model and baseline information of the structures, which facilitates the practical applications. To reduce the effects of measurement noise on damage identification, common principal component analysis is applied to obtain noise robust mode shapes for beam-type structures, and multi-scale approaches and polynomial fitting techniques are investigated to enhance the estimation of mode shape curvatures for plate-type structures. To extract the damage-induced singularities in mode shapes or mode shape curvatures without baseline data of healthy structures, polynomial fitting technique and low-rank modelling are explored.

1. New output-only non-parametric mode shape estimation. A unique contribution of this dissertation is the application of common principal component analysis to diagonalise a set of covariance or power spectral density matrices for robust mode shape estimation. The common principal component analysis is conducted via joint approximation diagonalisation according to the least-squares criterion, which provides a kind of ‘average Eigen-structure’ shared by a matrix set. Therefore, the estimated mode shapes will be statistically more noise robust, which has been validated in the numerical studies involving simulated Gaussian white noise.

2. Noise reduction using polynomial fitting and multi-scale approaches. For beam-type structures, an adaptive gapped smoothing method is proposed based on cross-validation approach to determine the optimal polynomial order. By doing this, the extracted damage-induced mode shape changes will be robust to measurement noise. For plate-type structures, both polynomial fitting and multi-scale approaches are applied to estimate the robust mode shape curvatures based on the acquired noisy mode shapes. Multi-scale approaches such as wavelet transform and Gaussian smoothing are adopted to estimate the robust mode shape curvatures along *x* and *y* directions instead of the traditional second-order central difference approach. A local bivariate polynomial fitting is integrated into the process of evaluating the principal curvatures, Gaussian curvature and mean principal curvature in order to improve their noise robustness. By reducing the effects of measurement noise on the damage sensitive features, both the type I and type II errors are reduced. Here, type I error refers to false detection of the existence of damage when in fact there is not damage and type II error denotes the failure to detect the damage when in fact there is damage.

3. Baseline-free robust multi-damage identification methods. In this research, robust multi-damage identification indexes are proposed for beam- and plate-type structures by using only the vibration data of damaged structures. The basic idea of using a single mode shape in damage identification is not reliable and robust, as the mode shape associated with a certain natural frequency is normally sensitive to damage at some locations whilst less sensitive to damage at other locations. Thus, a robust damage localisation index should incorporate the damage-induced shape changes of several modes. Moreover, the damage-induced shape changes of several modes should be normalised before summation to avoid the changes of a certain mode shape dominating the damage localisation index.

   Another contribution is the investigation of baseline-free damage index. It is simple to calculate the mode shape or mode shape curvature differences before and after damage. However, this is hard to be implemented for practical applications, as baseline data of healthy structures is rarely available. Even

when baseline data of the healthy state is available, it may not be efficient for practical applications, as it was historical data of structures, which was normally acquired under different operational and environmental conditions with measurement noise. In this thesis, the smoothness of mode shapes, the low-rank structure of mode shape or curvature surface of plates, the sparsity of damage locations are investigated to extract the damage-induced information. Numerical and experimental studies have been performed to verify their feasibility and effectiveness.

4. Localisation of fatigue cracks in stepped beams or rotors. A fatigue crack (theoretically modelled as a breathing crack) opens and closes during vibration process, which introduces nonlinearities to structures. Unlike the traditional linear damage, damage-caused nonlinearities of vibration responses can be taken advantage of in fatigue crack detection. Therefore, the localisation of fatigue cracks is normally equivalent to the localisation of nonlinearity in the structures. It is known that geometrical steps of structures do not generate nonlinearity. Hence, the identification of nonlinearity is effective to localise fatigue cracks in stepped structures, especially for stepped beams or rotors.

   Two nonlinear damage identification approaches are proposed to localise single or multiple breathing cracks in stepped beams. The first method is a time domain method, which uses the deviation between empirical cumulative distributions of vibration responses at different locations for damage identification. The second method is a frequency domain method, which detects the breathing crack via the damage-induced shape distortions in super-harmonic characteristic deflection shapes. They all validated to be effective by three numerical examples of a stepped beam with breathing cracks.

8.2 Future work

Although this research concerns baseline-free robust multi-damage identification in beam- and plate-type structures, there are still many research problems in structural damage identification. Inspired by the research of this thesis, possible future work is summarised as follows:

1. The extension of the proposed damage identification methods to composite structures. Composite structures are widely used in various industrial fields, especially in aircraft and aerospace industries due to their excellent mechanical properties and low density over traditional materials. Delamination is a typical mode of failure in composite structures, which compromises the mechanical performance and even cause the failure of structures. Appling the proposed damage identification methods to delamination identification in composite beams and plates is useful and significant. However, the challenging problem is the anisotropic property of composite structures, which may degrade the effectiveness of damage information extraction when baseline data of the healthy state is not available.
2. Uncertainty quantification of damage features or damage identification index. One of the main tasks of this thesis is to reduce the effects of measurement noise on damage features and damage identification index via statistical approaches or filtering techniques. The uncertainty quantification of damage features and damage identification index due to measurement noise will be helpful in order to understand and quantify the effects of measurement noise.
3. Physics-based structural model for damage quantification. This research is mainly about data-driven damage localisation by using the properties of acquired spatial vibration data. Although the traditional non-destructive testing can be carried out when the location information of damage is available, it is useful to establish an accurate analytical or FE model of structures to quantify the damage or predict the remaining service life. This physics-based structural model is also useful to understand the mechanical properties of structures. Moreover, the modelling of damage is helpful to interpret the damage mechanics and predict the damage propagation.

Appendix A

Joint approximate diagonalisation

The following procedure is inspired by the work published in [63]. Joint approximate diagonalisation can be applied to simultaneously diagonalise a set of real or complex matrices.

Consider a set of power spectral density (PSD) matrices $\underline{\mathbf{S}_r} = \{\mathbf{S}(\omega_{r+k})|k = -K, -K+1, \cdots, K\}\left(\underline{\mathbf{S}_r} \in \mathbb{R}^{N_\mathrm{m}\times(2K+1)N_\mathrm{m}}, \mathbf{S}(\omega_{r+k}) \in \mathbb{R}^{N_\mathrm{m}\times N_\mathrm{m}}\right)$ corresponding to frequencies around a resonant frequency ω_r. Since the PSD matrices $\mathbf{S}(\omega_{r+k})$ are Hermitian and positive definite, their off-diagonal terms can be transformed to zero by complex Givens rotation. In numerical analysis, the 'off' of $\mathbf{S}(\omega_{r+k})$ with entry $S_{ij}(\omega_{r+k})$ is expressed as

$$\mathrm{off}\big(\mathbf{S}(\omega_{r+k})\big) = \sum_{i=1}^{N_\mathrm{m}} \sum_{j=1, j\neq i}^{N_\mathrm{m}} \left| S_{ij}(\omega_{r+k}) \right|^2 \tag{A1}$$

where 'off' denotes the sum of squares of all off-diagonal entries. Joint approximate diagonalisation is implemented by complex Givens rotation to estimate the joint unitary diagonaliser $\mathbf{U}_r \in \mathbb{R}^{N_\mathrm{m}\times N_\mathrm{m}}$, which simultaneously diagonalises all the PSD matrices in $\underline{\mathbf{S}_r}$. Estimating joint diagonaliser $\mathbf{U}_r$ can be formulated to minimise the following cost function:

$$J_1\left(\underline{\mathbf{S}_r}, \mathbf{U}_r\right) = \sum_{k=-K}^{K} \mathrm{off}(\mathbf{U}_r^\mathrm{H} \mathbf{S}(\omega_{r+k}) \mathbf{U}_r) \tag{A2}$$

If each PSD matrix in $\underline{\mathbf{S}_r}$ can be decomposed as $\mathbf{S}(\omega_{r+k}) = \mathbf{U}_r \mathbf{\Sigma}(\omega_{r+k}) \mathbf{U}_r^\mathrm{H}$, where $\mathbf{\Sigma}$ is a diagonal matrix, then, the global minimum of $J_1\left(\underline{\mathbf{S}_r}, \mathbf{U}_r\right)$ is zero. In fact, the value of $J_1\left(\underline{\mathbf{S}_r}, \mathbf{U}_r\right)$ will be greater than zero due to slight correlation of modal coordinates (caused by damping or noise, for example).

The unitary rotation matrix $\mathbf{V}_\mathrm{g}(i, j, a, b) \in \mathbb{R}^{N_\mathrm{m}\times N_\mathrm{m}}$ is set as an identity matrix except the following four entries

$$\begin{bmatrix} v_{g_{ii}} & v_{g_{ij}} \\ v_{g_{ji}} & v_{g_{jj}} \end{bmatrix} = \begin{bmatrix} a & b^{\mathrm{H}} \\ -b & a^{\mathrm{H}} \end{bmatrix} \tag{A3}$$

Sweep $i = 1,2,3,\cdots,N_{\mathrm{m}} - 1$ and $j = i+1, i+2, \cdots, N_{\mathrm{m}}$ to iteratively calculate a and b for each pair of (i,j), which minimises the following cost function.

$$J_2(a,b) = \sum_{k=-K}^{K} \mathrm{off}\left(\mathbf{V}_{\mathrm{g}}(i,j,a,b)\mathbf{S}(\omega_{r+k})\mathbf{V}_{\mathrm{g}}{}^{\mathrm{H}}(i,j,a,b)\right) \tag{A4}$$

For a given pair of (i,j), the PSD matrix after unitary rotation becomes

$$\mathbf{S}^{*}(\omega_{r+k}) = \mathbf{V}_{\mathrm{g}}(i,j,a,b)\mathbf{S}(\omega_{r+k})\mathbf{V}_{\mathrm{g}}{}^{\mathrm{H}}(i,j,a,b) \tag{A5}$$

Since the norm of unitary transforms remains the same, the following equation holds.

$$\begin{aligned} &\mathrm{off}\left(\mathbf{S}^{*}(\omega_{r+k})\right) + |S_{ii}^{*}(\omega_{r+k})|^2 + \left|S_{jj}^{*}(\omega_{r+k})\right|^2 \\ &= \mathrm{off}\left(\mathbf{S}(\omega_{r+k})\right) + |S_{ii}(\omega_{r+k})|^2 + \left|S_{jj}(\omega_{r+k})\right|^2 \end{aligned} \tag{A6}$$

Now, the minimisation of $\mathrm{off}\left(\mathbf{S}^{*}(\omega_{r+k})\right)$ is equivalent to maximisation of $|S_{ii}^{*}(\omega_{r+k})|^2 + \left|S_{jj}^{*}(\omega_{r+k})\right|^2$. And the maximisation of $|S_{ii}^{*}(\omega_{r+k})|^2 + \left|S_{jj}^{*}(\omega_{r+k})\right|^2$ can be converted to the maximisation of $\left|S_{ii}^{*}(\omega_{r+k}) - S_{jj}^{*}(\omega_{r+k})\right|^2$ due to the invariance of the trace as shown in Eq. (A7) and Eq. (A8).

$$\begin{aligned} &2\left(|S_{ii}^{*}(\omega_{r+k})|^2 + \left|S_{jj}^{*}(\omega_{r+k})\right|^2\right) \\ &= \left|S_{ii}^{*}(\omega_{r+k}) + S_{jj}^{*}(\omega_{r+k})\right|^2 + \left|S_{ii}^{*}(\omega_{r+k}) - S_{jj}^{*}(\omega_{r+k})\right|^2 \end{aligned} \tag{A7}$$

$$S_{ii}^{*}(\omega_{r+k}) + S_{jj}^{*}(\omega_{r+k}) = S_{ii}(\omega_{r+k}) + S_{jj}(\omega_{r+k}) \tag{A8}$$

Then, in each unitary rotation step, the joint approximate diagonalisation is formulated to maximise

$$J_2(a,b) = \sum_{k=-K}^{K}\left|S_{ii}^{*}(\omega_{r+k}) - S_{jj}^{*}(\omega_{r+k})\right|^2 \tag{A9}$$

It is easy to find that

$$\begin{aligned} S_{ii}^{*}(\omega_{r+k}) - S_{jj}^{*}(\omega_{r+k}) &= (|a|^2 - |b|^2)\left(S_{ii}(\omega_{r+k}) - S_{jj}(\omega_{r+k})\right) \\ &+2abS_{ij}(\omega_{r+k}) + 2a^{\mathrm{H}}b^{\mathrm{H}}S_{ji}(\omega_{r+k}) \end{aligned} \tag{A10}$$

In order to denote as the inner product $S_{ii}^{*}(\omega_{r+k}) - S_{jj}^{*}(\omega_{r+k}) = \mathbf{g}^{\mathrm{H}}\left(\mathbf{S}(\omega_{r+k})\right)\mathbf{u}(a,b)$, a 3×1 complex vector $\mathbf{g}\left(\mathbf{S}(\omega_{r+k})\right)$ is defined as

$$\mathbf{g}\left(\mathbf{S}(\omega_{r+k})\right) = \left[s_{ii}(\omega_{r+k}) - s_{jj}(\omega_{r+k}),\right.$$

$$S_{ij}(\omega_{r+k}) + S_{ji}(\omega_{r+k}), \mathrm{j}\left(s_{ij}(\omega_{r+k}) - s_{ji}(\omega_{r+k})\right)\Big]^{\mathrm{H}} \quad \text{(A11)}$$

Then, $\mathbf{u}(a,b)$ can be expressed as a 3×1 vector

$$\mathbf{u}(a,b) = [|a|^2 - |b|^2, ab + a^{\mathrm{H}}b^{\mathrm{H}}, \mathrm{j}(ab - a^{\mathrm{H}}b^{\mathrm{H}})]^{\mathrm{T}} \quad \text{(A12)}$$

Under the condition that $\mathbf{u}(a,b)$ is a real vector, a is required to be real according to Eq. (A12). Now, the maximisation of Eq. (A9) can be rewritten as

$$\sum_{k=-K}^{K}\left|S_{ii}^{*}(\omega_{r+k}) - S_{jj}^{*}(\omega_{r+k})\right|^2 = \sum_{k=-K}^{K}\left|\mathbf{g}\big(\mathbf{S}(\omega_{r+k})\big)\mathbf{u}(a,b)\right|^2 = \mathbf{u}^{\mathrm{T}}(a,b)\Big(\sum_{k=-K}^{K}\mathbf{g}\big(\mathbf{S}(\omega_{r+k})\big)\mathbf{g}^{\mathrm{H}}\big(\mathbf{S}(\omega_{r+k})\big)\Big)\mathbf{u}(a,b) \quad \text{(A13)}$$

Since $\mathbf{G} = \sum_{k=-K}^{K}\mathbf{g}\big(\mathbf{S}(\omega_{r+k})\big)\mathbf{g}^{\mathrm{H}}\big(\mathbf{S}(\omega_{r+k})\big)$ is Hermitian and its imaginary part is antisymmetric, the imaginary part of $\mathbf{G}$ does not contribute to the summation in Eq. (A13) when $\mathbf{u}(a,b)$ is a real vector. Therefore, the right side of Eq. (A13) is equivalent to $\mathbf{u}^{\mathrm{T}}(a,b)\mathrm{real}(\mathbf{G})\,\mathbf{u}(a,b)$. Under the constraint of unit norm ($|a|^2 + |b|^2 = 1$), the solution is the eigenvector $[z_1, z_2, z_3]^{\mathrm{T}}$ of $\mathrm{real}(\mathbf{G})$ corresponding to the largest eigenvalue.

If $[z_1, z_2, z_3]^{\mathrm{T}}$ is not a zero eigenvector, the maximization of Eq. (A13) is obtained at

$$a = \sqrt{(1+z_1)/2}\,, b = (z_2 - z_3\mathrm{j})/(2a) \quad \text{(A14)}$$

Here, during the solution for Eq. (A12), a is always chosen as the real positive. This choice is always possible, since an elementary complex rotation can be parameterized in terms of real angles θ and φ

$$\begin{bmatrix} a & b^{\mathrm{H}} \\ -b & a^{\mathrm{H}} \end{bmatrix} = \begin{bmatrix} \cos\theta & \mathrm{e}^{\mathrm{j}\varphi}\sin\theta \\ -\mathrm{e}^{-\mathrm{j}\varphi}\sin\theta & \cos\theta \end{bmatrix} \quad \text{(A15)}$$

With the estimated $\mathbf{V}_{\mathrm{g}}(i,j,a,b)$ for each pair (i,j), matrices $\underline{\mathbf{S}_r} = \{\mathbf{S}(\omega_{r+k})|k = -K, -K+1, \cdots, K\}$ and joint diagonaliser $\mathbf{U}_r$ are updated iteratively as follows

$$\mathbf{S}^{*}(\omega_{r+k}) = \mathbf{V}_{\mathrm{g}}(i,j,a,b)\mathbf{S}(\omega_{r+k})\mathbf{V}_{\mathrm{g}}{}^{\mathrm{H}}(i,j,a,b) \quad \text{(A16)}$$

$$\mathbf{U}_r = \mathbf{U}_r\mathbf{V}_{\mathrm{g}}{}^{\mathrm{H}}(i,j,a,b) \quad \text{(A17)}$$

where $\mathbf{U}_r$ is set as an identity matrix initially. The updating procedure ends when all the $|b|$ in a sweep is smaller than the pre-set threshold ϵ.

References

[1] Gopalakrishnan S, Ruzzene M, Hanagud S. Computational techniques for structural health monitoring. Springer Science & Business Media. 2011.

[2] Worden K, Dulieu-Barton JM. An overview of intelligent fault detection in systems and structures. Structural Health Monitoring. 2004; 3(1): 85-98.

[3] Farrar CR, Worden K. Structural health monitoring: a machine learning perspective. John Wiley & Sons. 2012.

[4] Vanlanduit S, Guillaume P, Schoukens J, Parloo E. Linear and nonlinear damage detection using a scanning laser vibrometer. Shock and Vibration. 2002; 9(1-2): 43-56.

[5] Rajani B, Makar J. A methodology to estimate remaining service life of grey cast iron water mains. Canadian Journal of Civil Engineering. 2000; 27(6): 1259-1272.

[6] Atkinson K, Whiter J, Smith P, Mulheron M. Failure of small diameter cast iron pipes. Urban water. 2002; 4(3): 263-271.

[7] Worden K, Friswell MI. Modal-vibration-based damage identification. Encyclopedia of Structural Health Monitoring. 2009.

[8] Maia NMM, Almeida RAB, Urgueira APV, Sampaio RPC. Damage detection and quantification using transmissibility. Mechanical Systems and Signal Processing. 2011; 25(7): 2475-2483.

[9] Sinha JK, Friswell MI, Edwards S. Simplified models for the location of cracks in beam structures using measured vibration data. Journal of Sound and Vibration. 2002; 251(1): 13-38.

[10] Kong X, Cai CS, Hu JX. The state-of-the-art on framework of vibration-based structural damage identification for Decision Making. Applied Sciences. 2017; 7(5): Article 497:1-31.

[11] Staszewski W, Boller C, Tomlinson GR. Health monitoring of aerospace structures: smart sensor technologies and signal processing. John Wiley & Sons. 2004.

[12] Grediac M. The use of full-field measurement methods in composite material characterization: interest and limitations. Composites Part A: applied science and manufacturing. 2004; 35(7): 751-761.

[13] Wang W, Mottershead JE, Mares C. Vibration mode shape recognition using image processing. Journal of Sound and Vibration. 2009; 326(3): 909-938.

[14] Rucka M, Wilde K. Application of continuous wavelet transform in vibration based damage detection method for beams and plates. Journal of Sound and Vibration. 2006; 297(3–5): 536-550.

[15] Sadhu A, Narasimhan S, Antoni J. A review of output-only structural mode identification literature employing blind source separation methods. Mechanical Systems and Signal Processing. 2017; 94: 415-431.

[16] Bouwmans T, Zahzah EH. Robust PCA via principal component pursuit: A review for a comparative evaluation in video surveillance. Computer Vision and Image Understanding. 2014; 122: 22-34.

[17] Yao Y, Tung STE, Glisic B. Crack detection and characterization techniques-An overview. Structural Control and Health Monitoring. 2014; 21(12): 1387-1413.

[18] Montalvao D, Maia NMM, Ribeiro AMR. A review of vibration-based structural health monitoring with special emphasis on composite materials. Shock and Vibration Digest. 2006; 38(4): 295-326.

[19] Andreaus U, Baragatti P. Cracked beam identification by numerically analysing the nonlinear behaviour of the harmonically forced response. Journal of Sound and Vibration. 2011; 330(4): 721-742.

[20] Surace C, Ruotolo R, Storer D. Detecting nonlinear behaviour using the Volterra series to assess damage in beam-like structures. Journal of Theoretical and Applied Mechanics. 2011; 49: 905-926.

[21] Vanlanduit S, Parloo E, Cauberghe B, Guillaume P, Verboven P. A robust singular value decomposition for damage detection under changing operating conditions and structural uncertainties. Journal of Sound and Vibration. 2005; 284(3-5): 1033-1050.

[22] Reynders E, Wursten G, De Roeck G. Output-only structural health monitoring in changing environmental conditions by means of nonlinear system identification. Structural Health Monitoring. 2014; 13(1): 82-93.

[23] Farrar CR, Doebling SW, Nix DA. Vibration–based structural damage identification. Philosophical Transactions of the Royal Society of London A: Mathematical, Physical and Engineering Sciences. 2001; 359(1778): 131-149.

[24] Kess HR, Adams DE. Investigation of operational and environmental variability effects on damage detection algorithms in a woven composite plate. Mechanical Systems and Signal Processing. 2007; 21(6): 2394-2405.

[25] Dimarogonas AD. Vibration of cracked structures: a state of the art review. Engineering Fracture Mechanics. 1996; 55(5): 831-857.

[26] Broda D, Staszewski WJ, Martowicz A, Uhl T, Silberschmidt VV. Modelling of nonlinear crack–wave interactions for damage detection based on ultrasound—a review. Journal of Sound and Vibration. 2014; 333(4): 1097-1118.

[27] Friswell MI, Penny JET. Crack modeling for structural health monitoring. Structural Health Monitoring. 2002; 1(2): 139-148.

[28] Christides S, Barr ADS. One-dimensional theory of cracked Bernoulli-Euler beams. International Journal of Mechanical Sciences. 1984; 26(11-12): 639-648.

[29] Lee YS, Chung MJ. A study on crack detection using eigenfrequency test data. Computers & structures. 2000; 77(3): 327-342.

[30] Chu YC, Shen MHH. Analysis of forced bilinear oscillators and the application to cracked beam dynamics. AIAA Journal. 1992; 30(10): 2512-2519.

[31] Chatterjee A. Structural damage assessment in a cantilever beam with a breathing crack using higher order frequency response functions. Journal of Sound and Vibration. 2010; 329(16): 3325-3334.

[32] Chondros TG, Dimarogonas AD. Identification of cracks in welded joints of complex structures. Journal of Sound and Vibration. 1980; 69(4): 531-538.

[33] Bilello C, Bergman LA. Vibration of damaged beams under a moving mass: theory and experimental validation. Journal of Sound and Vibration. 2004; 274(3): 567-582.

[34] Labib A, Kennedy D, Featherston CA. Crack localisation in frames using natural frequency degradations. Computers & structures. 2015; 157: 51-59.

[35] Andreaus U, Casini P, Vestroni F. Non-linear dynamics of a cracked cantilever beam under harmonic excitation. International Journal of Non-linear Mechanics. 2007; 42(3): 566-575.

[36] Voyiadjis GZ. Advances in damage mechanics: metals and metal matrix composites. Elsevier. 2012.

[37] Georgiou G, Manan A, Cooper JE. Modeling composite wing aeroelastic behavior with uncertain damage severity and material properties. Mechanical Systems and Signal Processing. 2012; 32: 32-43.

[38] Kopsaftopoulos FP, Fassois SD. Vibration based health monitoring for a lightweight truss structure: experimental assessment of several statistical time series methods. Mechanical Systems and Signal Processing. 2010; 24(7): 1977-1997.

[39] Ren WX, Sun ZS. Structural damage identification by using wavelet entropy. Engineering Structures. 2008; 30(10): 2840-2849.

[40] Yao R, Pakzad SN. Damage and noise sensitivity evaluation of autoregressive features extracted from structure vibration. Smart Materials and Structures. 2013; 23(2): 025007.

[41] Dorvash S, Pakzad SN. Effects of measurement noise on modal parameter identification. Smart Materials and Structures. 2012; 21(6): 065008.

[42] Mao Z, Todd MD. Statistical quantification of the uncertainty in transmissibility feature for structural condition binary classification. Health Monitoring and Biological Systems, Proceedings of SPIE. 2011; 7984:79842H.

[43] Mao Z, Todd MD. Statistical modeling of frequency response function estimation for uncertainty quantification. Mechanical Systems and Signal Processing. 2013; 38(2): 333-345.

[44] Cornwell P, Farrar CR, Doebling SW, Sohn H. Environmental variability of modal properties. Experimental Techniques. 1999; 23(6): 45-48.

[45] Peeters B. System identification and damage detection in civil engeneering. Ph.D thesis, University of Leuven, Belgium. 2000.

[46] Peeters B, Maeck J, De Roeck G. Vibration-based damage detection in civil engineering: excitation sources and temperature effects. Smart Materials and Structures. 2001; 10(3): 518.

[47] Yu L, Zhu JH. Structural damage detection of truss bridge under environmental variability. Applied Mathematics & Information Sciences. 2015; 9(1L): 259-265.

[48] Feng Z, Zhou Y, Zuo MJ, Chu F, Chen X. Atomic decomposition and sparse representation for complex signal analysis in machinery fault diagnosis: A review with examples. Measurement. 2017; 103(Supplement C): 106-132.

[49] Devriendt C, Guillaume P. Identification of modal parameters from transmissibility measurements. Journal of Sound and Vibration. 2008; 314(1): 343-356.

[50] Maia NMM, Silva JMM. Theoretical and experimental modal analysis. Research Studies Press. 1997.

[51] Peeters B, De Roeck G. Stochastic system identification for operational modal analysis: a review. Journal of Dynamic Systems, Measurement, and Control. 2001; 123(4): 659-667.

[52] Deraemaeker A, Reynders E, De Roeck G, Kullaa J. Vibration-based structural health monitoring using output-only measurements under changing environment. Mechanical Systems and Signal Processing. 2008; 22(1): 34-56.

[53] Rainieri C, Fabbrocino G. Operational modal analysis of civil engineering structures. Springer. 2014.

[54] Antoni J, Chauhan S. A study and extension of second-order blind source separation to operational modal analysis. Journal of Sound and Vibration. 2013; 332(4): 1079-1106.

[55] Cao SC, Ouyang HJ. Output-only damage identification using enhanced structural characteristic deflection shapes and adaptive gapped smoothing method. Journal of vibration and acoustics. 2018; 140(1): 011005.

[56] Yuen KV, Katafygiotis LS. Bayesian time–domain approach for modal updating using ambient data. Probabilistic Engineering Mechanics. 2001; 16(3): 219-231.

[57] Au SK, Zhang FL, Ni YC. Bayesian operational modal analysis: theory, computation, practice. Computers & structures. 2013; 126: 3-14.

[58] Araújo IG, Laier JE. Operational modal analysis using SVD of power spectral density transmissibility matrices. Mechanical Systems and Signal Processing. 2014; 46(1): 129-145.

[59] Van Overschee P, De Moor BL. Subspace identification for linear systems: Theory-Implementation-Applications. Springer Science & Business Media. 2012.

[60] Brincker R, Zhang LM, Andersen P. Modal identification of output-only systems using frequency domain decomposition. Smart Materials and Structures. 2001; 10(3): 441.

[61] Au SK. Fast Bayesian FFT method for ambient modal identification with separated modes. Journal of Engineering Mechanics. 2011; 137(3): 214-226.

[62] McNeill SI, Zimmerman DC. A framework for blind modal identification using joint approximate diagonalization. Mechanical Systems and Signal Processing. 2008; 22(7): 1526-1548.

[63] Cardoso JF, Souloumiac A. Jacobi angles for simultaneous diagonalization. SIAM journal on matrix analysis and applications. 1996; 17(1): 161-164.

[64] Pandey AK, Biswas M, Samman MM. Damage detection from changes in curvature mode shapes. Journal of Sound and Vibration. 1991; 145(2): 321-332.

[65] Douka E, Loutridis S, Trochidis A. Crack identification in plates using wavelet analysis. Journal of Sound and Vibration. 2004; 270(1–2): 279-295.

[66] Xu W, Radzieński M, Ostachowicz W, Cao M. Damage detection in plates using two-dimensional directional Gaussian wavelets and laser scanned operating deflection shapes. Structural Health Monitoring. 2013; 12(5-6): 457-468.

[67] Razdan A, Bae M. Curvature estimation scheme for triangle meshes using biquadratic Bézier patches. Computer-Aided Design. 2005; 37(14): 1481-1491.

[68] Surace C. Damage assessment of structures using only post-damage vibration measurements. Key Engineering Materials. 2013;569-570:11-22.

[69] Li HN, Ren L, Jia ZG, Yi TH, Li DS. State-of-the-art in structural health monitoring of large and complex civil infrastructures. Journal of Civil Structural Health Monitoring. 2016; 6(1): 3-16.

[70] Doebling SW, Farrar CR, Prime MB. A summary review of vibration-based damage identification methods. Shock and Vibration Digest. 1998; 30(2): 91-105.

[71] Rytter A. Vibrational based inspection of civil engineering structures. Ph.D. thesis, Aalborg University, Denmark. 1993.

[72] Farrar CR, Doebling SW. An overview of modal-based damage identification methods. Proceedings of DAMAS conference. 1997; pp. 269-278.

[73] Husain NA, Snaylam A, Khodaparast HH, James S, Dearden G, Ouyang HJ. FE model updating for damage detection–application to awelded structure. Key Engineering Materials. 2009; Vols. 413-414:393-400.

[74] Gul M, Catbas FN. Statistical pattern recognition for structural health monitoring using time series modeling: Theory and experimental verifications. Mechanical Systems and Signal Processing. 2009; 23(7): 2192-2204.

[75] Sohn H, Farrar CR, Hunter NF, Worden K. Structural health monitoring using statistical pattern recognition techniques. Journal of Dynamic Systems, Measurement, and Control. 2001; 123(4): 706-711.

[76] Friswell MI, Mottershead JE. Finite element model updating in structural dynamics. Springer Science & Business Media. 2013.

[77] Mottershead JE, Friswell MI, Mares C. A method for determining model‐structure errors and for locating damage in vibrating systems. Meccanica. 1999; 34(3): 153-166.

[78] Link M, Weiland M. Damage identification by multi-model updating in the modal and in the time domain. Mechanical Systems and Signal Processing. 2009; 23(6): 1734-1746.

[79] Gola MM, SomÀ A, Botto D. On theoretical limits of dynamic model updating using a sensitivity-based approach. Journal of Sound and Vibration. 2001; 244(4): 583-595.

[80] Mottershead JE, Link M, Friswell MI. The sensitivity method in finite element model updating: a tutorial. Mechanical Systems and Signal Processing. 2011; 25(7): 2275-2296.

[81] Shane C, Jha R. Proper orthogonal decomposition based algorithm for detecting damage location and severity in composite beams. Mechanical Systems and Signal Processing. 2011; 25(3): 1062-1072.

[82] Parloo E, Guillaume P, Van Overmeire M. Damage assessment using mode shape sensitivities. Mechanical Systems and Signal Processing. 2003; 17(3): 499-518.

[83] Lee U, Shin J. A frequency response function-based structural damage identification method. Computers & structures. 2002; 80(2): 117-132.

[84] Yoon MK, Heider D, Gillespie Jr JW, Ratcliffe CP, Crane RM. Local damage detection with the global fitting method using operating deflection shape data. Journal of nondestructive evaluation. 2010; 29(1): 25-37.

[85] Gentile A, Messina A. On the continuous wavelet transforms applied to discrete vibrational data for detecting open cracks in damaged beams. International Journal of Solids and Structures. 2003; 40(2): 295-315.

[86] Cao SC, Ouyang HJ. Robust structural damage detection and localization based on joint approximate diagonalization technique in frequency domain. Smart Materials and Structures. 2017; 26(1): 015005.

[87] Worden K, Manson G, Fieller NRJ. Damage detection using outlier analysis. Journal of Sound and Vibration. 2000; 229(3): 647-667.

[88] Marwala T, Hunt H. Fault identification using finite element models and neural networks. Mechanical Systems and Signal Processing. 1999; 13(3): 475-490.

[89] Worden K, Lane AJ. Damage identification using support vector machines. Smart Materials and Structures. 2001; 10(3): 540-547.

[90] Pawar PM, Ganguli R. Structural health monitoring using genetic fuzzy systems. Springer Science & Business Media. 2011.

[91] Li J, Hao H, Chen Z. Damage identification and optimal sensor placement for structures under unknown traffic-induced vibrations. Journal of Aerospace Engineering. 2015; 30(2): B4015001.

[92] Abu Husain N, Haddad Khodaparast H, Ouyang HJ. FE model updating of welded structures for identification of defects. International Journal of Vehicle Noise and Vibration. 2010; 6(2-4): 163-175.

[93] Yang YB, Chen YJ. Direct versus iterative model updating methods for mass and stiffness matrices. International Journal of Structural Stability and Dynamics. 2010; 10(02): 165-186.

[94] Marwala T. Finite element model updating using computational intelligence techniques: applications to structural dynamics. Springer Science & Business Media. 2010.

[95] Cichocki A, Zdunek R, Phan AH, Amari SI. Nonnegative matrix and tensor factorizations: applications to exploratory multi-way data analysis and blind source separation. John Wiley & Sons. 2009.

[96] Zhou YL, Maia NMM, Wahab MMA. Damage detection using transmissibility compressed by principal component analysis enhanced with distance measure. Journal of Vibration and Control. 2016; 1077546316674544.

[97] Doebling SW, Farrar CR, Prime MB, Shevitz DW. Damage identification and health monitoring of structural and mechanical systems from changes in their vibration characteristics: a literature review. Los Alamos National Lab., NM. 1996.

[98] Sohn H, Farrar CR, Hemez FM, Shunk DD, Stinemates DW, Nadler BR, et al. A review of structural health monitoring literature: 1996-2001. Los Alamos National Lab., NM. 2004.

[99] Fan W, Qiao PZ. Vibration-based damage identification methods: a review and comparative study. Structural Health Monitoring. 2011; 10(1): 83-111.

[100] Cao MS, Sha GG, Gao YF, Ostachowicz W. Structural damage identification using damping: a compendium of uses and features. Smart Materials and Structures. 2017; 26(4): 043001.

[101] Salawu OS. Detection of structural damage through changes in frequency: a review. Engineering Structures. 1997; 19(9): 718-723.

[102] Cawley P, Adams RD. The location of defects in structures from measurements of natural frequencies. The Journal of Strain Analysis for Engineering Design. 1979; 14(2): 49-57.

[103] Cerri MN, Vestroni F. Detection of damage in beams subjected to diffused cracking. Journal of Sound and Vibration. 2000; 234(2): 259-276.

[104] Gao HY, Guo XL, Ouyang HJ, Han F. Crack identification of cantilever plates based on a Kriging surrogate model. Journal of vibration and acoustics. 2013; 135(5): 051012.

[105] Chen HL, Spyrakos CC, Venkatesh G. Evaluating structural deterioration by dynamic response. Journal of Structural Engineering. 1995; 121(8): 1197-1204.

[106] Wang Z, Lin RM, Lim MK. Structural damage detection using measured FRF data. Computer methods in applied mechanics and engineering. 1997; 147(1-2): 187-197.

[107] Heylen W, Lammens S. FRAC: a consistent way of comparing frequency response functions. Proceedings of the Conference on Identification in Engineering Systems. 1996.

[108] Zang C, Friswell MI, Imregun M. Structural health monitoring and damage assessment using measured FRFs from multiple sensors, part I: The indicator of correlation criteria. Key Engineering Materials. 2003; 245: 131-140.

[109] Sampaio RPC, Maia NMM. Strategies for an efficient indicator of structural damage. Mechanical Systems and Signal Processing. 2009; 23(6): 1855-1869.

[110] Saravanan K, Sekhar AS. Crack detection in a rotor by operational deflection shape and kurtosis using laser vibrometer measurements. Journal of Vibration and Control. 2013; 19(8): 1227-1239.

[111] Salehi M, Ziaei-Rad S, Ghayour M, Vaziri-Zanjani MA. A frequency response based structural damage localization method using independent component analysis. Journal of Mechanical Science and Technology. 2013; 27(3): 609-619.

[112] Maia NMM, Urgueira APV, Almeida RAB. An overview of the transmissibility concept and its application to structural damage detection. Topics in Modal Analysis I. Springer. 2012;5: 137-151.

[113] Steenackers G, Devriendt C, Guillaume P. On the use of transmissibility measurements for finite element model updating. Journal of Sound and Vibration. 2007; 303(3): 707-722.

[114] Zhou YL, Figueiredo E, Maia NMM, Perera R. Damage detection and quantification using transmissibility coherence analysis. Shock and Vibration. 2015; 2015:290714.

[115] Fan Z, Feng X, Zhou J. A novel transmissibility concept based on wavelet transform for structural damage detection. Smart Structures and Systems. 2013; 12(3-4): 291-308.

[116] Shi ZY, Law SS, Zhang LM. Damage localization by directly using incomplete mode shapes. Journal of Engineering Mechanics. 2000; 126(6): 656-660.

[117] Chen HP, Bicanic N. Assessment of damage in continuum structures based on incomplete modal information. Computers & structures. 2000; 74(5): 559-570.

[118] Xiang JW, Liang M. A two-step approach to multi-damage detection for plate structures. Engineering Fracture Mechanics. 2012; 91: 73-86.

[119] Lee JJ, Lee JW, Yi JH, Yun CB, Jung HY. Neural networks-based damage detection for bridges considering errors in baseline finite element models. Journal of Sound and Vibration. 2005; 280(3): 555-578.

[120] Allemang RJ. The modal assurance criterion–twenty years of use and abuse. Sound and vibration. 2003; 37(8): 14-23.

[121] Salawu OS, Williams C. Bridge assessment using forced-vibration testing. Journal of Structural Engineering. 1995; 121(2): 161-173.

[122] Khan AZ, Stanbridge AB, Ewins DJ. Detecting damage in vibrating structures with a scanning LDV. Optics and Lasers in Engineering. 1999; 32(6): 583-592.

[123] Pawar PM, Venkatesulu Reddy K, Ganguli R. Damage detection in beams using spatial Fourier analysis and neural networks. Journal of Intelligent Material Systems and Structures. 2007; 18(4): 347-359.

[124] Fan W, Qiao PZ. A 2-D continuous wavelet transform of mode shape data for damage detection of plate structures. International Journal of Solids and Structures. 2009; 46(25–26): 4379-4395.

[125] Zhu XQ, Law SS. Wavelet-based crack identification of bridge beam from operational deflection time history. International Journal of Solids and Structures. 2006; 43(7): 2299-2317.

[126] Law SS, Li XY, Zhu XQ, Chan SL. Structural damage detection from wavelet packet sensitivity. Engineering Structures. 2005; 27(9): 1339-1348.

[127] Cao MS, Qiao PZ. Integrated wavelet transform and its application to vibration mode shapes for the damage detection of beam-type structures. Smart Materials and Structures. 2008; 17(5): 055014.

[128] Hadjileontiadis LJ, Douka E. Crack detection in plates using fractal dimension. Engineering Structures. 2007; 29(7): 1612-1625.

[129] Hadjileontiadis LJ, Douka E, Trochidis A. Fractal dimension analysis for crack identification in beam structures. Mechanical Systems and Signal Processing. 2005; 19(3): 659-674.

[130] Bai RB, Ostachowicz W, Radzieński M, Cao MS. Vibrational damage detection using fractal surface singularities with noncontact laser measurement. Journal of Vibration and Control. 2016; 22(11): 2569-2581.

[131] Qiao PZ, Cao MS. Waveform fractal dimension for mode shape-based damage identification of beam-type structures. International Journal of Solids and Structures. 2008; 45(22–23): 5946-5961.

[132] Xu YF, Zhu WD. Non-model-based damage identification of plates using measured mode shapes. Structural Health Monitoring. 2016; 16(1): 3-23.

[133] Pandey AK, Biswas M. Damage detection in structures using changes in flexibility. Journal of Sound and Vibration. 1994; 169(1): 3-17.

[134] Zhang Z, Aktan AE. Application of modal flexibility and its derivatives in structural identification. Journal of Research in Nondestructive Evaluation. 1998; 10(1): 43-61.

[135] Wang JL, Qiao PZ. Improved damage detection for beam-type structures using a uniform load surface. Structural Health Monitoring. 2007; 6(2): 99-110.

[136] Hu CS, Afzal MT. A statistical algorithm for comparing mode shapes of vibration testing before and after damage in timbers. Journal of Wood Science. 2006; 52(4): 348-352.

[137] Wahab MMA, De Roeck G. Damage detection in bridges using modal curvatures: application to a real damage scenario. Journal of Sound and Vibration. 1999; 226(2): 217-235.

[138] Cao MS, Xu W, Ren WX, Ostachowicz W, Sha GG, Pan LX. A concept of complex-wavelet modal curvature for detecting multiple cracks in beams under noisy conditions. Mechanical Systems and Signal Processing. 2016; 76: 555-575.

[139] Xu W, Cao MS, Ostachowicz W, Radzieński M, Xia N. Two-dimensional curvature mode shape method based on wavelets and Teager energy for damage detection in plates. Journal of Sound and Vibration. 2015; 347: 266-278.

[140] Ratcliffe CP. Damage detection using a modified Laplacian operator on mode shape data. Journal of Sound and Vibration. 1997; 204(3): 505-517.

[141] Yoon MK, Heider D, Gillespie JW, Ratcliffe CP, Crane RM. Local damage detection using the two-dimensional gapped smoothing method. Journal of Sound and Vibration. 2005; 279(1): 119-139.

[142] Rucevskis S, Janeliukstis R, Akishin P, Chate A. Mode shape-based damage detection in plate structure without baseline data. Structural Control and Health Monitoring. 2016; 23(9): 1180-1193.

[143] Stubbs N, Kim JT, Farrar CR. Field verification of a nondestructive damage localization and severity estimation algorithm. Proceedings-SPIE the international society for optical engineering. 1995; 2460:210-218.

[144] Maia NMM, Silva JMM, Almas EAM, Sampaio RPC. Damage detection in structures: from mode shape to frequency response function methods. Mechanical Systems and Signal Processing. 2003; 17(3): 489-498.

[145] Li H, Huang Y, Ou JP, Bao YQ. Fractal dimension - based damage detection method for beams with a uniform cross - section. Computer-Aided Civil and Infrastructure Engineering. 2011; 26(3): 190-206.

[146] Li YY. Hypersensitivity of strain-based indicators for structural damage identification: A review. Mechanical Systems and Signal Processing. 2010; 24(3): 653-664.

[147] Asnaashari E, Sinha JK. Crack detection in structures using deviation from normal distribution of measured vibration responses. Journal of Sound and Vibration. 2014; 333(18): 4139-4151.

[148] Douka E, Hadjileontiadis LJ. Time–frequency analysis of the free vibration response of a beam with a breathing crack. NDT & E International. 2005; 38(1): 3-10.

[149] Lu ZW, Dong DW, Ouyang HJ, Cao SC, Hua CR. Localization of breathing cracks in stepped rotors using super-harmonic characteristic deflection shapes based on singular value decomposition in frequency domain. Fatigue & Fracture of Engineering Materials & Structures. 2017;40:1825-1837.

[150] Todd MD, Nichols JM, Pecora LM, Virgin LN. Vibration-based damage assessment utilizing state space geometry changes: local attractor variance ratio. Smart Materials and Structures. 2001; 10(5): 1000-1008.

[151] Epureanu BI, Yin SH. Identification of damage in an aeroelastic system based on attractor deformations. Computers & structures. 2004; 82(31): 2743-2751.

[152] Carden EP, Fanning P. Vibration based condition monitoring: a review. Structural Health Monitoring. 2004; 3(4): 355-377.

[153] Yang J, Ouyang HJ, Zhang JF. A new method of updating mass and stiffness matrices simultaneously with no spillover. Journal of Vibration and Control. 2014; 1077546314535278.

[154] Yang ZB, Chen XF, Tian SH, He ZJ. Multiple damages detection in beam based approximate waveform capacity dimension. Structural Engineering and Mechanics. 2012; 41(5): 663-673.

[155] Pai PF, Young LG. Damage detection of beams using operational deflection shapes. International Journal of Solids and Structures. 2001; 38(18): 3161-3192.

[156] Xu H, Lu B, Su ZQ, Cheng L. Statistical enhancement of a dynamic equilibrium-based damage identification strategy: Theory and experimental validation. Journal of Sound and Vibration. 2015; 351: 236-250.

[157] Zhang C, Cheng L, Xu H, Qiu J. Structural damage detection based on virtual element boundary measurement. Journal of Sound and Vibration. 2016; 372: 133-146.

[158] Bai RB, Ostachowicz W, Cao MS, Su Z. Crack detection in beams in noisy conditions using scale fractal dimension analysis of mode shapes. Smart Materials and Structures. 2014; 23(6): 065014.

[159] Bellino A, Fasana A, Garibaldi L, Marchesiello S. PCA-based detection of damage in time-varying systems. Mechanical Systems and Signal Processing. 2010; 24(7): 2250-2260.

[160] Wu CG, Liang YC, Lin WZ, Lee HP, Lim SP. A note on equivalence of proper orthogonal decomposition methods. Journal of Sound and Vibration. 2003; 265(5): 1103-1110.

[161] Liang YC, Lee HP, Lim SP, Lin WZ, Lee KH, Wu CG. Proper orthogonal decomposition and its applications—Part I: Theory. Journal of Sound and Vibration. 2002; 252(3): 527-544.

[162] Kerschen G, Poncelet F, Golinval JC. Physical interpretation of independent component analysis in structural dynamics. Mechanical Systems and Signal Processing. 2007; 21(4): 1561-1575.

[163] Garcia D, Palazzetti R, Trendafilova I, Fiorini C, Zucchelli A. Vibration-based delamination diagnosis and modelling for composite laminate plates. Composite Structures. 2015; 130(Supplement C): 155-162.

[164] García D, Trendafilova I. A multivariate data analysis approach towards vibration analysis and vibration-based damage assessment: application for delamination detection in a composite beam. Journal of Sound and Vibration. 2014; 333(25): 7036-7050.

[165] Law SS, Liu K. Integrating singular spectrum analysis with damage detection of structure. Key Engineering Materials. 2013;569-570:831-838.

[166] Kerschen G, Golinval J-c, Vakakis AF, Bergman LA. The method of proper orthogonal decomposition for dynamical characterization and order reduction of mechanical systems: an overview. Nonlinear Dynamics. 2005; 41(1-3): 147-169.

[167] Dosiek L, Zhou N, Pierre JW, Huang ZY, Trudnowski DJ. Mode shape estimation algorithms under ambient conditions: A comparative review. IEEE Transactions on Power Systems. 2013; 28(2): 779-787.

[168] Trendafilova I, Cartmell MP, Ostachowicz W. Vibration-based damage detection in an aircraft wing scaled model using principal component analysis and pattern recognition. Journal of Sound and Vibration. 2008; 313(3): 560-566.

[169] Basseville M, Mevel L, Goursat M. Statistical model-based damage detection and localization: subspace-based residuals and damage-to-noise sensitivity ratios. Journal of Sound and Vibration. 2004; 275(3–5): 769-794.

[170] Antoni J, Castiglione R, Garibaldi L. Interpretation and generalization of complexity pursuit for the blind separation of modal contributions. Mechanical Systems and Signal Processing. 2017; 85: 773-788.

[171] Chelidze D, Zhou WL. Smooth orthogonal decomposition-based vibration mode identification. Journal of Sound and Vibration. 2006; 292(3-5): 461-473.

[172] Cichocki A, Amari SI. Adaptive blind signal and image processing: learning algorithms and applications. John Wiley & Sons. 2002.

[173] Zhou WL, Chelidze D. Blind source separation based vibration mode identification. Mechanical Systems and Signal Processing. 2007; 21(8): 3072-3087.

[174] Musafere F, Sadhu A, Liu K. Towards damage detection using blind source separation integrated with time-varying auto-regressive modeling. Smart Materials and Structures. 2016; 25(1): 015013.

[175] Pesquet-Popescu B, Pesquet JC, Petropulu AP. Joint singular value decomposition - a new tool for separable representation of images. Proceedings 2001 International Conference on Image Processing. 2001; 2: 569-582.

[176] Hori G. Comparison of two main approaches to joint svd. International Conference on Independent Component Analysis and Signal Separation. 2009; pp. 42-49.

[177] Congedo M, Phlypo R, Pham DT. Approximate joint singular value decomposition of an asymmetric rectangular matrix set. IEEE Transactions on Signal Processing. 2011; 59(1): 415-424.

[178] Kim BH, Stubbs N, Park T. A new method to extract modal parameters using output-only responses. Journal of Sound and Vibration. 2005; 282(1): 215-230.

[179] Flury B. Common principal components and related multivariate models. John Wiley & Sons. 1988.

[180] Galvanetto U, Violaris G. Numerical investigation of a new damage detection method based on proper orthogonal decomposition. Mechanical Systems and Signal Processing. 2007; 21(3): 1346-1361.

[181] Mendrok K, Uhl T. Experimental verification of the damage localization procedure based on modal filtering. Structural Health Monitoring. 2011; 10(2): 157-171.

[182] Feng X, Zhou J, Sun CS, Zhang XT, Ansari F. Theoretical and experimental investigations into crack detection with BOTDR-distributed fiber optic sensors. Journal of Engineering Mechanics. 2013; 139(12): 1797-1807.

[183] Yang ZC, Yu ZF, Sun H. On the cross correlation function amplitude vector and its application to structural damage detection. Mechanical Systems and Signal Processing. 2007; 21(7): 2918-2932.

[184] Asnaashari E, Sinha JK. Development of residual operational deflection shape for crack detection in structures. Mechanical Systems and Signal Processing. 2014; 43(1–2): 113-123.

[185] Chang CC, Chen LW. Detection of the location and size of cracks in the multiple cracked beam by spatial wavelet based approach. Mechanical Systems and Signal Processing. 2005; 19(1): 139-155.

[186] Cao MS, Radzieński M, Xu W, Ostachowicz W. Identification of multiple damage in beams based on robust curvature mode shapes. Mechanical Systems and Signal Processing. 2014; 46(2): 468-480.

[187] Masciotta MG, Ramos LF, Lourenço PB, Vasta M, De Roeck G. A spectrum-driven damage identification technique: Application and validation through the numerical simulation of the Z24 Bridge. Mechanical Systems and Signal Processing. 2016; 70-71: 578-600.

[188] Masciotta MG, Ramos LF, Lourenço PB, Vasta M. Spectral algorithm for non-destructive damage localisation: application to an ancient masonry arch model. Mechanical Systems and Signal Processing. 2017; 84: 286-307.

[189] Chondros TG, Dimarogonas AD, Yao J. Vibration of a beam with a breathing crack. Journal of Sound and Vibration. 2001; 239(1): 57-67.

[190] Rzeszucinski PJ, Sinha JK, Edwards R, Starr A, Allen B. Amplitude of probability density function (APDF) of vibration response as a robust tool for gearbox diagnosis. Strain. 2012; 48(6): 510-516.

[191] Qian GL, Gu SN, Jiang JS. The dynamic behaviour and crack detection of a beam with a crack. Journal of Sound and Vibration. 1990; 138(2): 233-243.

[192] ABAQUS. Version 6.14 User's Manual, Dassault Systemes Simulia Corp., Providence, RI, USA. 2014.

[193] Filliben JJ. The probability plot correlation coefficient test for normality. Technometrics. 1975; 17(1): 111-117.

[194] Bai R, Ostachowicz W, Radzieński M, Cao M. Vibrational damage detection using fractal surface singularities with noncontact laser measurement. Journal of Vibration and Control. 2014: 1077546314548088.

[195] Wildy SJ. Scanning laser doppler vibrometry for strain measurement and damage detection. Ph.D. thesis, University of Adelaide, Australia. 2012.

[196] Wu D, Law SS. Damage localization in plate structures from uniform load surface curvature. Journal of Sound and Vibration. 2004; 276(1): 227-244.

[197] Qiao PZ, Lu K, Lestari W, Wang JL. Curvature mode shape-based damage detection in composite laminated plates. Composite Structures. 2007; 80(3): 409-428.

[198] Surace C, Saxena R, Gherlone M, Darwich H. Damage localisation in plate like-structures using the two-dimensional polynomial annihilation edge detection method. Journal of Sound and Vibration. 2014; 333(21): 5412-5426.

[199] Chang CC, Chen LW. Damage detection of a rectangular plate by spatial wavelet based approach. Applied Acoustics. 2004; 65(8): 819-832.

[200] Rao SS. Vibration of continuous systems. John Wiley & Sons. 2007.

[201] Sirca GF, Adeli H. System identification in structural engineering. Scientia Iranica. 2012; 19(6): 1355-1364.

[202] Lindeberg T. Discrete scale-space theory and the scale-space primal sketch. KTH Royal Institute of Technology. 1991.

[203] Lindeberg T. Scale-space theory in computer vision. Springer Science & Business Media. 2013.

[204] Lindeberg T. Feature detection with automatic scale selection. International journal of computer vision. 1998; 30(2): 79-116.

[205] Lindeberg T. Image matching using generalized scale-space interest points. Journal of Mathematical Imaging and Vision. 2015; 52(1): 3-36.

[206] Timoshenko SP, Woinowsky-Krieger S. Theory of plates and shells. McGraw-hill. 1959.

[207] O'Neill B. Elementary differential geometry. Academic Press. 1997.

[208] Meyer M, Desbrun M, Schröder P, Barr AH. Discrete differential-geometry operators for triangulated 2-manifolds. Visualization and mathematics. 2002; 3(2): 52-58.

[209] Rusinkiewicz S. Estimating curvatures and their derivatives on triangle meshes. Proceedings 2nd International Symposium on 3D Data Processing, Visualization and Transmission. 2004; 486-493.

[210] Cazals F, Pouget M. Estimating differential quantities using polynomial fitting of osculating jets. Computer Aided Geometric Design. 2005; 22(2): 121-146.

[211] Goldfeather J, Interrante V. A novel cubic-order algorithm for approximating principal direction vectors. ACM Transactions on Graphics (TOG). 2004; 23(1): 45-63.

[212] Ferreira AJM. MATLAB codes for finite element analysis: solids and structures. Springer Science & Business Media. 2008.

[213] Reddy JN. An introduction to the finite element method. McGraw-Hill, New York. 1993.

[214] Yang YC, Sun P, Nagarajaiah S, Bachilo SM, Weisman RB. Full-field, high-spatial-resolution detection of local structural damage from low-resolution random strain field measurements. Journal of Sound and Vibration. 2017; 399: 75-85.

[215] Jones DR. A taxonomy of global optimization methods based on response surfaces. Journal of global optimization. 2001; 21(4): 345-383.

[216] Forrester A, Sobester A, Keane A. Engineering design via surrogate modelling: a practical guide. John Wiley & Sons. 2008.

[217] Candès EJ, Li XD, Ma Y, Wright J. Robust principal component analysis? Journal of the ACM. 2011; 58(3): Article 11:1-37.

[218] Zhou ZH, Li XD, Wright J, Candes E, Ma Y. Stable principal component pursuit. IEEE International Symposium on Information Theory Proceedings. 2010; 1518-1522.

[219] De la Torre F, Black MJ. Robust principal component analysis for computer vision. Proceedings Eighth IEEE International Conference on Computer Vision. 2001; 1:362-369.

[220] Kim JT, Stubbs N. Damage localization in structures without baseline modal parameters. AIAA Journal. 1996; 34(8):1644-1649.